ACCESSING NATURE'S TERPENOME

BY SQUALENE-HOPENE CYCLASE MEDIATED

ASYMMETRIC CATIONIC CYCLIZATION CASCADES

Von der Fakultät Chemie der Universität Stuttgart zur Erlangung der Würde eines Doktors der Naturwissenschaften (Dr. rer. nat.) genehmigte Abhandlung

Vorgelegt von

Andreas Schneider

aus Cottbus

Hauptberichter:	Prof. Dr. Bernhard Hauer
Mitberichter:	Prof. Dr. René Peters
Vorsitzender:	Prof. Dr. Elias Klemm
Tag der mündlichen Prüfung:	25.07.2022

Institut für Biochemie und Technische Biochemie

Abteilung Technische Biochemie

Universität Stuttgart

- 2022 –

Erklärung über die Eigenständigkeit der Dissertation

Ich versichere, dass ich die vorliegende Arbeit mit dem Titel „Accessing nature's terpenome by squalene-hopene cyclase mediated asymmetric cationic cyclization cascades" selbständig verfasst und keine anderen als die angegebenen Quellen und Hilfsmittel benutzt habe; aus fremden Quellen entnommene Passagen und Gedanken sind als solche kenntlich gemacht.

Declaration of Authorship

I hereby certify that the dissertation entitled „Accessing nature's terpenome by squalene-hopene cyclase mediated asymmetric cationic cyclization cascades" is entirely my own work except where otherwise indicated. Passages and ideas from other sources have been clearly indicated.

Name/Name: Andreas Schneider

Signed/Unterschrift: _____

Date/Datum: 06.05.2022

Die vorliegende Arbeit entstand unter der Anleitung von Herrn Prof. Dr. Bernhard Hauer in der Zeit von März 2017 bis Dezember 2021 am Institut für Biochemie und Technische Biochemie, Abteilung Technische Biochemie der Universität Stuttgart.

Im Rahmen dieser Dissertation wurden folgende Publikationen/ Patente veröffentlicht:

A. Schneider, B. Hauer, "Enzymatic monocyclization of acyclic monoterpenoids", Patent EP 21160100.0, **2021**.

A. Schneider, P. Jegl, B. Hauer. "Stereoselective Directed Cationic Cascades Enabled by Molecular Anchoring in Terpene Cyclases." *Angew. Chemie - Int. Ed.* **2021**, *60*, 13251–13256.
This paper has been highlighted by Nature Catalysis (J. S. Völler, *Nat. Catal.* **2021**, *4*, 262.), Synfacts (B. List, M. Turberg, *Synfacts* **2021**, *17*, 1137.) and as a VIP paper in Angewandte Chemie.

A. Schneider, B. Hauer. "Products and process for the production (–)-ambroxide." Patent EP 208910, **2021**.

A. I. Benítez-Mateos, **A. Schneider**, E. Hegarty, B. Hauer, and F. Paradisi. "Spheroplasts preparation boosts the catalytic potential of a terpene cyclase." *ChemRxiv* **2022**, doi: 10.26434/chemrxiv-2022-w08d0. Submitted.

A. Schneider, C. Curado, T. B. Lystbaek, S. Osuna, B. Hauer. "Tailoring the squalene-hopene cyclase for stereoconvergent and efficient cationic cyclizations." Submitted.

A. Schneider, J. Ruppert, T. B. Lystbaek, S. Bastian, B. Hauer. „Extending the cation cage: squalene-hopene cyclase-mediated enantioselective semi-pinacol rearrangement." Submitted.

DANKSAGUNG

An erster Stelle möchte ich mich bei Herrn Prof. Bernhard Hauer für die Aufnahme in den Arbeitskreis und die Ermöglichung dieses faszinierenden Projekts bedanken. Auch möchte ich mich ganz herzlich für die zahlreichen, sowie spannenden Diskussionen rund um neue kreative Syntheserouten und den tiefen Einblick in die Welt der industriellen Biokatalyse bedanken.

Herrn Prof. René Peters danke ich für freundlichen Übernahme des Mitberichters und Herrn Prof. Elias Klemm danke ich für die freundliche Übernahme des Vorsitzes des Prüfungsausschusses.

Weiterhin gilt ein besonderer Dank Jun.-Prof. Stephan Hammer, der mit seiner Passion für die Wissenschaft und Enzymologie auch meine Leidenschaft dafür erweckte. Vielen Dank für die zahlreichen Challenges, die mich jedes Mal dazu bewegten meinen Horizont noch etwas mehr zu erweitern. Ich bedanke mich auch besonders bei Frau Dr. Bettina Nestl für viele hilfreiche Diskussionen und Herrn Dr. Bernd Nebel für die umfassende Einführung und Unterstützung in allen Bereichen der analytischen Chemie. Beiden danke ich für die positive Energie und die ausgezeichnete Betreuung im Labor.

Ich möchte mich ganz herzlich bei meinen Kollegen als auch Freunden Dr. Peter Heinemann, Dr. Lea Rapp, Dr. Max Fischer und Dr. Andreas Hunold bedanken, die mir im Labor jederzeit mit Rat und Tat zur Hilfe standen und außerhalb vom Labor unvergessliche Abende bescherten. Ich bedanke mich auch bei allen anderen Mitgliedern des Arbeitskreises, die mich während dieser aufregenden Zeit begleitet haben: Dr. Benjamin Aberle, Kristina Schell, Julian Ludwig, Dr. Julian Wissner, Dr. Wendy Escobedo, Dr. Sebastian Gergel, Philip Horz, Natalie Härterich, Jonathan Berger, Jona Schelle, Dr. Ludwig Bengel, Dr. Niels Borlinghaus, Dr. Philipp Trauzettel, Dr. Leonie Weinmann, Dr. Jan Klenk, Dr. Matthias Wehrmann, Pascal Reis, Matus Gajdos, Cindy Klaus, Dr. Theresa Farr und viele mehr.

Für die permanente Instandhaltung des Labors möchte ich mich bei Melanie Allgaier, Lisa Kontny und Sven Richter bedanken.

Ich bedanke mich ganz herzlich bei meinen Bachlor- und Masterstudenten Jonathan Berger für die Mitentwicklung des 96-DW screening assays, Philipp Jegl für den unermüdlichen Einsatz während der Suche nach der Monozyklisierung und Jacqueline Ruppert für die tatkräftige Unterstützung während der Pinakol-Studien. Mein ganz besonderer Dank gilt Thomas Lystbaek, für die permanente Unterstützung in bis zu sechs Projekten gleichzeitig und die dänische Gelassenheit, die jederzeit eine angenehme Grundstimmung ins Labor brachte.

Ich danke Dr. Ana Benitez-Mateos, Prof. Dr. Francesca Paradisi, Christian Curado, Prof. Dr. Silvia Osuna, Prof. Dr. Niels Hansen und Dr. Daniel Markthaler für die fruchtbaren Zusammenarbeiten auf dem Gebiet der Squalen-Hopen-Zyklasen.

Ich möchte auch Herrn Prof. Andreas Schrell, Dr. Jakob Knelles, Herrn Prof. Nils Heide und Herrn Dr. Ralf Kaun für die Unterstützung bei der Ausarbeitung der Patente danken.

Für die Unterstützung während der Korrekturphase möchte ich mich bei Peter Heinemann, Kristina Schell, Julian Ludwig, Benjamin Aberle und Sebastian Gergel bedanken.

Ich bedanke mich bei der DFG für die finanzielle Unterstützung des Projekts.

Zum Ende möchte ich mich bei meiner Familie bedanken, ohne die diese Arbeit nicht möglich gewesen wäre. In diesem Zusammenhang möchte ich mich auch ganz besonders bei Johanna Haußmann bedanken, die mich zu jeder Zeit während der Dissertation unterstütze und mein Fels in der Brandung war. Danke.

Für Irina Schneider

CONTENTS

ABBREVIATIONS

96 DW	Polypropylene plate with 96 reaction chambers
2HPCD	2-hydroxypropyl-β-cyclodextrin
Aac	Alicyclobacillus acidocaldarius
CHAPS	3-[(3-Cholamidopropyl)-dimethylammonio]-1-propansulfonate
CH	Cyclohexane
CD	Cylodextrin
CDW	Cell dry weight
cf	Confer
CWW	Cell wet weight
d	Days
de	Diastereomeric excess
dr	Diastereomeric ratio
DMAPP	Dimethylallyl pyrophosphate
DMSO	Dimethylsulfoxid
DCM	Dichloromethane
ee	Enantiomeric excess
er	Enantiomeric ratio
e. g.	Example given
EtOAc	Ethyl acetate
eq	Equivalent
E. coli	Escherichia coli
FID	Flame ionization detector
FPP	Farnesyl pyrophosphate
GC	Gas chromatography
GPP	Geranyl pyrophosphate
GGPP	Geranyl geranyl pyrophosphate
h	Hour
i. a.	Inter alia
IDPi	Imidodiphosphorimidate
i. e.	Id est
ISPC	*In situ* product crystallization
ISPR	*In situ* product removal
ITB	Institute of Biochemistry and Technical Biochemistry
LB	Lysogeny broth
m	Mass
M	Molar
MD	Molecular dynamics
min	Minute
MHz	Megahertz
MS	Mass spectrometry

NMR	Nuclear magnetic resonance
OD_{600}	Optical density measured at 600 nm
PAGE	Polyacrylamid gel electrophoresis
PCR	Polymerase chain reaction
PDB	Protein data base
ppm	Parts per million
r. t.	Room temperature
s	Second
s. d.	Standard deviation
SDS	Sodium dodecyl sulfate
SHC	Squalene-hopene cyclase
STY	Space-time yield
TAE	Tris Acetate EDTA
TB	Terrific broth
T-DAB	Terrific-high density autoinduction broth
THF	Tetrahydrofurane
TOF	Turnover frequency
TRIS	Tris-(hydroxymethyl)-aminomethan
TTN	Total turnover number
WT	Wild-type
µ	Micro

"*It is the level of perfection achieved by organic chemistry [...] which is enabling biochemistry to penetrate the innermost secrets of life processes on a molecular basis, and this will more and more blur the distinction between the two disciplines*."

– Albert Eschenmoser, *Chimia 44*, 1990 –

ZUSAMMENFASSUNG

Das Terpenom umfasst die vielfältigste strukturelle Bibliothek natürlicher Verbindungen, die in allen Lebensformen allgegenwärtig sind, und stellt somit den Inbegriff der molekularen Biodiversität dar. Synthesechemiker waren seit jeher von der Komplexität der Terpene fasziniert, da es sie vor eine große intellektuelle Herausforderung stellte, die komplexen, meist polyzyklischen Kohlenwasserstoffgerüste, mit zahlreichen funktionellen Gruppen ausgestattet, zusammenzusetzen. Folglich umfassen die Bemühungen, das Terpenom der Natur zu erschließen, oft die modernsten synthetischen und katalytischen Werkzeuge, die der organischen Chemie zur Verfügung stehen. Mit dem Aufkommen der Biokatalyse wurde dieser konzeptionelle Werkzeugkasten erheblich erweitert, z. B. durch regio- und stereoselektive C(sp^3)-H-Oxidationen von Terpenen durch P450-Monooxygenasen. Diese Entwicklung eröffnete völlig neue retrosynthetische Betrachtungen mit Hilfe hybrider chemoenzymatischer Katalyse. Diese Arbeit konzentriert sich auf die Erweiterung des retrosynthetischen Werkzeugkastens durch biokatalytische *formkomplementäre* kationische Zyklisierungskaskaden und die damit verbundene Etablierung hybrider Totalsynthesewege zu komplexen Terpenen.

Eine bestehende Herausforderung in der Terpen-Totalsynthese ist der stereochemisch präzise Aufbau des zyklischen Kohlenwasserstoffgerüsts durch kationische Zyklisierung. Trotz vielversprechender Fortschritte in der nieder- als auch supramolekularen Katalyse ist ein Katalysator, der in der Lage ist, ein zyklisches Terpen zielgerichtet und mit absoluter Kontrolle über den Fortschritt, die Stereoselektivität und die Termination der kationischen Kaskade zu erzeugen, noch immer nicht vorhanden. Zu diesem Zweck hat die Natur Terpen-Zyklasen wie die Squalen-Hopen-Zyklase (SHC) entwickelt, die über die herausragende Fähigkeit der *formkomplementären* kationischen Zyklisierungskaskaden verfügen, die die absolute Kontrolle über mehrere Stereozentren innerhalb einer einzigen Cofaktor-unabhängigen Reaktion ermöglichen. Darüber hinaus haben wegweisende Arbeiten gezeigt, dass dieses Enzym sehr promiskuitiv ist und Dutzende von Substraten durch asymmetrische Brønsted-Säure-Katalyse umsetzen kann. Angesichts dieses enormen katalytischen Potenzials diente die SHC aus *Alicyclobacillus acidocaldarius* als Vorbild für eine ganzheitliche Untersuchung dieser

komplexen supramolekularen Maschinerie, um ihre präzise Katalyse für die organische Chemie nutzbar zu machen.

Im ersten Teil dieser Arbeit wurde das katalytische Repertoire der *Aac*SHC um die biokatalytisch gerichtete kationische Zyklisierungskaskade erweitert, eine in der chemischen Katalyse bisher beispiellose Art der Zyklisierung. Zunächst wurde hierfür ein GC/MS-basierter *in vivo* Screening-Assay etabliert, um den Durchsatz an Enzymvarianten von etwa 24 pro Woche auf über 200 pro Tag zu erhöhen. Als Modellreaktion wurde die Monozyklisierung von Nerylaceton zu (–)-γ-Dihydroionon ausgewählt, da sie in der Aroma- und Duftstoffindustrie von großem Interesse ist. Durch die Kombination von rationalen, ortsgerichteten und ortssättigenden Mutagenesemethoden mit *in silico* Docking-Untersuchungen wurde das Enzym in vier Runden evolviert, um die TTN von 3 auf 448 zu erhöhen und die gewünschte Monozyklisierung mit absoluter Kontrolle über Stereoselektivität (>99.5% *ee*), Regioselektivität (97%) und Kaskadenverlauf (99:1, Mono-:Bizyklisierung) im Gramm-Maßstab (89% isolierte Ausbeute) zu ermöglichen. Die Docking-Untersuchungen und ein systematischer Dekonvolutionsansatz legten eine durch Wasserstoffbrücken vermittelte Vorfaltung durch Verankerung der Ketogruppe des Substrats im aktiven Zentrum als Ursprung der Kaskadenkontrolle nahe. So wurde die formkomplementäre Zyklisierung durch die Ausnutzung der funktionellen Gruppe eines nicht-natürlichen Substrats erweitert. Die gerichtete kationische Kaskade ermöglichte die Substitution einer 5-stufigen Synthese von (–)-γ-Dihydroionon mit geringer Ausbeute und mäßiger Selektivität (25% Ausbeute, 55% *ee*) durch eine vollständig selektive einstufige Zyklisierung in Wasser.

Im zweiten Teil der Arbeit wurde die archetypische promiskuitive Reaktion des *Aac*SHC untersucht: die stereoselektive Trizyklisierung von Homofarnesol zu dem wertvollen Duftstoff (–)-Ambroxid. Zunächst wurde das Enzym innerhalb von drei Runden mit Hilfe eines Dualen-Standort-allokierten Mutagenese-Ansatzes zur bis zum heutigen Stand aktivsten (TOF >600 h^{-1}) und selektivsten (>99.5% *ee*, >99.5% *de*) Homofarnesol-Ambroxid-Zyklase evolviert. Diese Strategie kombiniert auf synergetische Weise die rationale strukturgeführte Mutagenese des aktiven Zentrums mit dem Engineering des dynamischen Eingangstunnels des Enzyms. Interessanterweise haben MD-Simulationen gezeigt, dass durch die Einführung der Mutationen im Eingangstunnel des Enzymes ein

Phenylalanin, welches das Eingangstor bildet, beeinflusst wird. Dadurch wird ein „immer-offen" Zustand erzwungen, was zu einer Erhöhung des enzymatischen Umsatzes führte. Ein Vergleich mit SHC Homologen verdeutlichte die Notwendigkeit zugänglicher Eletrinonendichte für die hohe Selektivität des Enzymes und eröffnete eine bisher unbekannte stereokonvergente kationische Zyklisierung eines *cis*/*trans* Isomerengemischs des Substrats. Anschließend ergaben kinetische Untersuchungen ausgewählter *Aac*SHC-Varianten *in vitro* und *in vivo*, dass eine starke Substrathemmung während des *in vivo* Experiments auftrat. Es wurde vermutet, dass die übermäßige Diffusion des Substrats Homofarnesol in die Biomembran, in der das Enzym verankert ist, eine Störung der Membranintegrität verursachte, die schließlich das Enzym hemmte. Diese Ergebnisse lieferten wertvolle Einblicke in die physiologische Funktion und Regulation eines monotopisch membrangebundenen Enzyms und könnten sich auf medizinische Therapien, die auf verwandte Enzyme abzielen, auswirken. Mithilfe der *in situ* Produktkristallisation von (–)-Ambroxid wurde schließlich eine Fütterungsstrategie angewandt, um über 190.000 TTNs mit dem evolvierten Enzym zu erreichen.

Das Ziel des dritten Teils war die tatsächliche Implementierung der SHC-vermittelten formkomplementären Zyklisierung und der gerichteten kationischen Zyklisierung in Totalsyntheserouten für komplexe Terpene. Dazu wurde zunächst ein allgemeines Katalyse-Setup unter Verwendung von lyophilisiertem *E. coli* Pulver erstellt, wodurch der Katalysator lagerfähig und die anspruchsvolle Kopf-Schwanz Zyklisierung zu simpler Rührkessel-Chemie vereinfacht wurde. Anschließend wurde gezeigt, dass flüssige Zyklisierungsprodukte eine zeitabhängige Hemmung des Enzyms hervorrufen, die durch die Verwendung von 2-Hydroxypropyl-β-Cyclodextrin zur *in situ* Produktentfernung durch Enkapsulierung umgangen werden konnte. Computergestützte Untersuchungen zeigten, dass der hydrophobe Kern des Cyclodextrins und das Innere der Membran konkurrierende Umgebungen für die Diffusion von Terpenen sind. Diese Daten lieferten weitere Beweise für die regulierende Funktion der Membran auf dem SHC. Nachdem die optimalen Bedingungen für die Katalyse erarbeitet worden waren, wurden drei komplexe Meroterpene retrosynthetisch in hybride chemoenzymatische Syntheserouten zerlegt, die der hier etablierten biokatalytischen kationischen Zyklisierung beinhalteten. In der Vorwärtsreaktion wurden zunächst sechs lineare Terpene, die sich in Kettenlänge und funktioneller

Gruppe unterschieden, durch mehrere evolvierte SHC-Varianten zyklisiert, die eine ausgezeichnete Kontrolle über den Fortschritt, die Stereoselektivität (bis zu fünf Stereozentren) und die Termination der kationischen Kaskade ermöglichten. Diese chiralen Templates wurden dann mit einfachen katalytischen und synthetischen Methoden in komplexe Meroterpene umgewandelt, wodurch der schwierige Schritt der kationischen Zyklisierung entschärft und frühere langwierige Synthesewege um über 50% verkürzt werden konnten.

Insgesamt wurde die Implementierung biokatalytischer *formkomplementärer* kationischer Zyklisierungskaskaden in der organischen Chemie nicht nur erfolgreich demonstriert, sondern auch durch die Einführung von präzise gesetzten Wasserstoffbrückenbindungen zur Steuerung der kationischen Zyklisierungskaskade sinnvoll ergänzt. Des Weiteren ermöglichte diese präzise Vorfaltung des Substrats eine stereokonvergente kationische Zyklisierung. Eine ganzheitliche Betrachtung des Enzyms und seiner physiologischen Funktion ermöglichte darüber hinaus Raum-Zeit-Ausbeuten, die weit über die bisher ermittelten Grenzen hinausgehen und es auf eine Stufe mit industriell eingesetzten Enzymen stellen. Zusammenfassend lässt sich sagen, dass diese Arbeit das übergreifende Bestreben der Chemie unterstützt, die *ideale Synthese* zu erreichen, indem sie die Katalysatoren der Natur nutzbar macht.

ABSTRACT

The terpenome comprises the most diverse structural library of natural compounds ubiquitous in all life forms, and thus represents the epitome of molecular biodiversity. Synthetic chemists were particularly drawn to the intrinsic complexity of terpenes, as it deserves a significant intellectual challenge to assemble the structurally restricted polycyclic hydrocarbon scaffolds decorated with multiple functional groups. Consequently, laboratory efforts to access nature's terpenome often encompass the state-of-the-art synthetic and catalytic methods available to organic chemistry. With the ascent of biocatalysis, this conceptual toolbox was vastly expanded, e.g., by regio- and stereoselective late-stage C(sp^3)-H oxidations of terpenes by P450 monooxygenases. This development unlocked entirely new retrosynthetic considerations with the aid of hybrid chemoenzymatic catalysis. This thesis focuses on the expansion of the retrosynthetic toolbox by biocatalytic *shape-complementary* cationic cyclization cascades and the related establishment of hybrid total synthesis routes towards complex terpenes.

A remaining challenge in terpene total synthesis is the stereochemically precise assembly of the cyclic hydrocarbon skeleton by means of cationic cyclization. Despite promising advances in small-molecule and supramolecular catalysis, a catalyst which is able to generate a target-oriented cyclic terpene with absolute control over progress, stereoselectivity and termination of the cationic cascade is still elusive. To this end, nature evolved terpene cyclases such as the squalene-hopene cyclase (SHC) with the powerful ability of *shape-complementary* cationic cyclization cascades enabling the absolute control over multiple stereocenters within a single cofactor-independent reaction. Moreover, seminal works have shown the SHCs broad promiscuity, converting dozens of substrates via asymmetric Brønsted acid catalysis. Given this enormous catalytic potential, the SHC from *Alicyclobacillus acidocaldarius* served as a role model for a holistic investigation on this complex supramolecular machinery to ultimately harness their precise catalysis for organic chemistry.

In the first part of this work, the catalytic repertoire of the SHC was extended by the biocatalytic directed cationic cyclization cascade, which was so far unprecedented in chemocatalysis. Initially, a GC/MS based *in vivo* screening assay was established to increase the assaying throughput of enzyme variants from about 24 per week to over 200

per day. As a model reaction, the monocyclization of neryl acetone towards (–)-γ-dihydroionone was chosen as it is of high interest in the flavor and fragrance industry. Merging rational site-directed and site-saturation mutagenesis methods with *in silico* docking investigations, the enzyme was evolved in four rounds to increase the TTN from 3 to 448 and permit the desired monocyclization with absolute control over stereoselectivity (>99.5% *ee*), regioselectivity (97%) and cascade progress (99:1, mono-:bicyclization) on a gram-scale (89% isolated yield). The docking investigations and a systematic deconvolution approach suggested hydrogen-bond mediated pre-folding by means of anchoring the substrate's keto-group in the active site as the source of cascade control. Thus, the *shape-complementary* cyclization was enhanced by leveraging a non-natural substrate's functional group. The directed cationic cascade enabled the substitution of a 5-step synthesis of (–)-γ-dihydroionone with low yield and moderate selectivity (25% yield, 55% *ee*) by a fully selective one-step cyclization in water.

In the second part, the archetype promiscuous reaction of the *Aac*SHC was investigated: the stereoselective tricyclization of homofarnesol towards the high-value fragrance ingredient (–)-ambroxide. First, the enzyme was evolved within three rounds to the most active (TOF >600 h^{-1}) and selective (>99.5% *ee*, >99.5% *de*) homofarnesol-ambroxide cyclase to this day using a dual-site allocated mutagenesis approach. This strategy synergistically combined the rational structure-guided mutagenesis of the active site with engineering the enzyme's dynamic entrance tunnel. Intriguingly, MD-simulations have shown that by introducing the mutations in the entrance channel, a gate-keeping phenylalanine was forced into an 'always-open' state, which ultimately increased enzymatic turnover. Comparing SHC homologs highlighted the requirement for accessible electron density for the high selectivity of the enzyme and revealed an unprecedented stereoconvergent cationic cyclization of a *cis*/*trans* isomeric mixture of the substrate. Afterwards, kinetic investigations of selected *Aac*SHC variants *in vitro* and *in vivo* disclosed substrate inhibition occurring solely during the *in vivo* experiment. It was suggested that the excess diffusion of the substrate into the biomembrane, where the enzyme is anchored, caused a disturbance of the membrane integrity which ultimately inhibited the enzyme. These results provided valuable insights into the physiological function and regulation of a monotopic membrane enzyme and may impact medical treatment targeting related enzymes. Leveraging the *in situ* product

crystallization of (–)-ambroxide, a feeding strategy was finally employed to perform over 190.000 TTNs with the engineered enzyme.

The aim of the third part was the actual implementation of the SHC-mediated *shape-complementary* cyclization and directed cationic cyclization into total synthesis routes towards complex terpenes. Therefore, a general setup was established first employing lyophilized *E. coli* powder, which made the catalyst storable and the sophisticated cyclization as simple as batch chemistry. Next, it was demonstrated that liquid cyclization products induce a time-dependent inhibition of the enzyme, which could be circumvented by using 2-hydroxypropyl-β-cyclodextrin as an encapsulation agent for *in situ* product removal. Computational investigations clearly showed that the interior of the cyclodextrin and the interior of the membrane are competing environments for the diffusion of terpenes. This data provided further evidence for the regulative function of the membrane on the SHC. Having elaborated the optimal conditions for catalysis, three complex meroterpenes were retrosynthetically dissected into hybrid chemoenzymatic synthesis routes, including the herein established biocatalytic cationic cyclization. In the forward reaction, first, six linear terpenes varying in chain length and functional group were cyclized by several engineered SHC variants granting high yields (up to 90%) and excellent control over progress, stereoselectivity (up to five stereocenters) and termination of the cationic cascade. These chiral templates were then transformed by simple catalytic and synthetic methods towards complex meroterpenes, thereby debottlenecking the challenging cationic cyclization step and cutting down previous lengthy synthetic routes by more than 50%.

Overall, the implementation of biocatalytic *shape-complementary* cationic cyclization cascades in organic chemistry has not only been successfully demonstrated but has also been usefully supplemented by the introduction of precisely set hydrogen bonds to direct the cationic cyclization cascade and demonstrate a stereoconvergent cationic cyclization. Furthermore, a holistic consideration of the enzyme and its physiological role enabled space-time-yields way beyond its priorly determined limits, putting it on par with industrially applied enzymes. In summary, this work promotes the overarching endeavor of chemistry to achieve the *ideal synthesis* by embracing nature's catalysts.

Chapter 1

INTRODUCTION – NATURE'S TERPENOME

1.1 Programming terpenes by divergent synthesis

The sheer infinite variety of terpenes is truly a remarkable art of natural evolution. With over 170.000 known compounds, this class of biomolecules accounts for almost one-third of all known natural products in the *Dictionary of Natural Products*[1] subsummarized as the terpenome.[2] The origin of the terpenome is unambigously linked with the of origin of life on earth, evidenced by findings of fossilized bacterial hopanoids **1** in geological deposits billions of years old (**Figure 1-1**).[3] These 'ancient lipids' may even have coexisted with the three molecules of life DNA, RNA and proteins[4] (according to the central dogma) in the early beginnings of natural evolution.[5]

As a result, terpenes are ubiquitous in all kingdoms of life with vital impact on individual as well as population survival. For example, animal cell membranes require cholesterol **2** to preserve cell membrane function and homeostasis of the cell, which otherwise leads to diseases such as cancer or Alzheimer's disease.[6] Addtionally, cholesterol **2** is the precursor of diverse steroid hormones regulating vital processes such as reproduction or neuron function in animals.[7] Plants produce and expell volatile terpenes like dihydroionones **3** or pinenes **4** to defend themselves against herbivores.[8,9] Interestingly, turpentine oil, which is the eponym of this molecule class, predominantly constitutes from pinene **4** which thus is the archetype terpene.[10] Other volatile terpenes e.g., based on the bisabolene scaffold **5** are universally applied as pheromones in plants, fungi and bugs to transmit signals and attract partners.[11–13] Beyond the terrestrial life, marine sponges produce so-called meroterpenes, e.g., α-pyrone meroterpenes **6** in order to protect themselves against viral or bacterial infections.[14] Finally, humans generate so many terpenes that isoprene is the main endogenous hydrocarbon of our breath.[15] Their high abdundance in nature as well as their exceptionally broad functional and chemical diversity, has attracted chemists around the world to make use of terpenes in diverse applications. Historically, the first recorded application of terpenes dates far back to the ancient times of Egypt. Merchants reported from an enigmatic perfume material of marine origin with a strong animalic, sweet and woody smell, called '*the treasure of the sea'* or '*Amber gris'*.[16]

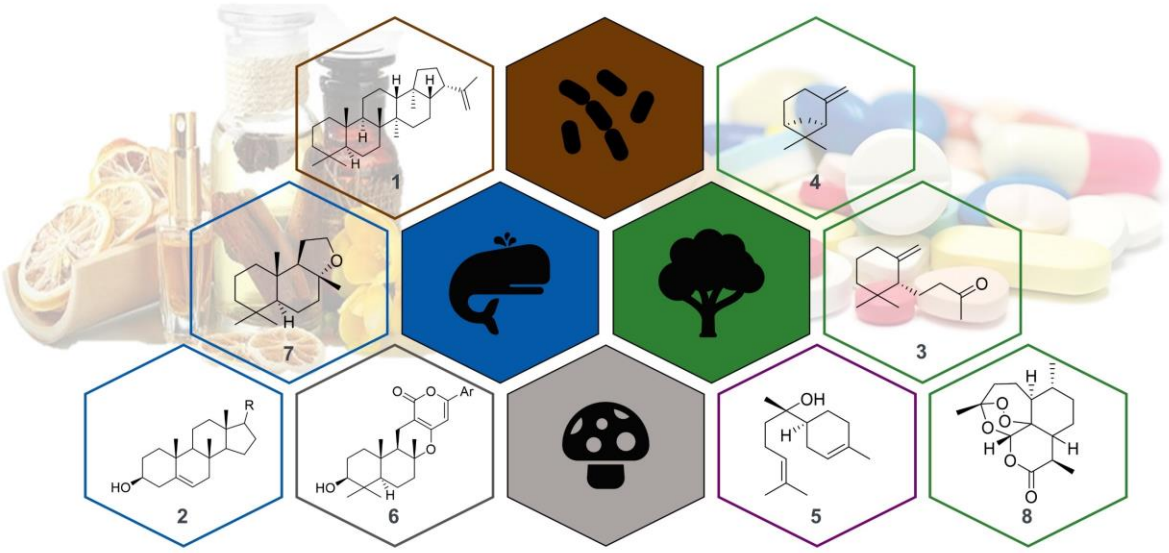

Figure 1-1: The terpenome in different kingdoms of life – bacteria (brown), vertebrates (blue), plants (green) and fungi (gray). Colored outline means affiliation to the respective kingdom. Purple outline means affiliation to multiple kingdoms.[2] Applications of terpenes as flavors, fragrances or pharmaceuticals indicated in the background.

Nowadays, we are aware that this unique smell mainly derives from (–)-ambroxide **7**, which is an auto-oxidative degradation product of the grey, waxy ambergris formed in the intestines of sperm whales. After expelling it to the ocean, these organic clumps are floating on the surface until they are washed up at beaches. Given the rarity of such an event, (–)-ambroxide **7** is often referred to as the '*floating gold*' and is one of the most expensive fragrance ingredients on earth.[17] Indeed, terpenes represent a huge market for the flavor and fragrance industry.[18] The flavor ingredient menthol is produced on a huge 30.000 t/year scale to meet the world's demands for the peppermint flavor.[19] Pleasant fragrances like the rose or violet scent originate in rose ketones like dihydroionone 3.[20] Terpenes delight this market owing to their intrinsically low vapour pressure and manifold scents.[21] Apart from that area, terpenes are used as vitamins and are frequently consulted as drug candidates in the pharma industry.[22] The most promiment example of a medical application is artemisinin **8** extracted from the plant *Artemisia annua.* This terpene is the leading component in therapies to treat Malaria, a disease which caused over 600.000 deaths in the year 2021.[23] Its unique sesquiterpene lactone structure which is bridged by a peroxide ensures the rapid and full elimination of *Plasmodium* parasites from a patient's bloodstream.[24] Moreover, α-pyrone meroterpenes **6** are increasingly employed as agents against arteriosclerosis, mainly because of their hybrid structure

consisting of the three-dimensional terpene scaffold fused to a flat aromatic moiety.[25] It is indeed the unique chemical structure of terpenes what makes them so valuable for the fine chamical industry: A cyclic core comprising multiple quaternary carbon and consecutive chiral centres. This feature renders them conformationally restricted and facilitates highly specific substrate recognition in biological receptors such as the human nose or pathogens.[18,26]

The question arose as to how nature is forging such a wealth of molecular complexity to fulfill a plethora of biological tasks. In the late 19th century Otto Wallach deciphered this fundamental issue with the '*isoprene rule'*, which was further advanced to the '*biogenetic isoprene rule'* by Leopold Ružička.[27,28] Both chemists identified the unifying C5 hydrocarbon isoprene as a key repetitive motif throughout the whole terpenome. Consequently, every terpene originates from the same precursor dimethyl allyl pyrophosphate **9** (DMAPP, **Figure 1-2**, the biogenetic analogue to isoprene) which is diverged in the secondary metabolism to fulfill its role within the ecological environment.[29] This paradigm is known as *divergent synthesis* and is often adapted in chemical synthesis approaches.[30–33] In the case of terpene biosynthesis, divergency is accomplished by three modules (**Figure 1-2**): In the first module, the achiral chain length is definded. In the second module, the linear substrate may either be functionalized (scaffold derivatization) or cyclized (scaffold diversification). In the third module, the functionlized terpene is cyclized and the cyclized terpene is functionlized. In this particular case, the precursor **9** is enzymatically isomerized to isopentenyl pyrophosphate **10** (IPP) and is fused with another DMAPP **9** in a head-to-tail fashion to give C10-geranyl pyrophosphate (GPP) **11**. This producedure can be repeated to give e.g., C15-farnesyl pyrophosphate (FPP) **12** and further C20-geranylgeranyl pyrophosphate (GGPP) **13**. From this first module in principle every chain length may enter the second module. Starting from scaffold **13** one route (left, Route A) starts with an iron-porphyrin catalyzed epoxidation of the terminal double-bond and a cationic prenyl transfer onto a phenyl-α-pyrone to give linear **14** (scaffold derivatization). Next, **14** is protonated by a class II cyclase to open the epoxide and initiate a stereoselelctive cationic cyclization cascade to obtain phenylpyropene **15** (Module 3, scaffold diversification).[25]

Alternatively (right, Route B), scaffold **13** may undergoe first a cationic cyclization cascade initiated via pyrophosphate abstraction facilitated by a class I cyclase to give

taxadiene **16** (Module 2, scaffold diversifaction). Afterwards, the cyclic carbon skeleton is derivatized (Module 3) by multiple hydroxylations, acetylations, benzoylations and polyketide transfer to give Paclitaxel **17**.[34] The *divergent synthesis* strategy illustrates how nature reuses one simple, achiral scaffold to generate the immense variety of the terpenome in a most efficient way. Such efficiency is achieved by nature's chemists, the enzymes that have evolved over billions of years and perfectly adapted to their substrates.

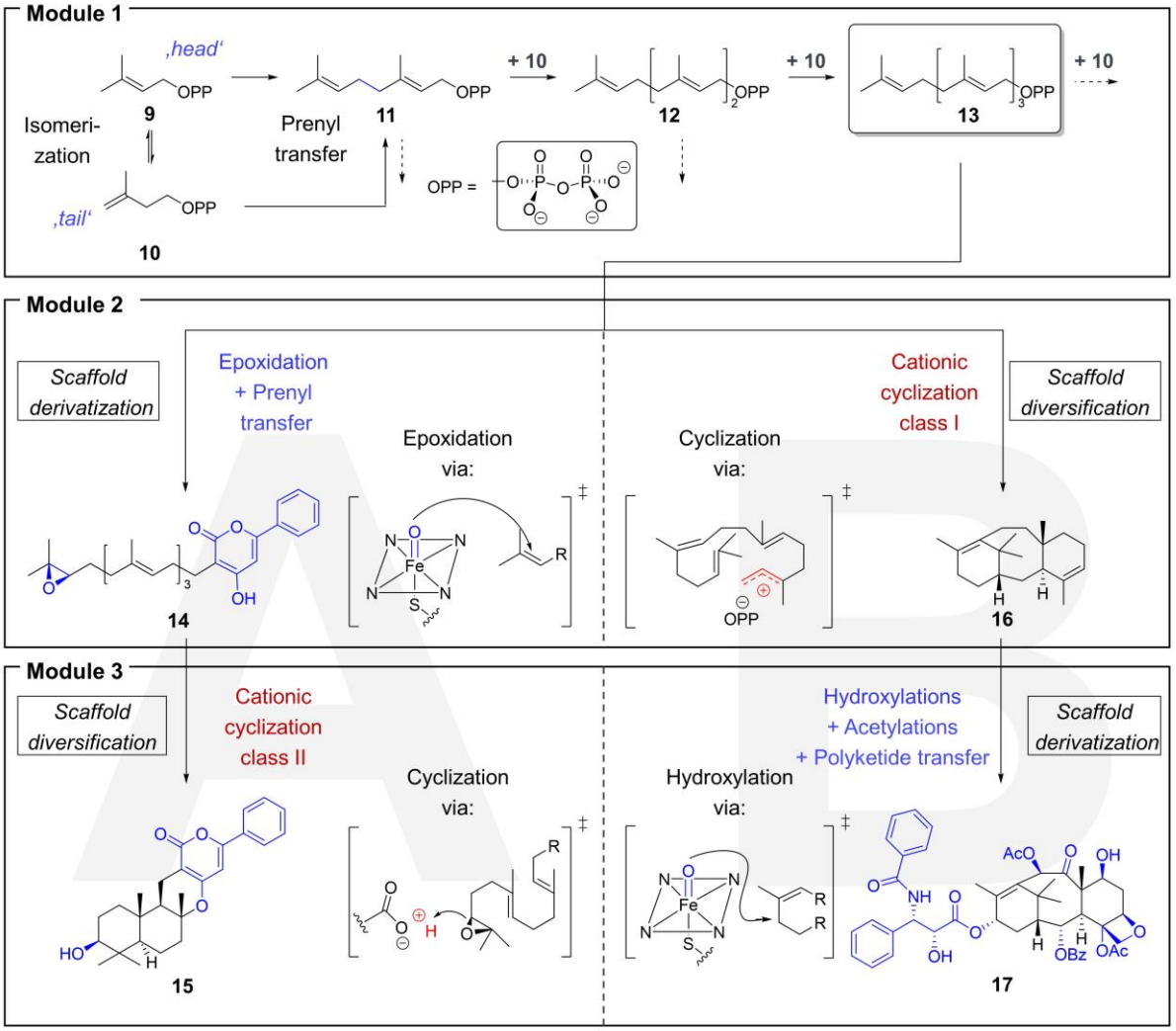

Figure 1-2: Divergent synthesis of terpenes in the secondary metabolism. In module 1 the chain length of the linear precursor is defined by head-to-tail prenyl transfer reactions. These linear scaffolds are derivatized (Route A) or diversified (Route B) in module 2 and are diversified or derivatized vice versa in the final module 3 to give the complex terpene scaffolds.[29]

In contrast, modern organic chemistry has only developed in the last 100 years, enabling chemists to elucidate and synthesize the complex structure of terpenes.[35] As a consequence, many chemists took the challenge to create terpenes by total synthesis.[36]

1.2 Accessing the terpenome by chemical synthesis

Terpene total syntheses are adventures in classical organic transformations coupled with state-of-the-art catalytic asymmetric methods.[37] Challenges of the synthesis endeavor are to properly control stereochemistry of the carbon skeleton as well as to densely and selectively adjust all functional groups. Retrosynthetic approaches in this thriving field are generally governed by four strategies (**Figure 1-3**): The ex chiral pool method is by far the most applied strategy and makes use of abundant chiral building blocks provided by nature (**Figure 1-3A**). Iconic chemists like E. J. Corey[38], K. C. Nicolaou[39] or S. J. Danishefsky[40] applied this strategy to accomplish their total syntheses towards complex terpenes. A prominent example of the 20th century was the concise and stereocontrolled synthesis of Paclitaxel **17** within 37 steps (20 in nature[34]) from verbenone **18** demonstrated by Paul Wender's group.[41,42] Key transformations of the synthetic route included photochemical carbon chain elongation followed by an intramolecular cyclization and fragmentation to form rings A and B (**Figure 1-3A**). Aldol reaction would finally give the full taxane skeleton. Paclitaxel **17** also known as Taxol® is one of the most successful cancer treatment agents, owing to its complex structure and the manifold interactions it may exert with various tumor cell types.[43] However, the harvesting from its natural resource, the *Taxus brevolia* bark, is unproductive and therefore synthetic efforts to produce this compound are still highly desired.

The second strategy makes use of certain structural motifs within the terpene skeleton, which can be created by a known or a newly invented synthetic strategy and therefore ease the synthesis pathway (**Figure 1-3B**). The group of Scott Snyder successfully demonstrated this approach in their concise synthesis of conidiogenones **19** from ketone **20** in 13 steps.[44] In their seminal study, they demonstrated that each quaternary center can be leveraged to simplify the construction of the following one, either by rate acceleration or blocking effects. The authors took advantage of the Thorpe-Ingold effect, which induces large rate enhancements during the formation of quaternary carbon centers in cyclization reactions. With this strategy, they were able to cut down the previous route by 11 steps and produce the desired products in high agreement (99%, NMR comparison) with the natural resource.

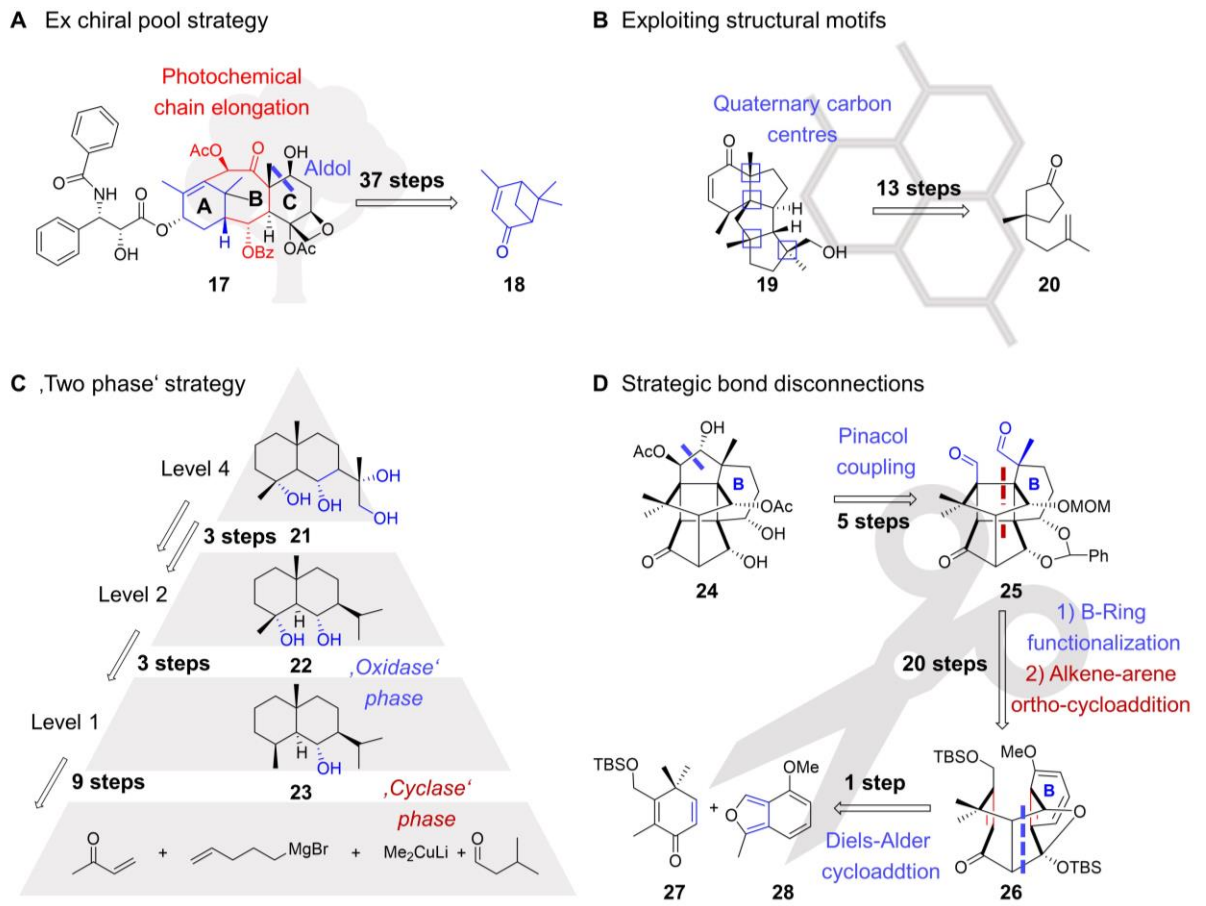

Figure 1-3: Contemporary synthetic strategies towards biologically active terpenes. (**A**) The ex chiral pool method starting from naturally abundant chiral building blocks. (**B**) The second strategy exploits structural motifs within the terpene skeleton, which can be made via a certain methodology. (**C**) The 'Two phase' strategy developed by the Baran group[45] mimics nature's modular approach (cf. Figure 1-2) towards the final terpene scaffold. (**D**) The fourth strategy is based on contemporary retrosynthetic logic and strategic bond disconnections, making use of state-of-the-art synthesis strategies.

The third strategy illustrated in **Figure 1-3C** is an exclusive contribution from the group of Phil Baran and is based on mimicking nature's *divergent synthesis*.[45] In their endeavor to synthesize eudesmantetraol **21**, the authors produced multiple members of the eudesmane family with different oxidation stages ranging from four oxidations (level 4) over three to two oxidations (level 2), e.g., in 4-epiajanol **22** to a single oxidation in dihydrojunenol **23** (level 1) by site-selective inter- and intramolecular oxidations, analogously to nature's *oxidase phase*. The carbon skeleton **23** was manufactured by simple carbocycle-forming (Aldol, Grignard, Pd-coupling) reactions to mimic the *cyclase phase*. This 'Two phase' strategy was further applied in different synthetic approaches such as synthesis of Taxol® **17,** which reduced former approaches to 23 steps.[46,47]

The fourth approach involves the classical retrosynthetic analysis of the desired terpene scaffold (**Figure 1-3D**). This strategy particularly relies on the contemporary retrosynthetic logic, which includes state-of-the-art synthetic and catalytic methods available in the chemical toolbox. The group of Tanja Gaich recently applied this methodology to synthesize one of the most complex natural product ever isolated: the canataxpropellane **24**.[48] This terpene exceeds all aforementioned scaffolds in their complexity, owing to twelve contiguous stereocenters, six quaternary carbon centers, two propellane motifs and the highest functional density of any known molecule.[49] Despite all these given challenges, the group achieved the convergent synthesis of **24** in 26 steps by strategic bond disconnections and the key transformations of Pinacol coupling of **25**, ring re-functionalization as well as alkene-arene-ortho-cycloaddition of **26** and Diels-Alder reaction of the precursors **27** and **28**.

Notwithstanding the boundless creativity of synthesis tactics and maneuvers in all of these strategies, none of them incorporated a 'true' cationic cyclization cascade to forge the cyclic terpene scaffolds. Yet, the ability to change the orientation and hybridization of multiple carbon atoms within a single cationic cyclization to produce the carbon scaffold would be of benefit in every respect. To understand how enzymes control and manipulate these sophisticated reactions, a comparison of terpene cyclases and man-made cation-controlling catalysts is discussed in the following part.

1.3 Terpene cyclases and the manipulation of reactive cations

Cationic cyclization cascades have long been recognized as one of the most elegant tools for the rapid assembly of high molecular complexity.[50] They appeal with their simplicity – proton transfer across the molecule – and effectiveness – extensive scaffold diversification – at the same time. However, due to their highly reactive nature, the fate of intermediary carbocations is usually governed by migratory aptitudes,[51] resulting in bifurcating cationic pathways and ultimately product mixtures.[52] It becomes evident that for convergent synthesis approaches, which are usually applied in chemical syntheses, such serendipitous taken pathways are detrimental. Nature perfectly exploits the inherent substrate reactivity and potential energy bifurcations for the divergent synthesis of an array of terpene scaffolds fulfilling most diverse tasks in the kingdoms of life (cf. chapter 1.2).[53] Extreme examples such as the delta-selinene synthase and the gamma-humulene synthase produce 34 and 52 cyclization products from the same

precursor FPP **12**, respectively.[54,55] Conversely, triterpene cyclases like the squalene-hopene cyclase (cf. chapter 1.3.2) produce unique polycyclic products with a remarkable selectivity of one out of 512 stereoisomers. This precision is facilitated by tightly chaperoning substrates in their confined active sites and guiding cationic intermediates via multiple partial reactions to their final destination.[2] Mechanistically, the initiation of such *shape-complementary* cationic cyclization cascades permits the differentiation between two classes of terpene cyclases.[56]

1.3.1 Class I terpene cyclases and their artificial mimic

Class I terpene cyclases initiate the cationic cascade by abstraction of a pyro-/ diphosphate group leaving behind a highly reactive allylic carbocation (**Figure 1-4**). The crystal structure of bornyl diphosphate synthase (BPPS) with several bound aza-substrate analogs was one of the first solved class I terpene cyclase crystal structures examples, allowing the elucidation of structure-function relationships and the 'chemical wizardry' of these enzymes.[57,58] BPPS shares the common 'isoprene' or 'terpene synthase-fold' broadly distributed among class I cyclases.[59,60] It is characterized by an αβ architecture, multiple α-helices and the aspartate-rich DDXXD motif in the otherwise hydrophobic active site with the size of 222 Å^3 (**Figure 1-4A+B**). This motif along with three additional arginine residues facilitate the coordination of three Mg^{2+}-ions necessary for the abstraction of the substrate's pyrophosphate group (**Figure 1-4B**). Remarkably, binding of the three metal ions and the substrate triggers conformational change of the enzyme from an open active site to closed, which exemplifies the induced-fit mechanism in class I terpene cyclases.[61] The electronically closed-shell rearrangement sequence of monoterpene GPP **11** to bornyl diphosphate **29** (**Figure 1-4C**) starts with ionization followed by isomerization to the *cisoid* linalyl pyrophosphate **30** via rotation around the 2,3-carbon bond (**Figure 1-4D**). Subsequent second ionization allows the intramolecular S_N' C1-C6 cyclization to form (4*R*)-α-terpinyl cation **31**, which in turn undergoes *anti*-Markovnikov cyclization to form the secondary (+)-bornyl cation **32**.

Finally, this cation forms a C-O bond with the bound diphosphate in an *endo* fashion to generate and release the product (+)-bornyl diphosphate **29.**

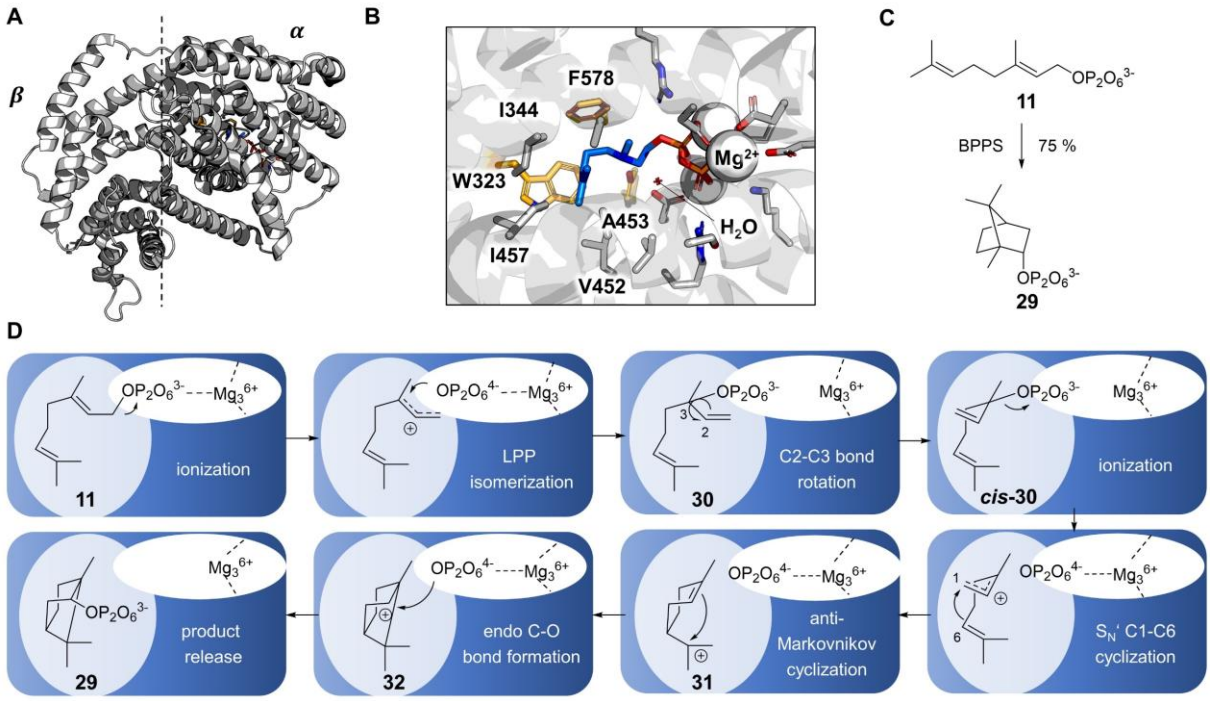

Figure 1-4: Class I terpene cyclase bornyl diphosphate synthase (BPPS). (**A**) Crystal structure (PDB: 1N20) of BPPS demonstrates a wealth of α-helices. The active site is located in the α-domain. Domains are divided by dashed line. (**B**) Active site of BPPS with mainly unpolar amino acids and a trapped water molecule, which enforce the bound substrate mimic aza-**11** into precise folding for catalysis. Three Mg^{2+} ions are ligated by aspartates and arginines. Amino acid side chains shown as sticks. Aromatic side-chains for cation-π interactions shown as bright orange sticks. Aza-analog of substrate **11** shown as blue sticks with diphosphate moiety in dark orange/ red. (**C**) Natural reaction of BPPS. (**D**) Proposed intramolecular cationic cyclization/ rearrangement pathway of **11**.[57]

Hallmarks of this sequential catalysis are the strict stereocontrol by enforcing the left-handed helical conformation of the substrate **11** (*shape complementarity*), the allylic cation stabilization by the bound counterion diphosphate as well as cation-π stabilization e.g., by residues W323 and F578. Unexpectedly, a hydrogen-bound water molecule in the active site serves to pre-fold the substrate rather than prematurely quench the occurring cationic intermediates (**Figure 1-4B**). Noteworthy, it was demonstrated that the secondary bornyl cation **32** is actually a transition state rather than an actual intermediate which results in the above-mentioned bifurcation of the potential energy surfaces.[62] On the one hand, this bifurcation hampers the cyclization fidelity of the enzyme and may explain the limited 75% selectivity towards the final

product (**Figure 1-4C**). On the other hand, reasonable doubt arose concerning the herein proposed mechanism and the existence of the secondary bornyl cation **32**.[62]

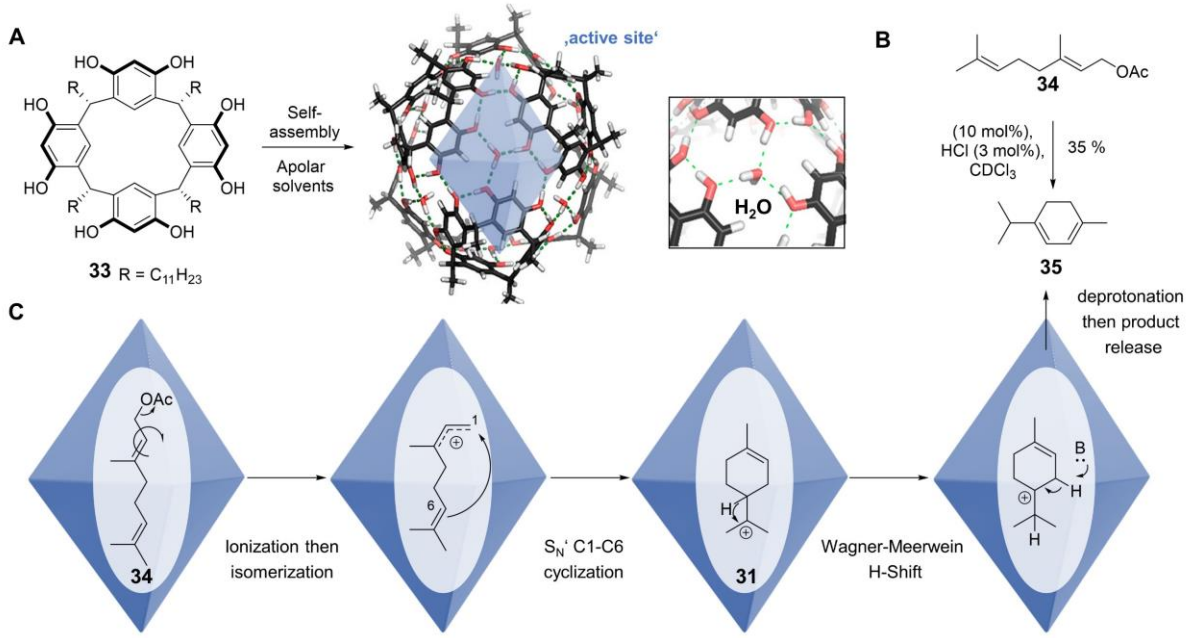

Figure 1-5: The resorcinarene capsule introduced by the Tiefenbacher lab.[63] (**A**) Resorcinarene **33** self-assembles in apolar solvents to a hexameric supramolecular catalyst that is able to guide cationic pathways. Main features of the catalysts are the hydrogen-bound water molecules in the supramolecular framework responsible for 'proton-shuffeling' and the aromatic cation-π interactions for cation stability. (**B**) Geranyl acetate **34** cyclizes in the presence of **33** and HCl in $CDCl_3$ to **35** with 35% selectivity. (**C**) Proposed intramolecular cationic cyclization/ rearrangement pathway of **34**.

Man-made catalysts facilitating intramolecular tail-to-head S_N' cyclizations have long been elusive in chemistry, due to inevitable E1 or S_N1 reactions. Few successful studies employed specifically synthesized substrates with demanding protection or activation groups.[64,65] In 2015 the group around Konrad Tiefenbacher presented a catalyst that was finally able to mimic the *modus operandi* of class I terpene cyclases (**Figure 1-5**).[63] The catalyst is formed by the hexameric self-assembly of resorcinarene **33** in apolar solvents (**Figure 1-5A**). This supramolecular capsule in combination with an externally added acid like HCl serves as an artificial cyclase facilitating non-stop cationic rearrangements within its 'active site'.[66] In analogy to nature's GPP **11** the authors used i. a. geranyl acetate **34** to demonstrate the capabilities of the resorcinarene capsule (**Figure 1-5B+C**). After acidic ionization, the allylic carbocation isomerizes and undergoes the desired S_N' C1-C6 cyclization to form terpinyl cation **31**. Subsequent Wagner-Meerwein-H shift and deprotonation lead to the product α-terpinene **35** with 35% selectivity.

The essential feature of cation-π stabilization was exploited here as well, but was already a common element in small-molecule catalysis.[67,68] More importantly, by creating resorcinarene **33** analogues, the authors proved that bound water molecules in the supramolecular framework served as a 'proton-shuffle' and are indispensable for catalytic activity (**Figure 1-5A**).[69] With this supramolecular strategy, the Tiefenbacher group is constantly producing new cyclic terpene scaffolds that depend on the substrate's geometry and leaving group.[70–72] Despite these pioneering efforts on cyclase mimics, the rather low yields (up to 40%) and broad product mixtures render this catalyst inferior to the chiral enzyme scaffold.

1.3.2 Class II terpene cyclases and their artificial mimic

The second class of terpene cyclases is characterized by the protonation of a terminal prenyl or epoxide moiety to generate a tertiary carbocation for the cyclization cascade.[73] Given the fact that tertiary carbocations, in comparison with allylic cations in class I, are 'only' stabilized by hyperconjugation,[74] the enzyme has to be even more involved. Furthermore, the unprecedented control of up to nine stereocenters in a single catalytic step has led chemists to ponder about these enigmatic enzymes. Fortunately, the 1997 solved crystal structure of the bacterial squalene-hopene cyclase from *Alicyclobacillus acidocaldarius* (*Aac*SHC) gave valuable insights into the structural and chemical biology of SHCs.[75]

In the physiological context, SHCs produce lipids (hopanoids **1**) to regulate membrane fluidity and thus ensure the functionality of bacterial membranes, similar to cholesterols **2** in animals.[76,77] The SHC architecture comprises a β- and a γ-domain both consisting of an α(outer)-α(inner) barrel (**Figure 1-6A**). The enzyme is embedded into the membrane of its host by an reentrant α-helix in the γ-domain, which defines it as a monotopic membrane-enzyme.[78] The concentric α-barrels point with their inner α-helices towards the 1200 Å^3 big hydrophobic active pocket that is mainly formed of loops (**Figure 1-6A**, top view). The ~30 Å long active site is made of 75% aromatic amino acids, which form a huge cation cage (**Figure 1-6B**, bright orange side chains, PDB: 1UMP) protecting the transient cations from premature quenching. Additionally, hydrophobic residues (**Figure 1-6B**, gray side chains) flank the cation cage to support in pre-folding of squalene **36**.

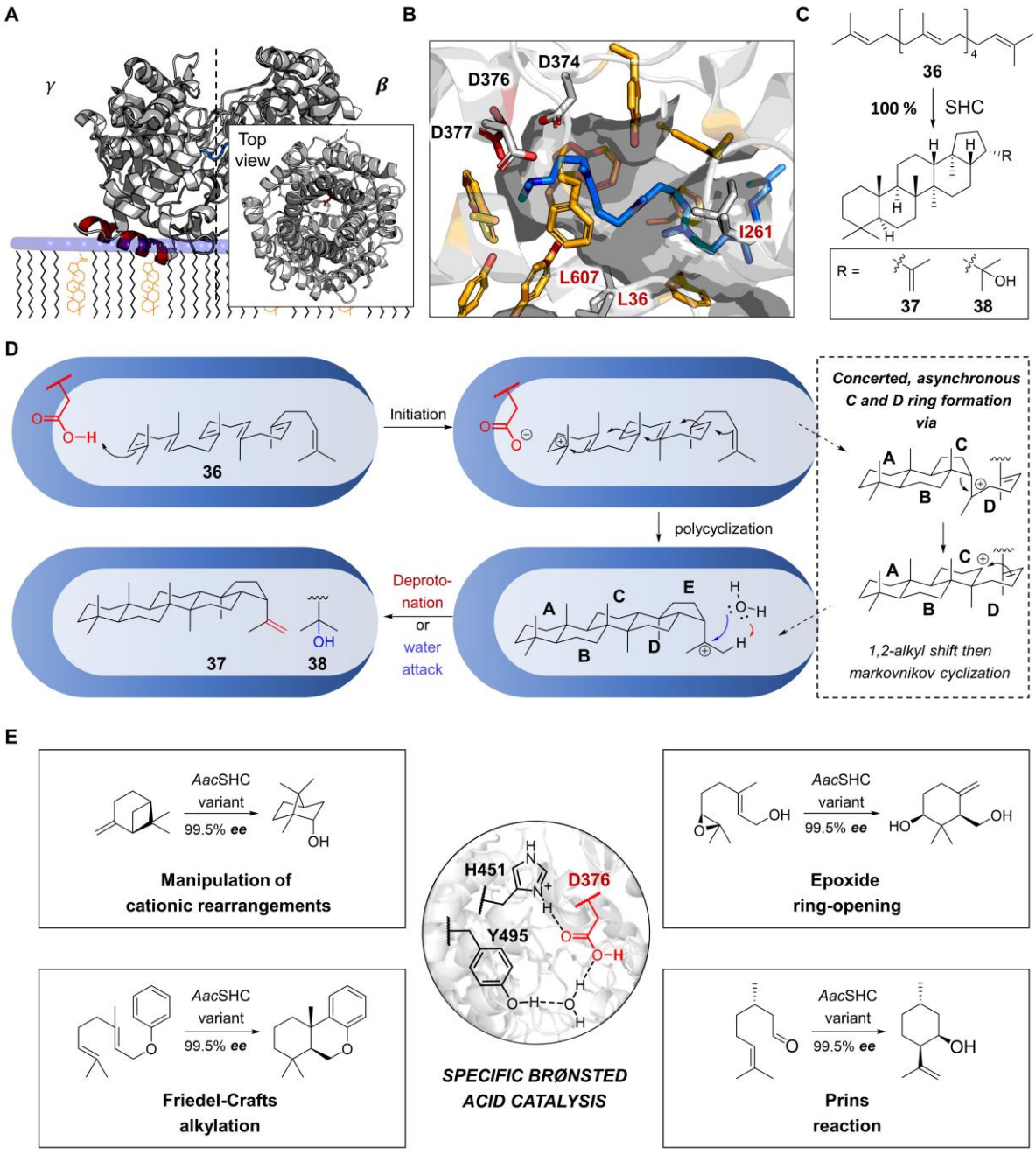

Figure 1-6: Class II terpene cyclase squalene-hopene cyclase from *Alicyclobacillus acidocaldarius* (*Aac*SHC). (**A**) Crystal structure (PDB: 1UMP)[79] and top view of the *Aac*SHC (grey cartoon) co-crystallized with the aza-analog of **36** (blue sticks) and artificially[80] embedded into phospholipid layer by the reentrant α-helix (red cartoon). The enzyme produces hopanoids **37**/**38** (yellow scaffolds) to ensure membrane functionality.[76] (**B**) Active site of *Aac*SHC with pre-folded aza-**36** (blue sticks) demonstrates high abundance of aromatic amino acids (orange sticks) forming the cation cage. Scattered non-aromatic residues supporting the enzyme in pre-folding of **36** are also present (grey sticks, bold red font). Protonation machinery DXDD in grey with D376 in red sticks. (**C**) Natural reaction of *Aac*SHC with absolute control over nine stereocenters. (**D**) Proposed mechanism by DFT calculations.[81] (**E**) Reaction scope demonstrates the broad substrate promiscuity of the *Aac*SHC.[82–84]

Co-crystallization experiments with the aza-analog of **36** demonstrated the substrate perfectly aligning into the SHC's active site, almost as a punched out missing puzzle

piece (*shape complementarity*) (**Figure 1-6B**, blue sticks).[79] This elucidated the power of a strongly confined active site, which eliminates degrees of freedom and permits the sole generation of one of 512 potential stereoisomers of the product hopene/hopanol **37**/**38** (**Figure 1-6C**). After the exact pre-folding, **36** is protonated by the hallmark of class II cyclases: the cofactor-independent protonation machinery with the D(374)XD(376)D(377) motif. The proton of aspartic acid 376 is oriented in an *anti*-fashion by a hydrogen-bonding network, which improves its acidity by four orders of magnitude compared to a *syn*-oriented proton.[85] This rare feature enables SHCs to act as specific organic Brønsted acids and protonate unbiased olefin double-bonds to start the cationic cyclization cascade (**Figure 1-6D+E**).

The following cyclization/ rearrangement mechanism is under lively discussion and still has to be fully clarified.[79,81,86–89] However, there is consensus on a concerted, but asynchronous mechanism without discrete intermedia (energy minima), via multiple 'events', e.g., cation-olefin cyclizations or 1,2-alkyl shifts. The first three cation-olefin cyclizations for ring A, B and C (6,6,5) are presumably concerted, which the enzyme facilitates via precise positioning of π-orbitals adjacent to forming cations, thus leveraging the stereoelectronic effect.[81,90] To expand the cyclopentyl-C-ring, it deserves a 1,2-alkyl shift generating a secondary carbocation, which is immediately quenched by the adjacent π-orbital resulting in Markovnikov cyclization for the D-ring. This ring expansion/ cyclization is repeated to form the E-ring, which is finally quenched via deprotonation or nucleophilic water attack to yield **36** and **37** in a ratio of 5:1 presumably by polarized water molecules.[91,92]

The synergy of cation-π stabilization, dipolar interaction and substrate pre-folding in a confined active site enables these enzymes to balance kinetic and thermodynamic control during the cyclization, which indeed resembles 'chemical wizardry'.[58] To perform catalysis, SHCs expel water molecules from their active sites, which renders them entropy-driven enzymes.[93,94] Intriguingly, the overall reaction is highly exergonic and releases a free energy of ~200 kJ/mol, which is partially used to release the bulky **37** from the active site.[79]

The absence of the pyrophosphate group within the substrate (compared to class I cyclases), eases the substrate tolerance studies of class II cyclases. As a result, their promiscuity was already discovered in 1986 by Neumann and Simon and the

(–)-ambroxide **7** cyclization.[95] Since then Hoshino and Hauer mainly contributed to the enlargement of the substrate scope of the *Aac*SHC with various truncated and elongated terpenes.[96–98] Remarkably, Hammer et al. recognized the general applicability of the *Aac*SHC as a specific Brønsted acid and demonstrated intramolecular Friedel-Crafts reactions[99,100], acidic isomerizations[82], Prins/En cyclizations[101] as well as epoxide ring openings catalyzed by the SHC (**Figure 1-6E**) with excellent stereoselectivities facilitated by *Aac*SHC and mutants thereof.[84]

In principle one may also imagine these enzymes as a gigantic counterion-directing organocatalysts with confined spaces facilitating reaction- and stereocontrol simultaneously. While asymmetric counterion-directed catalysis was already established in chemocatalysis[102] the group around 2021 nobel laureate Benjamin List was inspired by the strong confinement for the design of their Brønsted acid catalysts. In 2012, the group presented the C_2-symmetric imidodiphosphate catalyst as the first organocatalytic Brønsted acid catalyst design comprising a confined 'active site'.[103]

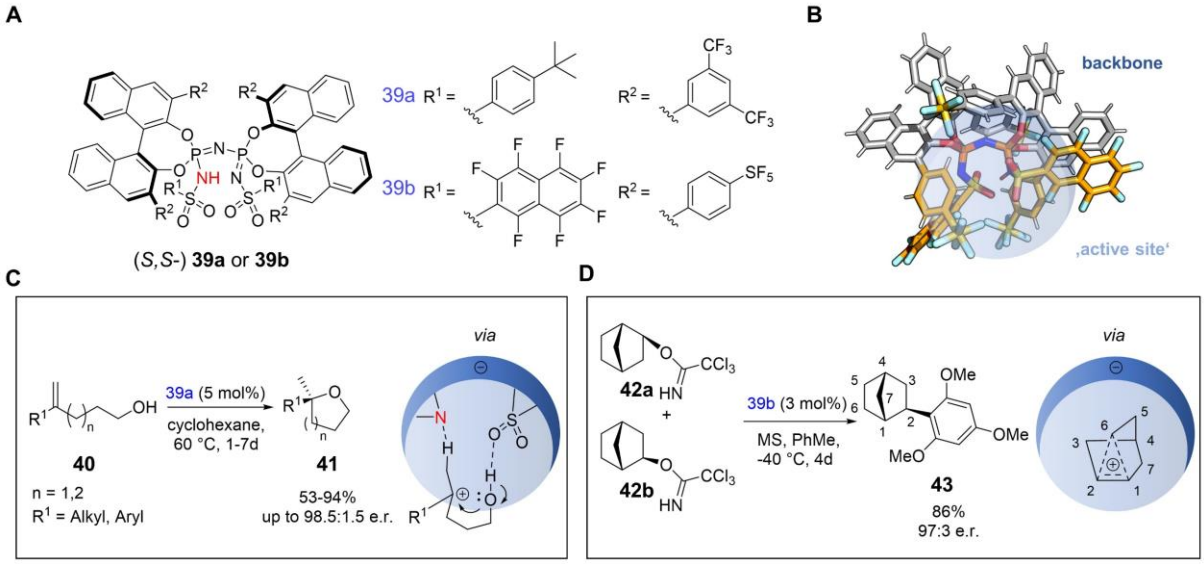

Figure 1-7: Imidodiphosphorimidate (IDPi) catalysts by the List lab**.** (**A**) Structure of IDPi **39** with protonating nitrogen in red. (**B**) Three-dimensional structure of **39b** highlights the interlocked BINOL backbone (grey sticks) and the artificial 'active site' formed by aromatic perfluorinated naphtyl (R^1) and *p*-pentafluorosulfanylbenzene (R^2) residues (bright orange sticks). (**C**) Activation of olefins via asymmetric Brønsted acid catalysis.[104] The mechanism proceeds via a concerted, asynchronous protonation/ hydroalkoxylation. (**D**) Diastereo- and enantioconvergent nucleophilic substitution of 2-*exo*-norbornyl derivatives.[105] The substitution follows the same 2-norbornyl carbonium ion intermediate.

Hallmarks of this catalyst and follow-up catalysts are the interlocked BINOL subunits, which are unable to freely rotate due to sterically demanding 3,3'-substituents as well as

a single catalytically active bifunctional acid/base pair in the artificial 'active site' (**Figure 1-7A+B**). Equipped with these features, the stage was set for Brønsted acid catalysis empowering the activation of small and unfunctionalized molecules e.g., for asymmetric spiroacetalization[103] (imidiphosphate, p*K*a ~11) or asymmetric hydroalkoxylation (imidodiphosphorimidate **39**, p*K*a ~ 3).[104,106] The latter reaction-type requires the activation of simple olefins **40** and the close juxtaposition of the cation to the π-orbital of the nucleophile (**Figure 1-7C**), which are features that strongly reminiscent of cyclase catalysis. Consequently, catalyst **39a** was able to control the stereochemical outcome of the intramolecular hydroalkoxylation towards **40** showing excellent selectivities with up to 98.1:1.5 *er*. The authors further could show a broad substrate scope that was mainly attributed to the substrate's bulky residue (**Figure 1-7C**, R_1) pointing toward the outside of the 'active site'.

With this powerful catalyst in hands, the List group next envisioned the stereocontrol over an archetypical non-classical carbocation, the 2-norbornyl cation.[105] In this endeavor, the group performed the reverse of the original Winstein experiment[107], by means of a diastereo- and enantioconvergent nucleophilic substitution of racemic 2-norbornyl trichloroacetamide with 1,3,5-trimethoxybenzene. This notoriously challenging reaction was accomplished by catalyst **39b** with an excellent stereocontrol of 97:3 *er* using the racemic mixture of 2-exo-norbornyl derivatives **42a** and **42b**. Intriguingly, various substrates following the same intermediary 2-norbornyl carbonium ion were transformed into the same product **43**, which demonstrates an unprecedented control over a non-classical cation in chemistry. Mechanistic investigations revealed the strong confinement of **39b** and short non-covalent C-H···O, C-H···N and C-H···F interactions as the source of selectivity. Furthermore, deuterium-labelling experiments could show a fast exchange of hydrides between positions 1, 2 and 6 of **42a**/**b**, which further proofs the existence of the carbonium ion. Such cations are often abundant in complex biosynthetic routes of terpenes,[108] which substantiates the importance of Lists work in the context of terpene biosynthesis.

The outlined comparisons showcase how terpene cyclases achieve unparalleled rate-enhancements and selectivity by one-step *shape-complementary* cationic cyclization cascades and the urge of mankind to understand and mimic this 'chemical wizardry' of these enzymes. Gratifyingly, the main catalytic principles of cyclases such as cation-π

stabilization, counterion-direction or strong confinement were successfully conceptualized in small-molecule organocatalysis with huge impact on the chemistry world.[109–111] However, these static elements are just one part of the dynamic supramolecular chiral machinery called enzyme, which is required to selectively control concerted multi-event reactions like cationic cyclization cascades.

In the age of biocatalysis, chemists are now able to design and repurpose enzymes to provide them with expanded or even non-natural functionalities.[55,112] As a result, enzymes are increasingly applied in synthetic approaches targeting molecules like Islatravir or Molnupiravir that are otherwise cumbersome to access.[113,114] However, squalene-hopene cyclases, providing valuable *shape-complementary* cationic cyclization cascades, have not yet found their way into organic chemistry.

MOTIVATION

The cationic cyclization cascade is one of the most elegant and atom-economic methods to access high molecular complexity[115] within a single step. Nature exploits this powerful tool to streamline the assembly of most diverse terpene skeletons, which are increasingly employed as bio-flavors[116], -fragrances[18], pharmaceuticals[43,117] or phermomones[16]. In contrast, chemical access to terpenes still relies on ex chiral pool and classical step-by-step chemistry (cf. chapter 1.2). Therefore, sqaulene-hopene cyclases, being co-factor independent, highly selective and promiscuous enzymes serve as promising catalysts to introduce *shape-complementary* cationic cyclizations to organic chemistry as an extension to the chemical synthesis toolbox.

In the pursuit of the *ideal synthesis,*[118] the overarching goal of this work was to fundamentally grasp and reinvigorate the chemical biology of squalene-hopene cyclases on the molecular as well as macromolecular level to render them easy-to-use catalysts. First, a squalene-hopene cyclase being able to direct the cationic cyclization cascade in product- and stereoselective fashion should be rationally designed, employing the tools of enzyme engineering and *in silico* evaluation. Moreover, the catalytic performance of squalene-hopene cyclases in their natural membrane environment should be analyzed kinetically to identify and circumvent potential nature-given limitations. The accumulated knowledge should be merged to ultimately aid concurrent and devise new synthetic routes to terpenes – the most abundant biomolecules on earth.

Chapter 2

DIRECTED CATIONIC CASCADES

2.1 Introduction – Catalyst-controlled cationic cyclizations cascades

During the last two decades, substantial progress has been made towards the initiation and stereocontrol of biomimetic cationic cyclization cascades employing tailor-made small-molecule catalysts. Such catalysts were based on inventive concepts e.g., Lewis-acid assisted Brønsted-acids[119,120] **44**, chiral phosphorus complexed *N*-iodosuccinimides[121] **45** or hydrogen-bonding thiourea catalysts[65,122] **46** to generate the desired carbocation (**Figure 2-1A**). However, these catalysts require harsh conditions, Lewis-base assistance, halogen activation or specifically designed substrates,[121–123] and challenges such as absolute stereocontrol, regioselectivity in the termination step and cascade control remain (F**igure 2-1B,** left). The latter is of major importance for many industrially relevant products (**Figure 2-1C**, **47-51**) as the non-stop cationic cascade entails further synthetic effort to reopen the cyclic structure.[124] Accordingly, a catalyst which is able to quench a cationic cascade at a preferred intermediary progress in a regio- and stereoselective way, i.e., effecting directed cationic cascades would be highly desirable (**Figure 2-1D**).

In this context, natural as well as engineered cyclases have been reported to catalyze such `short-circuit´ polycyclization cascades and thereby yielding less complex cyclic products.[87,125–127] The groups of Hoshino and Peters demonstrated this ability of class I and class II terpene cyclases by introducing amino acids comprising additional steric bulk[87] or function as catalytic Brønsted bases.[128] However, these approaches result in unwanted product mixtures and low yields (<10 mg/L), which precludes their industrial application. On the other hand, the *Aac*SHC has been reported to give reasonable product titers (>100 g/L) in the biocatalytic production of (–)-ambroxide **7**.[129]

Given the ability of converting non-natural substrates harboring polar functional groups, this work focused on the design of molecular amino acid anchors inside the active site of *Aac*SHC. Such anchors are widespread core elements in catalysis,[130,131] computational enzyme design[132] and materials science.[133] As a result, the variation of

these directing (= hydrogen bonding) groups by way of rational enzyme design appeared promising for directing cationic cyclization cascades.

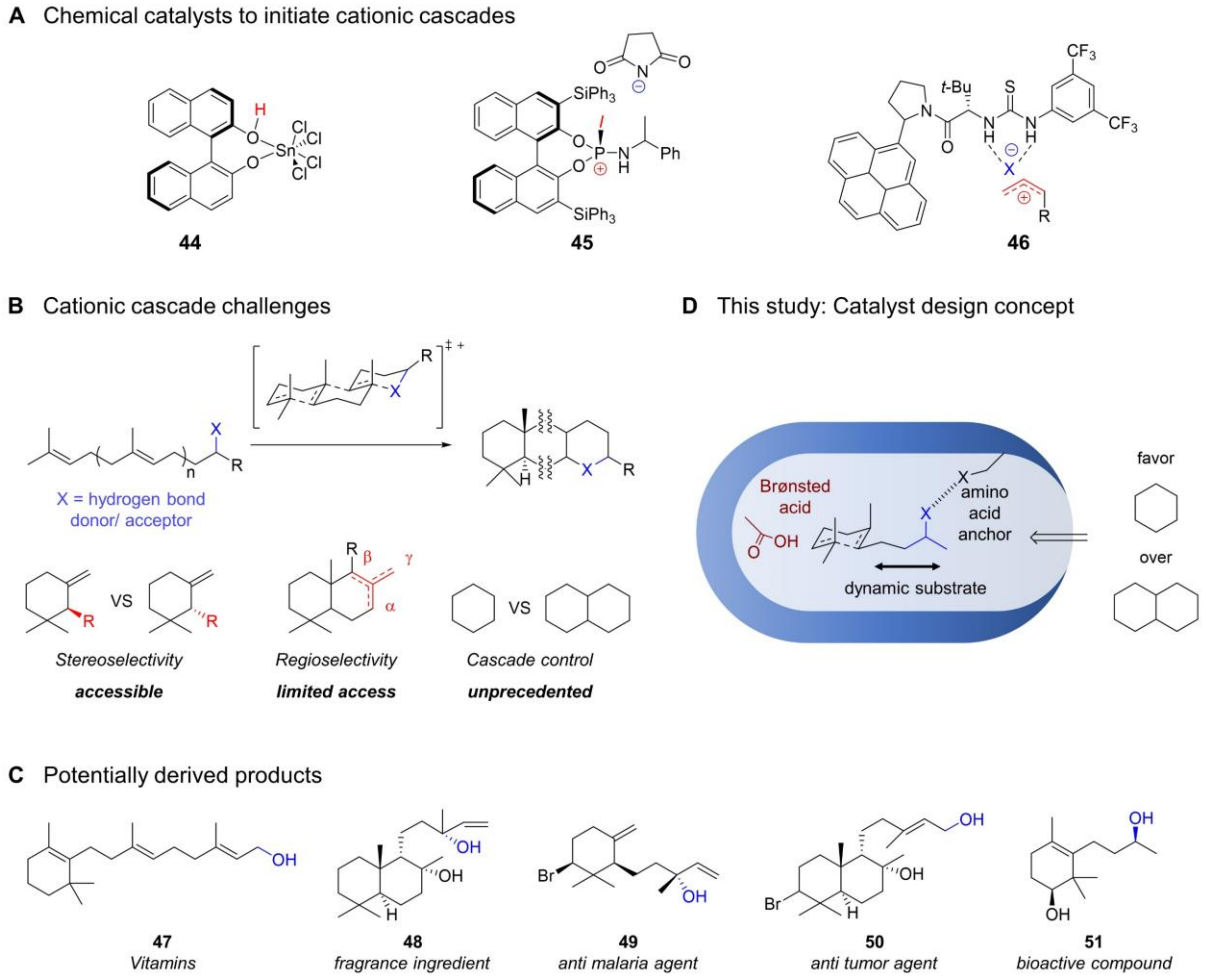

Figure 2-1: Cationic cyclization cascades and catalyst design concept to direct them. (**A**) Small-molecule cationic cyclization catalyst by Yamamoto,[120] Ishihara[121] and Jacobsen.[122] Drawbacks are the requirement of Lewis-base assistance (**44**), halogens (**45**) or initiation motifs (**46**). (**B**) Challenges of a cationic cascade (left). The catalyst design concept is based on introducing amino acid anchors in the hydrophobic active site to bind the substrate's polar functional group (blue) at chosen sites consequently directing the cascade reaction. (**C**) Industrially relevant products (**47-51**), which can be obtained by the demonstrated strategy of anchoring the functional group (blue).

2.2 Results and discussion

The very first goal of this work was to elaborate a practical enzyme screening assay. Enzyme engineering approaches highly rely on the throughput the assay can provide.[134] For instance, whereas directed evolution approaches based on random mutagenesis using error-prone PCR require enzyme libraries of 10^{6-10} enzyme variants and High-Throughput techniques, more rational design approaches based on site-saturation mutagenesis require 'smarter' libraries of only 10^{2-4} variants and therefore Medium-

Throughput techniques. Rational approaches, however, require more information beforehand about the target enzyme, e.g., a crystal structure or preliminary mutagenesis studies.[135] Regarding terpene cyclase assays few reports exist in the literature using either specially modified substrates[136] or coexpression systems,[137] both designed for class I terpene cyclases. Furthermore, the low functional density of linear terpenes and the isomerase activity of the SHC is detrimental for the application of colorimetric High-Throughput evolutionary approaches. Since both a crytsal structure (PDB: 1UMP) and preliminary mutagenesis studies are available for the *Aac*SHC, a rational, structure-guided approach combining site-saturation mutagenesis[138] and computational modelling was chosen for evolving the enzyme.

2.2.1 Establishment of an *in vivo* Medium-throughput assay

At that point the workflow for the evaluation of the membrane-bound SHCs was based on producing the enzymes in *E. coli* cells and tediously isolating them from their host using detergents as membrane mimics (four labor days in total).[84,139,140] This procedure disclosed the application in 96-DW format, which is obligatory for the site-saturation mutagenesis and a Medium-Throughput assay. As outlined before, it was reported that SHCs are also capable of performing catalysis in their producing *E. coli* host, without any background reactions catalyzed by other enzymes within the cell.[129] Accordingly, a whole-cell based 96-DW screening assay, which avoids the unfeasible work-up procedure in that format was established within a Bachelor thesis (J. Berger) (**Figure 2-2**).[141] As the model reaction the promsicuous cyclization[140] of *E*-geranyl acetone **52t** towards (*S,S*)-2,5,5,9-tetramethylhexahydrochromene **53t** using the *Aac*SHC variant G600L was selected, deduced from the results of a prior Master thesis (A. Schneider) (**Figure 2-2C**).[142] Gratifyingly, acceptable yields were achieved using the whole-cell approach in combination with 0.2 wt% SDS (up to 20% relative conversion, data not shown). Next, the variation coefficient C_V across the 96-DW plate should be determined. To that end, expression conditions in 96-DW format were improved (data now shown) and the same target reaction was conducted in all 96 DWs which resulted in an acceptable C_V of ~11.1% (**Figure 2-2D**). Furthermore, o-xylene was evaluated as the most suitable extraction solvent for direct measurement from the 96-DW plates (Supporting Figure S 1), due to low evaporation as well as good phase separation and minimal cell debris layer.

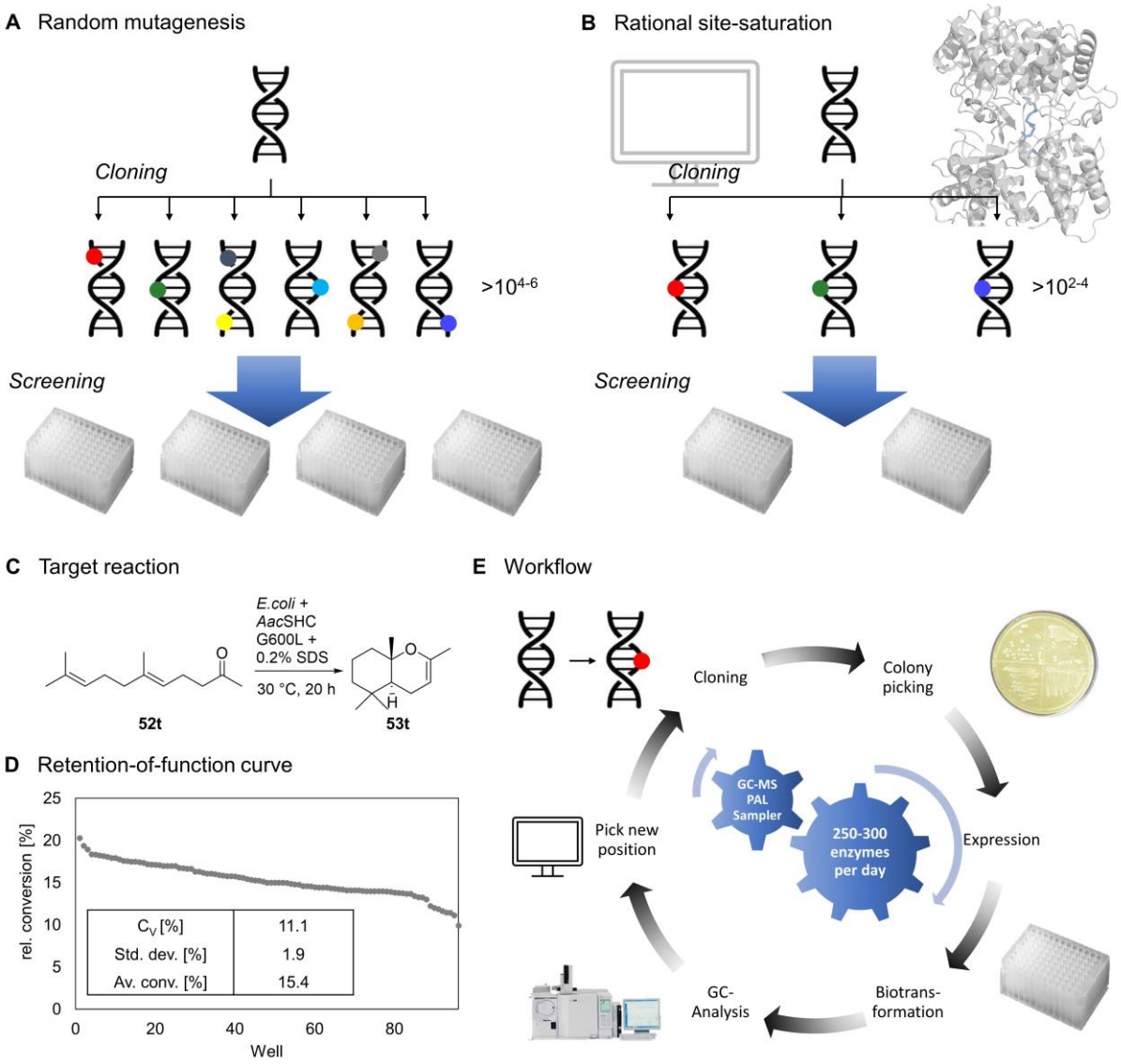

Figure 2-2: Enzyme engineering approaches and the establishment of a Medium-Throughput assay for site-saturation mutagenesis. (**A**) Directed evolution approaches are based on a given sequence which is randomly mutated all over the sequence which generates a high amount of variants that are screened afterwards using an efficient assay such as a colorimetric assay.[143] (**B**) Rational site-saturation approaches require information like a crystal structure of the enzyme beforehand. This data can be used to rationally target a desired amino-acid position within the sequence which is then saturated.[138] This approach generates less variants and reduces the screening effort. (**C**) Model cyclization reaction *E*-geranyl acetone **52t** to (*S,S*)-2,5,5,9-tetramethylhexahydrochromene **53t** using *Aac*SHC G600L embeddedinto the *E. coli* whole cell environment. (**D**) Retention-of-function curve of the model reaction in 96-DW plates. (**E**) Overall established Medium-Throughput assay.

Combined with a short GC method (cf. chapter 6.4.3) the elaborated Medium-Throughput assay permitted the screening of 250-300 enzyme variants per day, which is sufficient for the rational site-saturation approach. Finally, for quality control reasons all *Aac*SHC variants rationally designed up to that point, as well as SHCs from alternative organisms were transformed into 96-DW plates (Supporting Table S 1) and surveyed

with the established assay for conversion of **52t**. The results obtained from the sreening of 96 enzymes within one day reflected the identical trends that were obtained in the period of a master thesis[142] using the previous enzyme isolation method (Supporting Figure S 2). These results in combination with the low C_V allowed the establishment of the Medium-Throughput assay for the efficient screening of site-saturation libraries in workflow as depicted in **Figure 2-2E**.

2.2.2 Target reaction and initial activity screening

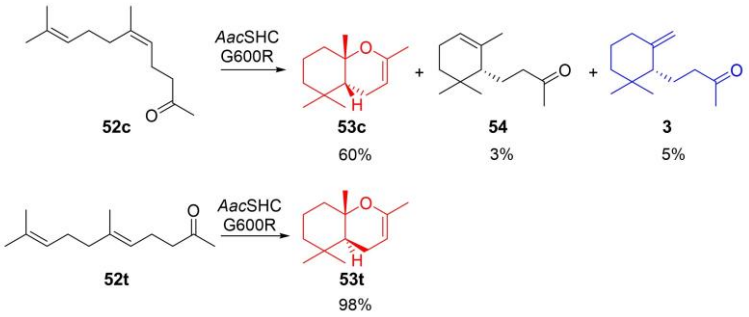

Scheme 1: Biotransformation of neryl acetone **52c** and geranyl acetone 52t with variant G600R. The *E*-isomer **52t** was almost fully converted to the bicyclic product **53t** (red, bottom) and the *Z*-isomer **52c** to bicyclic product **53c** (red, top) as well as monocyclic products **3** (blue) and **54** (black). Relative conversions are given below the products. Reaction conditions: *E. coli* whole cells harboring *Aac*SHC variant resuspended in whole-cell buffer (0.1 M citric acid, 0.1% SDS, pH = 6.0) with an OD_{600} = 20, 20 h, 30 °C, 4.4 mM substrate (=1 µL in 1 mL cell suspension). Error bars represent the s. d. between technical triplicates.

Having proved the feasibility of the screening assay, the study began by testing the *E*- and *Z*-isomer of geranyl acetone **52t** (*trans*)/**c** (*cis*) with *Aac*SHC variant G600R. This approach was chosen since it was recently discovered that position G600 in *Aac*SHC is a hot spot position for conversion of smaller substrates and the Arginine having bulky but fairly flexible properties.[84,142] The result of this approach showed that the *E*-isomer **52t** was almost fully converted to the bicyclic product **53t** (**Scheme 1**, red scaffold). The *Z*-isomer or neryl acetone **52c** was mainly converted to a bicyclic product **53c** as well as to the monocyclic products α-**54** and γ-dihydroionone **3** (**Scheme 1**, blue scaffold). This means that products **3** and **54** can only be manufactured by way of an engineered enzyme controlling the directed cascade cyclization. Since product **3** is of high demand in the flavor & fragrance industry– mainly due to its precursor aptitude for most ambra compounds[144] – the enzyme was engineered towards generation of this compound.

2.2.3 Enzyme engineering towards stereoselective directed cationic cascade

The *Aac*SHC-catalyzed cyclization of substrate **52c** may result in five potential products: three monocyclic deprotonation products α-**54**, β-**55** and γ-dihydroionone **3**, the water-addition product **56** as well as the bicyclic product **53c** (**Figure 2-3A**). The enzyme was challenged to direct the cascade towards monocyclization, as well as to control this reaction in terms of regio- and stereoselectivity. As a starting point for engineering, particular attention was paid to position G600 and therefore saturated to examine each resulting amino acid in the cyclization reaction. Intriguingly, the results disclose that mainly small and polar amino acids drive the monocyclization reaction at position G600. In terms of selectivity, G600T (**Figure 2-3B**), i.e., variant II, performed best. Product **55** was not observed at all, and the amount of hydration product **56** was negligible (>1%). In order to rationalize these findings, computational docking studies of substrate **52c** in the active site of variant II were performed using YASARA.[145] This software allows the *in silico* mutation of an enzyme based on its crystal structure or homology model. Moreover, the tool enables the modelling of substrate **52c**, into the active site of the enzyme based on AMBER forcefields. It is common that challenges arise with docking substrates and homology modelling of terpene cyclases.[146] However, based on results that show the substrate-bound[79] and the apo-form[147] of the enzyme as essentially equal crystal structures and comparing the pre-folding of the squalene-analog aza-squalene **36** bound[79] (Supporting Figure S 3) with the docking results, the approach seemed legitimate. Thereby, the most probable pre-folding states of **52c** should be determined and mutational hot spots located. Docking results are depicted in **Figure 2-3C** and suggest two major pre-folding states: Pre-folding state 1 favors bicyclization due to the coordination of the carbonyl moiety by the Y420-hydroxy group. The resulting second carbocation of the cationic cascade may interact with one lone-pair of the oxygen and thereby form a covalent bond.[148] The saturation of the position G600 demonstrated how bulky amino acids at position G600 favor this pre-folding state (**Figure 2-3B**, G600R,M;L). However, there is a turning point at the size of threonine, where polarity seems to play a more significant role.

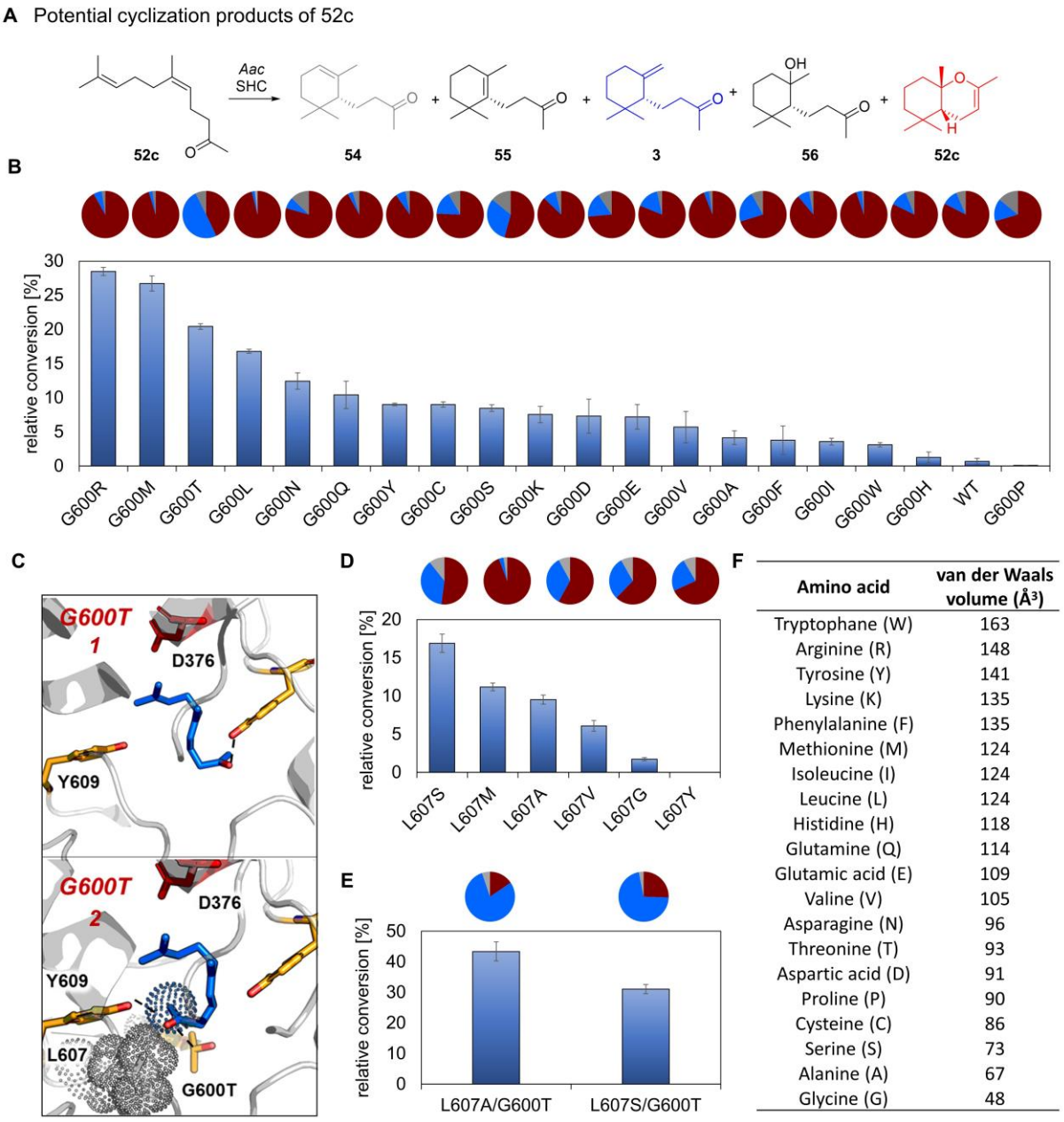

Figure 2-3: Structure-guided engineering of *Aac*SHC towards monocyclization of **52c**. (A) *Aac*SHC catalyzed reaction of **52c** may result in five products. Colored scaffolds correspond to the pie charts in (**B**), (**D**) and (**E**). (**B**) Biotransformations using variants rationally saturated at position G600 with selectivities towards the cyclic products given above the columns. Error bars represent the standard deviation of technical triplicates. (**C**) Docking of neryl acetone **52c** into the active site of *Aac*SHC G600T (catalytic aspartic acid shown as red sticks; hydrogen-bond donating residues shown as orange sticks). The results suggest two pre-folding states with similar binding energies (7.37 kcal/mol vs. 7.16 kcal/mol). (**D**) Biotransformations using variants of rationally mutated position L607. (**E**) Biotransformations using combinatorial variants of positions 600 and 607. Reaction conditions: *E. coli* whole cells harboring *Aac*SHC variant resuspended in whole-cell buffer (0.1 M citric acid, 0.1% SDS, pH = 6.0) with an OD_{600} = 20, 20 h, 30 °C, 4.4 mM substrate (= 1 µL in 1 mL cell suspension). Error bars represent the s. d. between technical triplicates. (**F**) Amino acids sorted by their van-der-Waals volume.[149]

Earlier studies by Peters and co-workers on terpene cyclases demonstrated that the introduction of threonines or serins as potential catalytic Brønsted bases adjacent to an intermediary carbocation result in deprotonation and consequently cascade interruption.[127]However, it was assumed that in this particular case this is due to the hydrogen-bonding capabilities of polar residues. Pre-folding state 2 shows the carbonyl moiety hydrogen-bonded by G600T and Y609. Thus, the lone-pairs of the oxygen are facing away from the resulting second carbocation, ultimately resulting in monocyclic products. Furthermore, steric interaction of the C1-methyl group of the substrate **52c** and the leucine at position 607 can be assumed in this pre-folding state (**Figure 2-3C**, dots).

Based on the docking results, site-directed mutagenesis at the position L607 was performed and determined amino acids – smaller in size than leucine – as beneficial for the monocyclization reaction (**Figure 2-3D**). Interestingly, a recombination of variant II with the best mutation L607S did not lead to the most active double-variant, which was ascribed to literature known antagonistic epistatic effects (**Figure 2-3E**).[150] Instead G600T/L607A (variant III) turned out to be the best double variant showing almost twice the conversion (TTN: 114 ± 13) compared to II (G600T, TTN: 62 ± 2) and higher selectivity (79%) towards the desired γ-dihydroionone **3** (**Figure 2-3E**). Next, position 420, which is stabilizing pre-folding state 1 was targeted for site-directed mutagenesis (**Figure 2-4A**). In particular, the hydrogen bond at this position was disrupted by introducing a phenylalanine (Y420F) at this position instead. The resulting variant IV showed 260 ± 4 total turnover, with a selectivity of 94% towards the desired product **3** (**Figure 2-4B**, IV). Bicyclization was reduced to only 2% and the traces of the hydration product were completely eliminated. In the final round of mutagenesis, the established site-saturation protocol was used by employing the 22c-trick[138] at sites adjacent to position 600 and 607, which resulted in final variant V with a slightly increased steric bulk at position 306 (A306V). The 22c-trick is used in directed evolution of enzymes to reduce the screening effort of protein libraries (for details see ref. 138). Overall, the total turnover number was increased 154-fold compared to the native enzyme and selectivity towards the desired product **3** (**Figure 2-4B**, V) reached 97%. Finally, sulfuric acid-catalyzed cyclization of γ-dihydroionone **3** was performed (**Scheme 2**) to obtain enantiopure (+)-α-ambrinol **57** which disclosed the (S)-/(–)-enantiomer of

γ-dihydroionone **3.** Thus, **57** was obtained in only two (bio-)synthetic steps compared to the five chemosynthetic steps for enantioenriched material.[151]

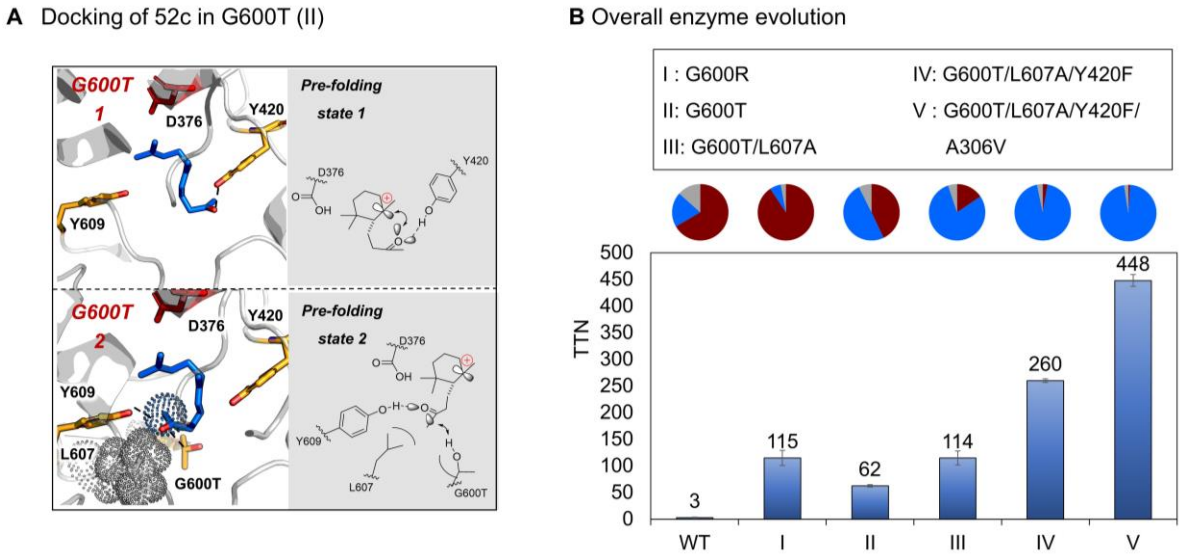

Figure 2-4: Overall engineering of *Aac*SHC towards monocyclization of neryl acetone **52c** (blue pie chart). (**A**) Docking of neryl acetone **52c** into the active site of *Aac*SHC G600T (catalytic aspartic acid as red sticks; hydrogen-bond donating residues as orange sticks). The results suggest two pre-folding states with similar binding energies (7.37 kcal/mol vs. 7.16 kcal/mol). In pre-folding state 1 the carbonyl moiety is coordinated by the Y420-hydroxy group. After protonation, this allows the resulting second carbocation of **52c** and one lone-pair of the oxygen to interact in the bicyclization of the substrate **53c**. In pre-folding state 2 the carbonyl moiety is flipped towards the residue G600T and Y609 and favors the monocyclization of the substrate 1c as the interaction of the orbitals is impeded. Steric interaction of the leucine at position 607 and the substrate 1c is shown in dots. (**B**) Improvement of *Aac*SHC towards monocyclization of neryl acetone **52c** by enzyme engineering. *Aac*SHC variants were compared by their total turnover number (TTN, blue bars) within 20h. Selectivities towards mono-/ bicyclic products are given in pie charts above. Reaction conditions: 10 mg lyophilized *E. coli* whole cells harboring *Aac*SHC variant (18-22 µM, 0.2-0.25 mol%) resuspended in 1 mL CD buffer (0.2% SDS, 10 mM 2-hydroxypropyl-β-cyclodextrin, pH = 6.0), 24 h, 30 °C, 8.8 mM substrate. Error bars represent the s. d. between technical triplicates.

As of now there was no chemical catalyst known which is able to direct a cationic cascade towards a desired intermediary cation (99:1 monocyclization vs. bicyclization) with high product selectivity (97% γ) and excellent enantiocontrol (>99.5% *ee*).

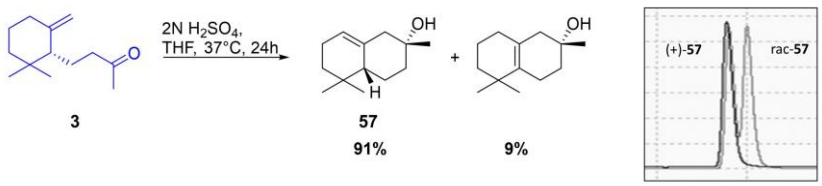

Scheme 2: Sulfuric acid-catalyzed cyclization of **3** towards enantiopure (+)-α-ambrinol **57**.

2.2.4 Mechanistic studies and expansion of the substrate scope

Encouraged by this high selectivity towards the formation of the desired product, the underlying mechanism was elucidated. Therefore, a systematical deconvolution approach of the variant IV was conducted at positions G600 (A), L607 (B) and Y420 (C). In order to highlight the beneficial hydrogen-bond at position Y609 (D), the hydrogen-bond here (Y609F) was also disrupted and combined with selected deconvolution variants. **Figure 2-5A** shows the resulting activities and selectivities of the generated variants compared with variant IV, whereas a letter means a mutation at the above-mentioned position, e.g., variant IV = ABC = G600T/L607A/Y420F. Increasing the steric bulk at position 607 resulted in 75% less conversion, albeit selectivity towards the monocyclic product **3** was still high at 89% (variant AC). The variant BC lacking the hydrogen-bond at position 600 showed almost 80% less conversion and 22% less selectivity towards the desired product **3**. Variant ABCD missed the important hydrogen-bond at position 609 and lost almost all activity and 50% of its selectivity towards the monocyclization. The last deconvolution variant BCD missed all hydrogen-bond donors and showed no conversion at all. Furthermore, we performed docking of **52c** in the final variant V and the result resembles a similar binding mode as depicted in pre-folding state 2, but even closer coordinated to the Y609 side chain (cf. **Figure 2-4A** and **Figure 2-5A**). Consequently, all the mutational experiments and the computational data led to the proposed mechanism depicted in **Figure 2-5B**: After entering the active site, the carbonyl moiety of **52c** is loosely coordinated by the Threonine at position 600. This attractive interaction and the created space at position L607 (L607A), facilitates the carbonyl moiety flip into the direction of the Tyrosine at position 609 for tight binding by a strong hydrogen-bond (cf. IV and variant ABCD). This hydrogen-bond mediated conformation steers away the orbitals of the carbonyl-oxygen from the carbocation and allows the highly product- and enantioselective monocyclization of neryl acetone **52c** in a single catalytic step. The mediating role of the T600 is emphasized by the variant BC, which still showed some conversion of the substrate with good selectivity, most likely due to the disabled hydrogen-bond donor at position 420 (Y420F) (**Figure 2-5A**). Adding the mediating T600, but reducing the size of the hydrogen-bond binding pocket, improved the selectivity towards monocyclic product, however, for the sake of activity (variant AC).

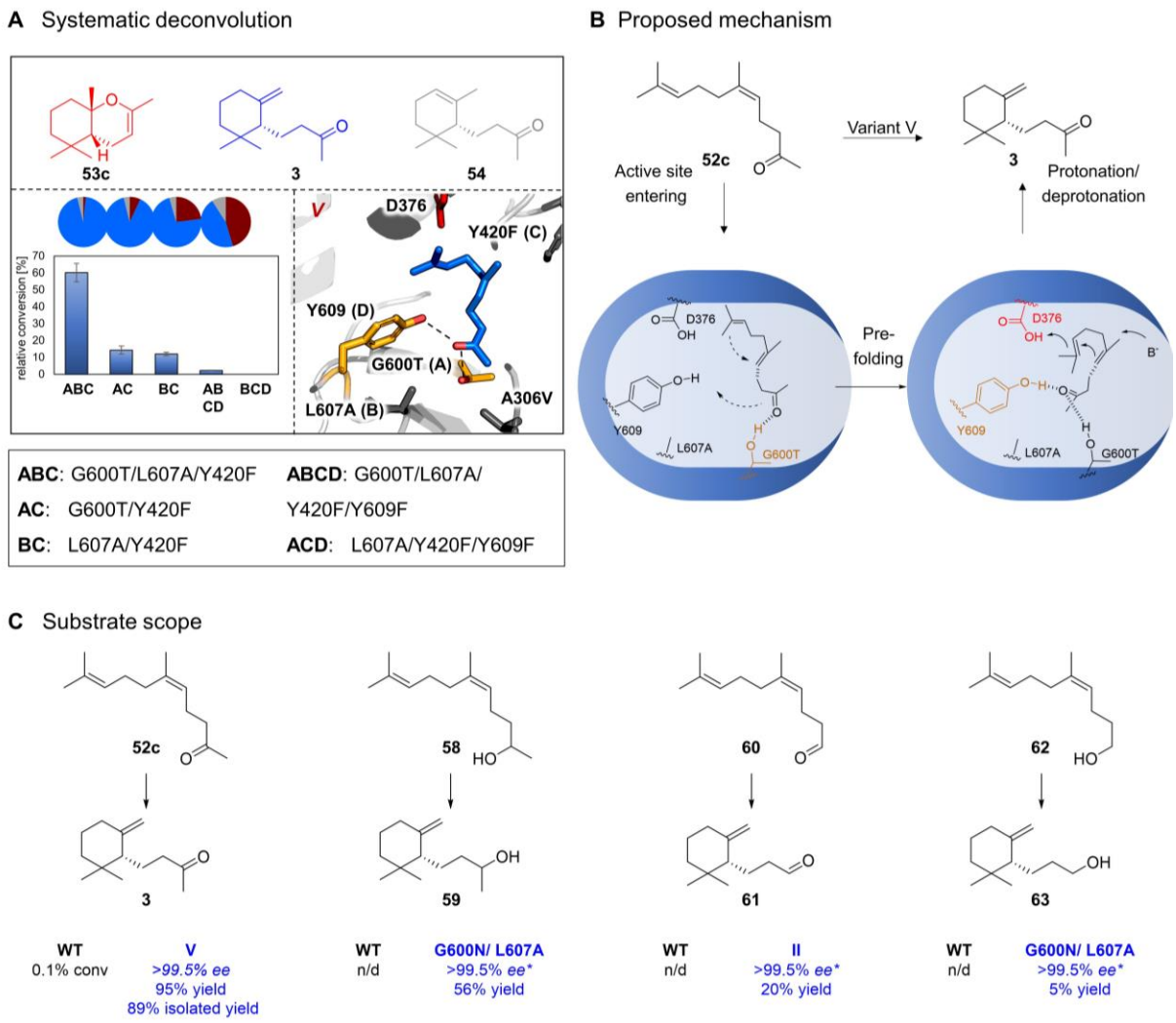

Figure 2-5: Mechanistic studies on stereoselective monocyclization of neryl acetone **52c** and substrate scope. (**A**) (Top) Three products of *Aac*SHC catalyzed cyclization of neryl acetone **52c**. Colors correspond to the selectivities below in pie charts (bottom left) Systematic deconvolution variants of IV sorted by relative conversion. Selectivities shown above in pie charts. Variant BCD showed no conversion at all. (bottom right) Docking of substrate **52c** into the active site of V with the best binding energy (protonating aspartic acid shown as red sticks; hydrogen-binding residues shown as orange sticks. (**B**) Proposed mechanism for the monocyclization of neryl acetone **52c**. After entering the active site, the substrate's carbonyl moiety is coordinated by the G600T (orange, left) somewhat loosely and mediated to the better coordinating Y609 (orange, right). The substrate's pre-folding results in a monocyclic product after protonation (red) /deprotonation (B^-). (**C**) Products generated *via* hydrogen-bond mediated pre-folding in the active site of *Aac*SHC. *E. coli* whole cells harboring *Aac*SHC variant resuspended in whole-cell buffer (0.1 M citric acid, 0.1% SDS, pH = 6.0) with an OD_{600} = 18, 20 h, 30 °C, 4.4 mM substrate. Error bars represent the s. d. between technical triplicates. *due to enantiopure conversion of *Z*-substrates.

The key role of the hydrogen-bond donors as molecular anchors is constituted by the variant BCD, in which all hydrogen bonds were deactivated and not a single cyclization product occurred. These mechanistic hypotheses are supported by the research of Chen et al.[152] where the hydrogen-bonding capabilities of water and several functional groups

were calculated, and experimental binding affinities were explained. The authors concluded that tyrosines – compared to the other polar amino acids – are able to bind ketones extremely tight due to matching binding capabilities.

Finally, the potential of pre-folding via molecular anchoring in the cyclization of analogues substrates was investigated (**Figure 2-5C**). All substrate analoga (**58**, **60**, **62**) of **52c**, varying in the anchor motive (functional group and chain length) were cyclized to monocyclic products (**59**, **61**, **63**) thereby providing access to megastigmane-based natural products, which exhibit great potential in biotechnology and pharmacy.[20] Interestingly, all four products contained the exocyclic double-bond at the cyclohexane ring which is chemically difficult to obtain.[144] Furthermore, the scalability of this reaction was validated by converting 2 g of neryl acetone **52c** with the engineered enzyme V expressed in *E. coli* whole cells (10 g_{CDW}/L) and resuspended in 1 L *dd*H2O (including 10 mM 2-hydroxypropyl-β-cyclodextrin and 0.2% SDS), with high selectivity (95% γ-**3**; 1% α-**54**; 4% **53c**) towards the desired product **3** (Supporting Figure S 4). Isolation of the product (89%) and subsequent cyclization confirmed enantiopure conversion. The use of cyclodextrin in the reaction mixture was inevitable when using higher substrate concentrations, i.e., 10 mM, which will be discussed in the upcoming chapters (cf. chapter 4.2.1). Noteworthy, when using the *E*/*Z*-mixture of geranyl acetone **52**, the engineered V converts the *Z*-isomer **52c** prior to the *E*-isomer **52t** (Supporting Figure S 5), which is another example for cyclization of unusual *Z*-isomers in class II terpene cyclases.[153] These examples show, first, the general feasibility of designing molecular anchors for substrate pre-organization and the associated high selectivity. Second, they constitute the scalability of this enzymatic reaction by producing high value products in gram-scale. Third, they demonstrate the importance of fine-tuning molecular anchors, since not every hydrogen-bond has the same power.[152]

2.3 Conclusion

Identification and variation of core elements in catalysis, e.g., cofactors or entrance channels, often lead to unexpected, yet very useful reaction pathways.[154,155] In this work on the *Aac*SHC, the focus was set on engineering polar amino acids as molecular anchors, which unlocked the ability of hydrogen-bond mediated pre-folding of substrates. This non-natural pre-folding emerged as a useful supplement to the *shape-complementary* cyclization. The artificial manipulation of the cation pathway

streamlined the unprecedented stereo- and regioselective monocyclization of neryl acetone **52c** and analoga. Potentially generated products are widely used in the flavor & fragrance[144] or pharmaceutical industry[124] and can be produced within a single enzymatic step in water, thus substituting established but cumbersome protection group-based chemistry. Going forward, molecular dynamic (MD) simulations should elucidate this precise catalysis on the molecular level in detail. Curiously, the full conversion of 10 mM (~2 g/L) substrate empolying 10 g_{CDW}/L (~40 g_{CWW}/L) took more than 160 h. In contrast, Eichhorn et al.[129] reported >50% conversion of 4 g/L substrate employing 12.2 g_{CWW}/L within 24 h in the production of (–)-ambroxide **7**. Given this temporal discrepancy, this reaction was investigated extensively in the next chapter, taking into account the macromolecular, subcellular evironment and the physiologcal function of the biocatalyst.

Chapter 3

HARNESSING THE CHEMICAL AND STRUCTURAL BIOLOGY OF SQUALENE–HOPENE CYCLASES FOR EFFICIENT CATALYSIS

3.1 Introduction – The physiological function of squalene-hopene cyclases

Monotopic membrane proteins like SHCs occupy a unique role in enzymology accounting for only 0.06% of all crystallized protein structures (**Figure 3-1A**).[78] These enzymes contain a special anchor motif which permits the penetration into the biomembrane by a hydrophobic α-helix and adjacent highly flexible basic residues to interact with anionic phosphate head groups of the biomembrane (**Figure 3-1B**). The interfacial localization of SHCs requires the 'channeling' of their substrates via π-stacking interactions along a hydrophobic tunnel into their distal active site. While that is energetically unfavorable, it is beneficial in terms of evolution leveraging the soluble domain, which was already evolved for catalysis in an aqueous environment. Indeed, the recruitment of water molecules from the aqueous bulk is pivotal for SHC catalysis, as they act as 'proton-shuttles', Brønsted-bases or even entropy drivers.[75,93,156] Resulting highly hydrophobic hopanoid products **1** are deposited in the membrane and counteract exterior stresses on their biological host.[157,158] Interestingly, it was shown that such depositions of terpenes as well as the integration of the enzyme itself into the membrane result in local perturbations within the membrane.[159,160] Furthermore, studies have shown that activity of membrane-bound enzymes relies on the current state of membrane integrity.[161–163] As a result, it can be speculated that terpene-induced local perturbations in the membrane entail the activation or reversible inhibition of SHCs and require careful consideration in the overall catalysis.

Despite these facts, terpene cyclases have so far primarly been investigated via active site (1) mutagenesis approaches (**Figure 3-1A**).[55,84,127,164] To examine SHC catalysis more holistically, this study additionally focused on the enzyme's entrance tunnel (2) and its membrane embedding into a biomembrane compared to a membrane mimic (3).

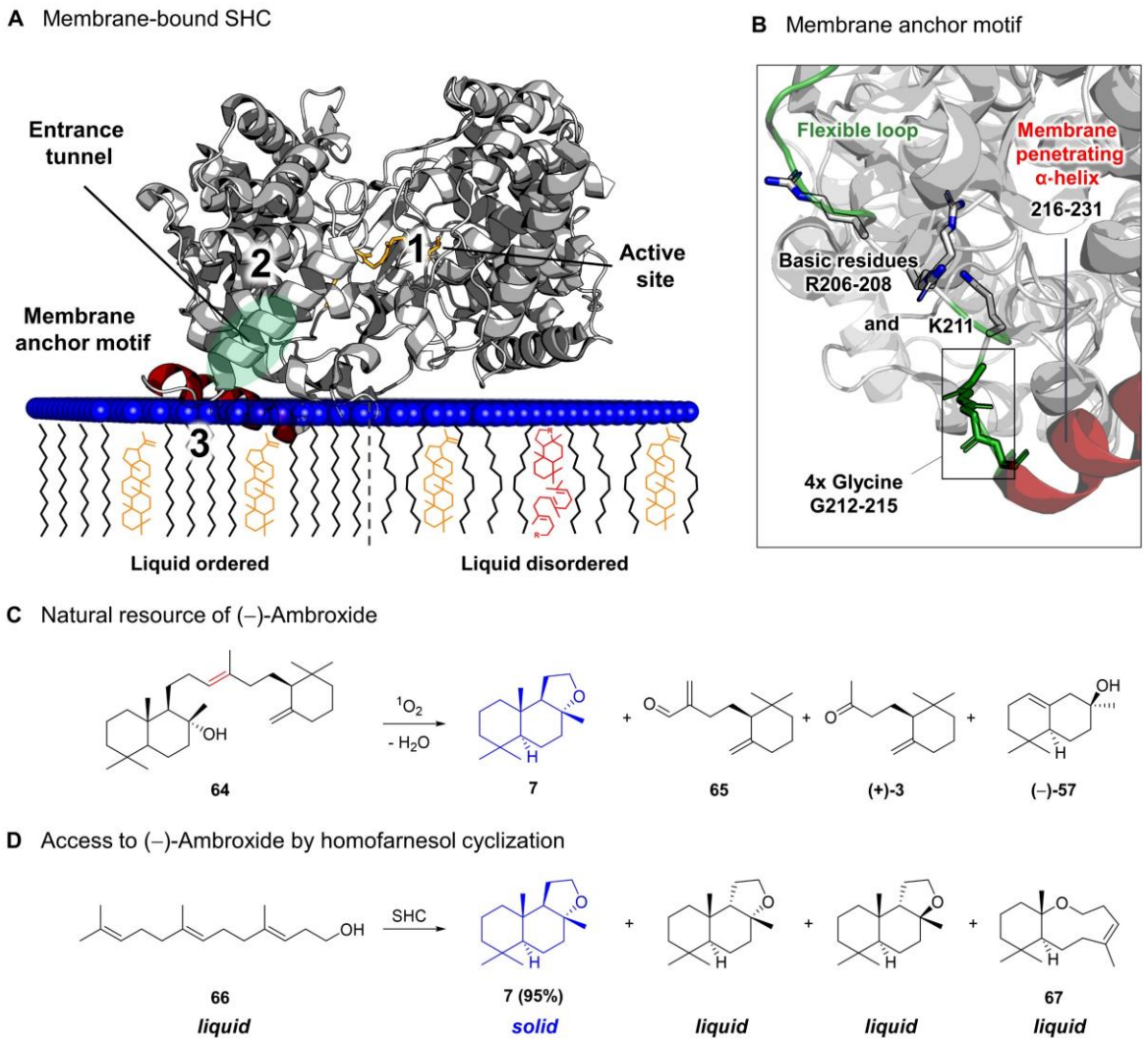

Figure 3-1: Holistic consideration of membrane-bound SHC embedded into the *E. coli* cytoplasmic membrane.[159] (**A**) SHCs (grey cartoon) are monotopically bound to the biomembrane (blue head groups and black tails) by an anchor motif (3) where they source their hydrophobic substrate **36** (orange sticks) through an entrance tunnel (2, green) into their distal active site (1). SHCs catalyze the polycyclization of **36** to pentacyclic hopene **37** (yellow scaffold). These molecules are subsequently stored within the membrane to ensure membrane integrity (left, liquid ordered) during exterior stresses.[77] Additional substrates as well as generated products (red scaffolds) may also be stored in the membrane interior, resulting in altered membrane order (right, liquid disordered) and ultimately in decreased enzyme activity. (**B**) The membrane anchor motif consists of a hydrophobic α-helix (red) and basic residues on a highly flexible loop (green) initiated by four glycines (green). (**C**) Ambergris **64**, the natural resource of (–)-ambroxide **7**, is degraded via autooxidation to various products,[144] i. a. (–)-ambroxide **7** and (+)-γ-coronal **65**. (**D**) Promiscuous cyclization of *E,E*-homofarnesol **66** towards solid (–)-ambroxide **7** and three liquid side products.[95,129]

The archetypical[95] promiscuos cyclization of *E,E*-homofarnesol **66** to (–)-ambroxide **7** was chosen as a model reaction. This reaction offers several advantages and opportunities: (a) Catalysis has been shown to work with both isolated enzyme and whole cells.[95,129,165,166] (b) As (–)-ambroxide **7** solely crystallizes from the reaction broth, this effect can be leveraged to overcome the downregulation, which is caused by the

terpene-induced local perturbations. (c) While naturally being produced by autooxidation of ambergris **64** (**Figure 3-1 C**), the *Aac*SHC catalyzed highly stereoselective cyclization (>99% *ee*, >95% *de*) of homofarnesol **66** towards **7** provides the most potent substitute for the scarce natural resource (**Figure 3-1D**).[17] Especially, given the fact that chemical catalysts need harsh conditions and are far inferior in terms of selectivity (50% *ee* and 64% *de*).[167] These facts render the promiscuous cyclization of homofarnesol **66** ideally suited for the endeavor to understand these enzymes more holistically – from an academic as well as an industrial point of view.

3.2 Results and discussion

The overall study was divided into three parts: First, the enzyme was investigated on the molecular level by means of structure-guided enzyme engineering. The focus of this part was set on achieving high selectivity for **7** (99% *ee*, *de*, no other cyclization products), rather than activity, which would strongly support the catalysis by continuous *in situ* product crystallization (ISPC) of the sole product **7** and the accompanied shift of the chemical equilibrium to the product side.[168] Afterwards, the introduced mutations were transferred to SHC homologs to analyze subtle changes in the confined active site. Second, the effects of the mutations on the entrance tunnel and the amino acid network were investigated in depth computationally. In the final part, the macromolecular level was approached by comprehensive enzyme kinetics *in vitro* and *in vivo*.

3.2.1 Dual-site allocated mutagenesis approach towards diastereo- and enantioselective cyclization of 66

To aid the structure-guided engineering, the 3*E*-isomer of **66** was docked into the active site of the *Aac*SHC wild type's (WT) crystal structure (PDB: 1UMP), which allowed the identification of four amino acid residues (W169, I261, G600, F601) within 5 Å to the functional group of **66** (**Figure 3-2A**). In the first engineering round, each of the four positions were randomized using the degenerated codon NVS, which encodes mainly polar amino acids (all except Ile, Leu, Met, Phe, Val). In accordance with chapter 2.1, this approach was chosen to potentially anchor the substrate's alcohol group in the active site. In total, 384 enzyme variants were compared *in vivo* and exhibited the two catalytically beneficial positions G600 and W169 (**Figure 3-2B**). As anticipated from

earlier studies[84,169] and the docking pose in **Figure 3-2A**, increased steric bulk at position G600 was beneficial for the tricyclization of **66** showing up to 8-fold improved activity and slightly improved selectivity. Unexpectedly, variants with reduced steric bulk at position W169 such as W169G also showed 6-fold improved activity as well as the desired selectivity of 99% towards **7**. As a result, this variant was chosen for further engineering.

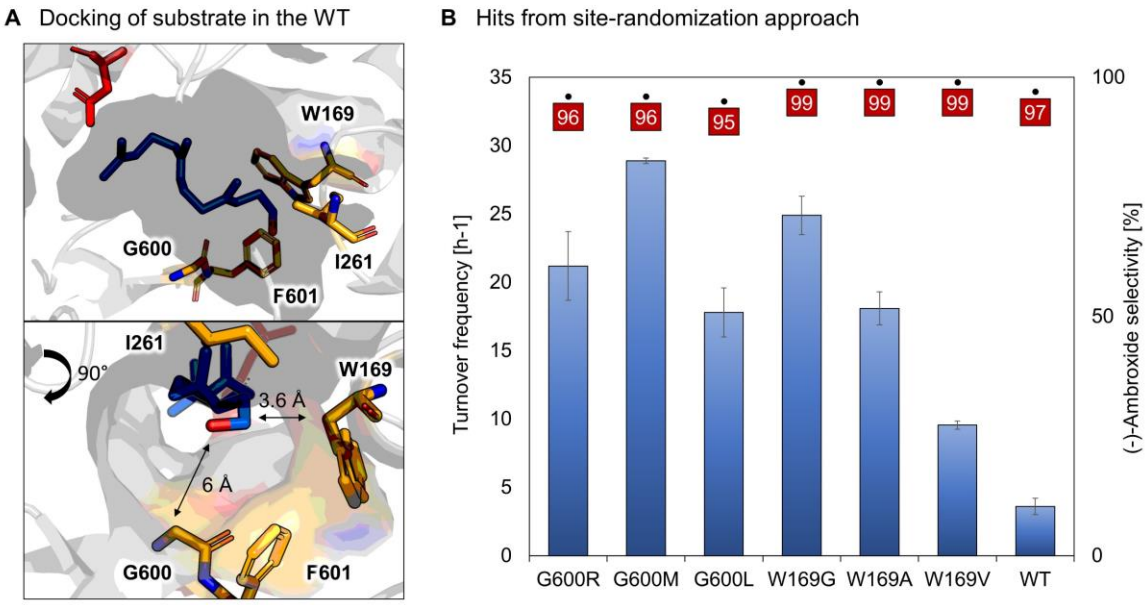

Figure 3-2: First round of structure-guided engineering. (**A**) Docking of substrate **66** in the *Aac*SHC WT shows the full chaperoning (grey surface) of the substrate in the hydrophobic active site and the *shape-complementary* pre-folding. Targeted positions for randomization 5Å away from the alcohol group are shown in bright orange sticks. Rotation around the Y-axis shows the distances to the hit positions G600 and W169. (**B**) Turnover frequencies (blue bars) of the hit variants and the corresponding selectivities (black dots) towards (–)-ambroxide **7**. Reaction conditions: 1 mM **66**, 0.1 g_{CDW}/ mL (~2 mol% SHC), 600 rpm, *dd*H_2O, 1 h. Error bars represent the s. d. of technical triplicates.

In the following engineering, the enzymes were also compared *in vitro* to exclude membrane-correlated mass transfer issues.[170] Turnover frequencies were reported at the optimal temperatures (Supporting Figure S 6) evaluated beforehand (**Figure 3-3A**). In the second engineering round, Variant W169G i. e., P1 was conducted site-saturation mutagenesis at the adjacent positions 600 and 607 which revealed variant P2 (W169G/G600M) with 4-fold improved turnover frequency of 391 h^{-1} while retaining 99% selectivity.

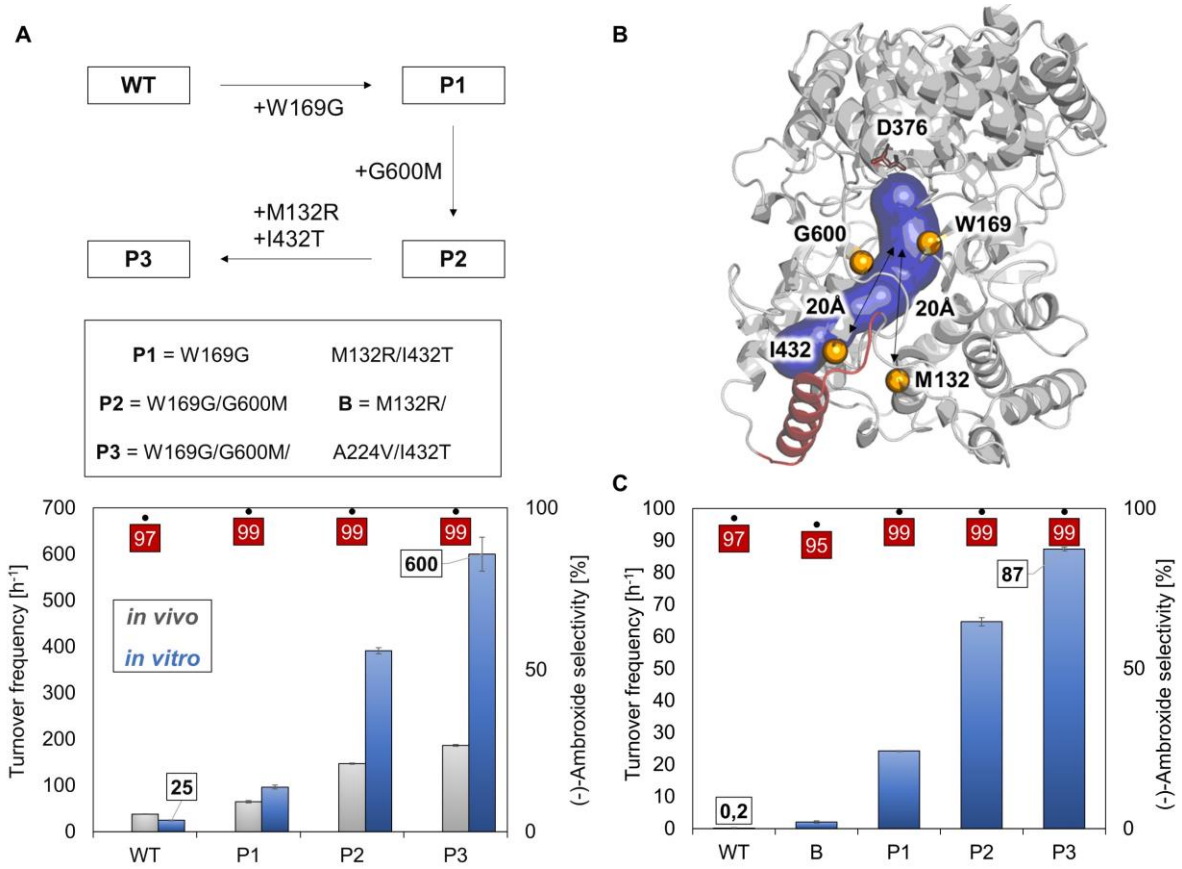

Figure 3-3: Dual-site allocated mutagenesis of *Aac*SHC towards enantio- and diastereoselective (–)-ambroxide **7** production. (**A**) *Aac*SHC variants generated during enzyme engineering (P1-P3) compared with the WT. Turnover frequencies (left y-axis) shown in grey (*in vivo*) and blue (*in* vitro) bars. (–)-ambroxide **7** selectivity (right y-axis) as black dots. Reaction conditions: *in vivo*: 1 mM **66**, 0.1 g_{CDW}/ mL, 600 rpm, *dd*H_2O, 1 h. *in vitro*: 0.018-0.025 mg/mL SHC (2-2.5 mol%), 20 mM citric acid, pH= 6.0, 0.2% CHAPS (3-[(3-Cholamidopropyl)-dimethylammonio]-1-propansulfonate). (**B**) Crystal structure of *Aac*SHC (PDB: 1UMP) with most putative entrance tunnel (blue surface) reported[75] and suggested by a CAVER analysis.[171] Membrane binding α-helix shown in red. Mutated amino acid locations shown as yellow spheres and protonating aspartate as red stick. (**C**) Comparison of the *Aac*SHC variants and the Benchmark *Aac* variant B[129] under process conditions derived from the Eichhorn et al. study.[129] Reaction conditions: 1 mL *dd*H2O + 0.2% SDS, 10 mg_{CDW} (=40 mg_{CWW}; g_{SDS}:g_{CWW} = 0.05) *E. coli* whole-cells harboring the corresponding *Aac*SHC variant (40-50 µM), 100 mM (≈ 50 g/L) 66, 19 h, 30 °C, 750 rpm. Error bars represent the s. d. of technical triplicates.

Further mutations in the active site disrupted the high selectivity of the enzyme (data not shown), which encouraged us to seek for alternative mutation hot spots, allocated distal from the active site. Consequently, a CAVER analysis of the *Aac*SHC crystal structure was performed (Supporting Figure S 7). The CAVER software tool allows the identification of potential enzyme tunnels and further predicts potential bottlenecks and related amino acids.[171] The analysis resulted in several potential tunnels, however we focused on one particular tunnel, which was published earlier as the putative enzyme's entrance tunnel (**Figure 3-3B**).[75] Intriguingly, two (M132R/I432T) out of three

positions (M132R/A224V/I432T) of the Benchmark enzyme B were located in the designated bottleneck area, with the third position described by the authors themselves as not being beneficial.[129] These results gave reason to perform site-saturation mutagenesis within this bottleneck area, which unfortunately resulted in only slight to no increases in TOF (Supporting Figure S 8). However, the addition of both published distal mutations (M132R/I432T) resulted in the final variant P3 with a 1.5-fold increase in TOF to 600 h^{-1} and no loss of selectivity. In a last experiment, the optimal process conditions reported by Eichhorn et al. were mimicked using high substrate loadings (50 g/L) and SDS in a ratio of 0.05 g_{SDS}:g_{CWW} (**Figure 3-3C**). This approach demonstrated the superior performance of P3 with 87.3 h^{-1} over the WT with 0.22 h^{-1} which is an over 397-fold improvement in TOF.

Taken together, the enzyme engineering results demonstrated several aspects that are of importance. First, the *in vivo* versus *in vitro* comparison mostly showed higher performance *in vitro* (up to 3-fold), which is most likely due to the slow permeability of **66** through the cell membrane.[172,173] Permeability issues are a well-known challenge in *in vivo* biocatalysis and alternative solutions to enzyme isolation comprise transporter enzymes as reported by the groups of Bühler[174] and Hartwig[175] or the application detergents as shown in the study of Eichhorn et al.[129] Second, the biotransformations under process conditions revealed much higher improvement in activity (397-fold) compared to the standard conditions (24-fold) which contained a 100-fold lower cell density and 50-fold lower substrate concentration. Here the high selectivity of variant P3 pays off, which omits the generation of liquid side products. Less selective enzymes like WT and B may therefore be hampered in activity by local perturbations caused by deposited products within the cell membrane.[160,176] However, the additional SDS within the reaction mixture may also account for this result. Last, the active-site mutagenesis usually conducted in terpene cyclase studies[91,128,177,178] was successfully extended by engineering the enzyme at a second, distal (~20 Å) allocated site. A similar strategy was also presented by the Reetz group in their engineering of a monoamine oxidase.[179] These dual site-allocated mutagenesis approaches represented a valuable advancement to the portfolio of structure-guided enzyme engineering strategies.

3.2.2 Computational insights for elucidation of the mutational synergy – collaboration with Osuna lab

In order to rationalize the effects of the introduced active site and distal mutations on the enzyme structures and the accompanied improvement in their catalytic efficiency, a deep computational exploration was performed by means of docking and MD simulations. The MD part was elaborated in a cooperation with the group of Silvia Osuna, which are specialists in computational enzyme modelling.[180] Since the majority of these results derive from the Osuna group, only a brief summary of the MD data is presented below.

The enzyme's high selectivity towards **7** may be ascribed to the emerging hydrogen-binding pocket created by the W169G mutation (**Figure 3-4A+B**). The glycine/serine-amides may interact with the alcohol group of **66** and therefore stabilize the pre-folding which results in (–)-ambroxide **7** after cationic cyclization. This interaction was observed in the docking of **66** into *in silico* generated W169G (**Figure 3-4C**). Interestingly, the substrate in the active site is flipped, but the methyl groups are still aligned in the same direction, which is pivotal for the stereochemical configuration of **7**.

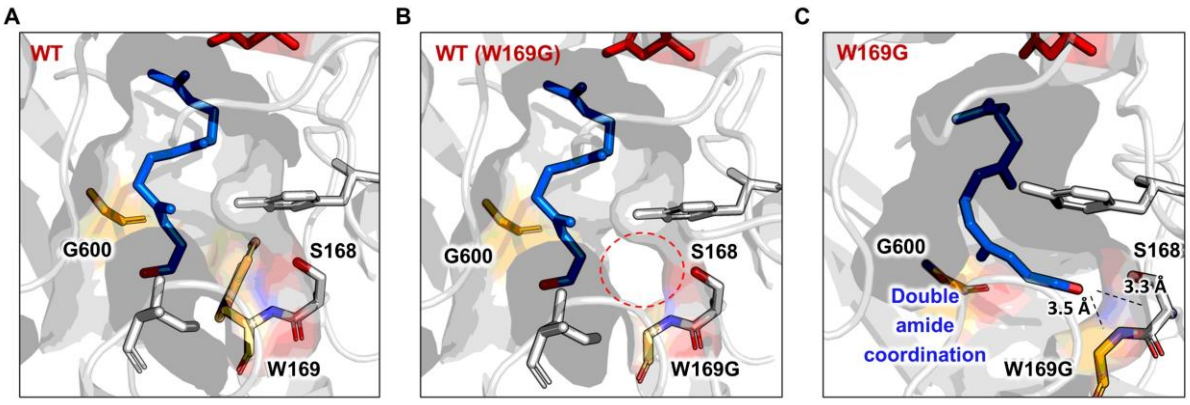

Figure 3-4: Molecular docking of *E,E*-homofarnesol **66** (blue sticks) into the active site of *Aac*SHC. Beneficially mutated amino acids shown as yellow sticks. Protonating aspartic acid shown as red sticks. (**A**) *Shape-complementary* pre-folding of **66** in the WT. (**B**) Identical docking as depicted in (A), but with W169G mutation artificially introduced. This mutation opens a hydrogen binding pocket W169G (red dashed circle). (**C**) Pre-folding of **66** in the homology modeled W169G. Homology model was created by SWISS-MODEL[181] and was energy minimized afterwards. The substrate's alcohol moiety coordinates into the new formed hydrogen binding pocket W169G/S168.

The MD-simulations of the Osuna group showed that in fact more than one stable conformation exists for the variants WT, P2 and P3. The table in **Figure 3-5A** elucidates

the impact of the mutations on the dynamic entrance tunnel of all these conformations, including the population of those. The data shows that during the course of engineering the main entrance tunnel in P3 was broadened from 1.19 to 1.83 Å (maxBR) and the population of this tunnel was increased from 5% to 58%. Finally, **Figure 3-5B** illuminates the extraordinary synergy of both entrance mutations on the active pocket's shape in P3. The newly introduced M132R mutation triggers a reconstructive chain reaction of amino acids F434, F437, F605, F601 and M600, thus improving the pre-folding of substrate **66**, which eases the concerted tricyclization. Intriguingly, this rearrangement forces the phenylalanine at position 437 from an entrance tunnel 'closed' into an 'open' state, thus widening a bottleneck area (**Figure 3-5C**, red square) from 0.91 Å to 1.09 Å.

A

Variant	Conf.	maxBR (Å)	Population (%)
WT	1	1.19	5
WT	2	1.17	3
WT	3	1.24	29
P1	4	1.45	28
P2	5	1.58	29
P2	6	1.01	5
P3	7	1.83	**38**
P3	8	1.74	**58**

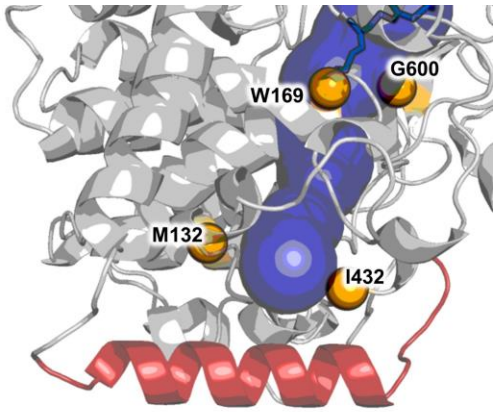

B

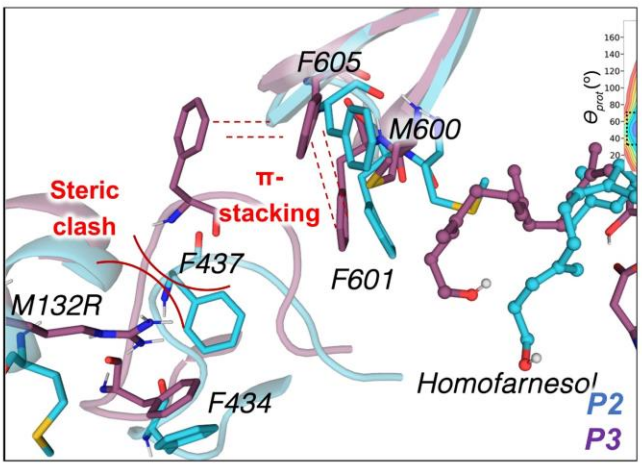

C

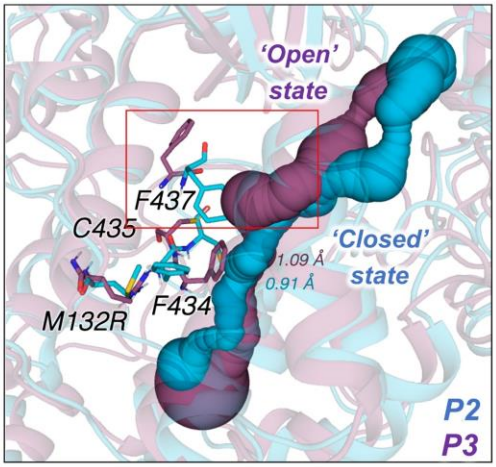

Figure 3-5: Computational elucidation of the mutations on the macromolecular enzyme scaffold. (**A**) Table demonstrates improved maxBR and population of the main tunnel (blue surface) induced by the mutations (orange spheres). Membrane-binding α-helix shown in red, entrance tunnel in blue and hit positions as orange spheres. (**B**) Overlay of substrate-bound conformation of P2 (blue) and P3 (purple) highlights the reconstructive chain reaction triggered by M132R interaction with the F434 backbone. (**C**) Tunnel analysis of variant P2 (blue) and P3 (purple) contrasts the 'open' state of P3 with a broader tunnel and the 'closed' state of P2 with a narrow tunnel.

The *in silico* results showcase the high level of complexity in enzyme catalysis: In synergy, the four mutations substantially improved substrate acquisition and chaperoning by global and local interactions. The substrate flow was increased by the manipulation of the enzymes' dynamic elements. Upon substrate binding, the enzyme would usually close the entrance tunnel by flipping the loop containing residue F437.[75] This regulative function was hampered by the mutation M132R, which resulted in higher catalytic performance of the enzyme by increased substrate flow. The investigation of dynamic elements to improve enzyme performance is constantly emerging also thanks to novel computational modelling tools.[171,182,183] However, the focused rational variation of dynamic elements in combination with active-site mutagenesis, as presented in this work, is still underrepresented.

3.2.3 Precision catalysis – Homologous transfer unveils stereoconvergent cationic cyclization

Having deciphered the mechanistic details of the catalysis, the next aim was to transfer these features to SHC congeners. To that end, we chose four SHC homologs *Zmo*1SHC, *Zmo*2SHC, *Tel*SHC and *Sco*SHC with low sequence identities of 38-51%, transferred the selectivity conferring mutation W169G into all homologs and compared the generated variants with the WT SHCs (**Figure 3-6A**). Considering only the WTs, the *Sco* stands out with almost no conversion and the *Zmo*1 with almost 4-fold conversion compared to *Aac*. A closer inspection of the active sites of these homologs revealed a cysteine for the *Sco*SHC in juxtaposition to the W169 instead of serine for the *Aac*SHC as the major difference (**Figure 3-6B**, I and II, see also Supporting Figure S 9). This hydrophobic cysteine may block the amide backbone due to its bigger Van-der-Waals radius, thus hampering the coordination of the substrate's alcohol moiety. In contrast, the *Zmo*1SHC harbors a glutamine at this position which protrudes into the active pocket and may ease the coordination of the substrate (**Figure 3-6B**, III). The results of the mutated variants disclosed that the (–)-ambroxide **7** selectivity of all selected SHCs arose to 99% when introducing the 'W169G' mutation, entailing higher activity. Interestingly, the herein used 90:10, 3*E*:3*Z* isomeric mixture always resulted in 99% **7** which suggested a stereoconvergent cyclization. Such a cyclization could only occur if the cationic transition state of the 3*Z* substrate is long-lived enough to undergo a *cisoid-transoid* bond rotation event during the cyclization (**Figure 3-6C**). To prove this hypothesis, a

55:45, 3*Z*:3*E* mixture of **66** was transformed with all generated catalysts. Intriguingly, all variants produced over 70% (–)-ambroxide **7** from the isomeric mixture. Even more remarkable, the variants from *Zmo*2, *Tel* and *Sco* showed selectivities over 95%, which in fact revealed a stereoconvergent cationic cyclization in the SHC's confined active site. It is worth mentioning that the natural stereoconvergence increased with accessible electron density at position 168 in the order *Sco* (cysteine)<*Aac* (serine + water; blocked by Y420)<Zmo1 (glutamine)<Tel (serine + water)<Zmo2 (tyrosine) (cf. Supporting Figure S 9C+D). The electron density at this position is presumably required to extend to cation's lifetime for the *cisoid-transoid* bond rotation. As the *Tel*W172G variant showed the best conversion combined with 96% selectivity, this enzyme was chosen for a docking investigation of both **66** isomers. **Figure 3-6B**, IV reveals that both isomers align similarly in the active site with their alcohol moiety coordinated to the newly created polar pocket of the W172G/S171 double amide backbone. As a result, this almost identical pre-folding of the isomers may be another reason for the stereoconvergence.

The herein presented homologous transfer substantiates the pivotal role of the hydrogen-binding capability exhibited by SHCs. Whereas blocking the polar binding site by a cysteine disrupted activity (cf. **Figure 3-6**, *Sco*SHC) an additional hydrogen-bond donor as in *Zmo*1 improves activity. Exposing the double amide backbone by the W to G mutation not only increased activity as well as selectivity for all SHCs, but further revealed the unprecedented ability of the stereoconvergent cationic cyclization of a *cis*/*trans* isomeric substrate mixture. This powerful ability is presumably facilitated by the *shape-complementarity* of the enzyme's active site, allowing only the distinct transition state structure that results (–)-ambroxide **7**, combined with locally enriched electron density.[184] Besides coordinating the substrate's alcohol moiety, the newly created polar space could serve to trap a water molecule, which could support in pre-folding of the substrate. Such a structure-giving role was described in the cationic rearrangement cascade of GPP **11** to bornyl diphosphate **29** (cf. chapter 1.3.1).[57] These results prove that the double-bond nature does not necessarily determine the fate of the final product as stated earlier[185] and makes the tedious separation of isomers beforehand obsolete. A similar stereocontrol over a cationic transition state was recently published by the List group,[105] which also leveraged the strongly confined active site of their Brønsted-acid catalyst (cf. chapter 1.3.2).

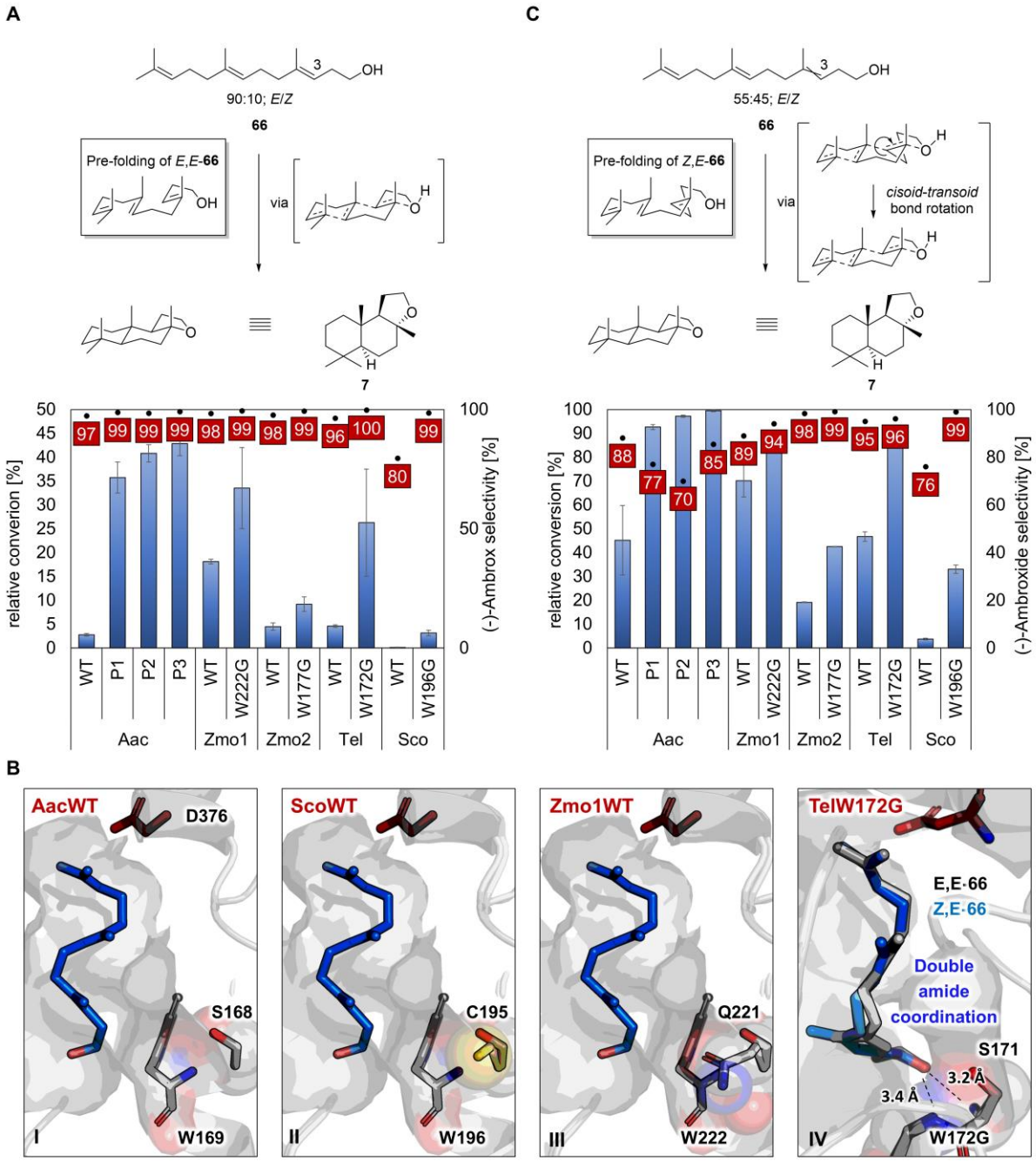

Figure 3-6: Stereoconvergent cationic cyclization of **66** in the active site of SHCs**. (A)** Stereoconvergent cyclization using of a 90:10 3*E*:3*Z* **66** isomeric mixture with different SHC homologs and variants thereof. The pre-folding of the *E*,*E*-isomer results in the right conformation of (–)-ambroxide **7**. Reaction conditions: 2 mM **66**, *E. coli* whole cell with OD_{600} = 10, 30 °C, 5 h. **(B)** Docking of **66** in the active site of the different variants reveal the key function of the position 169 (*Aac*SHC counting). See **(A)** and **(C)** for the related activities. Blocked 169 backbone by adjacent hydrophobic cysteine disrupts activity (*Sco*WT,). Additional adjacent hydrogen-bond donor/acceptor such as glutamine boosts activity (*Zmo*1WT). Opening the hydrogen-binding pocket by tryptophane to glycine mutation boosts activity and selectivity for all variants. **(C)** Stereoconvergent cyclization using of a 55:45, 3*E*:3*Z* **66** isomeric mixture with different SHC homologs and variants thereof. The pre-folding of the *Z*,*E*-isomer results in an unfavorable conformation of (–)-ambroxide **7** and therefore requires a *cisoid-transoid* bond rotation. Reaction conditions: 2 mM **66**, *E. coli* whole cell with OD_{600} = 10, 30 °C, 48 h. All biotransformation were carried out as analytical biotransformations (cf. chapter 6.7.1) and error bars represent the s. d. between technical triplicates.

Facing the question of the exact mechanism, the only comparable *cisoid-transoid* bond rotation during a cationic rearrangement cascade was postulated by the Tiefenbacher group in their study on the rearrangement of geranyl acetate **34**.[63] Herein, the linalyl cation must isomerize from *transoid* to *cisoid* prior to S_N' cyclization (cf. chapter 1.3.1).[72] This perception could facilitate the herein observed stereoconvergence of the reaction.

3.2.4 Kinetic analysis of the generated variants *in vitro* and *in vivo*

After the mechanistic investigations on the catalyst, the next target was to face real industrial application conditions by means of maximal substrate titers und turnovers. However, it is a common drawback that terpenes comprise high cytotoxic potential, partially due to diffusion into and desintegration of the cellular membrane.[160,186,187] Therefore, in addition to the mere application, the focus of this part was to understand the relation of substrate to cell concentration. First, the cytotoxic potential was demonstrated by simply increasing the substrate concentration 20-fold from 1 to 20 mM while keeping the cell concentration at 0.1 g/L, which indeed resulted in almost immediate inactivation of the enzyme (~2% conversion). Such an effect was not observed in the earlier study using high cell concentrations.[129] Therefore, the cell concentration was raised 50-fold to 5 g_{CDW}/L, which resulted in a linear conversion of 60% of **66** within 24 h (Supporting Figure S 10A+B). Despite the unambiguous results of these two simple experiments, it was not clear whether the first reaction stopped due to the enzymatic substrate/product inhibition, as stated by Simon,[95] or due to molecular toxification of the microbial host. To shed light on this issue, the four *Aac*SHC variants WT, B, P2 and P3 were kinetically analyzed *in vivo* and *in vitro* (**Figure 3-7**). These variants were chosen as they comprise the four stages of engineering: native enzyme, engineered entrance tunnel, engineered active site, and engineered active + entrance tunnel. Starting with the *in vitro* characterization, it is worth to mention that membrane-bound enzymes require detergents as an artificial membrane for isolation and solubilization.[95] The entrance tunnel mutations of the benchmark SHC B doubled the k_{cat}, while only slightly affecting K_M and therefore substrate affinity (**Table 3-1,** B, *in vitro*).

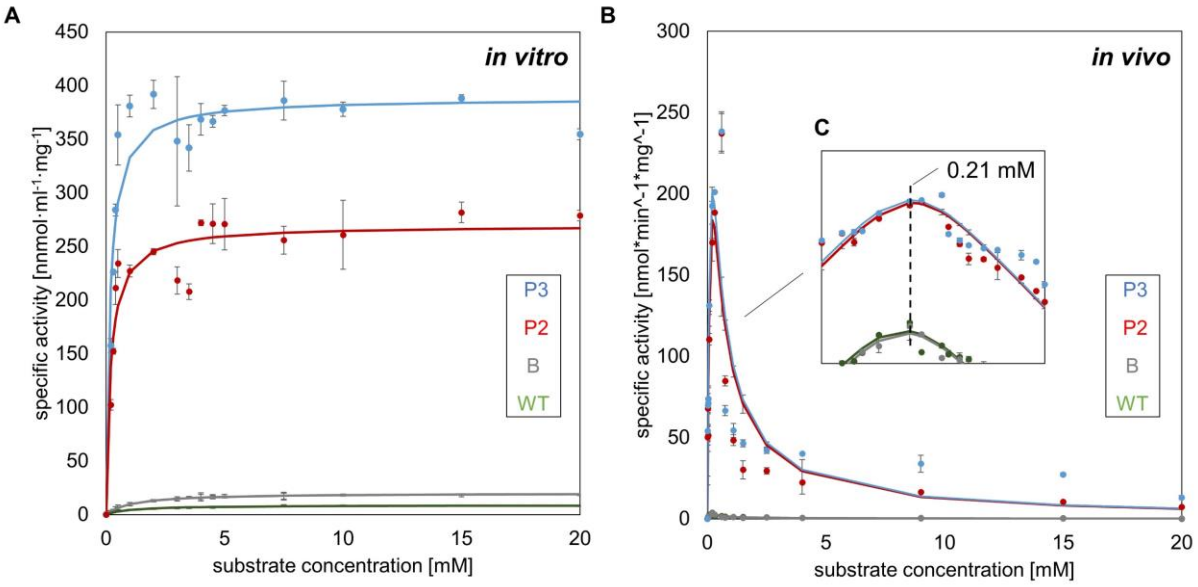

Figure 3-7: Kinetic investigations of selected *Aac*SHC variants *in vitro* and *in vivo*. For reaction conditions cf. chapter. 6.7.6. (**A**) Michaelis-Menten plots for the *Aac*SHC WT, B, P2, and P3 catalyzed cyclization of **66** *in vitro*. (**B**) Substrate-excess inhibition plots for the *Aac*SHC WT, B, P2, and P3 catalyzed cyclization of **66** *in vivo*. (**C**) Double-logarithmic plot of substrate concentration vs. specific activity. Error bars represent the s. d. between technical triplicates.

As expected from the active site mutations in P2, these alterations increased the substrate affinity and thus lowered the K_M 5-fold, which entailed a ~12-fold increase in k_{cat} (**Table 3-1,** P2, *in vitro*). Finally, the additional entrance tunnel mutations in P3 resulted in almost doubled k_{cat}, while K_M remained almost unchanged. In total, the structure-guided engineering of the WT in the active site and entrance tunnel led to a catalytic efficiency k_{cat}/K_M of 372.5 mM*min^{-1} (**Table 3-1,** P3, *in vitro*), which is an improvement of more than 250-fold. Noteworthy, all initial rate kinetics *in vitro* could be approximated by Michaelis-Menten plots (**Figure 3-7A**).

Table 3-1: Parameters of initial rate kinetics for *AacSHC* WT and variants B, P2 and P3 *in vitro* and *in vivo*. The *in vitro* kinetics were approximated by Michaelis-Menten plots. The *in vivo* kinetics were approximated by substrate-excess inhibition plots.

	in vitro			***in vivo***		
	K_M [mM]	k_{cat} [min^{-1}]	k_{cat}/K_M [mM*min^{-1}]	$K_{M,app}$ [mM]	$k_{cat,app}$ [min^{-1}]	$k_{cat,app}/K_{M,app}$ [mM*min^{-1}]
WT	0.94	1.38	1.47	0.16	0.52	3.14
B	1.06	2.81	2.65	0.17	0.60	3.44
P2	0.19	35.65	185.95	0.22	26.32	117.01
P3	0.16	61.62	372.48	0.21	28.70	135.12

In contrast, the *in vivo* kinetics had to be approximated by substrate-excess-inhibition plots with the inhibition constant $K_i = K_{M,app}$ occurring at ~0.21 mM for all characterized

variants (**Figure 3-7B+C**). Nevertheless, a 45-fold increase in catalytic efficiency of P3 ($k_{cat,app}$ /$K_{M,app}$ ~ 135 mM*min^{-1}) compared to the WT was determined (**Table 3-1,** P3, *in vivo*). Interestingly, the inhibition could be reduced by reducing the orbital shaking from 800 to 300 rpm, albeit resulting in a 9-fold lower catalytic efficiency $k_{cat,app}$ /$K_{M,app}$ of ~15 (**Table 3-2,** see also Supporting Figure S 10C).

Table 3-2: Parameters of initial rate kinetics for variant P3 under varying rotation speeds in vivo. Kinetics were approximated by substrate-excess inhibition. P3 at 300 rpm was also approximated by Michaelis-Menten, as substrate excess inhibition occurred only at high substrate concentration (20 mM).

	$K_{M,app}$ [mM]	$k_{cat,app}$ [min^{-1}]	$k_{cat,app}/K_{M,app}$ [mM*min^{-1}]
P3 (800 rpm)	0.21	28.7	135.12
P3 (600 rpm)	0.93	16.23	17.30
P3 (300 rpm)	2.57	13.03	5.05
P3 (300 rpm, Michaelis-Menten approx.)	0.20	2.99	14.86

Overall, the kinetic data disclosed meaningful differences in the *in vivo* and *in vitro* kinetics and further strengthens the synergistic impact of the dual-site allocated mutations. Congruent to the MD simulations, the alterations in the entrance tunnel mainly contributed to the enzyme's k_{cat}, which strengthens the hypothesized increased substrate flow (cf. **Table 3-2**, WT vs. B, P2 vs. P3). Compared to the native reaction of the *Aac*SHC, the catalytic efficiency of P3 for the non-natural **66** cyclization varies by a factor of almost 700, which is not unusual[188] as nature evolved the SHC's active site residues for precise *shape-complementary* binding interactions with squalene **36** that contribute substantially to the catalytic efficiency.[87] However, that study employed Triton-X instead of CHAPS as the detergent for enzyme solubilization, which may impact the enzymatic performance.[189–191] In their natural environment though, all SHC variants are strongly inhibited after the peak performance concentration of 0.21 mM (cf. **Figure 3-7**, *in vivo*). Both results suggest a regulative function of the lipid environment on the enzymatic activity. This inseparable relationship was recently demonstrated in the reconstitution of the *in vitro* activity of the membrane-bound particulate monooxygenase by mimicking the natural lipid environment.[192] Furthermore, the incorporation of terpenes into the cell's membrane entailing local perturbations were also studied before.[160,176,186] Together these results elucidate the effect of terpene concentrations beyond the enzyme's K_M: Due to their inherent hydrophobicity, terpenes

diffuse into the cell membrane causing local perturbations, whereupon the enzyme reacts downregulating its activity. This regulatory function by sensing membrane integrity would be a simple tool for nature to control activity of membrane-bound enzymes as already hypothesized in 1975.[193] To omit the downregulation, the local perturbations have to be 'widespread' by offering the terpenes more membrane area. This wide spreading can be achieved by the invagination of the cellular membrane as exemplified by Wang and co-workers[194] or simply by increasing the cell concentration.[129] Herein the molecular toxification was reduced by lowering the orbital shaking speed, which kept the aqueous cell suspension and organic substrate layer more separated, thus losing maximal reaction velocity for the sake of membrane integrity and enzymatic activity.

3.2.5 Fed-batch process for high turnover (–)-ambroxide production

In the final experiment, the new insights into the enzyme kinetics were used to achieve a maximal turnover number, thus pushing the SHC to its limits. Therefore, a feeding strategy was envisaged exploiting the enzyme's high selectivity and the constant ISPC of (–)-ambroxide **7**. Additionally, an *in vitro* approach was carried out to investigate the stability of the SHC in the membrane mimic. The SHC variant P3 was used in combination with 95% *E*,*E*-**66** as this combination showed the best catalytic performance (cf. chapters 3.2.1 and 3.2.3). An enzyme solution (0.015 mg/ml SHC, 0.2% CHAPS, 20 mM citric acid, pH = 6.0) and whole-cell suspension (0.1 g_{CDW} /L *E. coli* whole cells in *dd*H_2O) were prepared, supplemented with 200 µL (7 mM) pure **66** and shaken at 30 °C (*in vivo*) and 50 °C (*in vitro*), respectively. This substrate concentration was selected as it depicts the concentration before the inhibited and non-inhibited *in vivo* plots cross-over (cf. Supporting Figure S 10C). For comparative reasons, both reaction mixtures were shaken slowly at 300 rpm orbital shaking and the depletion of the substrate layer was observed (**Figure 3-8A**, I and II). During the *in vitro* approach almost no depletion occurred, and the reaction stopped after ~10 h and ~3.5% product formation, which equals a total turnover number of ~11000. Intriguingly, the SHC in the whole cells was active for 34-38 days using the feeding strategy (**Figure 3-8B**).

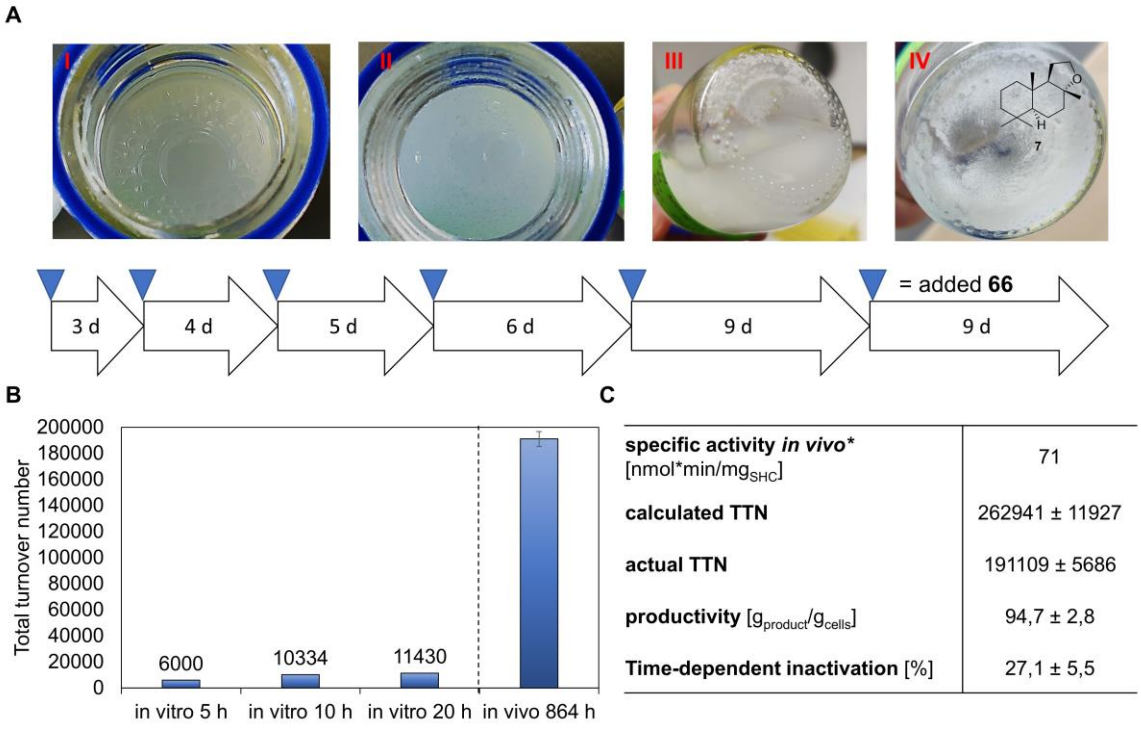

Figure 3-8: Fed-batch process for max. total turnover of *E, E*-homofarnesol **66** with an engineered *Aac*SHC P3 driven by continuous ISPC**.** For reaction conditions see chapter 6.7.7. (**A**) After addition of substrate **66,** depletion of organic substrate layer on top of the aqueous cell suspension was observed (cf. organic layer in I and II). After estimated 90% depletion (II), substrate **66** was repeatedly fed (blue triangles). After about seven days **7** started to crystallize from the reaction broth (III). The maximal reaction velocity decreased over time due and stopped after 34-38 days (IV). (**B**) Total turnover numbers achieved with the different approaches. (**C**) Table containing process-related data derived from three independent experiments. Error bars represent the s. d. between technical triplicates. *specific activity was deduced from Supporting Figure S 10C

Thus, a total turnover number (TTN) of an average of 191109 was achieved. Compared to the calculated TTN of 262941, the enzyme lost ~ 27% of its activity, indicating a time-dependent inactivation of the catalyst. Overall, 1 g of the desired product (–)-ambroxide **7** was produced employing only 10 mg of *E. coli* whole cells (**Figure 3-8C**). Despite showing higher TOF and catalytic efficiency $k_{cat,app}$ /$K_{M,app}$ compared to whole cells, the purified enzyme is more prone to inactivation in the membrane mimic and consequently stopped working after 10 h and 3% substrate conversion. These stability issues are a well-known challenge in membrane-protein science, most often encountered during enzyme structural studies.[195–198] Kotov et al.[199] have recently presented a high-throughput method to debottleneck the low stability of membrane enzymes, which may serve as a solution here as well. The feeding strategy which beneficially merges the constant ISPC and slow orbital shaking kept the enzyme stable

for several weeks, performing almost 200.000 turnovers. Such feeding approaches are often applied in biocatalysis to overcome immediate toxification of the catalysts.[200–202] Moreover, biocatalysts exhibiting turnover numbers in the 10^6 range are well positioned among the upper ranks of industrially applied enzymes.[203,204] The overall productivity of the *E. coli* whole cells were increased by a factor of 200[129] and the process delights with its excellent atom-economy. These results further substantiate the high catalytic potential, which slumbers in whole-cell biocatalysis.[205–207] An apparent drawback is the long time period of the presented process, which could be overcome by increasing the mass transfer across the biomembrane using membrane transporter enzymes[174] or spheroplast preparation.[208]

3.3 Conclusion

Biocatalytic terpene cyclizations are a thriving research area constantly growing and evolving mainly by e.g., active site mutational or substrate scope studies.[55,84] The underlying work represents a next step in engineering and understanding SHCs on the molecular as well as macromolecular level. Besides the active site, the enzyme's dynamic entrance tunnel was engineered to improve the catalytic efficiency by enhancing substrate flow and forcing an open tunnel. The synergy of such an approach originates from the huge amino acid network and its intramolecular communication, which was clearly elucidated computationally. The transfer of the beneficial mutations into SHC homologs revealed the stereoconvergent cationic cyclization, which will be further investigated in future work. As a new target, the membranous environment of the enzyme and terpene-induced local perturbations were considered, which are pivotal for membrane-bound enzyme activity.[78,209,210] The holistic view on the enzyme unlocked the true potential of the SHC and with this knowledge the actual implementation into industry seems more likely, even though it demands process optimization. Going forward, essential monotopic membrane-bound enzymes, e.g., the visual cortex protein RPE65 or the tumor protein COX-2 could be re-evaluated in terms of promiscuity or inhibition keeping the preservation of the membrane integrity in mind.[192,209,211] This case study on the *in vivo* application of SHCs strongly benefited from the ISPC of the crystalline product **7**. However, many terpenes are liquids and therefore alternative *in situ* product removal (ISPR) techniques must be employed to overcome the membrane-

dependent limitation. As presented before (cf. chapter 2.2.4) cyclodextrin represents a potent solution in this regard. The mode of action of the cyclodextrin-augmented SHCs and the opportunities offered by this beneficial supplementation are discussed extensively in the following chapter.

Chapter 4

EXPANDING THE RETROSYNTHETIC TOOLBOX BY BIOCATALYTIC *SHAPE-COMPLEMENTARY* CATIONIC CYCLIZATIONS

4.1 Introduction – Novel synthetic approaches in terpene total synthesis

Retrosynthetic logic is inherently limited to the contemporary synthetic and catalytic methods.[212] The age of biocatalysis largely enriched this conceptual toolbox by harnessing the catalytic power of enzymes.[213] As a result, this development gave rise to sophisticated new synthesis routes merging bio- and chemocatalysis in catalytic hybrid approaches.[214] Such approaches are also reflected in terpene total synthesis e.g., by the Renata lab.[32,215] In their endeavor to produce meroterpenes, the group reinvigorated the chiral terpene pool by chemically unparalleled regio- and stereoselective remote oxyfunctionalizations of unbiased terpenes e.g., sclareol **48** with the aid of engineered oxygenases.[216] The resulting oxidized scaffold **68** was then transformed into the meroterpene Taondiol **69** employing state-of-the-art synthetic and catalytic methods (**Figure 4-1A**).[217] Despite the innovativeness of this approach, a closer inspection of the synthetic route reveals that most of the synthetic effort (8 of 11 steps) is spent on the 'scaffold remodeling' of the cyclic terpene precursor (**Figure 4-1B**). Conversely, nature's convergent pathway employs a single cationic cyclization to construct the cyclic terpene scaffold (**Figure 4-1C**).[218] Consequently, these stereoselective cyclizations may shorten synthetic routes towards complex terpenes drastically (**Figure 4-1D**). Despite tremendous efforts in chemical catalysis to employ cationic cyclizations in total synthesis of terpenes (cf. chapter 2.1),[219–222] absolute control over selectivity has remained an outstanding challenge.[223] In contrast, highly selective terpene cyclases generally suffer from their nature-given limitations i.e., membrane integration and the toxicity of the substrates/ products (cf. chapter 3.1). As a result, most biocatalytic cyclizations end up in substrate/product mixtures, whose separation requires special equipment.[224,225] Moreover, titers of cyclase biocatalysis are in most cases far below 1 g/L, which precludes their broader application.[194,226,227] As demonstrated in chapter 3, ISPR techniques comprise a general strategy to increase the STY of enzymatic reactions.[168]

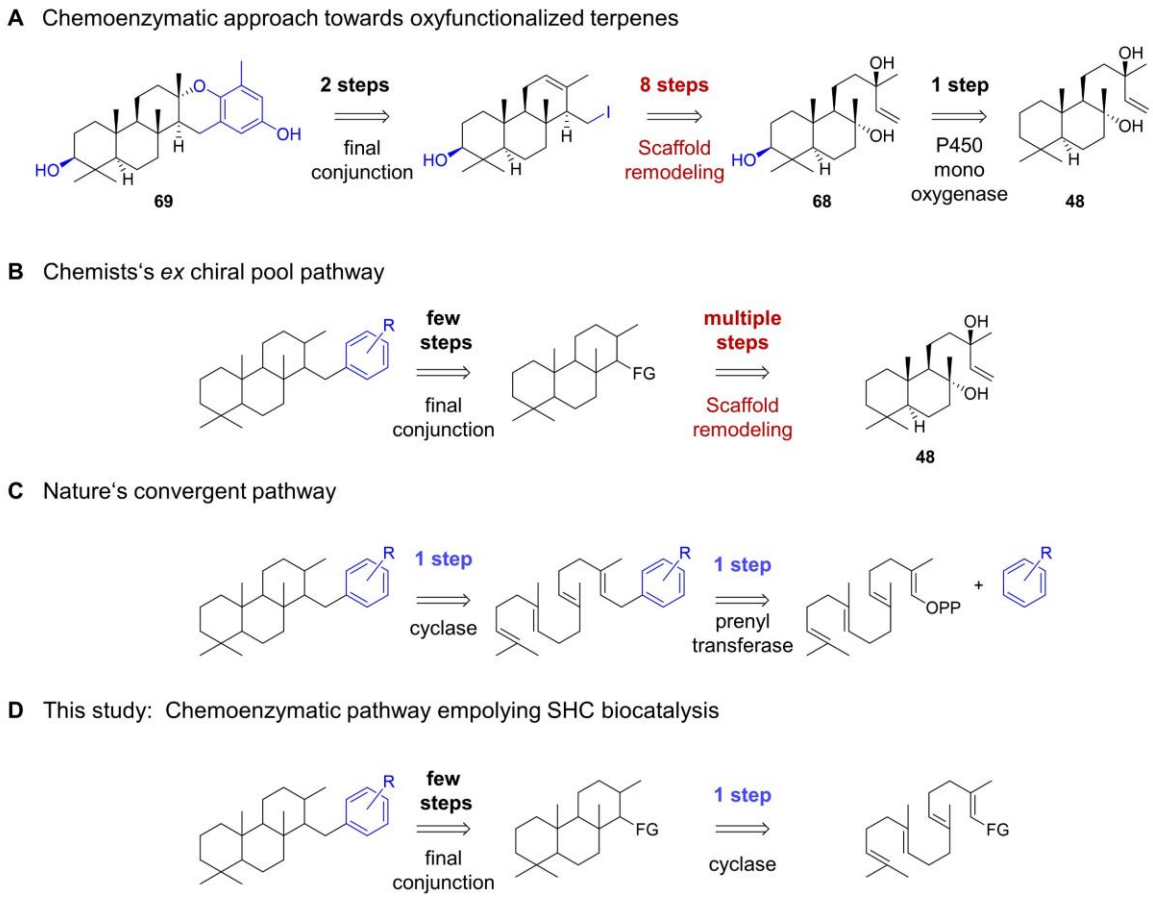

Figure 4-1: Retrosynthetic logic towards the construction of complex meroterpenes. (**A**) Chemoenzymatic route to oxidized meroterpenes by Hans Renata et al.[217] (**B**) Schematic synthetic pathway to meroterpenes employing the ex chiral pool method.[228] FG = Functional group. (**C**) Schematic synthetic pathway to meroterpenes found in Nature.[229] (**D**) Proposed novel synthetic pathway devised in this study employing squalene-hopene cyclases.

In this regard, cyclodextrins (CDs) serve as a non-denaturing alternative to organic solvents for the ISPR of non-precipitating liquid products.[230–232] CDs are ring-structured macromolecules universally applied[233–236] in the scientific world, owing to their amphiphilic properties and their potential to encapsulate hydrophobic molecules (**Figure 4-2**).[237] The literature-known ability of CDs to complex terpenes, interact with membranes, and increase terpene yields of plant-derived organisms prompted the idea to supplement SHC *in vivo* biocatalysis with CDs.[230,232,237–243] These cyclodextrin-augmented SHCs should therefore enable higher STYs in the generation of liquid products. With both ISPC and CD-driven ISPR in hand, the stereoselective generation of desired terpene scaffolds by biocatalytic *shape-complementary* cyclizations should enable novel chemoenzymatic routes towards complex terpenes.

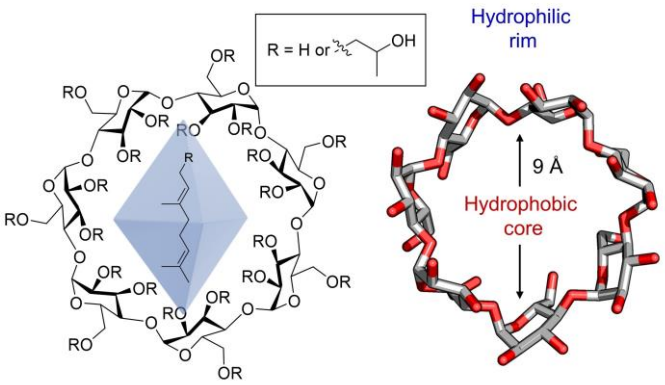

Figure 4-2: Cyclodextrins and their encapsulation potential of terpenes.[239] Due to higher water solubility, 2-hydroxypropyl-β-cyclodextrin (2HPCD) was used for this study.[230] The hydrophobic core diameter of β-CDs is around 9 Å. 2HPCD carries an average of 0.5-1.3 substitutions of 2-hydroxypropyl per glucose unit.

4.2 Results and discussion

The intial goal of this study was to set up optimal conditions for the *in vivo* biocatalysis. In this context, the cyclization towards liquid or solid products were compared in terms of cell specific activity. Moreover, the general applicability of CDs extending SHC performance should be demonstrated. Since 2-hydroxypropyl-β-cyclodextrin (2HPCD) exhibits the highest water solubility (compared with α- and β-CD) it was used for this study. It should be mentioned that during the course of the work organic/aqueous two-phase systems empolying selected organic solvents varying in their logP value were also tested, resulting in unsatisfying performance of the SHC (Supporting Figure S 11). In order to complement the experimental results, the encapsulation potential in comparison to the storage potential in the membrane interior was investigated computationally. After the proof-of-concept, multiple cyclic terpene scaffolds should be produced in reasonable yield and ready-to-use for total synthesis to demonstrate the synthetic usability of cyclodextrin-augmented SHCs.

4.2.1 Reaction condition evaluation and cyclodextrin-augmented SHCs from different organisms

To initiate the study, a model reaction was determined which results in liquid product. Unfortunately, the natural reaction of squalene **36** gave no acceptable conversions (<1%, data not shown), presumably due to the impermeability of the outer membrane for highly hydrophobic molecules.[157] Empirically, the promiscuos cyclization of *E*-geranyl acetone **52t** results in liquid chromene **53t** and is able to pass the outer membrane to

undergo cyclization *in vivo* (cf. chpater 2.2.1). As a result, this reaction was chosen as the model *liquid cyclization*, whereas the (–)-ambroxide **7** cyclization was chosen as the model *solid cyclization* (**Figure 4-3**).

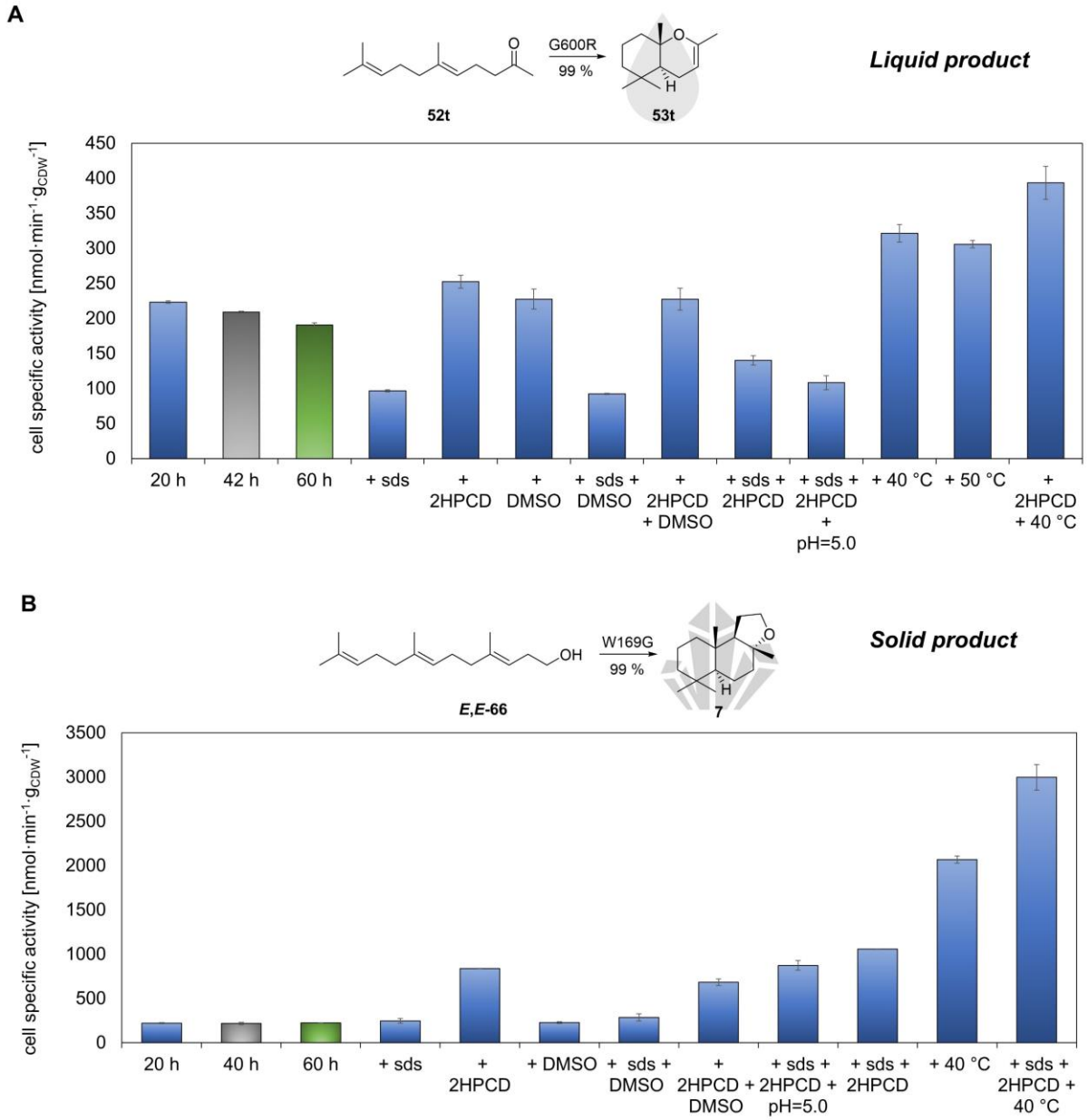

Figure 4-3: Evaluation of optimal conditions for the SHC-catalyzed *in vivo* cyclization reactions. Standard reaction conditions (blue bars): 20 mM substrate, 10 mg_{CDW}/mL whole cells, *dd*H_2O, 30 °C. Additives: SDS = 0.2%, 2HPCD = 20 mM, DMSO = 1% (v/v). For buffering at the pH = 5.0, 100 mM citric acid was chosen. Selectivity towards the products shown below arrows. (**A**) Model *liquid cyclization* of *E*-geranyl acetone **52t** towards chromene **53t** using the variant G600R. The cell specific activity suffers from time-dependent inactivation (grey and green bar). (**B**) Model *solid cyclization* of *E,E*-homofarnesol **66** towards (–)-ambroxide **7** using variant W169G. No time-dependent inactivation was observed within 60 h. All biotransformations were carried out as analytical biotransformations (cf. chapter 6.7.1) and error bars represent the s. d. between technical triplicates.

Based on earlier studies regarding detergents, co-solvents and cyclodextrins[129,231,244] the parameters of added SDS, DMSO, 2HPCD and the temperature were varied for both biotransformations (**Figure 4-3A+B**). In this regard, the optimal amount of SDS and 2HPCD were evaluated in the cyclization of **66** at 40 °C (Supporting Figure S 12). This temperature was chosen as it was priorly found to be advantageous for *in vivo* reactions (Supporting Figure S 6). The optimal SDS and 2HPCD concentrations were determined at $g_{SDS}:g_{CDW}$ = 0.2 and equimolar amount of 2HPCD, respectively. Interstingly, adding SDS to the reaction mixture of the liquid cyclization with **52t** lowered the activity. Additional DMSO had almost no effect on the cell specific activity for both examples. The supplementation of equimolar 2HPCD improved the *liquid cyclization* 1.1-fold and the *solid cyclization* 3.8-fold. Increasing the temperature improved both cyclizations 1.4- and 10-fold for liquid and solid cyclization, respectively. Higher temperatures were not beneficial. Setting the pH to 5.0 as suggested in a previous study[129] showed no positive effect on both reactions. Combining the optimal conditions at 40 °C further improved the *liquid cyclization* 1.2-fold and the *solid cyclization* 3.6-fold. Interestingly, both biotransformations started with an initial cell specific activity of ~220 $nmol \cdot min^{-1} \cdot g_{CDW}^{-1}$, however, were influenced to varying extent by the additives. Whereas the *liquid cyclization* was improved 'only' 1.8 fold, the *solid cyclization* was boosted 13.6-fold, which highlights the beneficial effect of the ISPC on the SHC biocatalysis (cf. chapter 3.2.5).[168] The exclusive improvement of the **66** cyclization by additional SDS was not surprising as it was already described by Eichhorn et al.[129] to be specific for this substrate. Curiosly, the cell specific activity of the *liquid cyclization* decreased within 60 h, whereas the *solid cyclization* kept a stable activity within this time frame. One explanation for such an effect would be the membrane-bound topology and inherent downregulation of the SHC as discussed in chapter 3. In particular, the generated liquid side-products may be stored in the *E. coli* membrane, which would cause local perturbations and ultimately affect enzymatic long-term activity.[176,198,245] To further study the generability of this effect, several SHCs were examined in the cyclization of **52t** (**Table 4-1**). Seven out of 13 SHCs (cf. Supporting Table S 1) showed activity with excellent stereoselectivity (> 99% *ee* and *de*) and low[246] but sufficient cell specific activities (28 – 278 $nmol*min^{-1}*g_{CDW}^{-1}$) under

the optimal conditions used in **Figure 4-3**. Next, the cell-specific activity of the enzymes at 20, 40, 60 h was determined, using a higher substrate concentration of 50 mM **52t**.

Table 4-1: Cell specific activities and stereoselectivities of SHCs towards cyclization of **52t** to **53t** originating from different hosts and their insertion depths into the membrane. Equal expression was determined by SDS-PAGE (cf. chapter 6.3.3). Insertion depths were calculated using the PPM server.[80] Reaction conditions: 20 mM **52t**, 10 g_{CDW}/L whole cells harboring the respective SHC, 30 °C, 20 h. Reactions were performed in technical triplicates

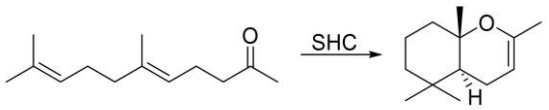

52t **53t**

Host	**Insertion depth** [Å]	**cell specific activity** [nmol·min^{-1}·g_{CDW} $^{-1}$]	***ee*/ *de*** [%]
Aac	7.4 ± 0.1	278.5 ± 0.8	99.5
Tel	4.9 ± 0.0	262.1 ± 0.8	99.5
Bja	7 ± 0.6	178.3 ± 0.3	99.5
Pca	7.3 ± 2.4	110.2 ± 1.1	99.5
Sco	2.3 ± 0.3	80.9 ± 0.2	99.5
Rpa	3.9 ± 1.2	78.1 ± 0.5	99.5
Zmo2	3 ± 1.3	28.6 ± 0.3	99.5

The results in **Figure 4-4A** clearly show a decreasing cell-specific activity over time for all tested SHCs. Interestingly, the impact on the activity differs among the cyclases correlated to their membrane embedding depth (**Table 4-1**).[80] Surprisingly, adding 2HPCD to the reaction mixture after 60 h restored the intial activity (**Figure 4-4A**, orange bar). Building on these results, 2HPCD was added from the beginning in the second experiment, resulting in stable cell-specific activity for all SHCs over 60 h (**Figure 4-3B**). The presented results proved that it is generally feasible to maintain and even restore the *in vivo* activity of SHCs by augmenting them with 2HPCD. In theory, this beneficial augmentation should enable the full conversion of various terpenes into their chiral cyclic analogs utilizing SHC variants with promiscuous engineered selectivities and activities.[247] Consequently, this strategy enables to bypass time-consuming strain engineering[248] and tedious substrate/ product separation[224,225] to obtain privileged terpene scaffolds. Intriguingly, the different SHCs responded to high terpene concentrations depending on their predicted membrane-embedding depth. This phenomenon further highlights the tight relationship of the monotopic enzyme and it's host, gives more insights into these proteins and further strengthens the hypothesis on the membrane-bound enzyme regulation raised in chapter 3.

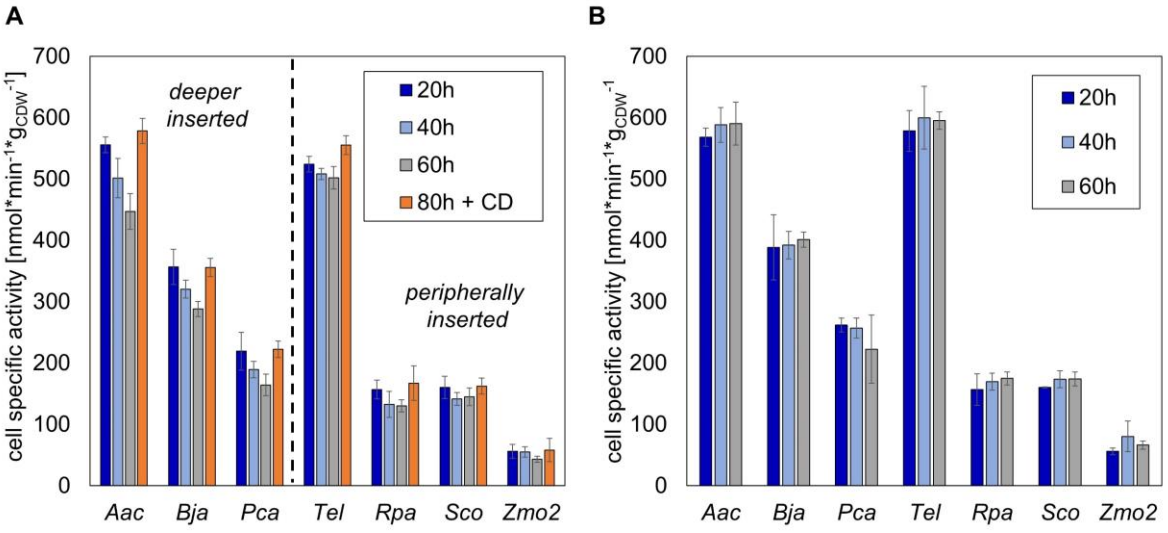

Figure 4-4: Cell specific activity of SHCs from different origins at high substrate concentrations (50 mM). The specific activities were determined as end-point detections. Equivalent expression of the variants was analyzed via SDS-PAGE (cf. chapter 6.3.3). (**A**) Cell specific activity of SHCs decreases over time (blue, light blue and grey bar) and was restored by adding equimolar 2HPCD (orange bar). The effect of the high substrate concentration is dependent on the membrane insertion depth of the SHCs (cf. Table 4-1). Reaction conditions: 50 mM 52t, 10 g_{CDW}/L whole cells, 40 °C. 2HPCD was added after 60 h. (**B**) Cell specific activities of the SHCs with equimolar amount of 2HPCD initially added shows constant cell specific activity over the course of 60 h. Reaction conditions: 50 mM 52t, 10 g_{CDW}/L whole cells, 40 °C, 50 mM 2HPCD. Error bars represent the s. d. of technical triplicates.

4.2.2 Computational and experimental elucidation of the comparative terpene encapsulation – collaboration with Niels Hansen

To further strengthen the experimental results, free energy calculations were invoked in explaining the partitioning of selected terpenes. The following computational results were generated in cooperation with Niels Hansen and Daniel Markthaler from the Institute of Thermodynamics and Thermal Process Engineering, University of Stuttgart. Therefore, only a brief summary of the computational results is given below. The computational results first showed that one terpene molecule fits into the hydrophobic core of one molecule 2HPCD, which correlates with the experimental results in Supporting Figure S 12. Next, terpene partitioning free energies for the terpenes neryl acetone **52c**, (–)-γ-dihydroionone **3**, *E*,*E*-homofarnesol **66** and (–)-ambroxide **7** from water into an artificial membrane approximated by liquid cyclohexane[249] or the 2HPCD core were calculated.

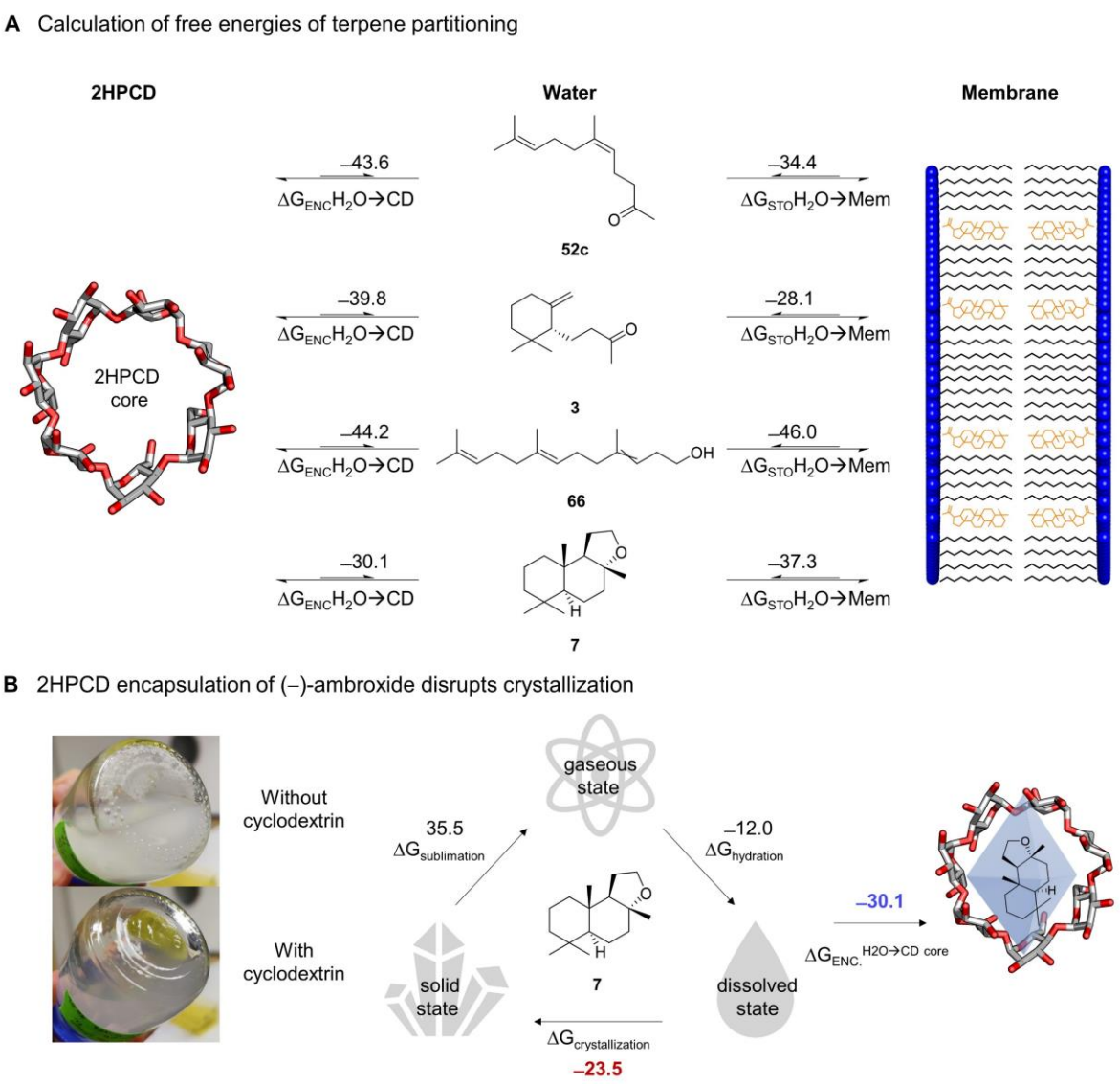

Figure 4-5: Computational elucidation of the 2HPCD terpene encapsulation potential. (**A**) Calculated free energies ΔG given in kJ/mol for the partitioning of molecules **52c**, **3**, **66** and **7** into the membrane interior and 2HPCD core, respectively. Membrane interior was emulated as cyclohexane-scaffold based on ref. [249]. The reversible processes are competing, which underpins the terpene extraction capability of 2HPCDs from the cell membrane. (**B**) Encapsulation (blue) of **7** is competing with its crystallization (red). Non-calculated free energy data for sublimation was estimated based on the vapor pressure taken from reference.[250]

The free energies for the 2HPCD encapsulation ΔG_{ENC} and membrane storage ΔG_{STO} in **Figure 4-5A** disclosed that the reversible partitioning of the terpenes from water into the membrane or into the inner core of 2HPCD are competing processes in all four systems. Lower values mean a higher energy gain for the system and thus a more likely occurrence of the partitioning. To substantiate the computational insights, the precipitation of **7** during its formation from **66** was observed in the presence of 2HPCD/water (**Figure 4-5B**). Suprisingly, no crystallization of **7** occurred, which

indicates that encapsulation of **7** is favoured over its precipitation. Indeed, this observation fits well to the calculated data of the encapsulation potential ΔG_{ENC} of 2HPCD and the crystallization $\Delta G_{crystallization}$ (–30.1 vs. –23.5 kJ/mol). In fact, this also applies for the membrane storage free energy ΔG_{STO} (–37.3 kJ/mol) where product **7** actually precipitates. However, the terpene storage capacities of 2HPCD with 20mM and that of the membrane with ~0.2 mM (cf. chapter 3.2.3) greatly differ, which could explain these observations.

In summary, the computational as well as experimental results of this part elucidated that the encapsulation of terpenes by 2HPCD is indeed competing with the partitioning into the *E. coli* membrane. This data strengthens the conception that 2HPCDs are able to extract terpenes from the membrane as shown in several independent studies before.[241,251–253]

4.2.3 Generation of diverse privileged terpene scaffolds with absolute stereocontrol and high conversion by employing the 2HPCD/ SHC system

Having deeply investigated the potential and the mode-of-action of 2HPCD in the *in vivo* biotransformation, the next objective was to apply the 2HPCD/ SHC system and generate a diverse panel of chiral terpenes by employing engineered SHCs converting non-natural terpenes with varying chain lengths. To this end, retrosynthetic analysis of selected meroterpenes was carried out to identify potential cyclic terpenes. The first route was inspired by nature itself in the design of linear meroterpene precursors by Friedel-Crafts alkylation chemistry, which resembles the prenyl transfer reaction in nature (cf. **Figure 4-1C+D**).[218] However, unlike nature in this route the cyclic skeleton should be forged first, followed by a Friedel-Crafts alkylation of the aromatic compound (**Figure 4-6A**). Such a pathway would tremendously shorten synthetic routes for an array of meroterpene scaffolds[33,254–257] e.g., (+)-β-makassaric acid **70** due to the omitted 'scaffold remodeling' step. The challenge, in addition to the conjunction of allylic alcohol **71** and *p*-hydroxy-benzoic acid **72**, is the selective tricyclization and β-deprotonation of **73**. The second route was inspired by Parker's[258] concise synthesis of α-pyrone based meroterpenes **74** (**Figure 4-6B**). This route appeals with the optional divergent synthesis of various α-pyrone meroterpenes which differ in their aromatic moiety e.g., arisugacins, pyripyropenes or phenylpyropenes.[25]

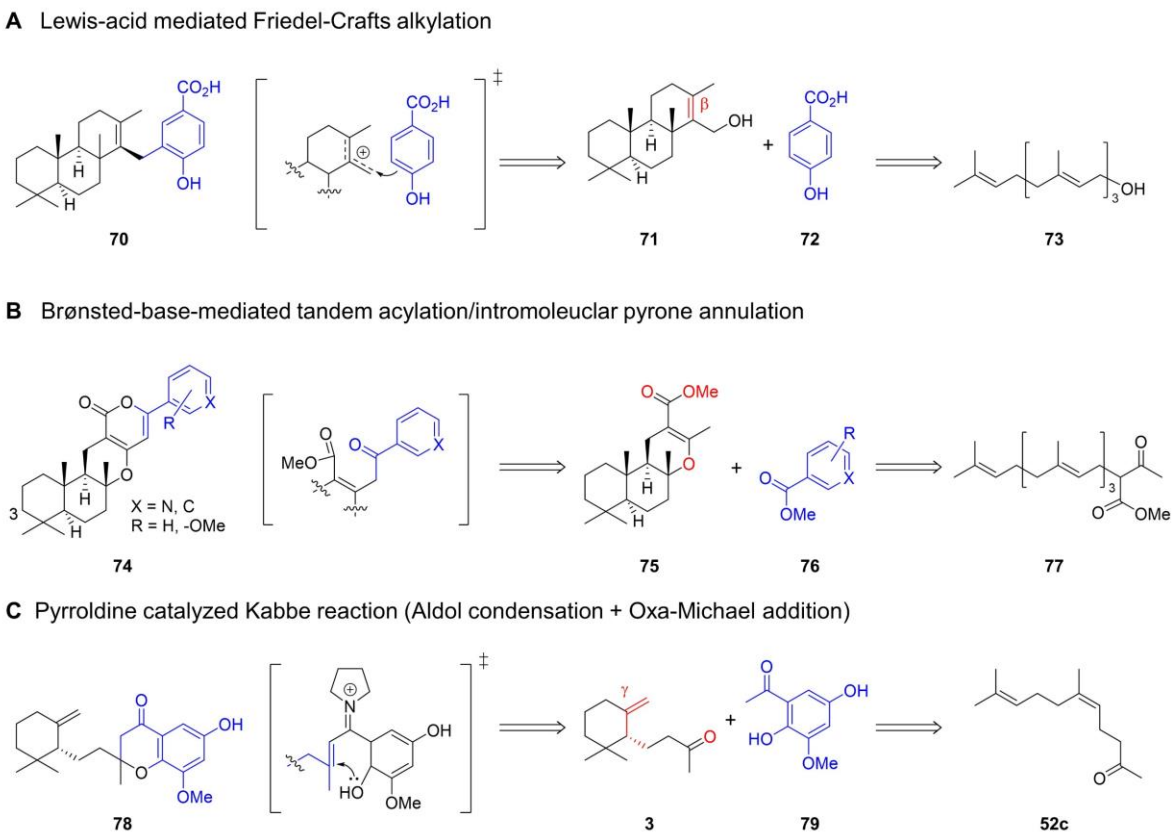

Figure 4-6: Retrosynthetic analysis of complex meroterpenes **70**, **74** and **78** inspired by Kumar Sau et al.[257], Parker et al.[258] and Kabbe et al.[259] Challenges for the cyclization reactions (except stereoselectivity) shown in red. (**A**) (+)-makassaric acid β-derivative **70** type meroterpenes could be produced by Friedel-Crafts alkylation of chiral cyclic terpenes e.g., *ent*-isocopolane **71** and arenes (blue) e.g., *p*-hydroxy-benzoic acid **72**. (**B**) α-pyrone based meroterpenes **74** could be produced by base-mediated γ-acylation/ intramolecular annulation of precursor **75** with various commercially available benzoic or nicotinoic esters **76**, hence exhibiting great divergency potential. (**C**) Chromanone-type meroterpenes **78** could be produced by pyrrolidine catalyzed intermolecular Aldol condensation followed by intramolecular Oxa-Michael addition.

The conjunction of precursor **75** with diverse and broadly commercially available benzoic or nictonoic acids **76** is facilitatzed by a Brønsted-base-mediated tandem γ-acylation/ intramolecular annulation. The selective tricyclization and termination of **77** discriminating between three potential cation quenchers (**75**, highlighted in red) would put the reaction into a new light. It should be noted that α-pyrone meroterpenes usually contain an OH-group in the C3 position (cf. **74**, terpene counting), which is not present in the underlying scaffold. Nonetheless, the focus of this work was to showcase the SHC-controlled highly stereoselective cationic cyclization, which is why prior epoxidation (cf. **Figure 1-2**) or late-stage hydroxylations were not taken into account. The last route is based on the Kabbe reaction, which represents a tandem Aldol-condensation/ Oxa-Michael addtion (**Figure 4-6C**).[259] This classical transformation gives direct access to

valuable chroman-type structures found in various terpenes in nature such as tetrahydrocannabinol or vitamine-E. While this reaction type was already demonstrated using substrate (+)-**3** by Castillo et al.[31] the herein presented synthesis of the (–)-**3** precursor by a directed cationic cascade would shorten the overall synthesis route and give access to new diastereomers of the resulting chromanones.

Having determined the target terpene scaffolds of interest, the workflow for the survey of the in-house SHC library was as follows: First all chosen substrates were docked into the *Aac*SHC WT crystal structure to define hot-spot amino acid positions in juxtaposition to the functional group in the active site, ultimately creating smaller and smarter enzyme libraries for screening (**Figure 4-7**, blue sticks). These libraries were then screened for an enzyme variant exhibiting maximal selectivity towards a single product and maximal activity using 2 mM substrate and 10-20 g_{CDW}/L cells (4-7 mol-% SHC) at given temperature within 20 h. Hit positions are depicted in the respective **Figure 4-7A-F** as yellow sticks, albeit only the two best hits in comparison to the wildtype are shown in the adjacent chart. Finally, upscaling of the biocatalysis was carried out with the SHC/ 2HPCD system employing 20 g_{CDW}/L lyophilized cells, 7.5-20 mM substrate, 10-20 mM 2HPCD and 0.4% SDS (cf. ref. 129) in *dd*H_2O. The lyophilized cell powder was used as it exhibtited the same performance as freshly expressed cells (data not shown) and facilitated their simply storage in Falcon® tubes at room-temperature.

Starting with the smallest terpene size, the monoterpenoid *E*-geranyl acetate **34** was chosen for screening (**Figure 4-7A**). Noteworthy, *E*-geraniol was also tested based on earlier published results using purified SHC,[84] which did not result in any conversion, thus constituting a limitation of the 2HPCD/ SHC system. Besides stereoselectivity, a challenge for the Brønsted-acid catalyst was to discriminate between solvolysis and cation-olefin cyclization. *Aac*SHC variants at positions L607 and G600 exhibited cyclization products with G600R having 7-fold improved activity (compared to the WT) and exclusive stereo (>99% *ee,* >99% *de*) as well as high product selectivity (95%) towards the cyclohydration product (*S)*-cyclogeranyl acetate hydrate **80**. Employing the SHC/ 2HPCD system enabled high conversion (71% isolated yield) after 7 weeks at 50 °C. The chiral precursor **80** created in that way gives direct access to numerous important megastigmane-based terpenes e.g., vitamins[260] by nuleophilic substitution chemistry

eased by the acetate as the leaving group. The only comparative cyclization study (without ionization of the acetate[63]) of Tsangarakis et al.[261] also reported monocyclization of **34** employing an NaY zeolite with confined active sites, albeit with racemic cyclization products.

Moving along the isoprene chain length, sesquiterpene *E,E*-farnesol **81** was selected as the next linear precursor (**Figure 4-7B**). The resultant cyclic drimane skeleton is the basis for multiple natural products e.g. chromazonarols, puupehenols or yahazunols exhibiting bioactivities.[33,256,257] The Hauer group already published the selective cyclization of this substrate towards cyclic deprotononation and hydration products utilizing various SHC variants.[169] However, that study empolyed purified *Aac*SHC variants which lacked full selectivity (88%) and did not completely convert **81** to the desired product **82** (up to 65%). Chemical approaches towards **82** employ the remodeling of chiral pool terpenes or stereospecific cyclization using superacids.[262–264] During the course of this survey three hit positions W169, I261 and A306 were identified, of which variant A306W achieved full conversion (99.5%) and excellent product selectivity (98%). Advantageously, it was known that **82** precipitates from the reaction broth which considerably boosted (3 d, 88% yield) the upscaled biocatalyis by ISPC and made the use of 2HPCD obsolete.

Next, diterpene *E,E,E*-geranyl geraniol **73** was screened for cyclization products. Conveniently, this substrate simultaneously serves as a precursor for the terpene scaffolds of *ent*-isocopolanes (**Figure 4-7C**) and labdanes (**Figure 4-7D**), which are able to control anti-inflammatory processes.[254,265] Labrotary efforts towards these compounds encompass tedious multistep synthesis pathways with low yields.[254,266] Biocatalytic access to labdane diterpenes was reported by the Peters group, but required the extraction of 3L fermentation broth and yielded only 3 mg product.[267] In 2004, Hoshino reported the promiscuous cyclization (3% yield) of **73** to the desired tricyclic **71**, albeit as the α-regioisomer, utilizing purified *Aac*SHC.[97] Building on these results, hot-spot amino acids for tricyclization were identified at positions F601 and F605. It turned out that most of the hits, e.g., F601W were more active (up to 8-fold) as the WT but less selective (53%) towards α-**71**. Unfortunately, the screening afforded no β-deprotonation product, which is required for the Friedel-Crafts alkylation. However, variant F605W produced the α-product with 5-fold improved conversion and ~90% selectivity.

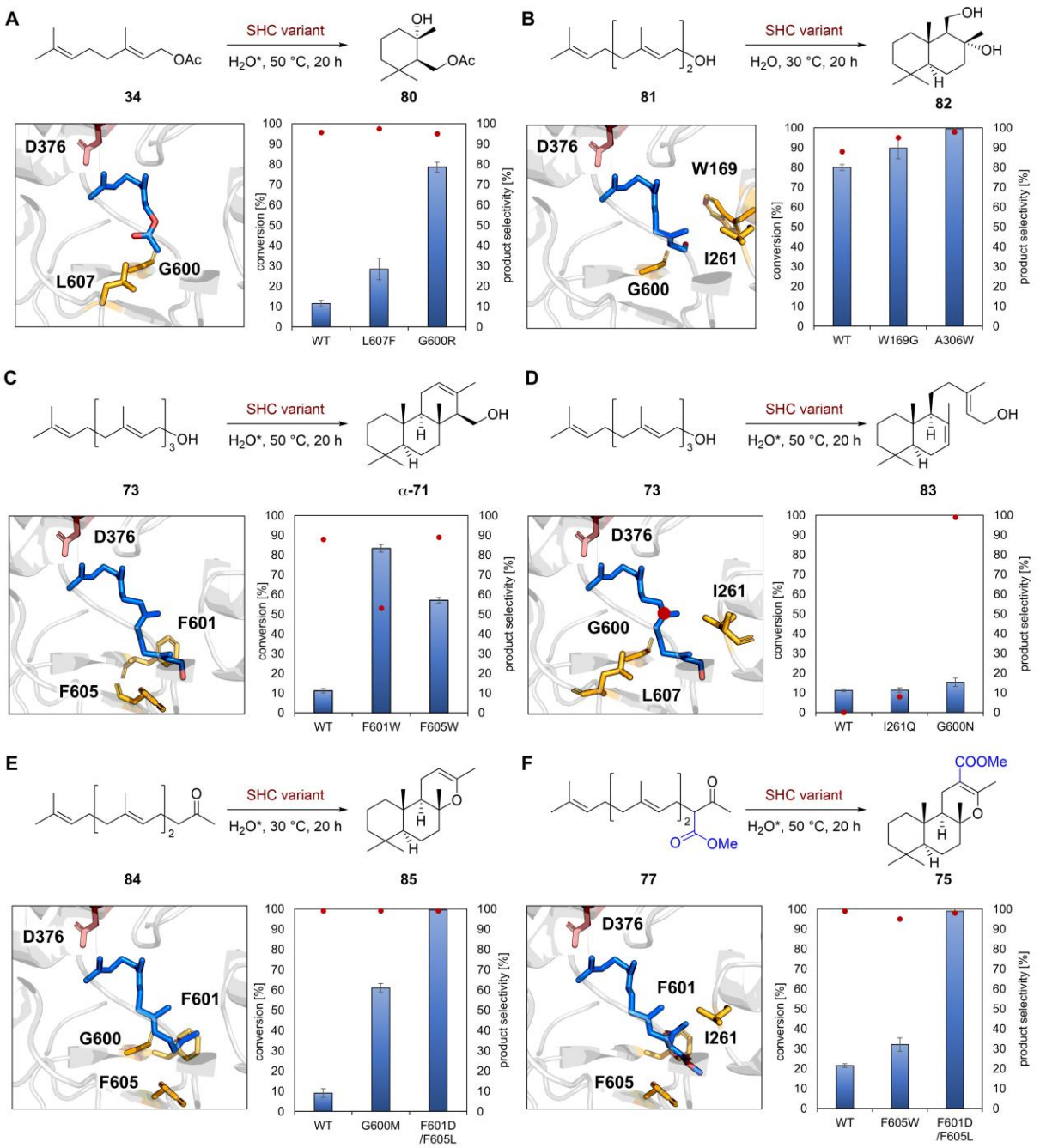

Figure 4-7: Survey of engineered SHCs converting non-natural substrates (**A**) *E*-geranyl acetate **34**, (**B**) *E*,*E*-farnesol **81**, (**C+D**) *E*,*E*,*E*-geranylgeraniol **73**, (**E**) *E*,*E*-farnesyl acetone **84** and (**F**) *E*,*E*-keto ester **77** towards chiral terpene scaffolds. *In silico* docking of the substrates (blue sticks) with hit positions (orange sticks) depicted below each reaction scheme. Best variants and *Aac*SHC WT shown in the chart adjacent to the respective docking. Columns represent conversion and dots represent selectivity. Error bars represent the s. d. of technical triplicates. Reaction conditions for initial screening: 2 mM substrate, 10-20 g_{CDW}/L cells, *dd*H_2O, 20 h at given temperature below each arrow. Reaction conditions for the upscalings: 7.5 – 20 mM substrate, 10-20 mM 2HPCD, 20 g_{CDW}/L cells, *dd*H_2O at given temperature. For a summary of the upscales see **Table 4-2**. Product **82** was produced without the use of 2HPCD. Error bars represent the s. d. of technical triplicates.

For the more challenging bicyclization reaction, amino acid positions around the third transient carbocation (**Figure 4-7D**, red dot) were screened and revealed positions I261, G600 and L607 as hot spots. This alternative strategy for short-cutting cationic cascades was reported by the Peters[268] group and was chosen due to already available in-house SHC variants. Congruent to the tricyclization, these variants mostly yielded product mixtures (cf. I261Q). Merely, the asparagine at position 600 resulted in the sole (99%) formation of the bicyclic labdane scaffold **83** with a conversion comparable to the WT (15%). Empolying the SHC/ 2HPCD system facilitated isolation of products α-**71** and **83** after 8 d and 5 weeks with 78% and 90% yield, respectively, and confirmed α-deprotonation in both scaffolds. Finally, the cyclization of Parker's linear precursor **77** should be realized using SHC variants. As **77** is not naturally available, *E*,*E*-farnesyl acetone **84** was used as a substrate mimic for a pre-screening. This natural substrate was chosen due to the almost identical positioning in the active site of the *Aac*SHC WT (cf. **Figure 4-7E** and **F**). Promiscuous and highly selective cyclization of **84** towards sclareoloxide **85** with purified *Aac*SHC was already reported by Seitz et al.,[140] albeit with low conversions (0.7%). In order to increase activity, double site-saturation mutagenesis was performed combining pairs of G600, F601 and F605. The approach yielded variant F601D/F605L, which outperformed the WT 10-fold and the best in-house variant G600M 1.6-fold. Curiously, the amino acid exchanges F601D and F605L both presumably result in less confinement around the functional group of **84** in the active site, which is contrary to the increased conversion at the first glance. However, the introduced aspartate at position 601 should be able to hydrogen-bond[152] the keto-group of **84** and therefore stabilize the tricyclic pre-fold (cf. chapter 2). Motivated by these results, precursor **77** was synthesized and screened with few selected SHC variants at positions I261, F601 and F605 as well as the newly engineered SHC F601D/F605L. Intriguingly, the latter showed excellent conversion (>99%) and selectivity (>99%) towards the desired cyclic product **75**. This result further suggests some divergency potential for the residue in α-position of the carbonyl group (**Figure 4-7F**, blue). Upscaling of the reaction yielded pure **75** (88%) within 5 d. A summary of all upscales is given in **Table 4-2**.

Table 4-2: Summary of all performed upscales. Reaction times of solid cyclization products are shorter than for the liquid cyclization products.

product	**titer** [g/L]	**reaction time** [h]	**TOF** [h^{-1}]	**yield** [g] (%)	**aggregation state**
80	1.96	1176	0.08	0.14 (71)	liquid
82	4.36	72	6.64	0.38 (88)	solid
83	2.23	840	0.1	0.17 (78)	liquid
71	2.23	192	0.5	0.2 (90)	solid
75	2.23	120	1.4	0.19 (88)	solid

To sum up, a general strategy for the efficient screening of SHC libraries was demonstrated, combining *in silico* and *in vivo* methods. Owing to the confined active site, the *shape-complementary* cyclization was controlled by rationally chosen variants adjacent to the substrate's functional group. Furthermore, the directed cationic cascade for product **83** was enabled by polar asparagine, which could possibly serve as a catalytic Brønsted-base to quench the transient carbocation at the desired carbon.[268] Limitations of the presented approach, however, are the necessary *all-trans* configurations of the substrates and their imperative ability to pass the *E. coli* membrane. Moreover, not a single β-deprotonation product could de detected during the screening. The long reaction times could be drastically shortened by evaluating the optimal reaction condtions for each enzyme/substrate combination. Finally, the biotransformation could be improved by tuning the microbial host.[174,208] This novel approach enabled the catalytic target-oriented generation of six megastigame-, labdane-, ent-isocopolane and drimane-type terpenes, harboring up to five setereocenters, in 100-500 mg scale (up to 4.2 g/L) under ambient conditions in *dd*H_2O (**Figure 4-8**). These terpene motifs are found in more than 5000 natural products[2] and were generated with excellent stereo- (>99.5% *ee*, >99.5% *de*) as well as product selectivities (up to 99%) which makes them an ideal starting point for divergent/collective synthesis approaches.[30,31] Consequently, the stage was set to transform these chiral templates to more complex terpenes employing contemporary synthetic and catalytic methods in the sense of nature's scaffold derivatization.

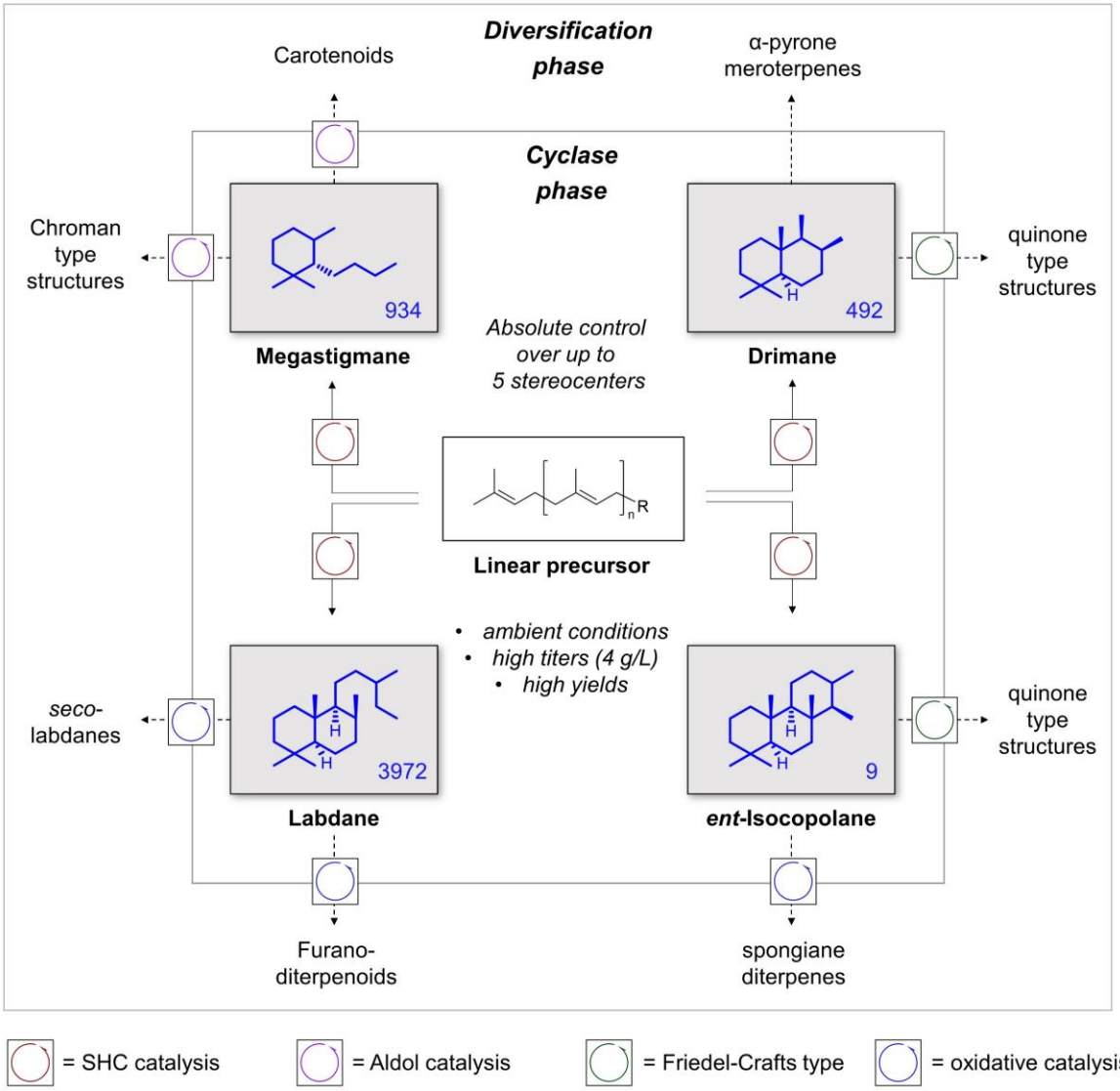

Figure 4-8: Summary of the herein presented approach towards higher molecular terpenes. In accordance with one of nature's strategies (cf. chapter 1.1), the achiral linear precursors are biocatalytically cyclized towards privileged megastigmanes, labdanes, drimanes and *ent*-isocopolanes (blue scaffolds) with the aid of SHCs within one step. These chiral scaffolds can be leveraged in a divergent/collective synthesis approaches[30] towards chroman-type[259] structures, carotenoids[20], seco-labdanes[269], spongianes[270], quinone-type structures[33,254,255,271] or α-pyrone meroterpenes[25] employing synthetic and catalytic methods. Accessible terpene structures based on the four scaffolds shown as blue numbers in the lower right corner of each scaffold.[2]

4.2.4 Implementing the generated terpene scaffolds in total synthesis of complex meroterpenes

In the final task of this study, the retrosynthetically devised routes from **Figure 4-6** towards complex meroterpenes were realized. Starting with the Friedel-Crafts alkylation reactions, a suitable aromatic compound first had to be found for the electrophilic aromatic substitution (S_EAr) reaction. Compared to nature's Friedel-Crafts alkylations,

it was not possible to simply combine the terpene scaffold with *p*-hydroxy-benzoic acid **72** due to the lack of a supramolecular environment deactivating the acidic moiety of **72** and preventing it from overalkylation (cf. Figure 4-6).[74] Instead, methyl-4-hydroxy-3-iodobenzoate **86** was chosen as the aromatic compound owing to the three substituent's properties to direct the S_EAr into the 5-position (red carbon, **Figure 4-9A**) of the aromatic compound and the simple non-reductive deiodination protocol described by Talekar et al.[272] The basic conditions of the reaction should inherently induce the saponification of the ester moiety of **86**, ultimately resulting in the desired Friedel-Crafts adduct.

Regarding the forward reactions, the bicyclic labdane **83** was selected as the allylic alcohol and subjected to boron trifluoride etherate (10 mol-% $BF_3{\cdot}OEt_2$) catalyzed Friedel-Crafts alkylation with **86** which gave a crude adduct in moderate (58%) yield. Without further purification, this adduct was directly used in the pyridine-mediated non-reductive deiodination/ saponification generating the desired meroterpene (+)-α-subersic acid **87** in good yield (40%) and comprising the shortest total synthesis of this bioactive molecule.[255]

Next, chiral terpene scaffold **75** was treated with lithium bis(trimethylsilyl)amid for the base-catalyzed γ-acylation/ pyrone-annulation reaction with ethyl nicotinaote **88** (**Figure 4-9B**). The reaction generated α-pyrone meroterpene **89** in 40% cutting down the previous total synthesis by at least 50%, albeit without the hydroxy group at the 3-position. Finally, (–)-γ-dihydroionone **3** was coupled with resorcinol **90** in the pyrrolidine catalyzed Kabbe reaction to generate chromanone **91** with 90% yield and 50:50 ***dr***. Noteworthy, L-proline and 2-methoxy-pyrrolidine were tested as alternative catalysts with potential stereocontrol which, however, did not result in any conversion (data not shown). Taken together, three highly complex meroterpenes were produced by transforming the priorly generated cyclic terpene templates making use of contemporary or classical synthetic and catalytic tools. Noteworthy, all devised routes encompassed only commercially available substrates and were shorter as well as more productive than the concurrent devised routes in the literature.[25,31,33,217,255] This shortening is mainly attributed to the SHCs ability of *shape-complementary* cyclization generating desired chiral terpene precursors in a single step.

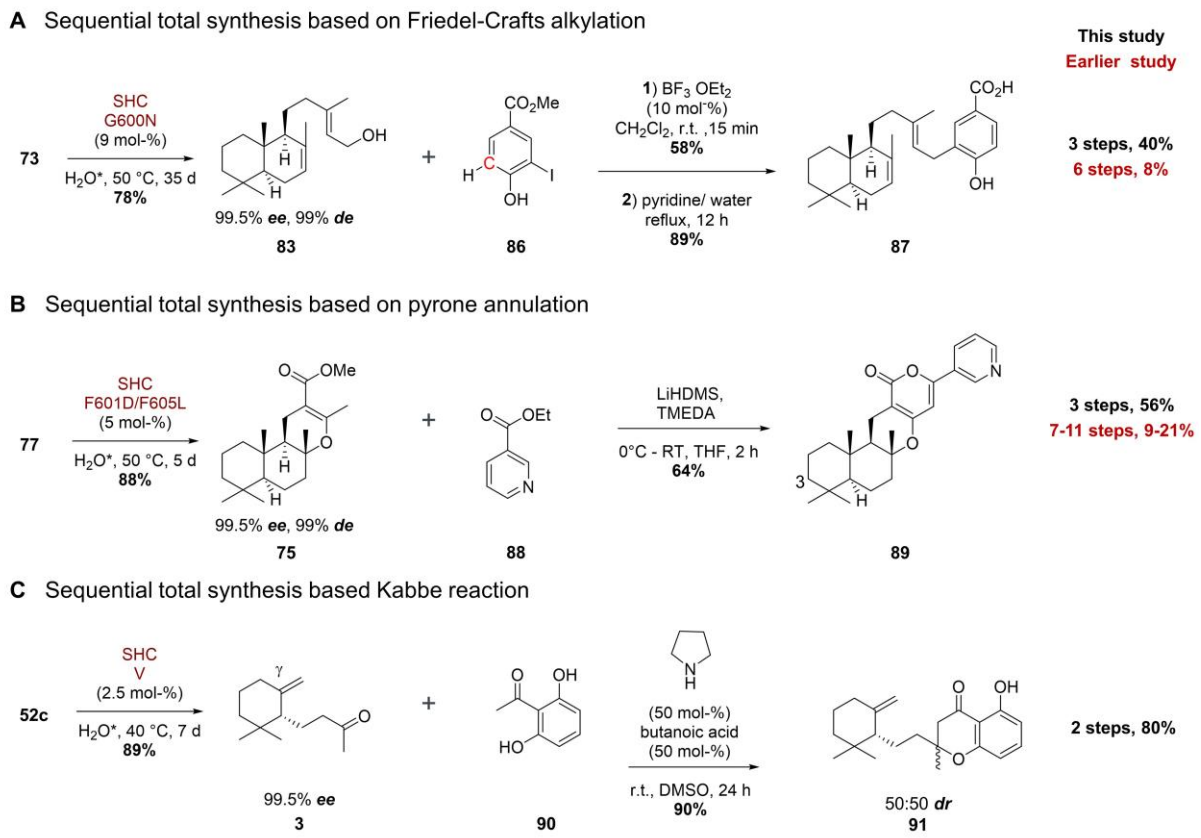

Figure 4-9: Forward reaction schemes of the suggested synthetic routes towards complex meroterpenes **87**, **89** and **91**. (**A**) The chiral terpene **71** derived from the SHC reaction harbored a primary alcohol functionality and was successfully implemented into a Friedel-Crafts alkylation with aromatic compound **86** using BF_3OEt_2.[273] The crude adduct was directly used in the basic non-reductive deiodination/ saponification reaction ultimately yielding the desired products **87** in three steps. (**B**) The chiral terpene scaffold **75** derived from SHC reaction was successfully implemented into the base-catalyzed γ-acylation/ intramolecular annulation reaction with ethyl nicotinoate **88** to pyropene **89**. (**C**) Chiral terpene scaffold **3** (produced by SHC variant V from chapter 1) was subjected a Kabbe-type reaction with aromatic compound **90** and pyrrolidine to yield chromanone **91** in two steps. All devised synthetic routes were superior to the literature in terms of synthetic steps and overall yield. *including equimolar amount of 2HPCD.

4.3 Conclusion

Accessing nature's terpenome requires a significant intellectual challenge in retrosynthetic analysis and planing (cf. chapter 1.2).[37] Nowadays, this challenge is increasingly addressed by the merger of bio- and chemocatalysis.[214] This study expands this strategy and adds SHCs as exceptionally stereoselective cationic cyclization catalysts to the chemical toolbox. *En route* to complex terpenes, which are increasingly used as natural substitutes to artificial compounds in medicinal chemistry,[274–276] this powerful approach provides unparalleled step- as well as atom-economy. Furthermore, the procedure captivates through its easy and general applicability of the SHCs combined

with the simple paradigm for the screening of fitting SHC/terpene combinations. A drawback of this methodology is the obligatory *all-trans* configuration of the substrates. In this regard, the key for the efficient conversion of the epimers could be engineered *cis*/trans-isomerases[277] or preceding photochemical *cis*/*trans* isomerization[278] facilitating dynamic kinetic resolution. Finally, the in chapter 3 presented stereoconvergent cyclization could be introduced by precisely engineering the active site of SHCs.

Chapter 5

OUTLOOK – THE PROSPECTS OF CYCLASE CATALYSIS

What is the ideal synthesis? According to a pioneering statement of James Hendrickson in 1975,[279] it "[…] c*reates a complex molecule* […] *in a sequence of only construction reactions involving no intermediary refunctionalizations, and leading directly to the target, not only its skeleton but also its correctly placed functionality*." Squalene-hopene cyclases genuinely epitomize this ambition by exhibiting unparalleled atom- and step-economy in accessing nature's terpenome. As the terpene market is vastly expanding (2020: 536 million $, forecast 2028: 1 billion $)[280], it can be expected that terpene cyclases and their biomimetic catalysis will become of huge value for the chemical industry, as exemplified by the biocatalytic production of (–)-ambroxide **7** at Givaudan.[281,282] Synthetic routes towards complex terpenes will probably be drastically shortened, while ensuring excellent product- and stereoselectivities owing to the *shape-complementary* cyclization cascade. In this regard, the promiscuous ability of hydrogen-bond mediated pre-folding leveraging the functional group of non-natural substrates has proven to be a valuable addition to the polyfunctional active site of squalene-hopene cyclases (**Figure 5-1**). The thereby obtained unique ability to direct cationic cyclizations should be further explored in target-oriented synthesis designs e.g., for the vitamin A precursor tetrahydroretinol **47** (chapter 2.1). Moreover, creating locally enriched electron density in the active site unlocked the stereoconvergent cyclization of a *cis*/trans-isomeric substrate mixture, which provides a huge benefit for industry and raises questions about the intricate mechanism of SHCs. In the future, the specific anchoring of molecules by hydrogen-bonds could further enable the cofactor-independent intermolecular cationic C-C bond formation, similar to the recently presented radical-based approach by Zhao and co-workers.[130] This ambitious endeavor is already being pursued by the List group employing their IDPi catalysts.[104] Mimicking the anchoring strategy, these small-molecule catalysts could be enhanced by precisely positioned functional groups within the aromatic ligands to control selectivity as proposed in List's catalytic control over a carboniumion.[105] Such a strategy would merge cooperative/ polyfunctional catalysis[283] with the element of confinement[284] to create a new generation of powerful small-molecule catalysts. Along with rapidly advancing synthesis skills in small-molecule and

supramolecular catalysis,[285,286] this development will gradually blur the boundaries between confined, supramolecular and polyfunctional catalysis to mimic nature's catalysts.

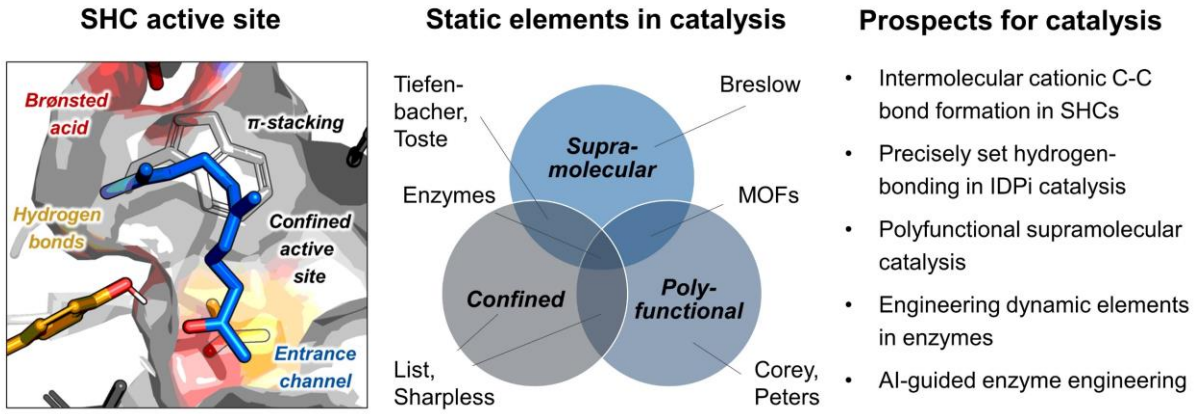

Figure 5-1: The polyfunctional active site of SHCs combines the static elements of catalysis for selectivity control and rate enhancement with dynamic elements like the entrance tunnel. Few selected examples of catalytic systems in the frontiers to enzyme catalysis: Polyfunctional catalysts by Corey and Peters.[283,287] Confined and polyfunctionally confined catalysts by List and Sharpless.[105,288] Supramolecular and confined catalysts by Tiefenbacher and Toste.[71,289] Early examples of supramolecular catalysis by Breslow.[290] Metal-organic-frameworks (MOFs) as polyfunctional supramolecular catalysts.[291] Prospects for catalysis derived from the results in this work.

Beyond the static features of the SHC, the dynamic entrance tunnel proved to be an effective complement to the active site mutagenesis of these enzymes (cf. chapter 3.2.2). The pioneering works of the Damborsky group[155] on dynamic elements of enzymes already set the stage for such novel engineering approaches. Going forward, it can be expected that with rising AI performance such (so far) unpredictable dynamic impacts on enzyme catalysis will be increasingly considered in rational enzyme engineering approaches. Initial works using AI-guided enzyme design have been demonstrated by Hilvert, Baker and Green.[292,293]

Considering enzyme catalysis holistically at the macromolecular level, the whole biocatalytic environment and physiological function of the enzyme should be taken into account more often to ensure efficient biocatalysis. For the *in vivo* cyclase catalytic system simplified in **Figure 5-2** that means the consideration of the multiphasic environment with the potential regulatory function of the membrane. This assumption opens up alternative views on diseases related to similar enzymes such as the visual impairment, Alzheimer's or Parkinson's disease.[209,294–297] However, the exact mechanism of this regulation on the molecular level might be difficult to prove due to the highly

sophisticated structure of biological membranes.[298,299] A potent solution in this regard comprises fluorescence imaging as demonstrated by Weber et al.[300] Nonetheless, there is meaningful evidence for this regulatory function of the membrane and in the words of Engasser and Horvath: *"It is unlikely that nature would not use such a simple tool to control and trigger physiological processes".*[245]

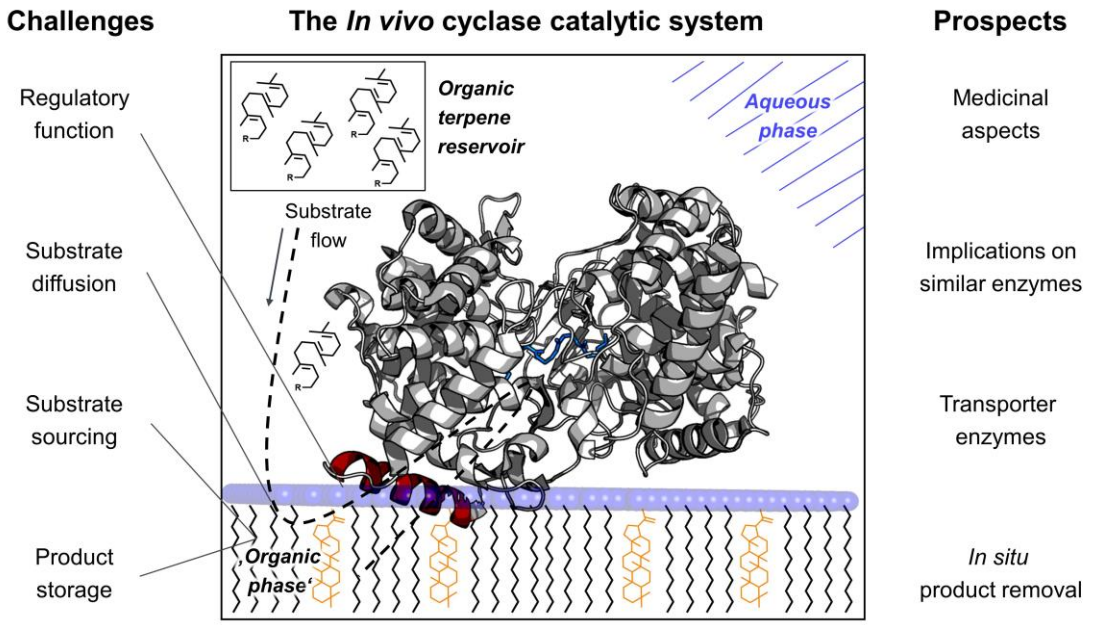

Figure 5-2: A simplified illustration of the *in vivo* cyclase catalytic system. The catalysis takes place in a multiphasic, living and dynamic environment.[77] Several aspects such as the regulatory function of the membrane or substrate concentration and diffusion must be considered to ensure efficient biocatalysis. These considerations may further affect the medicinal view on human diseases related to similar enzymes[209,294–297] and the applicability of such monotopic membrane-bound enzymes for industrial purposes.[129]

From an industrial point of view, this assumption implies the use of outer membrane lacking spheroplasts[208] or the implementation of intramembranous transporter proteins such AlkL[174] for the faster diffusion of substrates. Alternatively, *in situ* product removal techniques e.g., microemulsion systems[301] or pickering emulsions[302] could be used in order to improve the overall space-time-yield of terpene cyclases. In summary, a vibrant future can be expected for the investigation of terpene cyclases with major implications on enzymology, biomimetic catalysis, medicine, and green chemistry.

Chapter 6

MATERIALS AND METHODS

6.1 Materials

6.1.1 Chemicals

Unless otherwise noted, all chemicals and reagents for chemical reactions were purchased from Carl-Roth GmbH + Co. KG (Karlsruhe, DE), VWR GmbH (Pennsylvania, US), Sigma-Aldrich/ Merck KGaA (St. Louis, US), Alfa-Aesar GmbH + Co. KG (Ward Hill, US) and TCI Deutschland GmbH (Tokyo, JP) at the highest quality and used without further purification. 2-Hydroxypropyl-β-cyclodextrin was purchased from Wacker Chemie (München, DE).

6.1.2 Molecular biological kits & biochemical material

The molecular biological kits for DNA-purification (Zymoclean DNA Clean & Concentrator Kit), Agarose gel-extraction (Zymoclean Gel DNA Recovery Kit) and plasmid isolation (Zyppy™Plasmid Miniprep Kit) were purchased from ZymoResearch (Irvine, US). SDS-PAGE materials including gels, sample buffer, running buffer, staining solution and destaining solution was bought from Expedeon, UK.

6.1.3 Buffers and media

A comprehensive list of all buffers and media that were used in this work is given in **Table 6-1**.

Table 6-1: Buffers and media for protein production, biotransformations and molecular biological methods.

Entry	Buffer/ Medium	Components
1	10x phosphate buffer (KP_i-buffer)	0.17 M KH_2PO_4, 0.72 M K_2HPO_4, pH = 7.4
2	Lysis buffer	200 mM Citric acid, 0.1% EDTA, pH = 6.0
3	Extraction buffer	100 mM Citric acid, 1% CHAPS, pH = 6.0
4	Whole cell buffer	100 mM Citric acid, 0.1% SDS, pH = 6.0
5	Cyclodextrin (CD) buffer	0.2% SDS, 10 mM (2-Hydroxypropyl)-β-cyclodextrin

6	Lysogeny broth (LB medium)	10 g/L tryptone, 10 g/L NaCl, 5 g/L yeast extract
7	Terrific broth (TB medium)	12 g/L tryptone, 24 g/L yeast extract, 4 g/L Glycerol
8	Auto-induction medium (**T-DAB**[303])	12 g/L tryptone, 24 g/L yeast extract, 2.9 g/L glucose, 11.1 g/L Glycerol, 7.6 g/L Lactose
9	TbfI buffer	30 mM Potassium acetate, 100 mM RbCl, 10mM $CaCl_2$, 15% Glycerol, 1 M Potassiumhydroxide, pH = 5.8
10	TbfII buffer	100 mM MOPS, 10 mM RbCl, 75 mM $CaCl_2$, 15% Glycerol, 1 M Poatssium hydroxide, pH = 6.5

6.1.4 Enzymes

All enzymes for cloning purposes including Phusion HF DNA Poylmerase, *DpnI*, T5 Exonuclease and *Tag* DNA Ligase were purchased from New England Biolabs GmbH (Ipswich, US).

6.1.5 Plasmids

This work included the use multiple plasmids, each encoding a squalene-hopene cyclase gene originating from a different organism (Table 6-2). The vector pET-22b(+) (Figure 5-1) was used as a standard. Transcription occurs by the T7 RNA polymerase and is controlled by the lac repressor[303]. The vector has a pBR322 origin and confers ampicillin resistance. Gene expression was induced by lactose using the autoinduction protocol (cf. chapter 6.3.1)

Table 6-2: Plasmids including their ITB accession number used in this work.

ITB accession number	Organism (short)	Mutations
pITB285	*Alicyclobacillus acidocaldarius (Aac)*	WT
pITB105	*Zymomonas mobilis (Zmo1)*	WT
pITB282	*Zymomonas mobilis (Zmo2)*	WT
pITB312	*Acetobacter pasteurianus (Apa)*	WT
pITB313	*Pelobacter carbinolicus (Pca2)*	WT
pITB314	*Rhodopseudomonas palustris (Rpa1)*	WT
pITB315	*Streptomyces coelicolor (Sco)*	WT
pITB316	*Syntrophobacter fumaroxidans (Sfu1)*	WT
pITB317	*Bradyrhizobium japonicum (Bja)*	WT
pITB318	*Burkholderia ambifaria (Bam1)*	WT

pITB319	*Burkholderia ambifaria (Bam2)*	WT
pITB320	*Teredinibacter turnerae (Ttu)*	WT
pITB170	*Thermosynechococcos elangatus (Tel)*	WT
pITB5928	*Alicyclobacillus acidocaldarius (Aac)*	G600T/L60S
pITB5929	*Alicyclobacillus acidocaldarius (Aac)*	G600T/L607A
pITB5930	*Alicyclobacillus acidocaldarius (Aac)*	G600T/L607A/Y420F
pITB5931	*Alicyclobacillus acidocaldarius (Aac)*	G600T/L607A/Y420F/A306V
pITB5932	*Alicyclobacillus acidocaldarius (Aac)*	Y420F/G600T
pITB5933	*Alicyclobacillus acidocaldarius (Aac)*	Y420F/L607A
pITB5934	*Alicyclobacillus acidocaldarius (Aac)*	Y420F/Y609F
pITB5935	*Alicyclobacillus acidocaldarius (Aac)*	G600N/L607A
pITB5936	*Alicyclobacillus acidocaldarius (Aac)*	W169G
pITB5937	*Alicyclobacillus acidocaldarius (Aac)*	W169G/G600M
pITB5938	*Alicyclobacillus acidocaldarius (Aac)*	W169G/G600M/M132R/I432T
pITB5939	*Alicyclobacillus acidocaldarius (Aac)*	F601D/F605L
pITB5940	*Alicyclobacillus acidocaldarius (Aac)*	W169G/S168A
pITB5941	*Thermosynechococcos elangatus (Tel)*	W172G
pITB5942	*Zymomonas mobilis (Zmo1)*	W221G
pITB5943	*Zymomonas mobilis (Zmo2)*	W177G
pITB5944	*Streptomyces coelicolor (Sco)*	W196G

Figure 6-1: Standard plasmid map consisting of the *Aac*SHC gene (red band) cloned into the pET-22b(+) vector.

6.1.6 *E. coli* strains

Preparation of plasmids was carried out with XL-1 blue strain, which guarantees a high copy plasmid number and transformation of methylated DNA. E. coli strain BL21(DE3) was used for protein expression. The strain lacks the OmpT and Lon proteases, which could degrade the desired protein during isolation. As a result, the desired protein can be overproduced in the heterologous host.

6.1.7 Primers

A comprehensive list of all primers that were used in this work is given in **Table 6-3**.

Table 6-3: List of primers used in this work. Each position using either site-directed or site-saturation mutagenesis got one entry number.

Entry	Name	Sequence (5′→3′) Forward/Reverse
1	*Aac*SHC_G600C	CCGTATTATACCGGCACCTGCTTCCCGGGCG / CGCCCGGGAAGCAGGTGCCGGTATAATACGG
2	*Aac*SHC_G600D	CCGTATTATACCGGCACCGATTTCCCGGGCG / CGCCCGGGAAATCGGTGCCGGTATAATACGG
3	*Aac*SHC_G600E	CCGTATTATACCGGCACCGAATTCCCGGGCG / CGCCCGGGAATTCGGTGCCGGTATAATACGG
4	*Aac*SHC_G600H	CCGTATTATACCGGCACCCATTTCCCGGGCG / CGCCCGGGAAATGGGTGCCGGTATAATACGG
5	*Aac*SHC_G600I	CCGTATTATACCGGCACCATTTTCCCGGGCG / CGCCCGGGAAAATGGTGCCGGTATAATACGG
6	*Aac*SHC_ G600K	CCGTATTATACCGGCACCAAATTCCCGGGCG / CGCCCGGGAATTTGGTGCCGGTATAATACGG
7	*Aac*SHC_G600M	CCGTATTATACCGGCACCATGTTCCCGGGCG / CGCCCGGGAACATGGTGCCGGTATAATACGG
8	*Aac*SHC_G600N	CCGTATTATACCGGCACCAACTTCCCGGGCG / CGCCCGGGAAGTTGGTGCCGGTATAATACGG
9	*Aac*SHC_G600P	CCGTATTATACCGGCACCCCGTTCCCGGGCG / CGCCCGGGAACGGGGTGCCGGTATAATACGG
10	*Aac*SHC_G600Q	CCGTATTATACCGGCACCCAGTTCCCGGGCG / CGCCCGGGAACTGGGTGCCGGTATAATACGG
11	*Aac*SHC_ G600L	CCGTATTATACCGGCACCCTATTCCCGGGCG / CGCCCGGGAATAGGGTGCCGGTATAATACGG
12	*Aac*SHC_G600S	CCGTATTATACCGGCACCTCGTTCCCGGGCG / CGCCCGGGAACGAGGTGCCGGTATAATACGG
13	*Aac*SHC_G600T	CCGTATTATACCGGCACCACCTTCCCGGGCG / CGCCCGGGAAGGTGGTGCCGGTATAATACGG
14	*Aac*SHC_G600V	CCGTATTATACCGGCACCGTGTTCCCGGGCG / CGCCCGGGAACACGGTGCCGGTATAATACGG
15	*Aac*SHC_G600Y	CCGTATTATACCGGCACCTATTTCCCGGGCG / CGCCCGGGAAATAGGTGCCGGTATAATACGG
16	*Aac*NMC_Y609F	GGCGATTTTTATGCGGGCTTTACCATGTATCGCCATGTG/ CACATGGCGATACATGGTAAAGCCCGCATAAAAATCGC
17	*Aac*SHC_Y420F	CAACGGCGGCTGGGGCGCGTTTGATGTGGATAACACCAGC/ GCTGGTGTTATCCACATCAAACGCGCCCCAGCCGCCGTTG
18	*Aac*SHC_L607M	GGTTCCCGGGCGATTTTTATGCCATGTATACCATGTATCGCC/ GGCGATACATGGTATAGCCGGCATAAAAATCGCCCGGGAACC
19	*Aac*SHC_L607S	GGTTCCCGGGCGATTTTTATAGCCATTATACCATGTATCGCC/ GGCGATACATGGTATAGCCGCTATAAAAATCGCCCGGGAACC
20	*Aac*SHC_L607Y	GGTTCCCGGGCGATTTTTATTATGGCTATACCATGTATCGCC/ GGCGATACATGGTATAGCCATAATAAAAATCGCCCGGGAACC
21	*Aac*SHC_L607V	GGTTCCCGGGCGATTTTTGTCCCATGTATACCATGTATCGCC/ GGCGATACATGGTATAGCCGGGACAAAAATCGCCCGGGAACC
22	*Aac*SHC_L607RVT	GGTTCCCGGGCGATTTTTATRNTGGCTATACCATGTATCGC/ ATAAAAATCGCCCGGGAACCCGGTGCCGGTATAATACGG
23	*Aac*SHC_I261X	GCGATGGCAGCTGGGGCGGCNDTCAGCCGCCGTGGTTTTATGC/ GCGATGGCAGCTGGGGCGGCVHGCAGCCGCCGTGGTTTTATGC/ GCGATGGCAGCTGGGGCGGCTGGCAGCCGCCGTGGTTTTATGC/ TGCCGCCCCAGCTGCCATCGCCCGCCTGGCGTTCCAG
24	*Aac*SHC_L36X	GGCTATTGGTGGGGCCCGNDTCTGAGCAACGTGACCATG/ GGCTATTGGTGGGGCCCGVHGCTGAGCAACGTGACCATG/ GGCTATTGGTGGGGCCCGTGGCTGAGCAACGTGACCATG/ CGGGCCCCACCAATAGCCTTCATCTTTCTGGCAGCTCAG

26	*Aac*SHC_S307X	GGCTGGATGTTTCAGGCGNDTATTAGCCCGGTGTGGG/ GGCTGGATGTTTCAGGCGVHGATTAGCCCGGTGTGGG/ GGCTGGATGTTTCAGGCGTGGATTAGCCCGGTGTGGG/ CGCCTGAAACATCCAGCCGCCATAATCCAGTTCCACG
27	*Aac*SHC_A306X	GGCGGCTGGATGTTTCAGNDTAGCATTAGCCCGGTG/ GGCGGCTGGATGTTTCAGVHGAGCATTAGCCCGGTG/ GGCGGCTGGATGTTTCAGTGGAGCATTAGCCCGGTG/ CTGAAACATCCAGCCGCCATAATCCAGTTCCACGCCATACAG
28	*Aac*SHC_F601NVS	CGTATTATACCGGCACCGGGNVSCCGGGCGATTTTTATCTGGG/ CATGGTGCCGGTATAATACGGTTCATCCCAGCCGCCATCCGGGC
29	*Aac*SHC_F605NVS	GCACCGGGTTCCCGGGCGATNVSTATCTGGGCTATACCATGTATCGC/ ATCGCCCGGGAACATGGTGCCGGTATAATACGGTTCATCCCAGCC
30	*Aac*SHC_M132X	GCAGCCGCGTGTTTACCCGCNDTTGGCTGGCGCT/ GCAGCCGCGTGTTTACCCGCVHGTGGCTGGCGCT/ GCAGCCGCGTGTTTACCCGCTGGTGGCTGGCGCT/ GCGGGTAAACACGCGGCTGCTTTCAATGCCGCCCTG
31	*Aac*SHC_F129X	GCATTGAAAGCAGCCGCGTGNDTACCCGCATGTGGCTG/ GCATTGAAAGCAGCCGCGTGVHGACCCGCATGTGGCTG/ GCATTGAAAGCAGCCGCGTGTGGACCCGCATGTGGCTG/ CACGCGGCTGCTTTCAATGCCGCCCTGGCTCTGAAT
32	*Aac*SHC_F434X	GCGATCTGCCGAACCATATTCCGNDTTGCGATTTTGGC/ GCGATCTGCCGAACCATATTCCGVHGTGCGATTTTGGC/ GCGATCTGCCGAACCATATTCCGTGGTGCGATTTTGGC/ CGGAATATGGTTCGGCAGATCGCTGGTGTTATCCACATCATAC
33	*Aac*SHC_D436X	GAACCATATTCCGTTTTGCNDTTTTGGCGAAGTGACCGATCCG/ GAACCATATTCCGTTTTGCVHGTTTGGCGAAGTGACCGATCCG/ GAACCATATTCCGTTTTGCTGGTTTGGCGAAGTGACCGATCCG/ GCAAAACGGAATATGGTTCGGCAGATCGCTGGTGTTATCCAC
34	*Aac*SHC_F437X	GAACCATATTCCGTTTTGCGATNDTGGCGAAGTGACCGATCCGC/ GAACCATATTCCGTTTTGCGATVHGGGCGAAGTGACCGATCCGC/ GAACCATATTCCGTTTTGCGATTGGGGCGAAGTGACCGATCCGC/ ATCGCAAAACGGAATATGGTTCGGCAGATCGCTGGTGTTATCCAC
35	*Aac*SHC_V440X	GTTTTGCGATTTTGGCGAANDTACCGATCCGCCGAGCG/ GTTTTGCGATTTTGGCGAAVHGACCGATCCGCCGAGCG/ GTTTTGCGATTTTGGCGAATGGACCGATCCGCCGAGCG/ TTCGCCAAAATCGCAAAACGGAATATGGTTCGGCAGATCGCTGG
36	*Aac*SHC_I261NVS	GCGATGGCAGCTGGGGCGGCNVSCAGCCGCCGTGGTTTTATGC/ TGCCGCCCCAGCTGCCATCGCCCGCCTGGCGTTCCAG
37	*Aac*SHC_W169NVS	GCTGAACATTTATGAATTTGGCAGCNVSTGCGCGCGCGACC/ GCTGCCAAATTCATAAATGTTCAGCGGCATGCGTTTGCCCAGAAAC
38	*Aac*SHC_G600NVS	GAACCGTATTATACCGGCACCNVSTTCCCGGGCGATTTTTATCTG/ GGTGCCGGTATAATACGGTTCATCCCAGCCGCCATC
39	*Aac*SHC_G600X	GAACCGTATTATACCGGCACCNDTTTCCCGGGCGATTTTTATCTG/ GAACCGTATTATACCGGCACCVHGTTCCCGGGCGATTTTTATCTG/ GAACCGTATTATACCGGCACCTGGTTCCCGGGCGATTTTTATCTG/ GGTGCCGGTATAATACGGTTCATCCCAGCCGCCATC
40	*Aac*SHC_F601NVS	CGTATTATACCGGCACCGGGNVSCCGGGCGATTTTTATCTGGG/ CATGGTGCCGGTATAATACGGTTCATCCCAGCCGCCATCCGGGC
41	*Aac*SHC_G600S	CCGTATTATACCGGCACCTCGTTCCCGGGCG/ CGCCCGGGAACGAGGTGCCGGTATAATACGG
42	*Aac*SHC_F605NVS	GCACCGGGTTCCCGGGCGATNVSTATCTGGGCTATACCATGTATCGC C/ ATCGCCCGGGAACATGGTGCCGGTATAATACGGTTCATCCCAGCC
43	TelSHC_W172G	GTTTACCATTTATGAAATGAGCAGCGGCGCACGTAGCAGCACCG/ CGGTGCTGCTACGTGCGCCGCTGCTCATTTCATAAATGGTAAAC
44	AacSHC_S168A	CTGAACATTTATGAATTTGGCGCGTGGGCGCGCGCG/ GCCAAATTCATAAATGTTCAGCGGCATGCGTTTGCC

6.2 Molecular biological methods

6.2.1 Preparation of chemically competent cells

The production of chemically competent *E. coli* cells was carried out using the rubidium chloride method.[304] For this purpose, 100 mL LB medium was inoculated with the respective E. coli cells (BL21(DE3) or XL-1 blue) and incubated in a shaking incubator at 37 °C and 180 rpm. At an optical density (OD_{600}) of 0.5, the cells were transferred to a cold room (4 °C) and centrifuged (4 °C, 15 min, 4000 rpm). The cell pellet was resuspended in 30 mL of cold TbfI buffer, incubated on ice for 90 min and then centrifuged again (4 °C, 15 min, 4000 rpm). After repeated resuspension of the pellet in 4 mL TbfII buffer and incubation on ice for 15 min the competent cells were aliquoted (15 µL) and stored at –80 °C until further use.

6.2.2 Polymerase-chain-reaction (PCR)

The polymerase chain reaction (PCR) is an *in vitro* method to specifically amplify a DNA template.[305] For this purpose, repetitive cycles of heat denaturation of the DNA, annealing and elongation are used to synthesize the target fragment by means of DNA polymerase and synthetic nucleotides. The temperature profile is given in Table 6-4.

Table 6-4: Temperature profile for the PCR using the KOD Hot start polymerase.

Step	**Temperature** [°C]	**Time** [s]	**Cycles**
Initial denaturation	95	120	1
Denature	95	30	
Annealing	60	30	30
Extension	70	210	
Final extension	72	420	1

6.2.3 Plasmid isolation

Isolation of the plasmids proceeded following to the standard protocol of *Zyppy™Plasmid Miniprep Kit* by *ZymoResearch*.[306] For the photometric determination of the plasmid DNA concentration, 2 µL of the isolated enzyme solution were measured on a *Nanodrop 1000* (Agilent, Santa Clara, US) at a wavelength of 260 nm.

6.2.4 Site-directed/-saturation mutagenesis

The gene encoding for *Aac*SHC (UniProt: P33247) or a variant based on this gene was cloned into a pET-22b(+) vector system (Merck, Darmstadt, Germany). SacI and NdeI were used as restriction sites. Cloning followed the standard protocol of *Novagene'*s KOD Hot Start DNA Polymerase. The composition of the PCR mixture and the temperature profile are described in **Table 6-4** and **Table 6-5**, respectively. Site-saturation libraries were generated employing the '22c-trick' method[138] PCR products were digested with 1 µL DpnI for 4 h at 37 °C, purified by agarose gel electrophoresis and ligated into the pET22b(+) vector by Gibson assembly[307]. After purification using the DNA Clean & Concentrator™-5 kit the plasmids were transformed via heat-shock method.

Table 6-5: Composition of the PCR mixture using the KOD Hot start polymerase.

Substance	Volume [µl]	Final concentration
ddH_2O	29.0	
DMSO	2.5	
KOD Hot Start Buffer (10x)	5.0	1x
dNTPs (2 mM each)	5.0	250 µM (each)
$MgSO_4$ (25 mM)	4.5	2 mM
Template DNA	1.0	0.5-5 ng/ µl
Primer *forward* (10 µM)	1.0	0,2 µM
Primer *reverse* (10 µM)	1.0	0,2 µM
KOD Hot Start DNA Polymerase	1.0	

6.2.5 Plasmid transformation

For site saturation libraries 3 µL of the purified PCR product was added to 25 µL XL1-blue competent cells and incubated for 30 min on ice, followed by a heat shock at 42 °C for 105 s with subsequent ice cooling for 3 min. After adding 500 µl of LB medium, the cells were incubated for 40min at 37 ° C and used for inoculation of a 5 mL LB medium (Ampicillin, c_{end} = 100 µg/mL) pre-culture overnight. After isolation of the plasmid, transformation into 50 µL BL21 (DE3) was performed using the heat shock method. After regeneration 150 µL were streaked out on an agar plate (Ampicillin, c_{end} = 100 µg/mL) and incubated at 37 °C overnight. For quality control the plasmid was isolated from another 150 µL and sent for sequencing. For site-directed mutants the PCR product was

digested with DpnI overnight and afterwards transformed into XL1-blue competent cells. After regeneration 300 µL were streaked out on an agar plate for single clone picking.

6.2.6 Agarose gel electrophoresis

Agarose gel electrophoresis enables the analytical and preparative separation of DNA fragments with respect to their size. The negatively charged DNA is transported through the pores of an agarose gel matrix by means of an applied voltage, whereby smaller fragments show a higher mobility. Agarose gels (1% (w/v) in TAE buffer, 0.1 µL/mL MidoriGreen) overlaid with TAE buffer (40 mM TRIS acetate, 10 mM EDTA, pH = 8.5) were used for electrophoresis. The respective samples were homogenised in a ratio of 5:1 with DNA sample buffer (R0611 DNA Loading Dye 6 x, ThermoFisher Scientific, DE). The GeneRuler™ DNA Ladder Mix (#SM0331, ThermoFisher Scientific, DE) was used as standard.

6.3 Biochemical methods

6.3.1 Protein expression

Erlenmeyer-flasks. Expression cultures were inoculated with 5 mL of the pre-culture into 500 mL of T-DAB autoinduction medium (Ampicillin, c_{end} = 100 µg/mL) with lactose as the inductor. The cultures were incubated for 20 h at 37 °C, 180 rpm and harvested afterwards (8000 rpm, 30 min). The resulting pellets were frozen at –80 °C overnight and lyophilized afterwards for storage. Alternatively, the cell pellets were directly used for biotransformations or thermolysis purification.

96-DWs. For the expression in 96-DW plates individual colonies were picked from generated agar plates and cultivated in 500 µL LB medium (Ampicillin, c_{end} = 100 µg/mL) for 18-20 h at 37 °C, 800 rpm. Expression cultures were inoculated with 10 µL of the pre-culture into 1 mL of T-DAB autoinduction medium (Ampicillin, c_{end} = 100 µg/mL) with lactose as the inductor. The cultures were incubated for 20h at 37 °C, 800 rpm and harvested afterwards (4000 x g, 20 min).

24-DWs. For the expression in 24-DW plates Individual colonies were picked from generated agar plates and cultivated in 2 mL LB medium (Ampicillin, c_{end} = 100 µg/mL) for 18-20h at 37 °C, 600 rpm. Expression cultures were inoculated with

40 µL of the pre-culture into 4 mL of T-DAB autoinduction medium (Ampicillin, c_{end} = 100 µg/mL) with lactose as the inductor. The cultures were incubated for 20h at 37 °C, 600 rpm and harvested afterwards (4000 x g, 20 min).

6.3.2 Thermolysis purification

The thermolysis purification protocol is a modified version of the literature known protocol for thermophilic enzymes.[308] Harvested or lyophilized cells were resuspended in 1 mL Lysis buffer and incubated for 60 min at 70 °C. The cell suspension was centrifuged (14000 x g, 1 min) and the supernatant was discarded. As the enzyme is membrane-bound, 1 mL 1%-CHAPS buffer was added to extract it from the cell pellet by shaking at room temperature for 1-2 d, 600 rpm. After subsequent centrifugation (14000 x g, 1 min) the supernatant containing the *Aac*SHC was transferred to a new tube followed by SDS-PAGE analysis and determination of enzyme concentration by using the Nanodrop 1000 (Agilent, Santa Clara, US). Therefore the "Protein A280" mode was chosen with MW= 71439 Da and molar extinction coeffizient ε = 185180 $M^{-1} \cdot cm^{-1}$ as protein specific data calculated using the online-software ProtParam.[309]

6.3.3 SDS-PAGE

Sodium dodecyl sulphate polyacrylamide gel electrophoresis (SDS-PAGE) has been used for qualitative analysis of protein solutions.[310] The addition of excess SDS to protein solutions leads to protein denaturation. The proportional addition of negatively charged SDS to the amino acid chains leads to a correlation between protein charge and protein size. Protein mixtures can thus be separated in the electric field due to different electrophoretic mobility in a gel matrix (Supporting Figure S 13). Materials Gels with an acrylamide content of 10 % in the separating gel and 4 % in the collecting gel were used (Expedeon, UK). The gel was mounted in the electrophoresis apparatus (Expedeon, UK) and overlaid with running buffer. Sample solutions were mixed 1:1 with the SDS sample buffer and heated to 95 °C for 5 min. For comparison, 5 µL of a molecular weight standard (PageRuler™, #26617, Fermentas, St. Louis, US) was used. Electrophoresis was performed at a current of 110 V. After electrophoresis, the gel first incubated in staining solution for 10 min and then in destaining solution overnight.

6.4 Analytical methods

6.4.1 Nuclear magnetic resonance

^{1}H- und ^{13}C-NMR, COSY, HSQC and HMBC spectra were recorded on a Bruker Avance 500 Spectrometer at 500.15 MHz for ^{1}H- and 125 MHz for ^{13}C. The chemical shifts δ are referred to tetramethylsilane (=TMS) in ppm set to 0. All substances were dissolved in $CDCl_3$ and recorded at room temperature.

6.4.2 Circular dichroism

The specific optical rotation of the terpenes was measured on a Perkin Elmer Polarimeter 241. Therefore, the substance was dissolved in CHCl3 (c = 0.5 mg/mL), and the specific rotation was measured with a sodium and a mercury spectral lamp.

6.4.3 Gas chromatography

GC analyses were performed using an Agilent GC 7820A equipped with a mass spectrometer MSD 5977B and a Zebron ZB-5HT Inferno capillary column (Agilent, 30 m x 250 µm x 0.25 µm) and helium as carrier gas with a constant pressure of 14.168 ψ. Injections (1 µL) were performed at 300 °C in split mode. Relative conversion rates were calculated directly from GC-MS spectra by integration-quotient of substrates and products. Chiral GC analysis was performed on a Shimadzu GC-2010 equipped with a CP ChiraSil-Dex CB capillary column (Agilent, 25 m x 250 µm x 0.25 µm) and hydrogen as carrier gas with constant velocity (linear velocity: 33.1 cm/s). Injections (1 µL) were performed in split mode (5:1). Temperature programs are listed in **Table 6-6**.

Table 6-6: GC-temperature profiles.

Name	**Rate** [°C/min]	**Temperature** [°C]	**Hold** [min]
Dihydroionone_long		120	0.1
	2	145	0.6
Dihydroionone_short		120	0.1
	2	137	0.6
Calmusal		110	0.1
	2	135	0.6
Scouting		50	1
	10	300	10
Chiral (on Shimadzu GC-FID)		70	3
	10	140	0
	8	180	2

ambroxide		172	5
	3	174	1.5
Geranyl acetate		120	10
Farnesol		182	7
Geranylgeraniol		215	7
Farnesyl acetone		184	8
Farnesyl acetone acetate		240	7

6.5 Chemical synthesis

6.5.1 Synthesis of *E*/*Z*-geranyl isopropanol 58

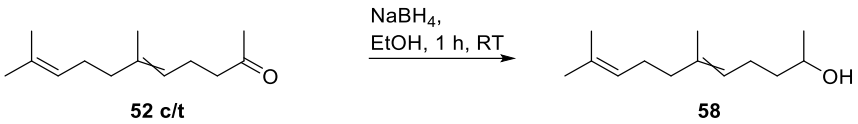

52 c/t **58**

The reaction was carried out under nitrogen atmosphere. For the reduction reaction geranyl acetone **52 c/t** (0.50 mL, 2.34 mmol 1.00 eq.) was dissolved in ethanol (10 mL). Sodium borohydride (0.087 g, 2.34 mmol, 1.00 eq.) was then added carefully and the reaction mixture was stirred at room temperature for 1 h. After the reaction was complete, the mixture was quenched with 0.5 N HCl (2 mL) and stirred again for 30 min. Then distilled water (50 mL) was added and the aqueous phase was extracted three times with DCM. The combined organic layers were dried over $CaCl_2$ and the geranyl isopropanol **58** was obtained as a clear oil (0.49 mL, 2.04 mmol, 87%).

^{1}H-NMR ($CDCl_3$, 500 MHz): δ (ppm) 1.19 (d, *J* = 2.9 Hz, 3H), 1.50 (quart, *J* = 7.7 Hz, 2H) 1.6 (s, 3H), 1.62 (s, 3H), 1.68 (s, 3H), 1.88-1.92 (t, *J* = 7.3 Hz, 2H), 2.04-2.12 (m, 4H), 3.77-3.84 (sept, *J* = 17.43 Hz, 1H), 5.05-5.10 (t, *J* = 6.7 Hz, 1H), 5.12-5.17 (t, *J* = 6.8 Hz, 1H). **^{13}C-NMR ($CDCl_3$, 125 MHz):** δ (ppm) 16.50 (1C), 16.66 (1C), 22.44-25.63 (4C), 38.15-38.70 (2C), 66.97 (1C), 75.67 (1C), 122.22-123.24 (2C), 134.9 (1C). **MS (EI)**: *m*/*z* (%) = 196 (0.3), 153 (32), 135 (21), 109 (58), 95 (21), 82 (19), 81 (21), 69 (100), 68 (13), 67 (44). The data is consistent with the literature.[311]

6.5.2 Synthesis of *E*/*Z*-5,9-dimethylundeca-4,8-dien-1-ol (Calmusol) 64

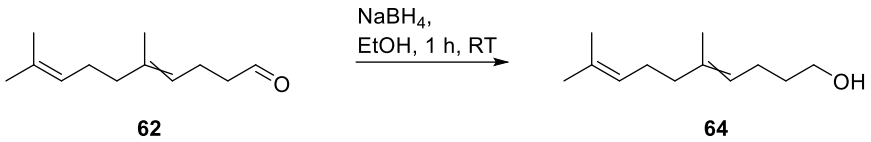

62 **64**

The reaction was carried out analog to synthesis 6.5.1. The product **64** was obtained as a clear oil (0.21 mL, 1.04 mmol, 43%).

^{1}H-NMR ($CDCl_3$, 500 MHz): δ (ppm) 1.19-1.34 (m, 2H), 1.55-1.59 (m, 2H) 1,61(s, 3H), 1.62-1.65 (m, 1H), 1.68 (s, 3H), 1.69-1.71 (m, 2H), 2.04-2.12 (m, 4H), 3.62-3.67 (t, *J* = 6.6 Hz, 2H), 5.03-5.19 (m, 2H). The data is consistent with the literature.[312]

6.5.3 Synthesis of (+)-α-ambrinol 57

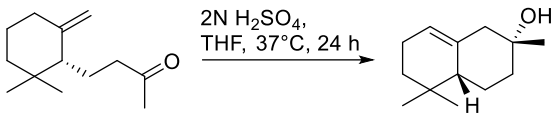

3 **57**

For the cyclization reaction (–)-γ-dihydroionone (400 µL, 1.8 mmol) was dissolved in THF (15 mL) in a 50 mL Schott-bottle. 2N sulfuric acid (5 mL) was then added and the reaction mixture was shaken at 37 °C for 24 h. The reaction was quenched by addition of water (20 mL) and extracted with diethyl ether (3 x 30 mL). The combined organic layers were dried over $MgSO_4$ and purified via silica chromatography (10:1, CH:EtOAc) to yield the slightly yellowish liquid (+)-α-ambrinol **57** (0.35 mL, 1.5 mmol, 88 %); ($[\alpha]_D^{20}$ = +84.6; Lit. = 81.8[151]).

^{1}H-NMR ($CDCl_3$, 500 MHz): δ (ppm) 0.87 (s, 3H), 0.91 (s, 3H) 1.14 (m, 1H), 1.22 (s, 3H), 1.24-1.40 (m, 3H), 1.45-1.51 (m, 2H), 1.67-1.74 (m, 2H), 1.98-2.02 (m, 2H), 2.06-2.17 (m, 2H), 5.45 (t, J = 3.84Hz, 1H). **^{13}C-NMR ($CDCl_3$, 125 MHz):** δ (ppm) 22.6 (1C), 23.8 (1C), 25.05 (1C), 26.02 (1C), 28.07 (1C), 29.24 (1C), 31.11 (1C), 28.95(1C), 47.25 (1C), 49.82 (1C), 70.28 (1C), 122.04 (1C), 137.39 (1C). The data is consistent with the literature.[144]

(+)-α-ambrinol **57: MS (EI):** m/z (%) = 194 (5), 176 (40), 161 (30), 136 (100), 121 (66), 120 (40), 109 (28), 105 (31), 95 (49), 93 (28).

Side product: (–)-β-ambrinol: **MS (EI):** m/z (%) = 194 (6), 176 (55), 161 (100), 136 (40), 121 (84), 107 (43), 106 (46), 105 (60), 93 (52), 91 (42).

6.5.4 Synthesis of *E*,*E*-homofarnesol 66

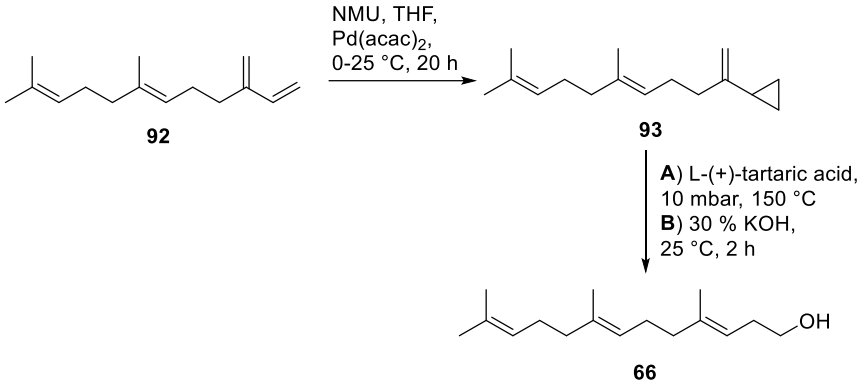

Cyclopropanation.[313] The reaction was carried out under nitrogen atmosphere. For the cyclopropanation reaction N-Methyl-N-nitroso urea (NMU) 1.35M in THF (136 ml, 184 mmol) was added dropwise at 0 °C to a stirred mixture of *E*-β-farnesene **92** (4.45 mL, 24.5 mmol) and aqueous KOH (10 mL, 40%) at 0-5 °C. After the addition of 0.8 mL of the MNU solution, $Pd(acac)_2$ (1.5 mg, 0.005 mmol, 0.02%) pre-dissolved in 0.5 mL dichloromethane was added. The remaining MNU solution was added over 4 h at 0 °C. After 16 h at 25 °C, the reaction was quenched by adding acetic acid (20 mL) then MTBE (50 mL). After phase separation, the organic phase was washed with 2M HCl (50 mL) and the aqueous phase was extracted with MTBE (50 mL). The combined organic layers were washed with water (2×100 mL), aqueous 10% NaOH dried over $MgSO_4$, filtered and concentrated to yield 5.1 g of a slightly yellow liquid which contained 7 % *E*-β-farnesene, 83 % of the desired monocyclopropane **93** compound and 10 % of a side product (GC control). The crude product was directly used in the next synthetic step without further purification.

Ring-opening.[313] The reaction was carried out under nitrogen atmosphere. A mixture of monocyclopropane **93** (5 g, 23 mmol) and L-(+)-tartaric acid (5 g, 34.5 mmol) was heated under reduced pressure stirring at 150 °C. After 18 h and complete conversion

(GC control), the mixture was poured on 100 mL of water:toluene, 1:1. The phases were separated and the aqueous phase extracted with toluene (250 mL). The combined organic layers were washed with conc. aqueous Na_2CO_3 (250 mL) and conc. NaCl (2×250 mL), dried over $MgSO_4$, filtered and evaporated under reduced pressure to give a brown solid which was mixed with 30% aqueous KOH (20.0 mL) and stirred at 25 ° C. for 2 h. GC analysis revealed formation of 96% homofarnesol **66** with an 3*E*/3*Z* ratio of 76:24. The reaction was quenched by addition of water (100 mL) and extracted with MTBE (3 x 150 mL). The combined organic layers were dried over $MgSO_4$ and purified via silver nitrate silica chromatography (CH:EtOAc, 100:1) to yield liquid homofarnesol **66** (4.5 mL, 17 mmol, 73%).

^{1}H-NMR ($CDCl_3$, 500 MHz): δ (ppm) 1.60 (s, 6H), 1.64 (s, 3H), 1.68 (s, 3H), 1.67 (s, 3H), 1.95-2.11 (m, 8H), 2.25-2.32 (q, *J* = 9.9 Hz, 2H), 3.59-3.63 (t, J=6.3, 2H), 5.07-5.15 (m, 3H). **^{13}C-NMR ($CDCl_3$, 125 MHz):** δ (ppm) 16.01 (1C), 16.2 (1C), 17.7 (1C), 25.7 (1C), 26.5 (1C), 26.7 (1C), 31.5 (1C), 39.7 (1C), 39.8 (1C), 62.4 (1C), 119.8 (1C), 123.8 (1C), 124.9 (1C), 131.3 (1C), 135.3 (1C), 138.9 (1C). The data is consistent with the literature.[129]

6.5.5 Synthesis of *E,E*-keto ester 77

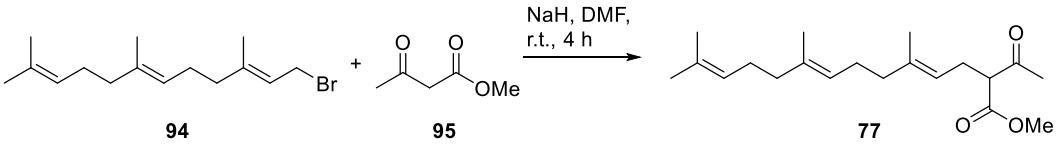

94 **95** **77**

The reaction was carried out under nitrogen atmosphere. A 60 % dispersion of NaH in mineral oil (210 mg, 5.25 mmol) was washed with hexane (3x1mL) and suspended in DMF (5mL). Methylacetoacetate **95** (580 µL, 5.4 mmol was added dropwise. After 30 min, the resulting solution was treated with *E,E*-farnesyl bromide **94** (0.5 g, 1.75 mmol) and stirred for 4 h. The reaction mixture was quenched with 5 mL of saturated $NaHCO_3$, extracted with EtOAc (3 x 10 mL), and washed with H_2O (4 x 5 mL). The combined organic layers were dried over $MgSO_4$ and concentrated. Column chromatography (CH:EtOAc, 1:20) afforded a colorless oil of **77** (0.43 mL, 1.36 mmol, 78 %).

^{1}H-NMR ($CDCl_3$, 500 MHz): δ (ppm) 1.58 (s, 3H), 1.60 (s, 3H), 1.62 (s, 3H), 1.67 (s, 3H), 1.94-1.99 (m, 4H), 2.03-2.07 (m, 4H), 2.22 (s, 3H), 2.54-2.57 (t, *J* = 7.5 Hz, 2H), 3.44-3.47 (t, *J* = 7.7 Hz, 1H), 3.72 (s, 3H), 5.02-5.08 (m, 3H). **^{13}C-NMR ($CDCl_3$, 125 MHz):** δ (ppm)

15.9 (1C), 16.1 (1C), 17.7 (1C), 25.7 (1C), 26.5 (1C), 26.7 (1C), 26.9 (1C), 29.2 (1C), 39.7 (1C), 52.3 (1C), 59.6 (1C), 119.5 (1C), 123.8 (1C), 124.3 (1C), 131.3 (1C), 135.2 (1C), 138.6 (1C), 170.1 (1C), 203.1 (1C). The data is consistent with the literature.[258]

6.5.6 Synthesis of (+)-α-subersic acid 87

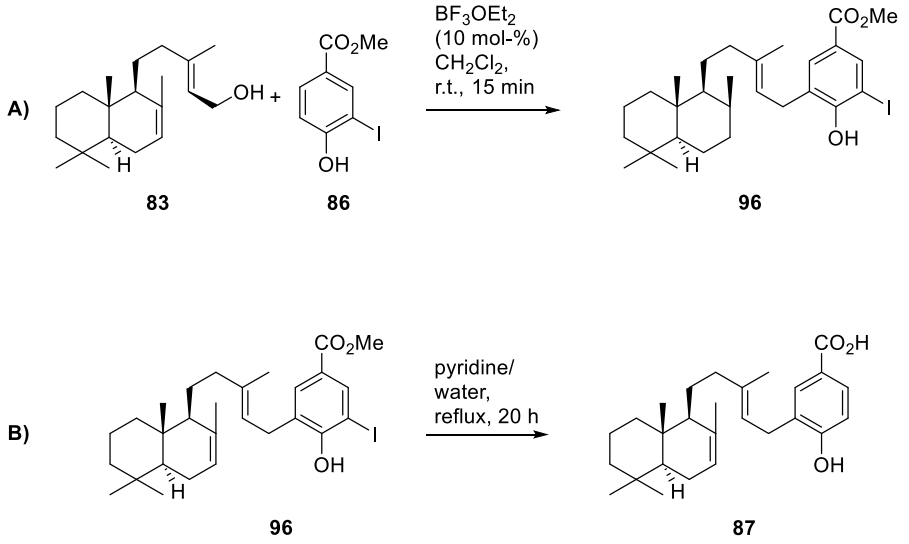

A) Friedel-Crafts alkylation.[273] Iodobenzoic acid methyl ester **86** (34 mg, 0.10 mmol) and bicyclic terpene **83** (30 mg, 0.10 mmol) in 1 mL anhydrous CH_2Cl_2 were stirred at room temperature for 5 min. Then $BF_3{\cdot}OEt_2$ (1.5 µL, 0.01 mmol) was added. The reaction mixture was stirred at room temperature for 30 min. When TLC indicated that the reaction was complete, a saturated solution of $NaHCO_3$ was added and the resulting mixture was extracted with CH_2Cl_2 (3 x 20 mL). The combined organic extracts were washed with brine and dried over $MgSO_4$. The solvent was evaporated, and the crude product was directly used in the next step.

B) Non-reductive deiodination/ saponification.[272] Crude **96** in pyridine (12 mL, 1.2 mmol) was heated at reflux for 24 h. When TLC indicated the completion of reaction, the reaction mixture was extracted with cyclohexane (3 x 10 mL). The combined organic layers were dried over $MgSO_4$, concentrated and purified by flash column chromatography (CH:EtOAc, 1:20) over silica to afford **87** as white solid (19 mg, 0.05 mmol, 52%).

^{1}H-NMR ($CDCl_3$, 500 MHz): δ (ppm) 0.81 (s, 3H), 0.87 (s, 3H), 0.92 (m, 3H), 1.13 (s, 3H), 1.49-1.55 (m, 3H), 1.01-1.35 (m, 5H), 1.41 (s, 3H), 1.42-2.01 (6H), 2.45 (s, 1H), 3.69 (d, J = 18.5

Hz, 1H), 3.70 (d, *J* = 18.5 Hz, 1H), 5.51 (m, 1H), 7.01 (d, *J* = 5.0 Hz, 1H), 7.89 (dd, *J* = 5.0 Hz, 1H), 7.91 (d, *J* = 1.3 Hz, 1H). **^{13}C-NMR ($CDCl_3$, 125 MHz):** δ (ppm) 14.8 (1C), 15.9 (1C), 18.7 (1), 19.3 (1C), 21.4 (1C), 21.9 (1C), 24.2 (1C), 27.3 (1C), 33.9 (1C), 34.4 (1C), 37.1 (1C), 37.7 (1C), 41.0 (1C), 41.7 (1C), 43.0 (1C), 44.7 (1C), 53.5 (1C), 54.9 (1C), 55.1 (1C), 116.7 (1C), 121.9 (1c), 123.3 (1C), 129,4 (1C), 130.2 (1C), 131.6 (1C) 134.8 (1C), 161.2 (1C), 171.6 (1C). The data is consistent with the literature.[255]

6.5.7 Synthesis of dehydroxy-Pyripyropene E 89

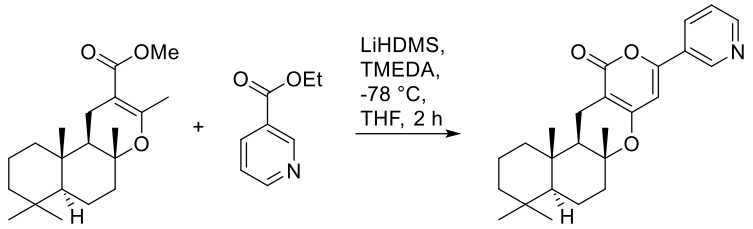

75 **88** **89**

The reaction is carried out under nitrogen atmosphere. A solution of LiHMDS (83.5 mg, 0.5 mmol) in THF (1 mL) was stirred at –78°C. To this was added a solution of a,ß-unsaturated ester **75** (40 mg, 0.125 mmol) in 3 mL of THF. The mixture was stirred for 25 min and then treated with ethyl benzoate **88** (59 µL, 0.375 mmol). After 2 h the reaction mixture was quenched with H_2O (15 mL) and extracted with EtOAc (3 x 20 mL). The combined organic layers were washed with brine (10 mL), dried over $MgSO_4$ and purified by flash chromatography (CH:EtOAc, 20:1) to afford **89** as orange solid (31 mg, 0.08 mmol, 64%).

^{1}H-NMR ($CDCl_3$, 500 MHz): δ (ppm) 0.85 (s, 3H), 0.91 (s, 3H), 0.88 (s, 3H)), 1.31-1.51 (m, 4H), 1.55 (s, 3H), 1.63-1.74 (m, 6H), 1.88-2.05 (m, 2H), 2.27-2.32 (dd, *J* = 8.7 Hz),), 6.43 (s, 1H), 7.38 (m, 1H), 8.1 (dd, *J* = 3.4 Hz, 1H), 8.65 (d, *J* = 3.4 Hz, 1H), 9.0 (s, 1H).

6.5.8 Synthesis of chromanone 91

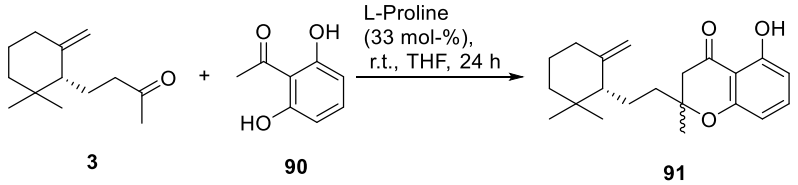

3 **90** **91**

The reaction was carried out under nitrogen atmosphere. To a solution of **3** (50 mg, 0.25 mmol) and 2,6-hydroxyacetophenon **90** (39 mg, 0.25 mmol) in dry THF (2 mL) and molecular sieves 4Å (400 mg), pyrrolodine was added (6.5 µL, 0.08 mmol). After stirring at room temperature for 24 h, MTBE was added (35 mL), washed with 2N HCl (3 x 15 mL) and brine (3 x 15 mL), dried over Na_2SO_4 and concentrated in vacuo. Purification by flash chromatography (cyclohexane: MTBE, 95:5) provided a 50:50 diastereomeric mixture of chromanone **91** (74 mg, 0.23 mmol, 90%).

^{1}H-NMR ($CDCl_3$, 500 MHz): δ (ppm) 0.83 (s, 3H), 0.91 (s, 3H), 1.19-1.27 (m, 2H), 1.4-1.83 (m, 8H), 1.57-169 (m, 4H) 1.89-2.01 (m, 2H) 2.56-2.85 (d, *J* = 16.0 Hz, 2H), 4.4 (d, *J* = 1.3 Hz, 1H), 4.7 (d, *J* = 1.5 Hz,1H), 6.4 (d, *J* = 1.5 Hz, 1H), 6.45 (d, *J* = 1.5 Hz, 1H), 7.33 t, *J*=9.0 Hz, 1H).

6.5.9 Chlorosulfonic acid catalyzed cyclizations of terpenes as racemic standards

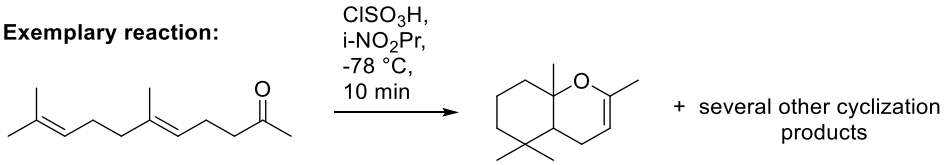

52t **53**

The reactions were carried out under nitrogen atmosphere. To a solution of 5 Eq. (2.5 mmol, 160µlL) of chlorosulfonic acid in 2-nitropropane (3 mL) was added a solution of terpene (0.5 mmol, 1 eq.) in 2-nitropropane (6 mL) at –78 °C and was stirred for 10 min. The reaction was quenched by adding saturated aq. $NaHCO_3$ solution (10 ml) and then further portions of solid $NaHCO_3$ were added to obtain basic pH. The reaction mixture was extracted with Et_2O (3x 15 mL), dried over $MgSO_4$ and the resulting crude product was used for chiral GC analysis. For exemplary chromatograms see A2.

6.6 Preparative scale biotransformations using *Aac*SHC variants

General procedure of preparative scale biotransformation. After the selective SHC variant producing the desired cyclic scaffold was identified, it was produced in large scale (6-12 Erlenmeyer flasks) following the protocol in chapter 6.3.1. The resulting cell pellets were lyophilized afterwards. The reaction mixture contained a given amount

cells, the given amount substrate, an equimolar amount 2-HPCD or no 2-HPCD (cf. chapter 4.2.3). The reactions were performed in closed Schott-flasks in an INFORS-HT incubator at 180 rpm for the given time. After the reaction was finished (GC-control) the cell suspension was extracted according to the procedures below. GC yield determined by area-% is given below the reaction arrow. Centrifugation was performed at 4000 rpm for 20 min.

6.6.1 *E*-geranyl acetone 52t with G600R

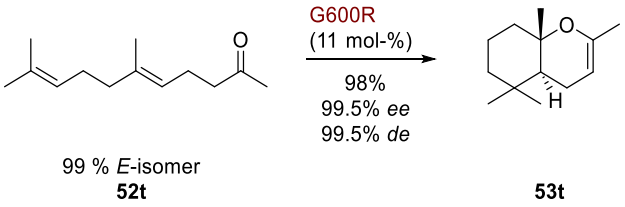

For the *E*-geranyl acetone **52t** biotransformation, 0.2 mL **52t** (0.92 mmol), 15 g_{CDW}/L cells (11 mol-% SHC) and 0.3 g/L SDS were mixed with 200 mL *dd*H_2O. The reaction was shaken at 30 °C for 168 h. The crude product mixture was extracted with diethyl ether (3x 200 mL) and centrifuged to separate the phases. The combined organic phases were dried over $MgSO_4$ and purified by flash chromatography (CH:EtOAc, 50:1) to yield chromene **53t** as a colorless oil (0.167 mL, 0.77 mmol, 85 %).

^{1}H-NMR ($CDCl_3$, 500 MHz): δ (ppm) 0.81 (s, 3H), 0.91 (s, 3H) 1.17 (s, 3H), 1.21-1.29 (m, 1H), 1.4-1.6 (m, 5H), 1.68 (s, 3H), 1.72-1.94 (m, 3H), 4.4-4.5 (m, 1H). **^{13}C-NMR ($CDCl_3$, 125 MHz):** δ (ppm) 19.07 (1C), 19.21 (1C), 19.82 (1C), 20.51 (1C), 20.77 (1C) 30.31 (1C), 32.25 (1C), 39.99 (1C), 41.65 (1C), 48. 37 (1C), 76.48 (1C), 94.97 (1C), 147.97 (1C). The data is consistent with the literature.[140]

6.6.2 Z-geranyl acetone 52c with G600R

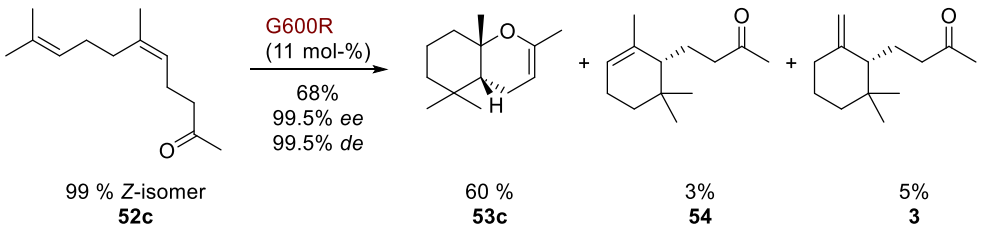

For the *Z*-geranyl acetone **52c** biotransformation, 0.2 mL **52c** (0.92 mmol), 15 g_{CDW}/L cells (11 mol-% SHC) and 0.3 g/L SDS were mixed with 200 mL *dd*H_2O. The reaction was shaken at 30 °C for 168 h. The crude product mixture was extracted with diethyl ether (3x200 mL) and centrifuged to separate the phases. The combined organic phases were dried over $MgSO_4$ and purified by flash chromatography (CH:EtOAc, 50:1) to yield chromene **53c** as a colorless oil (0.098 mL, 0.45 mmol, 49% yield).

^{1}H-NMR ($CDCl_3$, 500 MHz): δ (ppm) 0.85 (s, 3H), 0.87 (s, 3H) 1.16 (s, 3H), 1.32-1.39 (m, 1H), 1.54 (s, 3H), 1.6-1.66 (m, 3H), 1.68 (s, 3H), 1.72-1.97 (m, 3H), 2.14-2.27 (m, 1H), 4.4-4.5 (d, J = 2.6 Hz, 1H). **^{13}C-NMR ($CDCl_3$, 125 MHz)**: δ (ppm) 18.13 (1C), 19.79 (1C), 20.54 (1C), 21.19 (1C), 26.50 (1C) 32.46 (1C), 33.73 (1C), 39.66 (1C), 41.99 (1C), 44.00 (1C), 74.71 (1C), 94.56 (1C), 148.76 (1C).

6.6.3 *Z*-geranyl acetone 52c with V (A306V/Y420F/G600T/L607A)

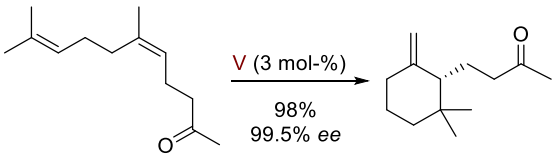

99 % *Z*-isomer
52c

3

For the *Z*-geranyl acetone biotransformation, 2.24 mL **52c** (10 mmol), 10 g_{CDW}/L cells (3 mol-% SHC), 0.2 g/L SDS and 14.6 g/L 2-HPCD (10.3 mmol) were mixed with 1L *dd*H_2O. The reaction was shaken at 30 °C for 648 h. The crude product mixture was extracted with diethyl ether (3x1 L) and centrifuged to separate the phases. The combined organic phases were dried over $MgSO_4$ and purified by flash chromatography (CH:EtOAc, 50:1) to yield **3** as a colorless oil (1.97 mL, 9.1 mmol, 89% yield).

^{1}H-NMR ($CDCl_3$, 500 MHz): δ (ppm) 0.87 (s, 3H), 0.92 (s, 3H) 1.10-1.30 (m, 2H), 1.42-1.62 (m, 2H), 1.66-1.70 (m, 1H), 1.76-1.83 (m, 1H), 1.97-2.04 (m, 2H), 2.11 (s, 3H), 2.22-2.45 (m, 2H), 4.50-4.51 (d, *J* = 1.03 Hz, 1H), 4.75-4.77 (m, 1H). **^{13}C-NMR ($CDCl_3$, 125 MHz):** δ (ppm) 20.31 (1C), 22.62 (1C), 23.52 (1C), 26.5 (1C), 28.3 (1C), 30.20 (1C), 32.00 (1C), 34.83 (1C), 42.38 (1C), 53.40 (1C), 109.5 (1C), 149.09 (1C), 209.52 (1C). The data is consistent with the literature.[144]

6.4.4 E/Z-geranyl isopropanol 58 with G600N/L607A

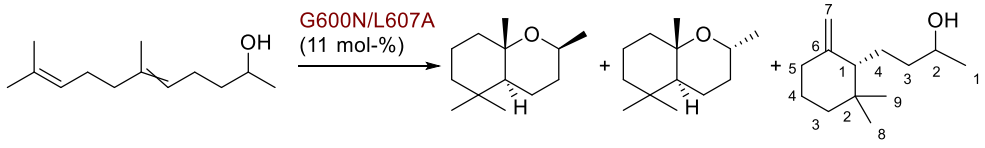

E:*Z*, 60:40
58

5.5%
97

5.4%
98

19%
59

For the *E*/*Z*-geranyl isopropanol **58** biotransformation, 0.2 mL **52c** (0.92 mmol), 15 g_{CDW}/L cells (11 mol-% SHC) and 0.3 g/L SDS were mixed with 200 mL *dd*H_2O. The reaction was shaken at 30 °C for 168 h. The crude product mixture was extracted with diethyl ether (3x200 mL) and centrifuged to separate the phases. The combined organic phases were dried over $MgSO_4$ and purified by flash chromatography (CH:EtOAc, 50:1) to yield a crude product mixture as a yellowish oil (0.020 mL, 0.09 mmol, 10 % yield).

^{1}H-NMR ($CDCl_3$, 500 MHz): δ (ppm) 2*S*,4*S*,8*S*-Tetrahydroedulane **97**: 0,81 (s, 3H), 0,89 (s, 3H), 1,14-1,15 (d, J = 3,1, 3H), 1,23 (s, 3H), 1,28 (s, 1H) 1,33 (s, 1H), 1,42-1,53 (m, 5H), 1,56 (s, 2H), 1,62-1,77 (m, 4H), 3,97-4,04 (m, 1H).
2*R*,4*S*,8*S*-Tetrahydroedulane **98**: 0,74 (s, 3H), 0,87 (s, 3H), 1,09-1,10 (d, J = 3,2, 3H), 1,23 (s, 3H), 1,28 (s, 1H) 1,33 (s, 1H), 1,42-1,53 (m, 5H), 1,56 (s, 2H), 1,62-1,77 (m, 4H), 3,72-3,79 (m, 1H). **^{13}C-NMR ($CDCl_3$, 125 MHz):** 2*R*,4*S*,8*S*-Tetrahydroedulane **98**: δ (ppm) 19.54 (1C), 19.59 (1C), 20.19 (1C), 20.78 (1C), 22.72 (1C), 32.11 (1C), 33.37 (1C), 35.61 (1C), 40.75 (1C), 41.67 (1C), 53.30 (1C), 65.51 (1C), 74.83 (1C). The data is consistent with the literature.[314]

4-(*R*-2,2-dimethyl-6-methylenecyclohexyl)butan-2-ol **59**: Characteristic methylene signals at **^{1}H-NMR ($CDCl_3$, 500 MHz)**: δ (ppm) 4.53 (d, *J* = 1.25 Hz, 1H) and 4.75 (t, *J* = 1.25 Hz, 1H). From the shape-complementary enantiopure monocyclization of **52c** and the observed depletion of mainly the *Z*-isomer of **58** it was assumed that the stereocenter here is *R*.

6.6.5 *E*/*Z*-calmusal 60 with G600T

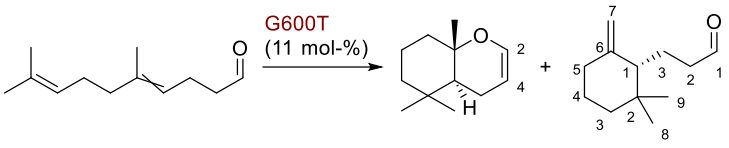

E:*Z*, 60:40 **60** | 40 % **99** | 16 % **61**

For the *E*/*Z*-calmusal **60** biotransformation, 0.2 mL **60** (0.98 mmol), 15 g_{CDW}/L cells (11 mol-% SHC) and 0.3 g/L SDS were mixed with 200 mL *dd*H_2O. The reaction was shaken at 30 °C for 168 h. The crude product mixture was extracted with diethyl ether (3x200 mL) and centrifuged to separate the phases. The combined organic phases were dried over $MgSO_4$ to yield a crude product mixture as a yellowish oil (0.078 mL, 0.39 mmol, 40 % yield).

Due to the instability of the products **99** and **61,** the products could not successfully be separated and therefore no yield could be determined. Nevertheless, the structures can be guessed from the crude NMR data: To obtain product **99** solely substrate **60** was converted with *Aac*SHC G600R, which favors bicyclization. Characteristic methyl- and dihydropyran-signals at **^{1}H-NMR ($CDCl_3$, 500 MHz)**: δ (ppm) 0.70 (s, 3H), 0.74 (s, 3H), 0.90 (s, 3H) and 6.81-6.84 (m, 1H) = C^2-H.

Product mixture **99** + **61** crude NMR data: Characteristic C7-methylene signals for **61** at **^{1}H-NMR ($CDCl_3$, 500 MHz)**: δ (ppm) 4.65 (*d*, *J* = 1.25 Hz, 1H) and 4.68 (*d*, *J* = 1.25 Hz, 1H). From the shape-complementary enantiopure monocyclization of **52c**, it was assumed that the stereocenter here is *R*. Characteristic C4-methylene signals for **99** at **^{1}H-NMR ($CDCl_3$, 500 MHz)**: δ (ppm) 4.66 (*d*, *J* = 1.10 Hz, 1H).

6.6.6 *E*/*Z*-calmusol 62 with G600T/L607A

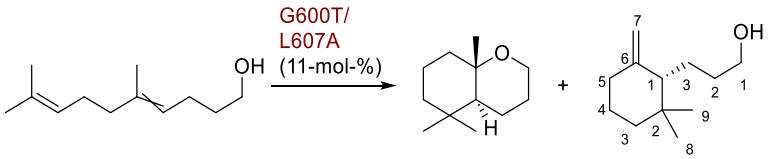

E:*Z*, 40:60 **62** | 3% **100** | 6% **63**

For the *E*/*Z*-calmusol **62** biotransformation, 0.2 mL **62** (0.98 mmol), 15 g_{CDW}/L cells (11 mol-% SHC) and 0.3 g/L SDS were mixed with 200 mL *dd*H_2O. The reaction was shaken

for at 30 °C 168 h. The crude product mixture was extracted with diethyl ether (3x200 mL) and centrifuged to separate the phases. The combined organic phases were dried over $MgSO_4$ and to yield a crude product mixture as a yellowish oil (0.01 mL, 0.05 mmol, 5 % yield).

Characteristic C7-methylene signals for **63** at **^{1}H-NMR ($CDCl_3$, 500 MHz)**: δ (ppm) 4.55 (*d*, *J* = 1.00 Hz, 1H) and 4.75 (*t*, *J* = 1.30 Hz, 1H). From the shape-complementary enantiopure monocyclization of **52c,** it was assumed that the stereocenter here is *R*.

6.6.7 *E,E*-homofarnesol 66 with B (M132R/A224G/I432T) and P3 (W169G/G600M/M132R/I432T)

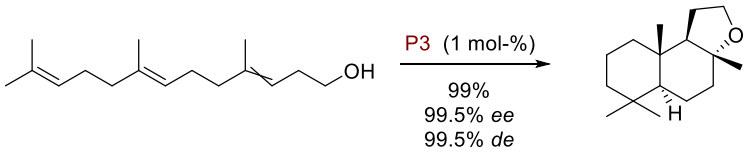

95 % *E,E*-isomer
66

7

In order to demonstrate the different state of aggregation (owing to liquid side products) of the product **7** after full conversion the optimal conditions from the Benchmark study[129] were chosen. Therefore, in a 10 mL reaction vessel, 500 µl (445 mg, 1.89 mmol, 90 g/L) **2**, 180 g_{CWW} /L cells (containing either the Benchmark cyclase B or the final variant P3) were mixed in the reaction buffer (100 mM citric acid, 0.048 c_{SDS}:c_{cells}, pH=5.1) and the suspension was shaken for 4 d at 37 °C at 800 rpm. The reaction mixture was extracted three times with toluene:heptane (1:1), dried over $MgSO_4$ overnight, filtrated and evaporated to yield 440 mg (B) and 437 mg (P3) crude **1** (98.9 % and 98.2 %), respectively. For the Benchmark variant (95 % ((–)-ambroxide **7** selectivity) the crude product was a blurry liquid. Variant P3 ((99 % ((–)-ambroxide **7** selectivity) yielded a solid product (Figure 3-7).

^{1}H-NMR ($CDCl_3$, 500 MHz): δ (ppm) 0.83 (s, 3H), 0.84 (s, 3H), 0.87 (s, 3H), 0.93-0.98 (*dd*, J = 6 Hz, J = 0.7 Hz, 1H), 1.0-1.07 (*td*, J = 13 Hz (t), J = 2 Hz (d), 1H), 1.1 (s, 3H), 1.14-1.22 (*td*, J = 13 Hz (t), J = 2 Hz (d), 1H), 1.24-1.34 (*qd*, J = 20.75 Hz (q), J = 1.5 Hz (d), 1H), 1.36-1.49 (m, 5H), 1.61-1.77 (m, 4H), 1.9-1.91 (*dt,* J = 6Hz (d), J = 3Hz (t), 1H), 3.82 (*d*, J= 12Hz, 1H), 3.91 (m, 1H). **^{13}C-NMR ($CDCl_3$, 125 MHz):** δ (ppm) 15.05 (1C), 18.42 (1C), 20.66

(1C), 21.15 (1C), 22.65 (1C), 33.08 (1C), 33.60 (1C), 36.21 (1C), 39.76 (1C), 39.97 (1C), 42.45 (1C), 57.27 (1C), 60.14 (1C), 64.99 (1C), 79.92 (1C). The data is consistent with the literature.[129]

6.6.8 *E*-geranyl acetate 34 with G600R

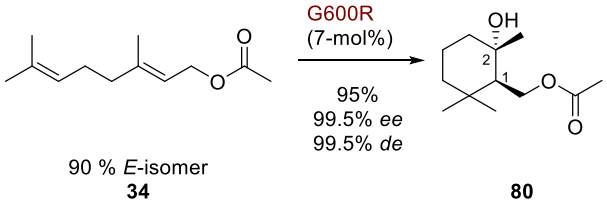

For the *E*-geranyl acetate **34** biotransformation, 0.22 mL **34** (0.97 mmol), 20 g_{CDW}/L cells (7 mol-% SHC) and 14 g/L 2-HPCD were mixed with 100 mL *dd*H_2O. The reaction was shaken at 30 °C for 1176 h. The crude product mixture was extracted with isooctane (3 x 100 mL) and EtOAc (3 x 100 mL) and centrifuged to separate the phases. The combined organic phases were dried over $MgSO_4$ and purified by flash chromatography (CH:EtOAc, 50:1) to yield 1*R*,2*S*-cyclogeranyl acetate hydrate **80** as a yellowish oil (0.136 g, 0.64 mmol, 71% yield).

^{1}H-NMR ($CDCl_3$, 500 MHz): δ (ppm) 0.86 (s, 3H), 1.01 (s, 3H), 1.21 (s, 3H), 1.26-1.32 (m, 3H), 1.33-1.40 (m, 3H), 1.59-1.63 (t, J = 6 Hz , 1H), 2.06 (s, 3H), 4.32-4.33 (d, J = 2.9 Hz, 1H). **^{13}C-NMR ($CDCl_3$, 125 MHz):** δ (ppm) 13.17 (1C), 19.02 (1C), 20.03(1C), 25.89 (1C), 33.12 (1C), 40.78 (1C), 41.37 (1C), 53.78 (1C), 62.51 (1C), 71.70 (1C), 169.98 (1C).

6.6.9 *E,E*-farnesol 81 with A306W

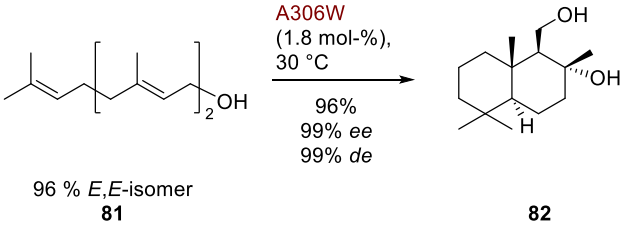

For the *E,E*-farnesol **81** biotransformation, 0.49 mL **81** (1.9 mmol), 10 g_{CDW}/L cells (1.8 mol-% SHC) were mixed with 100 mL *dd*H_2O. The reaction was shaken at 30 °C for 72 h. The crude product mixture was extracted with isooctane (3 x 100 mL) and EtOAc (3 x 100 mL) and centrifuged to separate the phases. The combined organic phases were

dried over $MgSO_4$ and purified by flash chromatography (CH:EtOAc, 50:1) to yield drimenol hydrate **82** as a white crystalline solid (0.38 g, 1.56 mmol, 88% yield).

^{1}H-NMR (CDCl$_3$, 500 MHz): δ (ppm) 0.79 (s, 6H), 0.88 (s, 3H), 0.95-0.98 (dd, *J*=6.1 Hz, 1H), 1.07-1.29 (m, 4H), 1.35 (s, 3H), 1.42-1.57 (m, 4H), 1.63.1.67 (m, 1H), 1.87-1.90 (tt, *J*=6.1 Hz, 1H), 3.91-3.93 (m, 1H). **^{13}C-NMR (CDCl$_3$, 125 MHz):** δ (ppm) 16.05 (1C), 18.61 (1C), 20.19 (1C), 21.62 (1C), 24.30 (1C), 33.28 (1C), 33.56 (1C), 37.53 (1C), 39.99 (1C), 41.69 (1C), 44.51 (1C), 55.92 (1C), 60.52 (1C), 61.15 (1C), 75.14 (1C). The data is consistent with the literature.[315]

6.6.10 *E,E,E*-geranyl geraniol 73 with F605W

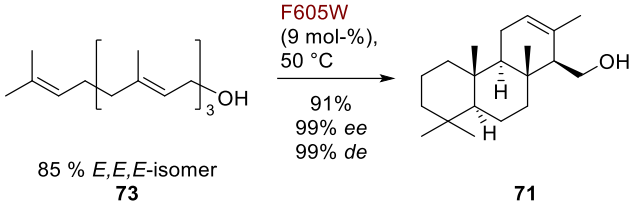

For the *E,E,E*-geranyl geraniol **73** biotransformation, 0.25 mL **73** (0.75 mmol), 20 g_{CDW}/L cells (9.3 mol-% SHC) and 10 g/L 2-HPCD were mixed with 100 mL *dd*H_2O. The reaction was shaken at 50 °C for 192 h. The crude product mixture was extracted with isooctane (3 x 100 mL) and EtOAc (3 x 100 mL) and centrifuged to separate the phases. The combined organic phases were dried over $MgSO_4$ and purified by flash chromatography (CH:EtOAc, 50:1) to yield *ent*-isocopalol **71** as a yellowish solid (0.196 g, 0.68 mmol, 90% yield).

^{1}H-NMR (CDCl$_3$, 500 MHz): δ (ppm) 0.81 (s, 3H), 0.83 (s, 3H), 0.86 (s, 3H), 0.88 (s, 3H), 1.1-1.4(m, 9H), 1.78 (m, 3H), 1.84-2.07 (m, 5H), 3.71-3.74 (dd, *J* = 6.3 Hz, 1H), 3.84-3.87 (dd, *J*= 6.3 Hz, 1H), 5.5-5.51 (m, 1H). **^{13}C-NMR (CDCl$_3$, 125 MHz):** δ (ppm) 15.83 (1C), 15.84 (1C), 18.52 (1C), 18.75 (1C), 21.68 (1C), 21.81 (1C), 22.55 (1C), 33.14 (1C), 33.40 (1C), 36.24 (1C), 37.24 (1C), 39.93 (1C), 41.54 (1C), 41.91 (1C), 54.84 (1C), 56.25 (1C), 57.89 (1C), 60.89 (1C), 123.95 (1C), 132.65 (1C). The data is consistent with the literature.[97]

6.6.11 *E,E,E*-geranyl geraniol 73 with G600N

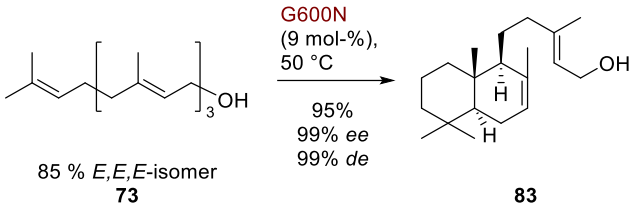

For the *E,E,E*-geranyl geraniol **73** biotransformation, 0.25 mL **73** (0.75 mmol), 20 g_{CDW}/L cells (9.3 mol-% SHC) and 10 g/L 2-HPCD were mixed with 100 mL *dd*H_2O. The reaction was shaken at 50 °C for 840 h. The crude product mixture was extracted with isooctane (3 x 100 mL) and ethyl aetate (3 x 100 mL) and centrifuged to separate the phases. The combined organic phases were dried over $MgSO_4$ and purified by flash chromatography (CH:EtOAc, 50:1) to yield labdane **83** as a colorless oil (0.17 g, 0.58 mmol, 78% yield).

^{1}H-NMR (CDCl$_3$, 500 MHz): δ (ppm) 0.76 (s, 3H), 0.82 (s, 3H), 0.84 (s, 3H), 0.80–1.09 (m, 2H), 1.56 (s, 3H), 1.69 (s, 3H), 1.02–2.01 (m, 12H), 2.13–2.31 (m, 1H), 4.09–4.20 (m, 2H), 5.10-5.13 (m, 1H), 5.40–5.43 (t, *J* = 7 .2 Hz, 1H). **^{13}C-NMR (CDCl$_3$, 125 MHz):** δ (ppm) 12.5 (1C), 15.9 (1C), 17.7 (1C), 20.1 (1C), 22.2 (1C), 23.7 (1C), 25.3 (1C), 30.9 (1C), 33.9 (1C), 37 (1C), 39.1 (1C), 42.0 (1C), 42.3 (1C), 50.1 (1C), 53.4 (1C), 59.4 (1C), 120.2 (1C), 121.3 (1C), 135.2 (1C), 141.4 (1C). The data is consistent with the literature.[266]

6.6.12 *E,E*-keto ester 77 with F601D/F605L

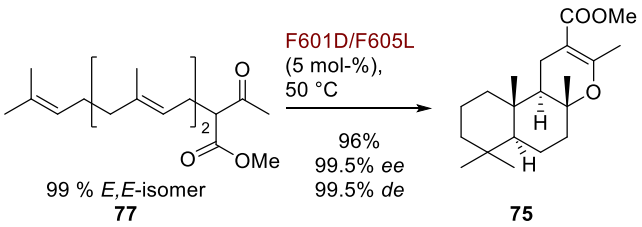

For the *E,E*-keto ester **77** biotransformation, 0.25 mL **77** (0.67 mmol), 10 g_{CDW}/L cells (5.2 mol-% SHC) and 10 g/L 2-HPCD were mixed with 100 mL *dd*H_2O. The reaction was shaken at 50 °C for 120 h. The crude product mixture was extracted with isooctane (3 x 100 mL) and EtOAc (3 x 100 mL) and centrifuged to separate the phases. The combined organic phases were dried over $MgSO_4$ and purified by flash chromatography (CH:EtOAc, 50:1) to yield acetate **75** as a white solid (0.19 g, 0.58 mmol, 88% yield).

^{1}H-NMR ($CDCl_3$, 500 MHz): δ (ppm) 0.82 (s, 3H), 0.88 (s, 3H), 0.91-0.98 (m, 2H), 1.13 (s,3H), 11.4-1.18 (m, 1H), 1.25-139 (m, 4H), 1.44-1.47 (m, 1H), 1.52-1.55 (m, 1H), 1.57-1.63 (m,1H), 1.68-174 (m, 2H), 2.19 (s, 3H), 2.26-2.32 (dd, *J* = 7.1 Hz, 1H), 3.69 (s, 3H). **^{13}C-NMR ($CDCl_3$, 125 MHz):** δ (ppm) 14.89 (1C), 18.48 (1C), 19.43 (1C), 19.64 (1C), 20.38 (1C), 20.58 (1C), 21.54 (1C), 33.17 (1C), 33.42 (1C), 36.75 (1C), 39.21 (1C), 40.60 (1C), 41.85 (1C), 50.87 (1C), 51.62 (1C), 56.09 (1C), 78.35 (1C), 99.96 (1C), 163.14 (1C), 169.29 (1C).

6.7 General methods

6.7.1 Analytical biotransformations in GC screw-cap-vials

Harvested or lyophilized cell pellets were resuspended in whole cell buffer. For harvested cells the OD_{600} was set to the given value and for lyophilized cells 10 mg cells per mL buffer were weighed in. 495 µL of the cell suspension were transferred to GC screw-cap-vials and 5 µL of a substrate/DMSO stock ($c_{end,\ substrate}$ = 2 mM) were added to start the reactions. Reactions were shaken at the respective temperature for 20 h. Reactions were stopped by adding 600 µL CH:EtOAc (1:1) and vortexing for 2 min. After centrifugation (4000 rpm, 5 min) the organic phase was analyzed via GC/MS/PAL-Sampler directly from the two-phase system. Quantification was made directly from the total ion count chromatogram by quotient $AREA_{product}$/ ($AREA_{substrate}$+$AREA_{product}$)*100.

6.7.2 Screening of SHC libraries using GC/MS

Harvested cell pellets from the 96-DW plate expression were resuspended in 396 µL whole cell buffer and transferred to another 96-DW plate equipped with 1.2 mL glass inlets. Then 4 µL substrate/DMSO stock solution ($c_{end,\ substrate}$ = 2 mM) was added directly into the cell suspension, the plates were sealed with PP-lids and shaken at the respective temperature at 600 rpm for 20 h. To stop the reaction 600 µL CH/o-xylene (1:1) was added and the mixture was inverted and vortexed for 10 min and incubated for another 30 min. The plates were centrifuged (4000 rpm, 5 min), sealed using PP-lids and a GC-MS equipped with a PAL-Sampler was used to inject directly from the organic phase. Quantification was made directly from the Total Ion Count chromatogramm by quotient $AREA_{product}$/ ($AREA_{substrate}$+$AREA_{product}$)*100. In total 90 new variants (3 x parent, 1 x *Aac*SHC WT, 1x negative control, 1x buffer control) per 96-DW plate were screened. Promising variants were rescreened by expression in 24 DW-plates.

6.7.3 Verification of promising hits

Promising candidates from the 96-DW screening were taken for inoculation of a new 5 mL LB pre-culture and subsequent expression in 24-DW plates (cf. chapter 6.3.1). After harvesting of the cells, the OD_{600} was set to 20 in whole cell buffer and substrate (c_{end} = 2mM) was added. The reactions were carried out at least in technical triplicates. Reactions were stopped by organic solvent. After two extractions with the respective organic solvent, the resulting organic phase was analyzed via GC-MS. Quantification was made directly from the Total Ion Count chromatogramm by quotient $AREA_{product}$/ ($AREA_{substrate}$+$AREA_{product}$)*100.

6.7.4 Determination of Total turnover number (TTN) and Turnover frequency (TOF) *in vivo* and *in vitro*

To determine the TTN of the *in vivo* biotransformation it deserves the absolute enzyme concentration per gram cell and the exact product concentration. Therefore, each SHC variant selected for TTN determination was expressed and lyophilized in *E. coli*. The SHC content of 10 mg_{CDW} cells was determined using the Thermolysis purification method (cf. chapter 6.3.2). Quality control of the purification was done by SDS-PAGE (cf. chapter 6.3.3). For the reaction setup in 2 mL GC vials, 10 mg of the *E. coli* whole cells from the same batch as used for Thermolysis purification were resuspended in 1 mL cyclodextrin buffer, the respective substrate was added to the suspension and the reaction was shaken at the respective temperature for the respective time. The reaction was stopped by adding 1 mL EtOAc:CH (1:1). The reaction was extracted three times and the combined organic phases were analyzed via GC/MS. For quantification, standard curves were prepared if the products were available. Error bars represent the standard deviation of technical triplicates.

Otherwise, 1 mM dodecane was added as an external standard and the product concentration was determined via the effective carbon number method.[316] The TTNs of the preparative scale reactions (cf. chapter 6.6) were determined from the isolated yield. The determination of the TTN *in vitro* was done directly after the Thermolysis protocol (only 1 d of enzyme extraction). The solubilized enzyme was diluted 5:1 with *dd*H_2O ($c_{end,citric\ acid}$ = 20 mM, $c_{end,\ CHAPS}$ = 0.2%, pH = 6.0) and 1 mL of the enzyme preparation was used for the biotransformation. The reactions were carried out, extracted, and

analyzed analogously to the *in vivo* approach. The TOF of the respective enzymes were determined by forming the quotient TTN/time in h.

6.7.5 *E,E*-Homofarnesol 66 excess addition experiments

The excess addition experiment in Supporting Figure S 10A+B were carried out to evaluate the performance of a highly selective SHC variant P1 (99% (–)-ambroxide **7** selectivity, W169G) and a more unselective variant B (95%) at more industrially relevant substrate concentrations (20-50 mM). First, the cyclization of 20 mM **66** was monitored over the period of 68 h using 0.1 g_{CDW}/L cells harboring P1 in *dd*H_2O. Four independent reactions were run at 30 °C and stopped by extracting twice with toluene:heptane (1:1) after 0.1, 20, 44, 68 h. To circumvent the inhibition effect, the cell concentration was raised to 5 g_{CDW}/L, and substrate concentration was kept at 20 mM. Eight independent reactions (triplicates) were run at 30 °C and stopped by extracting twice with toluene:heptane (1:1) after 0.1, 1, 2, 4, 20 and 24, 44 and 68 h. The *in vivo* performance was compared with the benchmark enzyme B. The final setup was performed using 30 g_{CDW}/L cells and 200 mM substrate. Reaction control was done by taking 0.1 µL samples from the organic substrate **66** layer on top the reaction mixture after 0, 20, 44, 68, 92, 264, 236, 432 and 1004 h. The *in vivo* performance was compared with the benchmark enzyme B.

6.7.6 Kinetic characterization of variants WT, B, P1, P2 and P3 during cyclization of 66

The characterization *in vivo* as well as *in vitro* were carried at 0.1 g_{CDW}/L cells and the respective extracted and solubilized enzyme content. To compare the **v**ariant**s *in vivo***, the SHC content of 10 mg_{CDW} of each batch was determined by Thermolysis protocol. Afterwards, 10 mg_{CDW} were resuspended in 100 mL *dd*H_2O and 495 µL of the cell suspension (triplicates per substrate concentration) were transformed into each well of a 96DW-plate. The reaction was started by adding 5 µL of **66** in DMSO ($c_{66,final}$ = 0.2 mM-20 mM) and was shaken at 30 °C and 800 rpm. Reactions were stopped after 1 h by adding 500 µL heptane:toluene (1:1), vortexing for 5 min and incubating for 30 min. 96DW-plates were centrifuged afterwards and conversions were analyzed directly from the organic phase using a GC equipped with a PAL-Sampler.

To compare the **v**ariant**s *in vitro***,** the enzymes were extracted, solubilized and diluted with buffer (20 mM citric acid, 0.2% CHAPS, pH = 6.0) to the final enzyme concentrations of *Aac*WT = 0.02 mg/ mL (0.28 µM), Benchmark = 0.016 mg/ mL (0.22 µM), P2 = 0.025 mg/ mL (0.35 µM) and P3 = 0.015 mg/ mL (0.21 µM). Afterwards 495 µL of the enzyme solution (triplicates per substrate concentration) was transferred into each well of a 96 DW-plate. The reaction was started by adding 5 µL of **66** in DMSO ($c_{66,final}$ = 0.2 mM - 20 mM) and was shaken at 50 °C at 800 rpm. Reactions were stopped after 1 h by adding 500 µL heptane:toluene (1:1), vortexing for 5 min and incubate for 30 min. 96 DW-plates were centrifuged afterwards and reaction progress was analyzed directly from the organic phase using a GC equipped with a CTC PAL-Sampler. The kinetics were fitted as initial rate $(v_{max}*c_{substrate})/(K_M+c_{substrate})$ or substrate-excess inhibition plots $(v_{max}/(1+(K_M/c_{substrate})+(c_{substrate}/K_M)$ with the assumption of $K_I=K_M$ using Excel solver.

6.7.7 Feeding strategy for keeping up the enzymatic activity of P3 in the *E. coli* host

The feeding experiments were carried out in 100 mL Schott-flasks, which were shaken at 30 °C for *in vivo* and 50 °C for *in vitro* at 300 rpm on the same plate shaker used in the kinetic studies. The *in vivo* and *in vitro* performances of P3 were compared using 0.1 g_{CDW}/L cells or 0.015 mg/mL extracted and solubilized (20 mM citric acid, 0.2% CHAPS, pH= 6.0) enzyme. The *in vivo* reactions were prepared by resuspending 10 mg_{CDW} whole cells in 100 mL *dd*H_2O. Reactions were started by adding 200 µL **66** onto the surface of the enzyme preparations. Depletion of the organic substrate phase was observed only in the reaction using *E. coli* whole cells. During the reaction the desired product **7** precipitated as white crystalline solid from the reaction broth. After the reaction was finished (t = 36 d) the reaction mixture was extracted with toluene (5 x 100 mL) centrifuged (4000 rpm, 10 min) and the combined organic phases were dried over Na_2SO_4. After concentrating the organic phase, the crude product was purified over silica (20:1, diethyl ether: hexane) to give 982 mg (4.16 mmol) of white crystalline (–)-ambroxide **7**. The *in vivo* reaction was repeated two times and yielded 946 mg in 34 days and 913 mg in 38 d, respectively.

6.7.8 Two-phase system evaluation for 52t biotransformation

A two-phase system was employed to implement *in situ* product removal of organic molecules into the biocatalytic system. The two-phase experiment was carried out in GC-screw-cap vials according to the analytical biotransformation protocol (cf. chapter 6.7.1) with variant G600R. After addition of 10 mM geranyl acetone **52t**, the reactions were overlayed with 100 µL of different organic solvents (cf. **Table 6-7**) varying in their logP-values. The biphasic reactions were shaken slowly (300 rpm) at 30 °C to avoid mixing of the phases. After 20 h, the reactions were stopped by adding 400 µL CH/EtOAC (1:1). After extraction and centrifugation, the organic phases were analyzed via GC/MS. Quantification was done by substrate and product standard curves, respectively.

Table 6-7: Organic solvents used in the two-phase experiment and the corresponding logP-values calculated by ChemDraw.[317]

Organic solvent	logP
Methylpropyl ether	0.9
Cyclooctanol	2.1
2-hexanol	1.7
Cyclohexylmethylether	1.7
Petroleum ether	3.5
Decane	6.0
1-Decanol	3.5
1-Nonanol	3.1
1-Octanol	2.9
Undecane	6.6
Dodecane	7.1
Tetradecane	8.1
1-Undecanol	3.9
Hexandecane	8.8
Diethyl phtalate	2.0

6.7.9 End-point determination of *in vivo* cell specific activity in the biotransformation of excess 52t and 66 with additives

To demonstrate the decreasing cell specific activity of *E. coli* over time, analytical biotransformations of **52t** with homologous SHCs (alternative organisms) were performed. 50 mM substrate **52t** was added to 10 mg_{CDW}/mL in 1 mL *dd*H_2O in four independent reactions, which were shaken at 30 °C. Each reaction was performed in triplicates. The four reactions were stopped after 20, 40, 60 and 80 h by adding 1 mL CH:EtOAc (1:1). The 80 h reaction was supplemented with 100 µL of a 500 mM 2HPCD stock (c_{end}= 45 mM) after 60 h. After extraction and centrifugation, the organic phases were analyzed via GC/MS. Quantification was done by substrate and product standard curves, respectively. Cell specific activities were calculated as: $(c_{product}/t)/g_{CDW}$. For the cell specific activity after 80 h, only the "regenerated" cell specific activity was considered. That means the product formation after 60 h was subtracted from the product formation after 80 h. The resulting $\Delta c_{product}$ was then divided by 20 h to determine the regenerated cell specific activity. 1 U = 1 µmol*min.

6.8 Computational methods

Docking studies were performed using YASARA,[145] which uses Autodock and VINA algorithms for the calculation of defined ligand-receptor interaction. *In silico* mutations were introduced by changing the specific amino acid in the sequence based on the *Aac*SHC WT (PDB: 1UMP), which homology structure was modeled by Swiss-Model.[181] The resulting binding energies of 25 runs were clustered. The most likely structures (=highest binding energies) were always chosen for visualization. Homology models of SHC homologs were produced using RoseTTaFold.[318] Enzyme tunnel analysis was performed using the CAVER web-tool[319] and the *Aac*SHC WT crystal structure as a template (PDB: 1UMP).

REFERENCES

1. Buckingham, J., Cooper, C. M. & Purchase, R. *Natural Products Desk Reference* . (2015).

2. Zeng, T. *et al.* TeroKit: A Database-Driven Web Server for Terpenome Research. *J. Chem. Inf. Model.* **60**, 2082–2090 (2020).

3. Burlingame, A. L., Haug, P., Belsky, T. & Calvin, M. Occurrence of Biogenic Steranes and Pentacyclic Triterpanes in an Eocene Shale (52 Million Years) and in an Early Precambrian Shale (2.7 Billion Years): a Preliminary Report. *Proc. Natl. Acad. Sci.* **54**, 1406–1412 (1965).

4. Hodge, R. *The Molecules of Life: DNA, RNA and Proteins*. *Genetics & Evolution* (2009).

5. Hillier, S. G. & Lathe, R. Terpenes, hormones and life: Isoprene rule revisited. *J. Endocrinol.* **242**, R9–R22 (2019).

6. Singh, P., Saxena, R., Srinivas, G., Pande, G. & Chattopadhyay, A. Cholesterol Biosynthesis and Homeostasis in Regulation of the Cell Cycle. *PLoS One* **8**, e58833 (2013).

7. Hu, J., Zhang, Z., Shen, W. J. & Azhar, S. Cellular cholesterol delivery, intracellular processing and utilization for biosynthesis of steroid hormones. *Nutr. Metab. 2010 71* **7**, 1–25 (2010).

8. Cáceres, L. A. *et al.* Repellent and Attractive Effects of α-, β-, and Dihydro-β- Ionone to Generalist and Specialist Herbivores. *J. Chem. Ecol.* **42**, 107–117 (2016).

9. Silva, A. C. R. da *et al.* Biological Activities of a-Pinene and β-Pinene Enantiomers. *Molecules* **17**, 6305–6316 (2012).

10. Mirov, N. T. Composition of Gum Turpentine of Coulter Pine. *Ind. Eng. Chem.* **38**, 405–408 (1946).

11. Dickschat, J. S., Brock, N. L., Citron, C. A. & Tudzynski, B. Biosynthesis of Sesquiterpenes by the Fungus Fusarium verticillioides. *ChemBioChem* **12**, 2088–2095 (2011).

12. Jo¨rg Bohlmann, J., Crock, J., Jetter, R. & Croteau, R. Terpenoid-based defenses in conifers: cDNA cloning, characterization, and functional expression of wound-inducible (E)-bisabolene synthase from grand fir (Abies grandis) [sesquiterpene synthasejuvenile hormone analogueplant defense gene(E)-4-(1,5-dimethyl-1,4-hexadienyl)-1-methylcyclohexenetodomatuic acid]. **95**, 6756–6761 (1998).

13. Brézot, P., Malosse, C., Mori, K. & Renou, M. Bisabolene epoxides in sex pheromone innezara viridula (L.) (Heteroptera: Pentatomidae): Role ofcis isomer and relation to specificity of pheromone. *J. Chem. Ecol. 1994 2012* **20**, 3133–3147 (1994).

14. Gordaliza, M. Cytotoxic terpene quinones from marine sponges. *Mar. Drugs* **8**, 2849–2870 (2010).

15. Gelmont, D., Stein, R. A. & Mead, J. F. Isoprene — The main hydrocarbon in human breath. *Biochem. Biophys. Res. Commun.* **99**, 1456–1460 (1981).

16. Breitmaier, E. *Terpenes. Flavors, Pharmaca, Pheromones* (2006).

17. Rowland, S. J., Sutton, P. A. & Knowles, T. D. J. The age of ambergris. *Nat. Prod. Res.* **33**, 3134–3142 (2019).

18. Armanino, N. *et al.* What's Hot, What's Not: The Trends of the Past 20 Years in the Chemistry of Odorants. *Angew. Chemie - Int. Ed.* **59**, 16310–16344 (2020).

19. Lange, B. M. Biosynthesis and biotechnology of high-value P-menthane monoterpenes, including menthol, carvone, and limonene. *Adv. Biochem. Eng. Biotechnol.* **148**, 319–353 (2015).

20. Cataldo, V. F., López, J., Cárcamo, M. & Agosin, E. Chemical vs. biotechnological synthesis of C13-apocarotenoids: current methods, applications and perspectives. *Appl. Microbiol. Biotechnol.* **100**, 5703–5718 (2016).

21. Schwab, W., Fuchs, C. & Huang, F. C. Transformation of terpenes into fine chemicals. *Eur. J. Lipid Sci. Technol.* **115**, 3–8 (2013).

22. Zhang, L. & Demain, A. L. *Natural products: Drug discovery and therapeutic medicine*. (2005).

23. Malaria. https://www.who.int/news-room/fact-sheets/detail/malaria. 06.05.2022

24. White, N. J. Qinghaosu (artemisinin): The price of success. *Science* **320**, 330–334 (2008).

25. Sunazuka, T. & Omura, S. Total synthesis of α-pyrone meroterpenoids, novel bioactive microbial metabolites. *Chemical Reviews* vol. 105 4559–4580 (2005).

26. Talele, T. T. Opportunities for Tapping into Three-Dimensional Chemical Space through a Quaternary Carbon. *J. Med. Chem.* **63**, 13291–13315 (2020).

27. Christmann, M. Otto Wallach: Founder of Terpene Chemistry and Nobel Laureate 1910. *Angew. Chemie Int. Ed.* **49**, 9580–9586 (2010).

28. Ruzicka, L. The isoprene rule and the biogenesis of terpenic compounds. *Exp. 1953 910* **9**, 357–367 (1953).

29. Stephanopoulos, G., King, J. R., Edgar, S. & Qiao, K. Accessing Nature's diversity through metabolic engineering and synthetic biology. *F1000Research* **5**, 1–11 (2016).

30. Jones, S. B., Simmons, B., Mastracchio, A. & MacMillan, D. W. C. Collective synthesis of natural products by means of organocascade catalysis. *Nature* **475**, 183–188 (2011).

31. Castillo, A., Silva, L., Briones, D., Quílez Del Moral, J. F. & Barrero, A. F. Collective Synthesis of Natural Products Sharing the Dihydro-γ-Ionone Core. *European J. Org. Chem.* **2015**, 3266–3273 (2015).

32. Zhang, X. *et al.* Divergent synthesis of complex diterpenes through a hybrid oxidative approach. *Science* **369**, 799–806 (2020).

33. Dixon, D. D., Lockner, J. W., Zhou, Q. & Baran, P. S. Scalable, divergent synthesis of meroterpenoids via 'borono- sclareolide'. *J. Am. Chem. Soc.* **134**, 8432–8435 (2012).

34. Croteau, R., Ketchum, R. E. B., Long, R. M., Kaspera, R. & Wildung, M. R. Taxol biosynthesis and molecular genetics. *Phytochemistry Reviews* vol. 5 75–97 (2006).

35. R., J. Modern organic chemistry. *Nature* **121**, 857–858 (1928).

36. Nicolaou, K. C., Vourloumis, D., Winssinger, N. & Baran, P. S. The Art and Science of Total Synthesis at the Dawn of the Twenty-First Century. *Angew. Chemie Int. Ed.* **39**, 44–122 (2000).

37. Maimone, T. J. & Baran, P. S. Modern synthetic efforts toward biologically active terpenes. *Nat. Chem. Biol.* **3**, 396–407 (2007).

38. Corey, E. J. & Pearce, H. L. Total Synthesis of Picrotoxinin. *J. Am. Chem. Soc.* **101**, 5841–4843 (1979).

39. Nicolaou, K. C. *et al.* Total Synthesis of Eleutherobin. *Angew. Chemie - Int. Ed.* **36**, 2520–2524 (1997).

40. Chen, X. T. *et al.* The total synthesis of eleutherobin. *J. Am. Chem. Soc.* **121**, 6563–6579 (1999).

41. Wender, P. A. *et al.* The pinene path to taxanes. 6. A concise stereocontrolled synthesis of taxol. *J. Am. Chem. Soc.* **119**, 2757–2758 (1997).

42. Wender, P. A. *et al.* The Pinene Path to Taxanes. 5. Stereocontrolled Synthesis of a Versatile Taxane Precursor. *J. Am. Chem. Soc.* **119**, 2755–2756 (1997).

43. Wang, G., Tang, W. & Bidigare, R. R. *Terpenoids As Therapeutic Drugs and Pharmaceutical Agents. Zhang L., Demain A.L. (eds) Natural Products* (Humana Press Inc., 2005).

44. Hu, P. *et al.* Quaternary-centre-guided synthesis of complex polycyclic terpenes. *Nature* **569**, 703–707 (2019).

45. Chen, K. & Baran, P. S. Total synthesis of eudesmane terpenes by site-selective C-H oxidations. *Nature* **459**, 824–828 (2009).

46. Kanda, Y. *et al.* Two-Phase Synthesis of Taxol. *J. Am. Chem. Soc.* **142**, 10526–10533 (2020).

47. Jørgensen, L. *et al.* 14-Step synthesis of (+)-ingenol from (+)-3-carene. *Science* **341**, 878–882 (2013).

48. Schneider, F., Samarin, K., Zanella, S. & Gaich, T. Total synthesis of the complex taxane diterpene canataxpropellane. *Science* **367**, 676–681 (2020).

49. Gomollon.Bel, F. Chemists complete synthesis of molecule 'at the limits of complexity'. *Chemistry world* https://www.chemistryworld.com/news/chemists-complete-synthesis-of-molecule-at-the-limits-of-complexity/4011165.article (2020). 06.05.2022.

50. Twilfer, H. *et al.* Charge as a Key Component in Reaction Design. The Invention of Cationic Cyclization Reactions of Importance in Synthesis. *J. Biochim. Biophys. Acta* **25**, 1559 (1992).

51. Feng, Z. & Tantillo, D. J. Dynamic Effects on Migratory Aptitudes in Carbocation Reactions. *J. Am. Chem. Soc.* **143**, 1088–1097 (2021).

52. Hong, Y. J. & Tantillo, D. J. A potential energy surface bifurcation in terpene biosynthesis. *Nat. Chem.* **1**, 384–389 (2009).

53. Tantillo, D. J. Importance of Inherent Substrate Reactivity in Enzyme-Promoted Carbocation Cyclization/Rearrangements. *Angew. Chemie - Int. Ed.* **56**, 10040–10045 (2017).

54. Little, D. B. & Croteau, R. B. Alteration of product formation by directed mutagenesis and truncation of the multiple-product sesquiterpene synthases δ-selinene synthase and γ-humulene synthase. *Arch. Biochem. Biophys.* **402**, 120–135 (2002).

55. Yoshikuni, Y., Ferrin, T. E. & Keasling, J. D. Designed divergent evolution of enzyme function. *Nature* **440**, 1078–1082 (2006).

56. Chappell, J. BIOCHEMISTRY AND MOLECULAR BIOLOGY OF THE ISOPRENOID BIOSYNTHETIC PATHWAY IN PLANTS. *Annu. Rev. Plant Physiol. Plant Mol. Bioi* **46**, 521–568 (1995).

57. Whittington, D. A. *et al.* Bornyl diphosphate synthase: Structure and strategy for carbocation manipulation by a terpenoid cyclase. *Proc. Natl. Acad. Sci. U. S. A.* **99**, 15375–15380 (2002).

58. Greenhagen, B. & Chappell, J. Molecular scaffolds for chemical wizardry: Learning nature's rules for terpene cyclases. *Proc. Natl. Acad. Sci. U. S. A.* **98**, 13479–13481 (2001).

59. Cao, R. *et al.* Diterpene cyclases and the nature of the isoprene fold. *Proteins Struct. Funct. Bioinforma.* **78**, 2417–2432 (2010).

60. Chen, M. Terpene Synthases : One Fold , Many Products Terpene Synthases : One Fold , Many Products. 180 (2016).

61. Baer, P. *et al.* Induced-fit mechanism in class i terpene cyclases. *Angew. Chemie - Int. Ed.* **53**, 7652–7656 (2014).

62. Hong, Y. J. & Tantillo, D. J. Quantum chemical dissection of the classic terpinyl/pinyl/bornyl/camphyl cation conundrum - The role of pyrophosphate in manipulating pathways to monoterpenes. *Org. Biomol. Chem.* **8**, 4589–4600 (2010).

63. Zhang, Q. & Tiefenbacher, K. Terpene cyclization catalysed inside a self-assembled cavity. *Nat. Chem.* **7**, 197–202 (2015).

64. Pronin, S. V. & Shenvi, R. A. Synthesis of highly strained terpenes by non-stop tail-to-head polycyclization. *Nat. Chem.* **4**, 915–920 (2012).

65. Kutateladze, D. A., Strassfeld, D. A. & Jacobsen, E. N. Enantioselective Tail-to-Head Cyclizations Catalyzed by Dual-Hydrogen-Bond Donors. *J. Am. Chem. Soc.* **142**, 6951–6956 (2020).

66. Köster, J. M. & Tiefenbacher, K. Elucidating the Importance of Hydrochloric Acid as a Cocatalyst for Resorcinarene-Capsule-Catalyzed Reactions. *ChemCatChem* **10**, 2941–2944 (2018).

67. Kennedy, C. R., Lin, S. & Jacobsen, E. N. The Cation–π Interaction in Small-Molecule

Catalysis. *Angew. Chemie Int. Ed.* **55**, 12596–12624 (2016).

68. Neel, A. J., Hilton, M. J., Sigman, M. S. & Toste, F. D. Exploiting non-covalent π interactions for catalyst design. *Nature* **543**, 637–646 (2017).

69. Merget, S., Catti, L., Piccini, G. & Tiefenbacher, K. Requirements for Terpene Cyclizations inside the Supramolecular Resorcinarene Capsule: Bound Water and Its Protonation Determine the Catalytic Activity. *J. Am. Chem. Soc.* **142**, 4400–4410 (2020).

70. Zhang, Q. & Tiefenbacher, K. Sesquiterpene Cyclizations inside the Hexameric Resorcinarene Capsule: Total Synthesis of δ-Selinene and Mechanistic Studies. *Angew. Chemie* **131**, 12818–12825 (2019).

71. Zhang, Q., Rinkel, J., Goldfuss, B., Dickschat, J. S. & Tiefenbacher, K. Sesquiterpene cyclizations catalysed inside the resorcinarene capsule and application in the short synthesis of isolongifolene and isolongifolenone. *Nat. Catal.* **1**, 609–615 (2018).

72. Zhang, Q., Catti, L., Pleiss, J. & Tiefenbacher, K. Terpene Cyclizations inside a Supramolecular Catalyst: Leaving-Group-Controlled Product Selectivity and Mechanistic Studies. *J. Am. Chem. Soc.* **139**, 11482–11492 (2017).

73. Racolta, S., Juhl, P. B., Sirim, D. & Pleiss, J. The triterpene cyclase protein family: A systematic analysis. *Proteins Struct. Funct. Bioinforma.* **80**, 2009–2019 (2012).

74. Clayden, J., Greeves, N., Warren, S. & Wother, P. *Organic chemistry*. (2001).

75. Wendt, K. U., Poralla, K. & Schulz, G. E. Structure and function of a squalene cyclase. *Science* **277**, 1811–1815 (1997).

76. Sáenz, J. P. *et al.* Hopanoids as functional analogues of cholesterol in bacterial membranes. *Proc. Natl. Acad. Sci. U. S. A.* **112**, 11971–11976 (2015).

77. Belin, B. J. *et al.* Hopanoid lipids: From membranes to plant-bacteria interactions. *Nat. Rev. Microbiol.* **16**, 304–315 (2018).

78. Allen, K. N., Entova, S., Ray, L. C. & Imperiali, B. Monotopic Membrane Proteins Join the Fold. *Trends Biochem. Sci.* **44**, 7–20 (2019).

79. Reinert, D. J., Balliano, G. & Schulz, G. E. Conversion of Squalene to the Pentacarbocyclic Hopene. *Chem. Biol.* **11**, 121–126 (2004).

80. Lomize, M. A., Pogozheva, I. D., Joo, H., Mosberg, H. I. & Lomize, A. L. OPM database and PPM web server: resources for positioning of proteins in membranes. *Nucleic Acids Res.* **40**, D370–D376 (2012).

81. Smentek, L. & Hess, B. A. Compelling computational evidence for the concerted cyclization of the ABC rings of hopene from protonated squalene. *J. Am. Chem. Soc.* **132**, 17111–17117 (2010).

82. Hammer, S. C. Zur Anwendbarkeit von Squalen-Hopen-Zyklasen als chirale Brønsted-Säuren in der asymmetrischen Katalyse. *Thesis* 1–160 (2014).

83. Hammer, S. C., Dominicus, J. M., Syrén, P. O., Nestl, B. M. & Hauer, B. Stereoselective

Friedel-Crafts alkylation catalyzed by squalene hopene cyclases. *Tetrahedron* **68**, 7624–7629 (2012).

84. Hammer, S. C., Marjanovic, A., Dominicus, J. M., Nestl, B. M. & Hauer, B. Squalene hopene cyclases are protonases for stereoselective Brønsted acid catalysis. *Nat. Chem. Biol.* **11**, 121–126 (2015).

85. Gandour, R. D. On the importance of orientation in general base catalysis by carboxylate. *Bioorg. Chem.* **10**, 169–176 (1981).

86. Schwab, F., Van Gunsteren, W. F. & Zagrovic, B. Computational study of the mechanism and the relative free energies of binding of anticholesteremic inhibitors to squalene-hopene cyclase. *Biochemistry* **47**, 2945–2951 (2008).

87. Hoshino, T. & Sato, T. Squalene-hopene cyclase: catalytic mechanism and substrate recognition. *Chem. Commun.* **4**, 291–301 (2002).

88. Rajamani, R. & Gao, J. Balancing Kinetic and Thermodynamic Control: The Mechanism of Carbocation Cyclization by Squalene Cyclase. *J. Am. Chem. Soc.* **125**, 12768–12781 (2003).

89. Tantillo, D. J. Biosynthesis via carbocations: Theoretical studies on terpene formation. *Nat. Prod. Rep.* **28**, 1035–1053 (2011).

90. Gorenstein, D. G. Stereoelectronic Effects in Biomolecules. *Chem. Rev.* **87**, 1047–1077 (1987).

91. Sato, T., Kouda, M. & Hoshino, T. Site-directed mutagenesis experiments on the putative deprotonation site of squalene-hopene cyclase from Alicyclobacillus acidocaldarius. *Biosci. Biotechnol. Biochem.* **68**, 728–738 (2004).

92. Hoshino, T., Nakano, S., Kondo, T., Sato, T. & Miyoshi, A. Squalene–hopene cyclase: final deprotonation reaction, conformational analysis for the cyclization of (3R,S)-2,3-oxidosqualene and further evidence for the requirement of an isopropylidene moiety both for initiation of the polycyclization cascade and for . *Org. Biomol. Chem.* **2**, 1456–1470 (2004).

93. Syrén, P. O., Hammer, S. C., Claasen, B. & Hauer, B. Entropy is key to the formation of pentacyclic terpenoids by enzyme-catalyzed polycyclization. *Angew. Chemie - Int. Ed.* **53**, 4845–4849 (2014).

94. Åqvist, J., Kazemi, M., Isaksen, G. V. & Brandsdal, B. O. Entropy and Enzyme Catalysis. *Acc. Chem. Res.* **50**, 199–207 (2017).

95. Neumann, S. & Simon, H. Purification, Partial Characterization and Substrate Specificity of a Squalene Cyclase from Bacillus acidocaldarius. *Biol. Chem. Hoppe. Seyler.* **367**, 723–730 (1986).

96. Takahashi, K., Sasaki, Y. & Hoshino, T. Squalene-Hopene Cyclase : On the Polycyclization Reactions of Squalene Analogues Bearing Ethyl Groups at Positions C-6 ,. *European J. Org. Chem.* **12**, 1477–1490 (2018).

97. Hoshino, T., Kumai, Y., Kudo, I., Nakano, S. I. & Ohashi, S. Enzymatic cyclization reactions of geraniol, farnesol and geranylgeraniol, and those of truncated squalene

analogs having C20 and C25 by recombinant squalene cyclase. *Org. Biomol. Chem.* **2**, 2650–2657 (2004).

98. Hammer, S. C., Syrén, P. O., Seitz, M., Nestl, B. M. & Hauer, B. Squalene hopene cyclases: Highly promiscuous and evolvable catalysts for stereoselective CC and CX bond formation. *Curr. Opin. Chem. Biol.* **17**, 293–300 (2013).

99. Hammer, S. C., Dominicus, J. M., Syrén, P. O., Nestl, B. M. & Hauer, B. Stereoselective Friedel-Crafts alkylation catalyzed by squalene hopene cyclases. *Tetrahedron* **68**, 7624–7629 (2012).

100. Henche, S., Nestl, B. M. & Hauer, B. Enzymatic Friedel-Crafts Alkylation Using Squalene-Hopene Cyclases. *ChemCatChem* **13**, 3405–3409 (2021).

101. Bastian, S. A., Hammer, S. C., Kreß, N., Nestl, B. M. & Hauer, B. Selectivity in the Cyclization of Citronellal Introduced by Squalene Hopene Cyclase Variants. *ChemCatChem* **9**, 4364–4368 (2017).

102. Mahlau, M. & List, B. Asymmetric counteranion-directed catalysis (ACDC): A remarkably general approach to enantioselective synthesis. *Angew. Chem. Int. Ed.* **52**, 630–638 (2012).

103. Čorić, I. & List, B. Asymmetric spiroacetalization catalysed by confined Brønsted acids. *Nature* **483**, 315–319 (2012).

104. Tsuji, N. *et al.* Activation of olefins via asymmetric Brønsted acid catalysis. **1505**, 1501–1505 (2018).

105. Properzi, R. *et al.* Catalytic enantiocontrol over a non-classical carbocation. *Nat. Chem.* **12**, 1174–1179 (2020).

106. Schwengers, S. A. *et al.* Unified Approach to Imidodiphosphate-Type Brønsted Acids with Tunable Confinement and Acidity. *J. Am. Chem. Soc.* **143**, 14835–14844 (2021).

107. Winstein, S. & Trifan, D. S. THE STRUCTURE OF THE BICYCLO[2.2.1]2-HEPTYL (NORBORNYL) CARBONIUM ION. *J. Am. Chem. Soc.* **71**, 2953–2953 (1949).

108. Tantillo, D. J. The carbocation continuum in terpene biosynthesis—where are the secondary cations? *Chem. Soc. Rev.* **39**, 2847–2854 (2010).

109. MacMillan, D. W. C. The advent and development of organocatalysis. *Nature* **455**, 304–308 (2008).

110. Jacobsen, E. N. & MacMillan, D. W. C. Organocatalysis. *Proc. Natl. Acad. Sci. U. S. A.* **107**, 20618–20619 (2010).

111. Welter, K. Die asymmetrische Organokatalyse – ein einfaches Werkzeug für die moderne Chemie. *Chemie unserer Zeit* **55**, 370–373 (2021).

112. Chen, K. & Arnold, F. H. Engineering new catalytic activities in enzymes. *Nat. Catal.* **3**, 203–213 (2020).

113. Huffman, M. A. *et al.* Design of an in vitro biocatalytic cascade for the manufacture of islatravir. *Science* **366**, 1255–1259 (2019).

114. Burke, A. J. *et al.* A Biocatalytic Approach to a Key Intermediate for the Synthesis of the COVID-19 Experimental Drug Molnupiravir. (2021) doi:10.26434/CHEMRXIV.13721692.V1.

115. Ardkhean, R. *et al.* Cascade polycyclizations in natural product synthesis. *Chem. Soc. Rev.* **45**, 1557–1569 (2016).

116. Monteiro, J. L. F. & Veloso, C. O. Catalytic conversion of terpenes into fine chemicals. *Top. Catal.* **27**, 169–180 (2004).

117. Tetali, S. D. Terpenes and isoprenoids: a wealth of compounds for global use. *Planta* **249**, 1–8 (2019).

118. Gaich, T. & Baran, P. S. Aiming for the ideal synthesis. *Journal of Organic Chemistry* vol. 75 4657–4673 (2010).

119. Corey, E. J. & Lin, S. A Short Enantioselective Total Synthesis ofDammarenediol II. *J. Am. Chem. Soc.* **118**, 8765–8766 (1996).

120. Ishihara, K., Nakamura, S. & Yamamoto, H. The first enantioselective biomimetic cyclization of polyprenoids. *J. Am. Chem. Soc.* **121**, 4906–4907 (1999).

121. Sakakura, A., Ukai, A. & Ishihara, K. Enantioselective halocyclization of polyprenoids induced by nucleophilic phosphoramidites. *Nature* **445**, 900–903 (2007).

122. Knowles, R. R., Lin, S. & Jacobsen, E. N. Enantioselective thiourea-catalyzed cationic polycyclizations. *J. Am. Chem. Soc.* **132**, 5030–5032 (2010).

123. Nakamura, S., Ishihara, K. & Yamamoto, H. Enantioselective biomimetic cyclization of isoprenoids using Lewis acid-assisted chiral Bronsted acids: Abnormal claisen rearrangements and successive cyclizations. *J. Am. Chem. Soc.* **122**, 8131–8140 (2000).

124. Snyder, S. A., Treitler, D. S. & Brucks, A. P. Simple reagents for direct halonium-induced polyene cyclizations. *J. Am. Chem. Soc.* **132**, 14303–14314 (2010).

125. Köksal, M., Hu, H., Coates, R. M., Peters, R. J. & Christianson, D. W. Structure and mechanism of the diterpene cyclase ent-copalyl diphosphate synthase. *Nat. Chem. Biol.* **7**, 431–433 (2011).

126. Moosmann, P. *et al.* A monodomain class II terpene cyclase assembles complex isoprenoid scaffolds. *Nat. Chem.* **12**, 968–972 (2020).

127. Wilderman, P. R. & Peters, R. J. A single residue switch converts abietadiene synthase into a pimaradiene specific cyclase. *J. Am. Chem. Soc.* **129**, 15736–15737 (2007).

128. Xu, M., Wilderman, P. R. & Peters, R. J. Following evolution's lead to a single residue switch for diterpene synthase product outcome. *Proc. Natl. Acad. Sci. U. S. A.* **104**, 7387–7401 (2007).

129. Eichhorn, E. *et al.* Biocatalytic Process for (-)-Ambrox Production Using Squalene Hopene Cyclase. *Adv. Synth. Catal.* **350**, 2339–2351 (2018).

130. Huang, X. *et al.* Photoenzymatic enantioselective intermolecular radical hydroalkylation. *Nature* **584**, 69–74 (2020).

131. Zhang, Z., Tanaka, K. & Yu, J. Q. Remote site-selective C-H activation directed by a catalytic bifunctional template. *Nature* **543**, 538–542 (2017).

132. Siegel, J. B. *et al.* Computational design of an enzyme catalyst for a stereoselective bimolecular diels-alder reaction. *Science* **329**, 309–313 (2010).

133. Mara, M. *et al.* Anchoring structure of smecti liquid-crystal layers on MoS2 observed by scannin tunneling microscopy. *Nature* **344**, 228–230 (1990).

134. Jäckel, C., Kast, P. & Hilvert, D. Protein design by directed evolution. *Annual Review of Biophysics* vol. 37 153–173 (2008).

135. Qu, G., Li, A., Acevedo-Rocha, C. G., Sun, Z. & Reetz, M. T. The Crucial Role of Methodology Development in Directed Evolution of Selective Enzymes. *Angew. Chemie - Int. Ed.* **59**, 13204–13231 (2020).

136. Lauchli, R. *et al.* High-Throughput Screening for Terpene-Synthase-Cyclization Activity and Directed Evolution of a Terpene Synthase. *Angew. Chemie Int. Ed.* **52**, 5571–5574 (2013).

137. Furubayashi, M. *et al.* A High-Throughput Colorimetric Screening Assay for Terpene Synthase Activity Based on Substrate Consumption. *PLoS One* **9**, e93317 (2014).

138. Kille, S. *et al.* Reducing codon redundancy and screening effort of combinatorial protein libraries created by saturation mutagenesis. *ACS Synth. Biol.* **2**, 83–92 (2013).

139. Hoshino, T., Kaneko, I. & Terasawa, Y. Squalene-hopene cyclase: mechanistic insights into the polycyclization cascades of squalene analogs bearing ethyl and hydroxymethyl groups at the C-2 and C-23 positions. *Chem. - A Eur. J.* **24**, 37–47 (2018).

140. Seitz, M. *et al.* Synthesis of Heterocyclic Terpenoids by Promiscuous Squalene-Hopene Cyclases. *ChemBioChem* **14**, 436–439 (2013).

141. Berger, J. Enzymatic monocyclization of Geranyl acetone. (2018).

142. Schneider, A. Zyklisierung terpenoider Systeme mittels Squalen-Hopen-Zyklase. (2016).

143. Arnold, F. H. Directed Evolution: Bringing New Chemistry to Life. *Angew. Chemie - Int. Ed.* **57**, 4143–4148 (2018).

144. Serra, S. An expedient preparation of enantio-enriched ambergris odorants starting from commercial ionone alpha. *Flavour Fragr. J.* **28**, 46–52 (2013).

145. Land, H. & Humble, M. S. YASARA: A tool to obtain structural guidance in biocatalytic investigations. in *Methods in Molecular Biology* vol. 1685 43–67 (Humana Press Inc., 2018).

146. O'Brien, T. E., Bertolani, S. J., Tantillo, D. J. & Siegel, J. B. Mechanistically informed predictions of binding modes for carbocation intermediates of a sesquiterpene synthase reaction. *Chem. Sci.* **7**, 4009–4015 (2016).

147. Wendt, K. U., Lenhart, a & Schulz, G. E. The structure of the membrane protein squalene-hopene cyclase at 2.0 A resolution. *J. Mol. Biol.* **286**, 175–187 (1999).

148. Krapp, A., Bickelhaupt, F. M. & Frenking, G. Orbital overlap and chemical bonding. *Chem.*

- *A Eur. J.* **12**, 9196–9216 (2006).

149. Creigthon, T. E. *Proteins: Structures and Molecular properties*. (1993).

150. Reetz, M. T. The importance of additive and non-additive mutational effects in protein engineering. *Angew. Chemie - Int. Ed.* **52**, 2658–2666 (2013).

151. Justicia, J. *et al.* Titanium-catalyzed enantioselective synthesis of α-ambrinol. *Adv. Synth. Catal.* **350**, 571–576 (2008).

152. Chen, D. *et al.* Regulation of protein-ligand binding affinity by hydrogen bond pairing. *Sci. Adv.* **2**, (2016).

153. Jia, M. & Peters, R. J. cis or trans with class II diterpene cyclases. *Org. Biomol. Chem.* **15**, 3158–3160 (2017).

154. Litman, Z. C., Wang, Y., Zhao, H. & Hartwig, J. F. Cooperative asymmetric reactions combining photocatalysis and enzymatic catalysis. *Nature* **560**, 355–359 (2018).

155. Gora, A., Brezovsky, J. & Damborsky, J. Gates of enzymes. *Chem. Rev.* **113**, 5871–5923 (2013).

156. Sato, T., Kouda, M. & Hoshino, T. Site-directed mutagenesis experiments on the putative deprotonation site of squalene-hopene cyclase from Alicyclobacillus acidocaldarius. *Biosci. Biotechnol. Biochem.* **68**, 728–738 (2004).

157. Darland, D. & Brock, T. D. *Bacillus acidocaldarius sp.nov., an Acidophilic Thermophilic Spore-forming Bacterium*. *Journal of General Microbiology* vol. 67 (1971).

158. Poralla, K., Kannenberg, E. & Blume, A. A glycolipid containing hopane isolated from the acidophilic, thermophilic bacillus acidocaldarius, has a cholesterol-like function in membranes. *FEBS Lett.* **113**, 107–110 (1980).

159. Balali-Mood, K., Bond, P. J. & Sansom, M. S. P. Interaction of monotopic membrane enzymes with a lipid bilayer: A coarse-grained MD simulation study. *Biochemistry* **48**, 2135–2145 (2009).

160. Camargos, H. S. *et al.* Terpenes increase the lipid dynamics in the Leishmania plasma membrane at concentrations similar to their IC50 values. *PLoS One* **9**, (2014).

161. Harb, F., Prunetti, L., Giudici-Orticoni, M. T., Guiral, M. & Tinland, B. Insertion and self-diffusion of a monotopic protein, the Aquifex aeolicus sulfide quinone reductase, in supported lipid bilayers. *Eur. Phys. J. E* **38**, 1–11 (2015).

162. Pande, A. H., Qin, S. & Tatulian, S. A. Membrane fluidity is a key modulator of membrane binding, insertion, and activity of 5-lipoxygenase. *Biophys. J.* **88**, 4084–4094 (2005).

163. Laganowsky, A. *et al.* Membrane proteins bind lipids selectively to modulate their structure and function. *Nature* **510**, (2014).

164. Morikubo, N. *et al.* Cation-π interaction in the polyolefin cyclization cascade uncovered by incorporating unnatural amino acids into the catalytic sites of squalene cyclase. *J. Am. Chem. Soc.* **128**, 13184–13194 (2006).

165. Seitz, M. *et al.* Substrate specificity of a novel squalene-hopene cyclase from Zymomonas

mobilis. *J. Mol. Catal. B Enzym.* **84**, 72–77 (2012).

166. Breuer, M., Hörster, A. & Hauer, B. Biocatalytic production of ambroxan; U.S. Patent No. 8,759,043. 24 Jun. 2014. (2014).

167. Ishihara, K., Ishibashi, H. & Yamamoto, H. Enantio- and diastereoselective stepwise cyclization of polyprenoids induced by chiral and achiral LBAs. A new entry to (-)-ambrox, (+)-podocarpa-8,11,13-triene diterpenoids, and (-)-tetracyclic polyprenoid of sedimentary origin. *J. Am. Chem. Soc.* **124**, 3647–3655 (2002).

168. Hülsewede, D., Meyer, L. E. & von Langermann, J. Application of In Situ Product Crystallization and Related Techniques in Biocatalytic Processes. *Chem. - A Eur. J.* **25**, 4871–4884 (2019).

169. Kühnel, L. C., Nestl, B. M. & Hauer, B. Enzymatic Addition of Alcohols to Terpenes by Squalene Hopene Cyclase Variants. *ChemBioChem* **18**, 2222–2225 (2017).

170. Schrewe, M. *et al.* Reaction and catalyst engineering to exploit kinetically controlled whole-cell multistep biocatalysis for terminal FAME oxyfunctionalization. *Biotechnol. Bioeng.* **111**, 1820–1830 (2014).

171. Jurcik, A. *et al.* CAVER Analyst 2.0: Analysis and visualization of channels and tunnels in protein structures and molecular dynamics trajectories. *Bioinformatics* **34**, 3586–3588 (2018).

172. Leive, L. Part 11. Functional Interrelationships of Walls and Membranes the Barrier Function of the Gram-Negative Envelope. *Ann. New York Acad. od Sci.* 109–129 (1974).

173. Chen, R. R. Permeability issues in whole-cell bioprocesses and cellular membrane engineering. *Applied Microbiology and Biotechnology* vol. 74 730–738 (2007).

174. Julsing, M. K. *et al.* Outer membrane protein alkL boosts biocatalytic oxyfunctionalization of hydrophobic substrates in Escherichia coli. *Appl. Environ. Microbiol.* **78**, 5724–5733 (2012).

175. Huang, J. *et al.* Unnatural biosynthesis by an engineered microorganism with heterologously expressed natural enzymes and an artificial metalloenzyme. *Nat. Chem.* **13**, 1186–1191 (2021).

176. Sikkema, J., De Bont, J. A. M. & Poolman, B. Interactions of cyclic hydrocarbons with biological membranes. *J. Biol. Chem.* **269**, 8022–8028 (1994).

177. Hoshino, T., Shimizu, K. & Sato, T. Deletion of the Gly600 residue of Alicyclobacillus acidocaldarius squalene cyclase alters the substrate specificity into that of the eukaryotic-type cyclase specific to (3S)-2,3-oxidosqualene. *Angew. Chemie - Int. Ed.* **43**, 6700–6703 (2004).

178. Potter, K. C. *et al.* Blocking Deprotonation with Retention of Aromaticity in a Plant ent-Copalyl Diphosphate Synthase Leads to Product Rearrangement. *Angew. Chemie - Int. Ed.* **55**, 634–638 (2016).

179. Li, G. *et al.* Simultaneous engineering of an enzyme's entrance tunnel and active site: The case of monoamine oxidase MAO-N. *Chem. Sci.* **8**, 4093–4099 (2017).

180. Maria-Solano, M. A., Serrano-Hervás, E., Romero-Rivera, A., Iglesias-Fernández, J. & Osuna, S. Role of conformational dynamics in the evolution of novel enzyme function. *Chem. Commun.* **54**, 6622–6634 (2018).

181. Waterhouse, A. *et al.* SWISS-MODEL: Homology modelling of protein structures and complexes. *Nucleic Acids Res.* **46**, W296–W303 (2018).

182. Maria-Solano, M. A., Kinateder, T., Iglesias-Fernández, J., Sterner, R. & Osuna, S. *In Silico* Identification and Experimental Validation of Distal Activity-Enhancing Mutations in Tryptophan Synthase. *ACS Catal.* **11**, 13733–13743 (2021).

183. Otten, R. *et al.* How directed evolution reshapes the energy landscape in an enzyme to boost catalysis. *Science* **1446**, eabd3623 (2020).

184. Pemberton, R. P. & Tantillo, D. J. Lifetimes of carbocations encountered along reaction coordinates for terpene formation. *Chem. Sci.* **5**, 3301–3308 (2014).

185. Eichenberger, M. *et al.* Asymmetric Cation-Olefin Monocyclization by Engineered Squalene–Hopene Cyclases. *Angew. Chemie - Int. Ed.* **60**, 26080–26086 (2021).

186. Mendanha, S. A. & Alonso, A. Effects of terpenes on fluidity and lipid extraction in phospholipid membranes. *Biophys. Chem.* **198**, 45–54 (2015).

187. Agus, H. H. Terpene toxicity and oxidative stress. in *Toxicology* 33–42 (Academic Press, 2021).

188. Babtie, A., Tokuriki, N. & Hollfelder, F. What makes an enzyme promiscuous? *Curr. Opin. Chem. Biol.* **14**, 200–207 (2010).

189. Rodi, P. M., Bocco Gianello, M. D., Corregido, M. C. & Gennaro, A. M. Comparative study of the interaction of CHAPS and Triton X-100 with the erythrocyte membrane. *Biochim. Biophys. Acta - Biomembr.* **1838**, 859–866 (2014).

190. Makino, S., Reynolds, J. A. & Tanford, C. The Binding of Deoxycholate and Triton X-100 to Proteins. *J. Biol. Chem.* **248**, 4926–4932 (1973).

191. Cockley, D. Detergents and their Uses in Membrane Protein Science. *Deterg. their Uses Membr. Protein Sci.* **1**, 1–17 (2007).

192. Koo, C. W., Tucci, F. J., He, Y. & Rosenzweig, A. C. Recovery of particulate methane monooxygenase structure and activity in a lipid bilayer. *Science* **375**, 1287–1291 (2022).

193. Farías, R. N., Bloj, B., Morero, R. D., Siñeriz, F. & Trucco, R. E. Regulation of allosteric membrane-bound enzymes through changes in membrane lipid composition. *Biochim. Biophys. Acta - Rev. Biomembr.* **415**, 231–251 (1975).

194. Meng, Y. *et al.* Extension of cell membrane boosting squalene production in the engineered Escherichia coli. *Biotechnol. Bioeng.* **1**, 1–9 (2020).

195. Nji, E., Chatzikyriakidou, Y., Landreh, M. & Drew, D. An engineered thermal-shift screen reveals specific lipid preferences of eukaryotic and prokaryotic membrane proteins. *Nat. Commun.* **9**, 1–12 (2018).

196. Krueger-Koplin, R. D. *et al.* An evaluation of detergents for NMR structural studies of membrane proteins. *J. Biomol. NMR* **17**, 43–57 (2004).

197. Breibeck, J. & Rompel, A. Successful amphiphiles as the key to crystallization of membrane proteins: Bridging theory and practice. *Biochim. Biophys. Acta - Gen. Subj.* **1863**, 437–455 (2019).

198. Lee, A. G. How lipids affect the activities of integral membrane proteins. *Biochimica et Biophysica Acta - Biomembranes* vol. 1666 62–87 (2004).

199. Kotov, V. *et al.* High-throughput stability screening for detergent-solubilized membrane proteins. *Sci. Rep.* **9**, (2019).

200. Salvachúa, D. *et al.* Bioprocess development for muconic acid production from aromatic compounds and lignin. *Green Chem.* **20**, 5007–5019 (2018).

201. Buque-Taboada, E. M., Straathof, A. J. J., Heijnen, J. J. & Van Der Wielen, L. A. M. In situ product removal using a crystallization loop in asymmetric reduction of 4-oxoisophorone by Saccharomyces cerevisiae. *Biotechnol. Bioeng.* **86**, 795–800 (2004).

202. Carsanba, E., Pintado, M. & Oliveira, C. Fermentation strategies for production of pharmaceutical terpenoids in engineered yeast. *Pharmaceuticals* **14**, (2021).

203. Wu, S., Snajdrova, R., Moore, J. C., Baldenius, K. & Bornscheuer, U. T. Biocatalysis: Enzymatic Synthesis for Industrial Applications. *Angewandte Chemie - International Edition* vol. 60 88–119 (2021).

204. Hauer, B. Embracing Nature's Catalysts: A Viewpoint on the Future of Biocatalysis. *ACS Catal.* **10**, 8418–8427 (2020).

205. Kadisch, M. *et al.* Maximization of cell viability rather than biocatalyst activity improves whole-cell ω-oxyfunctionalization performance. *Biotechnol. Bioeng.* **114**, 874–884 (2017).

206. Karande, R., Salamanca, D., Schmid, A. & Buehler, K. Biocatalytic conversion of cycloalkanes to lactones using an in-vivo cascade in Pseudomonas taiwanensis VLB120. *Biotechnol. Bioeng.* **115**, 312–320 (2018).

207. Hoff, B. *et al.* Unlocking Nature s Biosynthetic Power — Metabolic Engineering for the Fermentative Production of Chemicals Angewandte Reviews. *Angew. Chemie Int. Ed.* **59**, 2–23 (2020).

208. Benítez-Mateos, A. I., Schneider, A., Hegarty, E., Hauer, B. & Paradisi, F. Spheroplasts preparation boosts the catalytic potential of a terpene cyclase. *ChemRxiv* (2022) doi:10.26434/CHEMRXIV-2022-W08D0.

209. Golczak, M., Kiser, P. D., Lodowski, D. T., Maeda, A. & Palczewski, K. Importance of membrane structural integrity for RPE65 retinoid isomerization activity. *J. Biol. Chem.* **285**, 9667–9682 (2010).

210. Phillips, R., Ursell, T., Wiggins, P. & Sens, P. Emerging roles for lipids in shaping membrane-protein function. *Nature* vol. 459 379–385 (2009).

211. Uddin, M. J. *et al.* Antitumor activity of cytotoxic cyclooxygenase-2 inhibitors. *ACS Chem.*

Biol. **11**, 3052–3060 (2016).

212. Corey, E. J. Retrosynthetic Thinking - Essentials and Examples. *Chem. SOC. Rev* **17**, 111–133 (1988).

213. Green, A. P. & Turner, N. J. Biocatalytic retrosynthesis: Redesigning synthetic routes to high-value chemicals. *Perspect. Sci.* **9**, 42–48 (2016).

214. Rudroff, F. *et al.* Opportunities and challenges for combining chemo- and biocatalysis. *Nat. Catal.* **1**, 12–22 (2018).

215. Li, F. & Renata, H. A Chiral-Pool-Based Strategy to Access trans-syn-Fused Drimane Meroterpenoids: Chemoenzymatic Total Syntheses of Polysin, N-Acetyl-polyveoline and the Chrodrimanins. *J. Am. Chem. Soc.* **143**, 18280–18286 (2021).

216. Stout, C. N. & Renata, H. Reinvigorating the Chiral Pool: Chemoenzymatic Approaches to Complex Peptides and Terpenoids. *Acc. Chem. Res* **54**, 1143–1156 (2021).

217. Li, J., Li, F., King-Smith, E. & Renata, H. Merging chemoenzymatic and radical-based retrosynthetic logic for rapid and modular synthesis of oxidized meroterpenoids. *Nat. Chem.* **12**, 173–179 (2020).

218. Xu, G., Elkin, M., Tantillo, D. J., Newhouse, T. R. & Maimone, T. J. Traversing Biosynthetic Carbocation Landscapes in the Total Synthesis of Andrastin and Terretonin Meroterpenes. *Angew. Chemie Int. Ed.* **56**, 12498–12502 (2017).

219. Willot, M. & Christmann, M. Towards artificial terpene cyclases. *Nat. Chem.* **2**, 519–520 (2010).

220. Harmange Magnani, C. S., Thach, D. Q., Haelsig, K. T. & Maimone, T. J. Syntheses of Complex Terpenes from Simple Polyprenyl Precursors. *Acc. Chem. Res.* **53**, 949–961 (2020).

221. Alonso, P., Pardo, P., Galván, A., Fañanás, F. J. & Rodríguez, F. Synthesis of Cyclic Alkenyl Triflates by a Cationic Cyclization Reaction and its Application in Biomimetic Polycyclizations and Synthesis of Terpenes. *Angew. Chemie* **127**, 15726–15730 (2015).

222. Pronin, S. V. & Shenvi, R. A. Synthesis of highly strained terpenes by non-stop tail-to-head polycyclization. *Nat. Chem.* **4**, 915–920 (2012).

223. Zhang, Q., Catti, L., Syntrivanis, L. D. & Tiefenbacher, K. En route to terpene natural products utilizing supramolecular cyclase mimetics. *Natural Product Reports* vol. 36 1619–1627 (2019).

224. Kasai, H. F. *et al.* Separation of Stereoisomers of Some Terpene Derivatives by Capillary Gas Chromatography-Mass Spectrometry and High-Performance Liquid Chromatography Using b b-Cyclodextrin Derivative Columns. *Chem. Pharm. Bull* **52**, 311–315 (2004).

225. Coli, J. C. & Bowden, B. F. The application of vacuum liquid chromatography to the separation of terpene mixtures. *J. Nat. Prod.* **49**, 934–936 (1986).

226. Moser, S. *et al.* Whole-cell (+)-ambrein production in the yeast Pichia pastoris. *Metab.*

Eng. Commun. **7**, 1–9 (2018).

227. Hage-Hülsmann, J. *et al.* Biosynthesis of cycloartenol by expression of plant and bacterial oxidosqualene cyclases in engineered Rhodobacter capsulatus. *J. Biotechnol.* **306**, 100014 (2019).

228. Brill, Z. G., Condakes, M. L., Ting, C. P. & Maimone, T. J. Navigating the Chiral Pool in the Total Synthesis of Complex Terpene Natural Products. *Chem. Rev.* **117**, 11753–11795 (2017).

229. Xu, G., Elkin, M., Tantillo, D. J., Newhouse, T. R. & Maimone, T. J. Traversing Biosynthetic Carbocation Landscapes in the Total Synthesis of Andrastin and Terretonin Meroterpenes. *Angew. Chemie - Int. Ed.* **56**, 12498–12502 (2017).

230. Rapp, C., Nidetzky, B. & Kratzer, R. Pushing the limits: Cyclodextrin-based intensification of bioreductions. *J. Biotechnol.* **325**, 57–64 (2021).

231. Bonnet, V., Gervaise, C., Favrelle, A., Sarazin, C. & Djedaini-Pilard, F. Enzymatic Catalysis in Presence of Cyclodextrins. *Curr. Org. Chem.* **14**, 1323–1336 (2010).

232. Gidwani, B. & Vyas, A. A Comprehensive Review on Cyclodextrin-Based Carriers for Delivery of Chemotherapeutic Cytotoxic Anticancer Drugs. *Biomed Res. Int.* **2015**, (2015).

233. Astray, G., Gonzalez-Barreiro, C., Mejuto, J. C., Rial-Otero, R. & Simal-Gándara, J. A review on the use of cyclodextrins in foods. *Food Hydrocoll.* **23**, 1631–1640 (2009).

234. Jones, S. T. *et al.* Modified cyclodextrins as broad-spectrum antivirals. *Sci. Adv.* **6**, 9318 (2020).

235. Matsunaga, T. *et al.* α-Cyclodextrin Encapsulation of Bicyclo[1.1.1]pentane Derivatives: A Storable Feedstock for Preparation of [1.1.1]Propellane. *Angew. Chemie* **133**, 2610–2614 (2021).

236. Carneiro, S. B. *et al.* Cyclodextrin-drug inclusion complexes: In vivo and in vitro approaches. *Int. J. Mol. Sci.* **20**, 1–23 (2019).

237. Villalonga, R., Cao, R. & Fragoso, A. Supramolecular chemistry of cyclodextrins in enzyme technology. *Chemical Reviews* vol. 107 3088–3116 (2007).

238. Rasheed, A., Kumar C.K., A. & Sravanthi, V. V. N. S. S. Cyclodextrins as drug carrier molecule: A review. *Sci. Pharm.* **76**, 567–598 (2008).

239. Ajisaka, N., Hara, K., Mikuni, K., Hara, K. & Hashimoto, H. Effects of branched cyclodextrins on the solubility and stability of terpenes. *Biosci. Biotechnol. Biochem.* **64**, 731–734 (2000).

240. Lima, P. S. S. *et al.* Inclusion of terpenes in cyclodextrins: Preparation, characterization and pharmacological approaches. *Carbohydr. Polym.* **151**, 965–987 (2016).

241. Hammoud, Z. *et al.* Cyclodextrin-membrane interaction in drug delivery and membrane structure maintenance. *Int. J. Pharm.* **564**, 59–76 (2019).

242. López, C. A., De Vries, A. H. & Marrink, S. J. Computational microscopy of cyclodextrin mediated cholesterol extraction from lipid model membranes. *Sceintific Reports* **3**, 1–6

(2013).

243. María, L. A., Ngeles Pedreñ, A. ′, Almagro, L. & Pedreño, M. A. ′. Use of cyclodextrins to improve the production of plant bioactive compounds. *Phytochem. Rev.* **19**, 1061–1080 (2020).

244. Stepankova, V., Damborsky, J. & Chaloupkova, R. Organic co-solvents affect activity, stability and enantioselectivity of haloalkane dehalogenases. *Biotechnol. J.* **8**, 719–729 (2013).

245. Engasser, J.-M. & Horvath, C. SUBSTRATE INHIBITION OF BOUND ENZYMES Inhibition of Bound Enzymes. III. Diffusion Enhanced Regulatory Effect with Substrate Inhibition. *Biochemistry* **13**, 26 (1974).

246. Lundemo, M. T. & Woodley, J. M. Guidelines for development and implementation of biocatalytic P450 processes. *Appl. Microbiol. Biotechnol. 2015 996* **99**, 2465–2483 (2015).

247. Syren, P. O., Henche, S., Eichler, A., Nestl, B. M. & Hauer, B. Squalene-hopene cyclases - evolution, dynamics and catalytic scope. *Curr. Opin. Struct. Biol.* **41**, 73–82 (2016).

248. Marmulla, R. & Harder, J. Microbial monoterpene transformations-a review. *Front. Microbiol.* **5**, 1–14 (2014).

249. MacCallum, J. L., Drew Bennett, W. F. & Peter Tieleman, D. Distribution of Amino Acids in a Lipid Bilayer from Computer Simulations. *Biophys. J.* **94**, 3393–3404 (2008).

250. McDonagh, J. L., Palmer, D. S., Mourik, T. Van & Mitchell, J. B. O. Are the sublimation thermodynamics of organic molecules predictable? *J. Chem. Inf. Model.* **56**, 2162–2179 (2016).

251. Christian, E., Haynes, M. P., Phillips, M. C. & Rothblat', G. H. Use of cyclodextrins for manipulating cellular cholesterol content. *J. Lipid Res.* **38**, 2264–2272 (1997).

252. Kiss, T. *et al.* Evaluation of the cytotoxicity of β-cyclodextrin derivatives: Evidence for the role of cholesterol extraction. *Eur. J. Pharm. Sci.* **40**, 376–380 (2010).

253. Milles, S. *et al.* Organization of fluorescent cholesterol analogs in lipid bilayers — Lessons from cyclodextrin extraction. *Biochim. Biophys. Acta - Biomembr.* **1828**, 1822–1828 (2013).

254. Basabe, P. *et al.* Synthesis of (+)-makassaric acid, a protein kinase MK2 inhibitor. *Tetrahedron* **66**, 6008–6012 (2010).

255. Wang, P. *et al.* Concise synthesis of (+)-subersic acid from (–)-Sclareol. *Tetrahedron* **71**, 4647–4650 (2015).

256. Zhang, S. *et al.* Expediently Scalable Synthesis and Antifungal Exploration of (+)-Yahazunol and Related Meroterpenoids. *J. Nat. Prod.* **81**, 2010–2017 (2018).

257. Dethe, D. H., Murhade, G. M., Dherange, B. D. & Sau, S. K. Enantiospecific Syntheses of Hongoquercins A and B and Chromazonarol. *European J. Org. Chem.* **2017**, 1143–1150 (2017).

258. Parker, K. A. & Resnick, L. The First Total Synthesis of a Pyripyropene-Type ACAT

Inhibitor, (±)-GERI-BPooP. *J. Org. Chem* **60**, 5726–5728 (1995).

259. Kabbe, H.-J. & Widdig, A. Synthesis and Reactions of 4-Chromanones. *Angew. Chem. Int. Ed.* **21**, 247–256 (1982).

260. Harrison, E. H. & Quadro, L. Apocarotenoids: Emerging roles in mammals. *Annu. Rev. Nutr.* **38**, 153–172 (2018).

261. Tsangarakis, C. & Stratakis, M. Biomimetic cyclization of small terpenoids promoted by zeolite NaY: Tandem formation of α-ambrinol from geranyl acetone. *Adv. Synth. Catal.* **347**, 1280–1284 (2005).

262. Rauh, M. J. & Krystal, G. Synthesis of Pelorol and Analogues: Activators of the Inositol 5-Phosphatase SHIP ORGANIC LETTERS. *Biochem. Soc. Trans* **31**, 3 (2003).

263. Kamishima, T., Kikuchi, T., Narita, K. & Katoh, T. Biogenetically Inspired Total Synthesis of (+)-Liphagal: A Potent and Selective Phosphoinositide 3-Kinase α (PI3Kα) Inhibitor from the Marine Sponge Aka coralliphaga. *European J. Org. Chem.* **2014**, 3443–3450 (2014).

264. Polovinka, M. P. *et al.* Cyclization and Rearrangements of Farnesol and Nerolidol Stereoisomers in Superacids. *J. Org. Chem.* **59**, 1509–1517 (1994).

265. de las Heras, B. & Hortelano, S. Molecular basis of the anti-inflammatory effects of terpenoids. *Inflamm. Allergy - Drug Targets* **8**, 28–39 (2009).

266. Novaes, L. F. T., Gonçalves, K. D. A., Trivella, D. B. B. & Pastre, J. C. Formal Total Synthesis of Actinoranone: Synthesis Approaches and Cytotoxic Studies. *J. Org. Chem.* **83**, 5160–5176 (2018).

267. Criswell, J., Potter, K., Shephard, F., Beale, M. H. & Peters, R. J. A single residue change leads to a hydroxylated product from the class II diterpene cyclization catalyzed by abietadiene synthase. *Org. Lett.* **14**, 5828–5831 (2012).

268. Morrone, D., Xu, M., Fulton, D. B., Determan, M. K. & Peters, R. J. Increasing complexity of a diterpene synthase reaction with a single residue switch. *J. Am. Chem. Soc.* **130**, 5400–5401 (2008).

269. Grant, P. S. & Brimble, M. A. seco-Labdanes:AStudy of Terpenoid Structural Diversity Resulting from BiosyntheticC ÀCB ond Cleavage Chemistry-A European Journal. **27**, 6367–6389 (2021).

270. Keyzers, R. A., Northcote, P. T. & Davies-Coleman, M. T. Spongian diterpenoids from marine sponges. *Nat. Prod. Rep.* **23**, 321–334 (2006).

271. Menna, M., Imperatore, C., Aniello, F. D. ' & Aiello, A. Meroterpenes from Marine Invertebrates: Structures, Occurrence, and Ecological Implications. *Mar. Drugs* **11**, 1602–1643 (2013).

272. Talekar, R. S., Chen, G. S., Lai, S. Y. & Chern, J. W. Nonreductive deiodination of ortho-iodo-hydroxylated arenes using tertiary amines. *J. Org. Chem.* **70**, 8590–8593 (2005).

273. Zhang, S. *et al.* Unlocking the Friedel-Crafts arylation of primary aliphatic alcohols and epoxides driven by hexafluoroisopropanol. *Chem* **7**, 3425–3441 (2021).

274. Jansen, D. J. & Shenvi, R. A. Synthesis of medicinally relevant terpenes: Reducing the cost and time of drug discovery. *Future Medicinal Chemistry* vol. 6 1127–1148 (2014).

275. Rea, W. J., Patel, K. D., Rea, W. J. & Patel, K. D. Terpenes and Terpenoids. *Reversibility Chronic Dis. Hypersensitivity* **4**, 905–930 (2018).

276. Hanessian, S. Natural Products in Medicinal Chemistry. *Nat. Prod. Med. Chem.* **60**, 1–630 (2014).

277. Beltrán, J. *et al.* Control of carotenoid biosynthesis through a heme-based cis-trans isomerase. *Nat. Chem. Biol.* **11**, 598–605 (2015).

278. Hölzl-Hobmeier, A. *et al.* Catalytic deracemization of chiral allenes by sensitized excitation with visible light. *Nature* **564**, 240–243 (2018).

279. Hendrickson, J. B. Systematic Synthesis Design. IV. Numerical Codification of Construction Reactions. *J. Am. Chem. Soc.* **92**, 5784–5800 (1975).

280. Terpene Market Size, Share, Growth, Trends, Opportunities & Forecast. https://www.verifiedmarketresearch.com/product/terpene-market/. 06.05.2022

281. Eichhorn, E. Process for isolating and purifying ambrox; U.S. Patent No. 10,294,211. 21 May 2019. (2019).

282. Sanhaji, G., Rousseaux, A., Noel, S. & Eichhorn, E. Solid form of (–)-Ambrox formed by a bioconversion of homofarnesol in the presence of a biocatalyst; U.S. Patent No. 10,844,412. 24 Nov. 2020. (2019).

283. Peters, R. *Cooperative Catalysis: Designing Efficient Catalysts for Synthesis*. *Cooperative Catalysis: Designing Efficient Catalysts for Synthesis* (2015).

284. Mitschke, B., Turberg, M. & List, B. Confinement as a Unifying Element in Selective Catalysis. *Chem* vol. 6 2515–2532 (2020).

285. Schwengers, S. A. *et al.* Unified Approach to Imidodiphosphate-Type Brønsted Acids with Tunable Confinement and Acidity. *J. Am. Chem. Soc.* **143**, 14835–14844 (2021).

286. Morimoto, M. *et al.* Advances in supramolecular host-mediated reactivity. *Nature Catalysis* vol. 3 969–984 (2020).

287. Corey, E. J., Yuen, P.-W., Hannon, F. J. & Wierda, D. A. Polyfunctional, structurally defined catalysts for the enantioselective addition of dialkylzinc reagents to aldehydes. *J. Org. Chem.* **55**, 784–786 (1990).

288. Hentges, S. G. & Sharpless, K. B. Asymmetric induction in the reaction of osmium tetroxide with olefins. *J. Am. Chem. Soc.* **102**, 4263–4265 (1980).

289. Kaphan, D. M., Levin, M. D., Bergman, R. G., Raymond, K. N. & Toste, F. D. A supramolecular microenvironment strategy for transition metal catalysis. *Science* **350**, 1235–1238 (2015).

290. Breslow, R. Biomimetic Chemistry and Artificial Enzymes: Catalysis by Design. *Acc. Chem. Res.* **28**, 146–153 (1995).

291. Farrusseng, D., Aguado, S. & Pinel, C. Metal–Organic Frameworks: Opportunities for Catalysis. *Angew. Chemie Int. Ed.* **48**, 7502–7513 (2009).

292. Basler, S. *et al.* Efficient Lewis acid catalysis of an abiological reaction in a de novo protein scaffold. *Nat. Chem.* **13**, 231–235 (2021).

293. Crawshaw, R. *et al.* Engineering an efficient and enantioselective enzyme for the Morita–Baylis–Hillman reaction. *Nat. Chem.* **14**, 313–320 (2022).

294. Kiser, P. D., Golczak, M., Lodowski, D. T., Chance, M. R. & Palczewski, K. Crystal structure of native RPE65, the retinoid isomerase of the visual cycle. *Proc. Natl. Acad. Sci. U. S. A.* **106**, 17325–17330 (2009).

295. Nguyen, P. H. *et al.* Amyloid oligomers: A joint experimental/computational perspective on Alzheimer's disease, Parkinson's disease, type II diabetes, and amyotrophic lateral sclerosis. *Chemical Reviews* vol. 121 2545–2647 (2021).

296. Ashtari, M. *et al.* The Role of the Human Visual Cortex in Assessment of the Long-Term Durability of Retinal Gene Therapy in Follow-on RPE65 Clinical Trial Patients. *Ophthalmology* **124**, 873–883 (2017).

297. Winkler, E. *et al.* Generation of Alzheimer disease-associated amyloid β 42/43 peptide by γ-secretase can be inhibited directly by modulation of membrane thickness. *J. Biol. Chem.* **287**, 21326–21334 (2012).

298. Singer, A. S. J. & Nicolson, G. L. The Fluid Mosaic Model of the Structure of Cell Membranes. *Science* **175**, 720–731 (1972).

299. Engelman, D. M. Membranes are more mosaic than fluid. *Nature* vol. 438 578–580 (2005).

300. Weber, P., Wagner, M. & Schneckenburger, H. Fluorescence imaging of membrane dynamics in living cells. *J. Biomed. Opt.* **15**, 046017 (2010).

301. Maugeri, Z. & Rother, D. Application of Imine Reductases (IREDs) in Micro-Aqueous Reaction Systems. *Adv. Synth. Catal.* **358**, 2745–2750 (2016).

302. Röllig, R., Plikat, C. & Ansorge-Schumacher, M. B. Efficient and Selective Carboligation with Whole-Cell Biocatalysts in Pickering Emulsion. *Angew. Chemie - Int. Ed.* **58**, 12960–12963 (2019).

303. Li, Z., Kessler, W., Van Den Heuvel, J. & Rinas, U. Simple defined autoinduction medium for high-level recombinant protein production using T7-based Escherichia coli expression systems. *Appl. Microbiol. Biotechnol.* **91**, 1203–1213 (2011).

304. Renzette, N. Generation of transformation competent E. coli. *Curr. Protoc. Microbiol.* **22**, A.3L.1-A.3L.5 (2011).

305. Heckman, K. L. & Pease, L. R. Gene splicing and mutagenesis by PCR-driven overlap extension. *Nat. Protoc.* **2**, 924–932 (2007).

306. Zymo Research. Zyppy ™ Plasmid Miniprep Kit. *Instr. Man.* **4037**, 1–9 (2014).

307. Gibson, D. G. *et al.* Enzymatic assembly of DNA molecules up to several hundred

kilobases. *Nat. Methods* **6**, 343–345 (2009).

308. Koschorreck, K., Wahrendorff, F., Biemann, S., Jesse, A. & Urlacher, V. B. Cell thermolysis – A simple and fast approach for isolation of bacterial laccases with potential to decolorize industrial dyes. *Process Biochem.* **56**, 171–176 (2017).

309. Gasteiger, E. *et al. The Proteomics Protocols Handbook - Chapter 52: Protein Identification and Analysis Tools on the ExPASy Server*. *The Proteomics Protocols Handbook* (2005).

310. Laemmli, U. K. Cleavage of structural proteins during the assembly of the head of bacteriophage T4. *Nature* **227**, 680–685 (1970).

311. Li, Y., Lu, B., Li, C. & Li, Y. First total synthesis of (±) Hedaol B. *Synth. Commun.* **33**, 1417–1423 (2003).

312. Brooks, J. L., Xu, L., Wiest, O. & Tan, D. S. Diastereoselective Synthesis of Highly Substituted Tetrahydrofurans by Pd-Catalyzed Tandem Oxidative Cyclization-Redox Relay Reactions Controlled by Intramolecular Hydrogen Bonding. *J. Org. Chem.* **82**, 57–75 (2017).

313. Sanhaji, G., Rousseaux, A., Noel, S. & Eichhorn, E. Solid form of (–)-Ambrox formed by a bioconversion of homofarnesol in the presence of a biocatalyst. (2020).

314. Linares-Palomino, P. J., Salido, S., Altarejos, J., Nogueras, M. & S??nchez, A. Synthesis and odour evaluation of stereoisomers of octahydrobenzopyran derivatives. *Flavour Fragr. J.* **21**, 659–666 (2006).

315. Kulciţki, V., Ungur, N., Gavagnin, M., Carbone, M. & Cimino, G. Further Synthetic Studies Towards the Austrodorane Skeleton: Synthesis of Austrodoral. *European J. Org. Chem.* **2005**, 1816–1822 (2005).

316. Scanlon, J. T. & Willis, D. E. Calculation of Flame Ionization Detector Relative Response Factors Using the Effective Carbon Number Concept. *J. Chromatogr. Sci.* **23**, (1985).

317. Mills, N. ChemDraw Ultra 10.0. *J. Am. Chem. Soc.* **128**, 13649–13650 (2006).

318. Baek, M. & Baker, D. Deep learning and protein structure modeling. *Nature Methods* vol. 19 13–14 (2022).

319. Stourac, J. *et al.* Caver Web 1.0: Identification of tunnels and channels in proteins and analysis of ligand transport. *Nucleic Acids Res.* **47**, W414–W422 (2019).

APPENDIX

A1. Supporting Figures & Tables

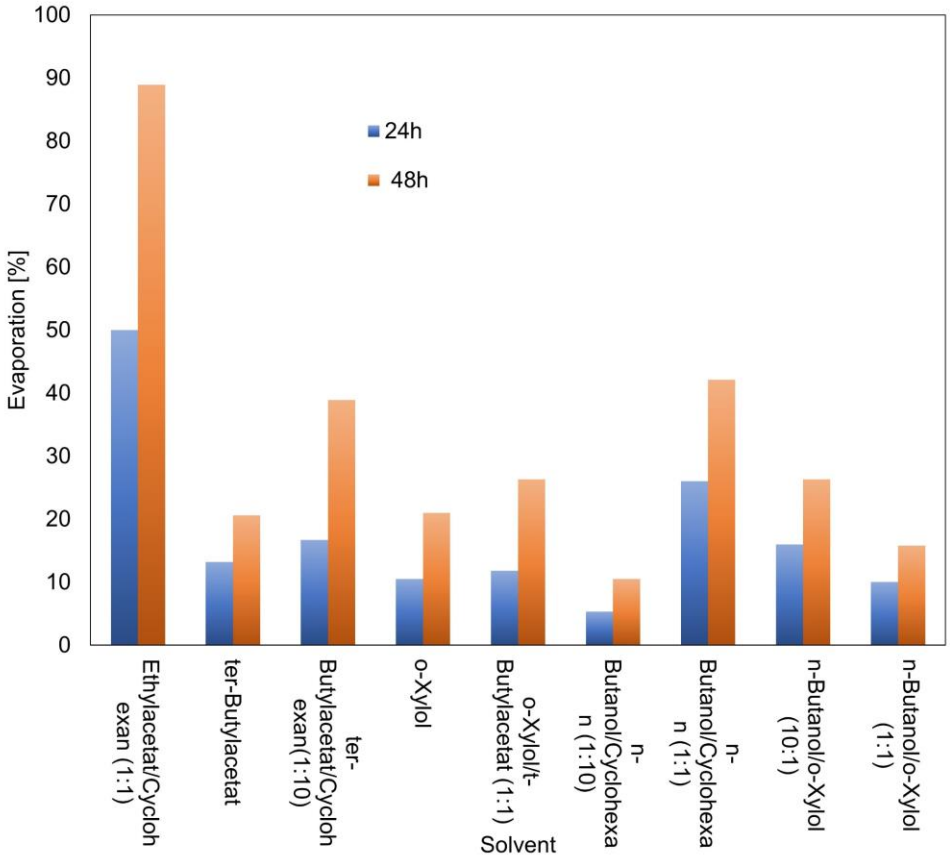

Supporting Figure S 1: Evaporation experiment for direct sample analysis from a two-phase system in a 96-DW. Glas inlets of 96-DW were filled with the corresponding organic solvent and the solvent front was marked. After 24 and 48 h hours the solvent front was marked again and evaporation ratio was determined as: d(solvent front,2)/d(solvent front,1). o-xylene was chosen as the most potent solvent due to low evaporation and best phase separation.

Supporting Table S 1: In-house SHC library stored in 96 DW plates.

NVP1

	1	2	3	4	5	6	7	8	9	10	11	12
A	WT	K.O	L36A	L36W	W169A	W169G	I261G	I261F	S307A	M132R	S307G	W312A
B	A419G	W312G	F365A	F365C	F365G	F365W	Q366A	Q366F	Q366G	M132R/A224V	A419F	V448G
C	A419W	A419Y	Y420A	Y420C	Y420G	Y420W	V448A	V448F	V448W	M132R/A224V/I432T	W489G	W489F
D	W489A	G490A	G490F	Y495G	Y495L	Y495W	G600A	G600F	G600L	M132R/432T	F601A	F601G
E	F601W	F605A	F605G	F605W	L607A	L607F	L607G	L607W	Y609G	D377L	Y609F	Y609L
F	S307F	G600W	Y612F	Y612G	Y612W	W312F	L36I	T.KO	BamSHC1	D377N/G600L	ZmoSHC1	SfuSHC
G	Q366W	Y609A	Y609T	Y609S	Y612S	D377N	L36V	TelSHC	RpaSHC	D377N	Sco/SfuSHC	BjaSHC
H	I261W	I261A	I261V	I261L	D377E	ApaSHC	S307C	ZmoSHC2	TtuSHC	FREI	PcaSHC	BamSHC2

NVP2

	1	2	3	4	5	6	7	8	9	10	11	12
A	L607C	L607D	L607E	L607H	L607I	L607K	L607M	L607N	L607P	L607Q	L607R	L607T
B	L607V	G600C	G600D	G600E	G600H	G600I	G600K	G600M	G600N	G600P	G600Q	G600R
C	G600S	G600T	G600V	G600Y	Y609E	Y609M	Y609V	I261C	I261D	I261E	I261H	I261K
D	I261M	I261N	I261P	I261Q	I261R	I261S	I261T	I261Y	T599A	T599I	T599L	T599M
E	T599V	S168Q	S307T	Q366E	Y420F	Y420F_G600V	Y420F_G600L	Y420F_G60oI	Y420F_L607A	Y420F_L607Q	Y420F_Y609D	Y420F_Y609L
F	TelSHC_S171Q	TelSHC_C312S	TelSHC_C312T	TelSHC_E371Q	TelSHC_F425Y	TelSHC_G609V	TelSHC_G609L	TelSHC_G609I	TelSHC_L616A	TelSHC_L616Q	TelSHC_Y618D	TelSHC_Y618L
G	ZmoSHC1_Q221S	ZmoSHC1_T369C	ZmoSHC1_T369S	ZmoSHC1_E429Q	ZmoSHC1_F486Y	ZmoSHC1_G667V	ZmoSHC1_G667L	ZmoSHC1_G667I	ZmoSHC1_L700A	ZmoSHC1_L700Q	ZmoSHC1_Y702D	ZmoSHC1_Y702L
H	Y420C/G600L	W312V/G600L	Y420R/G600L	Y420S/G600L	Y420Q/G600L	Y420T/G600L	Y420F/G600L	Y420W/G600L	Y420P/G600L	Y420I/G600L	Y420L/G600L	Y420M/G600L

NVP 1

	1	2	3	4	5	6	7	8	9	10	11	12
A			0.87		3.31	1.76	1.13		1.56			
B									1.38			
C				0.32			1.5			0.64		
D		1.73	0.31	2.29	1.54	1.62	0.61	1.59	11.4	3.21	5.12	1.98
E	0.77	1.91	2.74	0.38	0.55	4.87		1.82	1.17		1.73	
F	0.76	1.19	1.29	0.82	1.72	1.42	0.72				0.55	
G		1.43	0.78	2.28								
H												

Well	Variant	Conversion [%]
D9	G600L	11.38
E6	L607F	4.87
B9	Q366G	1.38
D10	G600W	3.21
E8	L607W	1.81
D3	G490A	0.31

Supporting Figure S 2: Evaluation of **52t** to **53t** biotransformation in 96-DW plate using the NVP1 showed the variants 600L and L607F as best variants and therefore confirmed the data which was obtained in a Master Thesis.[142]

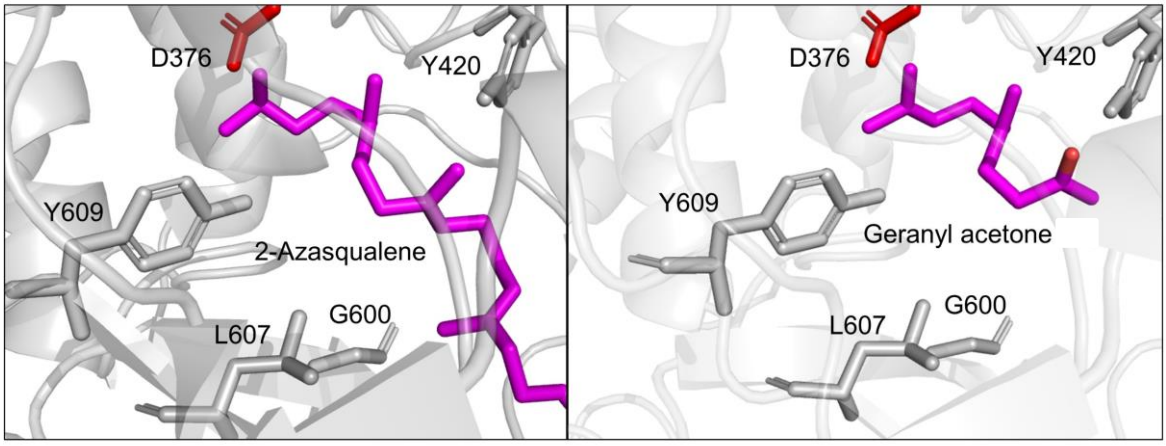

Supporting Figure S 3: Comparison of co-crystallized 2-Azasqualene in *Aac*SHC WT (left) with best result of docked substrate 52t in *Aac*SHC WT (right). Protonating aspartate shown in red sticks. Key mutated positions shown in grey sticks. 2-Azasqualene and geranyl acetone **52t** shown in magenta sticks. The comparison shows the similar pre-folding of both substrates in the active site.

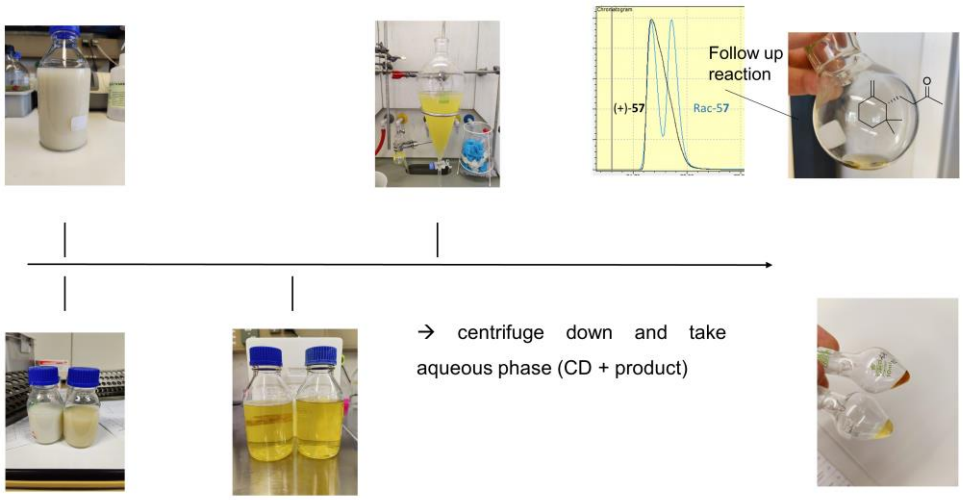

Supporting Figure S 4: Standard procedure for the upscaling reactions. *E. coli* whole cells expressing the desired variant, water, 2-hydroxypropyl-β-cyclodextrin and the desired substrate were shaken in Schott flask. Big 1 L upscale using **52c** on top. Smaller 200 mL upscales using the substrate **52c** analogues on the bottom.

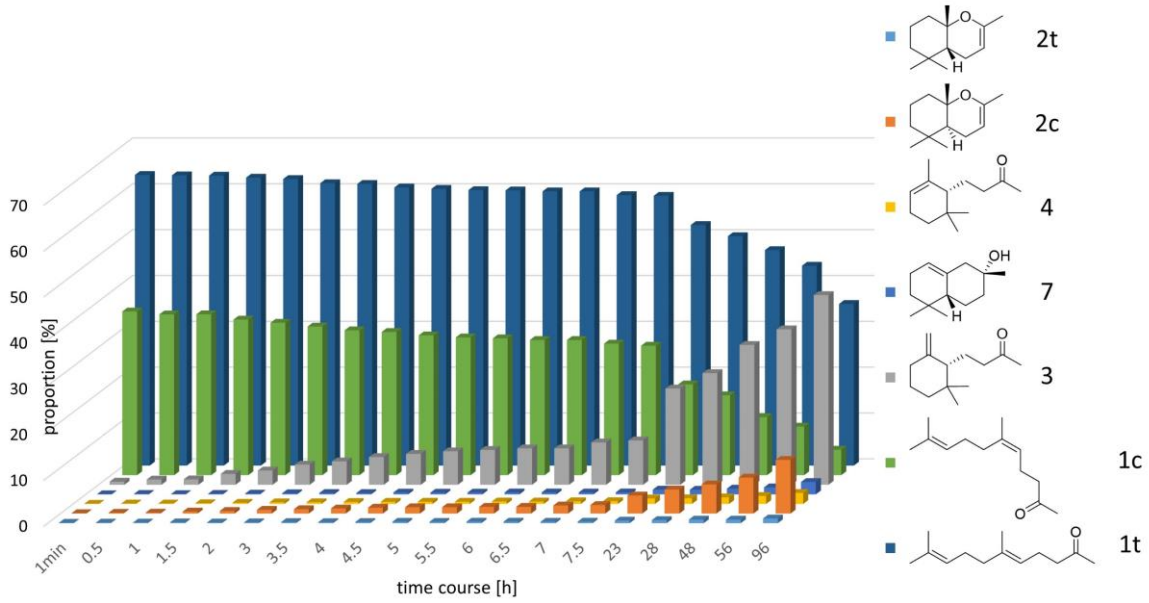

Supporting Figure S 5: Time course of the biotransformation of *E*/*Z*-geranyl acetone **52** (60:40) with the variant V. The variant V preferably converts the *Z*-geranyl acetone **52c** (green). (+)-ambrinol **57** is obtained as a side product by acid-catalyzed cyclization (buffer, pH = 6.0) of the product (–)-γ-dihydroionone **3** in the buffer.

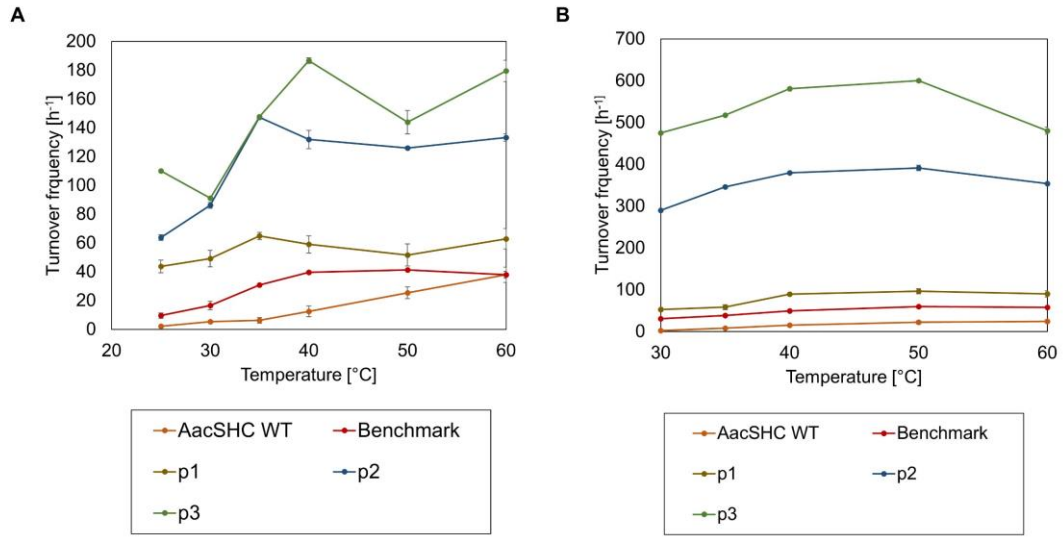

Supporting Figure S 6: Temperature profile of selected *Aac*SHC variants *in vivo* (A) and *in vitro* (B). Overall turnover frequencies are higher using the purified enzyme (B). Temperature optima differ in vivo and in vitro, presumably due to the phase transition of the membrane and the inherent activity affection of the membrane-bound SHC. Reaction conditions: 0.1 g_{CDW}/L cells, *dd*H2O, 1 mM **66**, 1 h for *in vivo*. 0.018-0.039 mg/mL SHC in 0.2% CHAPS, 20 mM citric acid, pH = 6.0, 1 mM 66 for *in vitro*. Error bars represent the s. d. between triplicates

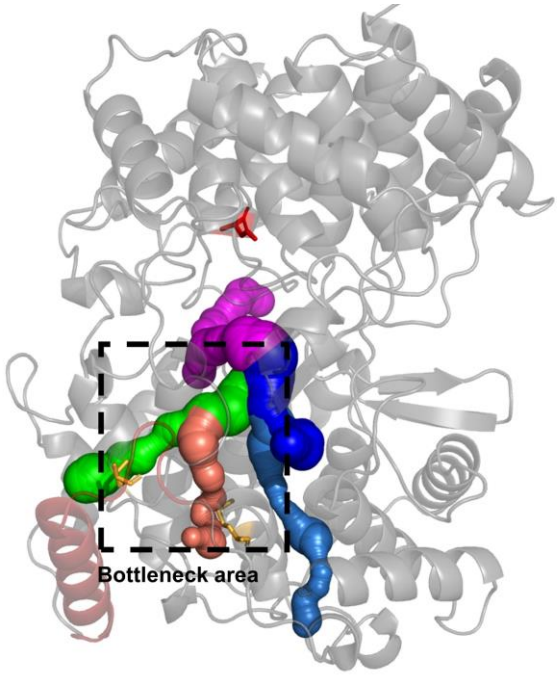

tunnel dark blue	tunnel green	tunnel light blue
N39	F129	V148
T41	K211	F166
L80	F434	A170
D87	C435	I432
D89	D436	F434
T90	F437	C435
R127	G438	V440
R208	F439	
F437	V440	
D604		
F505		

Supporting Figure S 7: CAVER[319] analysis of *Aac*SHC crystal structure (PDB: 1UMP). Protonating aspartate shown as red sticks. Benchmark enzyme B[129] mutations as bright orange sticks. Membrane-binding α-Helix shown as red cartoon. Most probable simulated entrance tunnels depicted in colored surface. Most of the entrance tunnels could be excluded, due to size and radii. Green entrance tunnel corresponds to the published putative entrance tunnel[75] and was also chosen for illustration in this work. On the right are the calculated bottleneck positions of the most

probable entrance tunnels. Highlighted in red are the positions accumulating in one area, here named 'bottleneck area'. The two mutations of the benchmark study are located within the bottleneck area and therefore may influence catalysis.

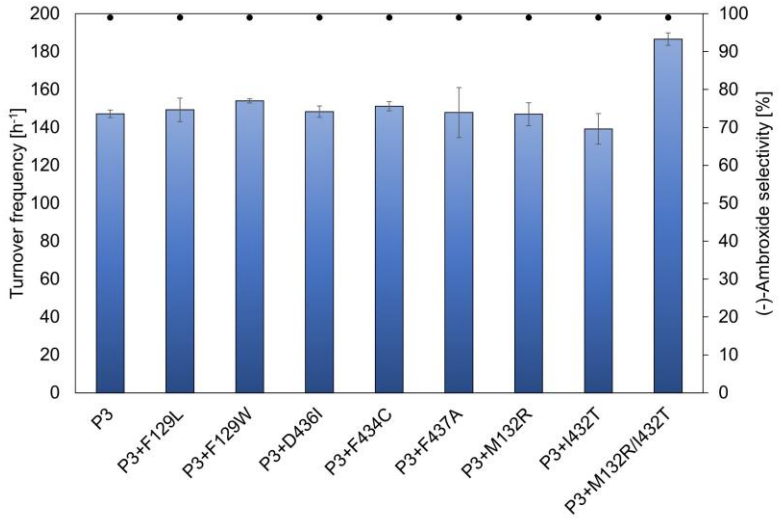

Supporting Figure S 8: Comparison of 'hit' variants from the entrance tunnel engineering by site-saturation mutagenesis in the bottleneck area *in vivo*. All introduced single-point mutations showed only slight to no increases in turnover frequency with no changes in (–)-ambroxide **7** selectvity. However, combination of the two mutations described as beneficial in the benchmark study[129] led to 1.3-fold improved turnover frequency, which suggests epistatic effects. Reaction conditions: 10 g_{CDW}/L cells, *dd*H2O, 10 mM **66**, 30°C, 20h. Reactions were performed in technical triplicates.

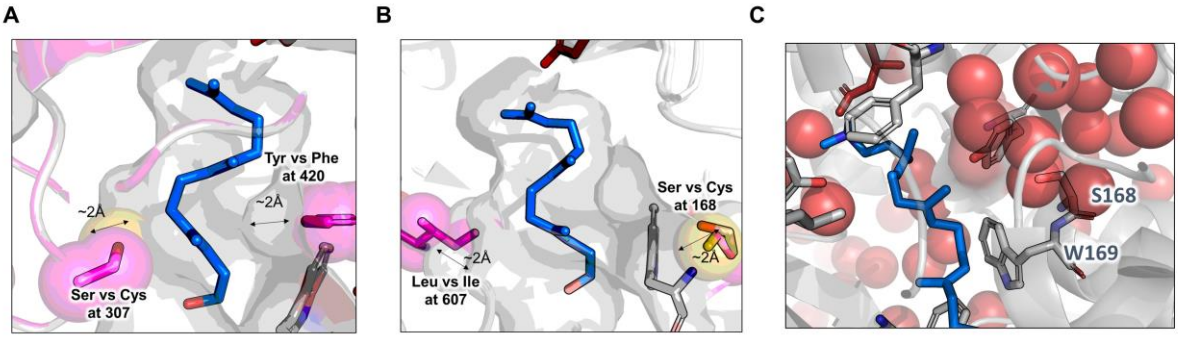

D

Sequence identity to *Aac* [%]		45.8	38.3	44.2	51	
active site amino acid position [based on *Aac*]	Aac	Zmo1	Zmo2	Tel	Sco	
36	L	V	L	L	L	
168	S	Q	Y	S	C	
169	W	W	W	W	W	
261	I	I	I	I	I	
306	A	A	P	P	A	
307	S	T	C	C	C	
312	W	W	W	W	W	
365	F	F	F	F	F	
366	Q	E	Q	E	E	
420	Y	F	F	F	F	
489	W	W	W	W	W	
600	G	G	G	G	G	
607	L	L	L	L	I	
609	Y	Y	Y	Y	Y	
612	Y	Y	Y	Y	Y	

conserved difference in hydrogen-binding pocket at 169

Supporting Figure S 9: Homologous SHCs and their subtle changes in the active site, which occurred during evolution. Substrate *E,E*-**66** shown as blue sticks. (**A**) Overlay of *Aac* and *Tel*SHC shows the two opposite positions 307 and 420. The *Tel* homolog creates ~2 Å space at position 420 with a phenylalanine instead of tyrosine, however, reduces space with a cysteine instead of a serine at position 307. (**B**) Overlay of *Aac* and *Sco*SHC shows the two opposite positions 607 and 168. *Sco* creates space at 607 and demands more space at position 168. (**C**) Active site of *Aac*SHC and co-crystallized aza-squalene **36** (blue sticks)**.** Water molecules in the crystal structures shown as red spheres. Water cluster around S168 may interact with transient carbocations by providing them electron density. (**D**) Active site residue comparison of *Aac*, *Zmo*1, *Zmo*2, *Tel* and *Sco*SHC.

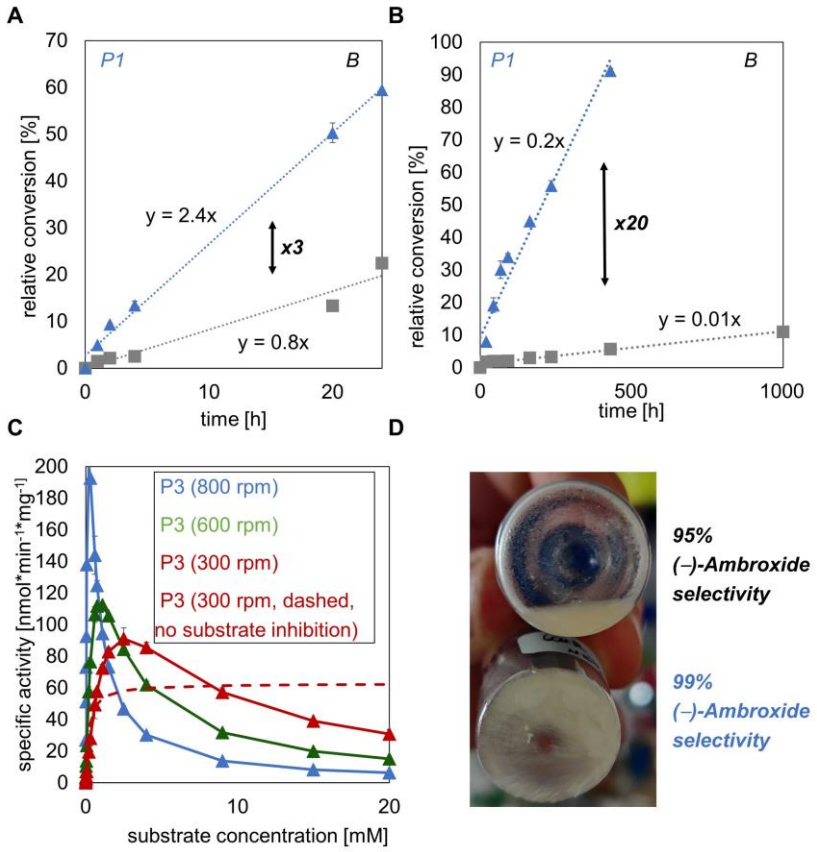

Supporting Figure S 10: (A) Comparison of variant P1 and B in the *in vivo* cyclization of *E,E*-**66**. Higher selective enzyme P1 shows 3-fold improved relative conversion. Conditions: 20 mM substrate, 5 g_{CDW}/L cells, *dd*H_2O, 30 °C, 800 rpm. (B) Second comparison *in vivo* of variant P1 and B with different conditions: 200 mM substrate, 30 g_{CDW}/L cells, H_2O, 30°C, 800 rpm. Interestingly, the more selective variant P1 shows 20-fold improved relative conversion, which may be to liquid side product produced by less selective variant B accumulating in the cellular membrane and downregulating the enzymatic activity.[160,245] **(C)** Substrate excess inhibition plots for the P3 catalyzed cyclization of **66** at varying shaking speeds (800, 600 and 300 rpm). The fourth graph (dashed lines) results from assuming no substrate inhibition, but standard initial rate kinetics. **(D)** Extracted and evaporated products from fully converted substrate **66** by P1 (bottom, blue) and B (top). Conditions: 500 µl 66 (90 g/L), 180 g_{CWW} /L cells, 100 mM citric acid, 0.048 g_{SDS}:g_{CWW}, pH = 5.1, 37 °C, 4 d. Only the 99% selective enzyme (blue) yields fully crystallized product.

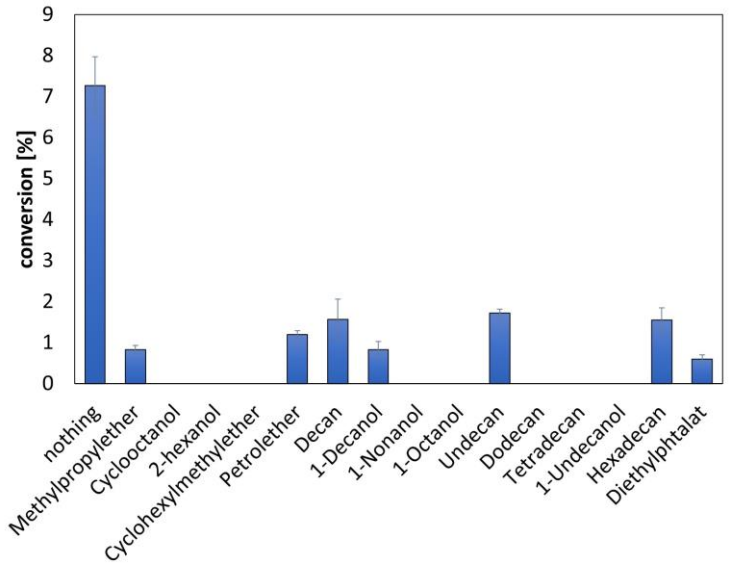

Organic solvent	logP
Methylpropyl ether	0.9
Cyclooctanol	2.1
2-hexanol	1.7
Cyclohexylmethylether	1.7
Petrolether	3.5
Decane	6.0
1-Decanol	3.5
1-Nonanol	3.1
1-Octanol	2.9
Undecane	6.6
Dodecane	7.1
Tetradecane	8.1
1-Undecanol	3.9
Hexandecane	8.8
Diethyl phtalat	2.0

Supporting Figure S 11: Two-phase system experiment in the cyclization of geranyl acetone **52t** towards hexahydrochromene **53t**. The reactione mixture consisting of 10 mg/mL *E. coli* whole cells in 500 µL *dd*H_2O and 10 mM substrate **52t** were overlayed with 100 µL organic solvents differing in their logP-values (proposed by ChemDraw) and stirred for 20 h at 30 °C. The reaction was stopped by adding 500 µL CH:EtOAc 1:1 and the organic extracts were analyzed via GS/MS.

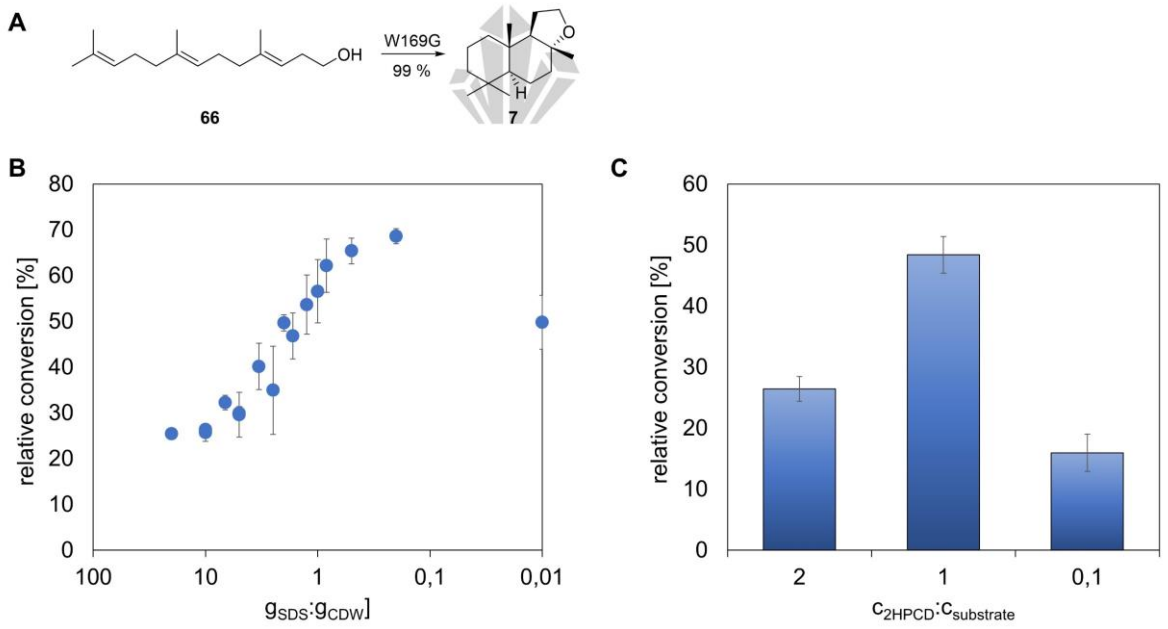

Supporting Figure S 12: Evaluation of optimal SDS and 2HPCD amount. (**A**) Cyclization of **66** by W169G was chosen as the model reaction for the evaluation. (**B**) SDS amount evaluation with the optimal ratio of 0.2 g_{SDS}:$g_{cell,CDW}$. Reaction conditions: 20 mM **66**, 10 mg_{CDW}/mL whole cells (W169G), *dd*H_2O, 40 °C, 20 h. (**C**) 2HPCD amount evaluation with the optimal ratio of equimolar amount. Reaction conditions: 10 mM **66**, 10 mg_{CDW}/mL whole cells (W169G), *dd*H_2O, 40 °C, 20 h. All biotransformations carried out as analytical biotransformations (cf. chapter 6.7.1)

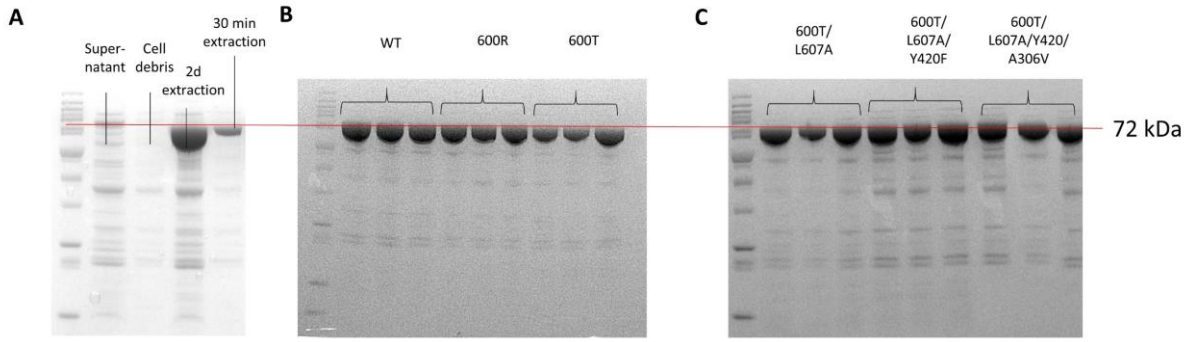

Supporting Figure S 13: Exemplary SDS-PAGE analysis of *Aac*SHC variants. (**A**) After thermolysis (cf. chapter 6.3.2) and extraction the supernatant and the cell debris contain no *Aac*SHC protein anymore. 2 d extraction was sufficient in extracting the enzyme form the cell debris. (**B**+**C**) Extraction of lyophilized whole cell batches containing the specific variants. Triplikates demonstrate the almost equal extraction among all whole cell pellets.

A2. Exemplary chromatograms